Analyzing and modeling environmental loading induced displacements with GPS and GRACE

A thesis accepted by the Faculty of Aerospace Engineering and Geodesy of the University of Stuttgart in partial fulfilment of the requirements for the degree of Doctor of Engineering Sciences (Dr.-Ing.)

by

Qiang Chen

born in Changde, China

Main referee:	Prof. Dr.-Ing. Nico Sneeuw
Co-referee:	Prof. Tonie Van Dam, Luxembourg
Date of defence:	06 August 2015

Institute of Geodesy
University of Stuttgart

2015

DGK Deutsche Geodätische Kommission
der Bayerischen Akademie der Wissenschaften

Reihe C Dissertationen Heft Nr. 752

Analyzing and modeling environmental loading induced displacements with GPS and GRACE

Von der Fakultät Luft- und Raumfahrttechnik und Geodäsie
der Universität Stuttgart
zur Erlangung der Würde eines
Doktors der Ingenieurwissenschaften (Dr.-Ing.)
genehmigte Abhandlung

Vorgelegt von

M.Sc. Qiang Chen

aus Changde – China

München 2015

Verlag der Bayerischen Akademie der Wissenschaften
in Kommission beim Verlag C. H. Beck

ISSN 0065-5325 ISBN 978-3-7696-5164-5

Adresse der Deutschen Geodätischen Kommission:

Deutsche Geodätische Kommission

Alfons-Goppel-Straße 11 ● D – 80 539 München

Telefon +49 – 89 – 23 031 1113 ● Telefax +49 – 89 – 23 031 - 1283 / - 1100

e-mail hornik@dgfi.badw.de ● http://www.dgk.badw.de

Hauptberichter: Prof. Dr.-Ing. Nico Sneeuw

Mitberichter: Prof. Tonie Van Dam, Luxembourg

Tag der mündlichen Prüfung: 06.08.2015

Diese Dissertation ist auch auf dem Dokumentenserver der Universität Stuttgart veröffentlicht

<http://elib.uni-stuttgart.de/opus/doku/e-diss.php>

ISSN 0065-5325 ISBN 978-3-7696-5164-5

Contents

Abstract

THE redistribution of atmospheric, oceanic and hydrological masses on the Earth's surface varies in time and this in turn loads and deforms the surface of the solid Earth. Analyzing such environmental loading signal and modeling its induced elastic displacements are of great importance for explaining geophysical phenomena. Based on the well-established loading theory, this thesis makes use of two different space-borne measurements, i.e. GPS and GRACE, along with other environmental loading data to investigate three different aspects of environmental loading and its induced elastic deformations:

Firstly, an increasing concern is observed recently over time variable seasonal signals in geodesy. Several model based approaches were applied to extract amplitude and phase modulated annual and semiannual signals. In view of this phenomenon, this thesis introduces an alternative approach, namely, singular spectrum analysis (SSA). With respect to these model-dependent approaches, the advantage of SSA lies in data-driven and model-independence. Several aspects regarding the application of SSA, e.g. optimal choice of window size, are investigated before showing its abilities. Through applying SSA to the lake level time series of Lake Urmia (Iran) and the basin averaged equivalent water height time series of the Congo basin, the capabilities of SSA in separating time varying seasonal signals are demonstrated. In addition, we find that SSA is also able to extract the non-linear trend as well as long-term oscillations from geodetic time series.

Secondly, we look into the comparison between GPS and GRACE with an emphasis on GRACE data filtering. Three types of deterministic filters and two types of stochastic filters are studied and compared over GPS sites from two regions, i.e. the Europe area and the Amazon area. The comparisons indicate that no single filtering scheme could provide consistently better performance over other considered filters. However, we find that the stochastic filters generally show better performance than the deterministic filters. The DDK 1 filter outperforms other filters in the Europe area and the regularization filter of parameter $\lambda = 4$, which follows the concept of the DDK filters, shows optimal performance in the Amazon area. The combination of the isotropic Gaussian filter of a low smoothing radius, e.g. around 300 km with the destriping filter is proved to be optimal filter choice if only the deterministic filters are considered.

Thirdly, based on an overview of displacements modeling at various spatial scales, we evaluate three methods, i.e. two types of half-space approaches and the classic Green function approach, by using a high spatial resolution local load data along the lower Mississippi river when a severe flood happened in 2011. The equivalence between the two half-space approaches, i.e. point load approach and surface load approach, are demonstrated with the local load data. However, the point load approach is recommended for practical use in terms of computational efficiency. In addition, within such a limited spatial extent, we investigate the differences between the half-space approach and the Green function approach. It is shown that the half-space approach predicts larger displacements than the Green function approach and agrees better with the observed deformations at 11 considered GPS sites. Meanwhile, strong global environmental

loading effects are found via two global hydrological models, i.e. GLDAS and MERRA. Thus, a reduction of these far-field loading effects beforehand is suggested before probing the local crustal structure using the half-space approach.

Last but not least, based on the local load data, the effects of site-dependent Green functions are studied with two types of site-dependent Green functions, which were generated by modifying the local crustal structure of the REF Earth model using the CRUST 1.0 and CRUST 2.0 models. A relative RMS of differences of more than 5 % in vertical component and 25 % in horizontal components are found with respect to the PREM Earth model based Green functions. It indicates that the Green functions could contribute more uncertainties in loading induced displacements modeling than reported in the literature.

Zusammenfassung

DIE Massenumverteilungen zwischen Atmosphäre, Ozeanen und Hydrologie der Erdoberfläche variieren stetig und führen im Gegenzug zu Auflasten und Deformationen der festen Erde. Die Untersuchung dieser Auflastsignale und die Modellierung der induzierten elastischen Verformungen sind von enormer Bedeutung für die Erklärungen geophysikalischer Phänomene. Basierend auf gängigen Theorien werden in dieser Dissertation die beiden Satellitenverfahren GPS und GRACE zusammen mit anderen Auflastdaten genutzt, um drei Aspekte von Auflasten und die von diesen verursachte elastischen Deformationen näher zu untersuchen:

Zunächst lässt sich in der Geodäsie eine wachsende Tendenz erkennen, auch zeitlich variable, saisonale Signale besser zu untersuchen. Zahlreiche, auf Modellen basierende Verfahren werden angewendet, um Amplituden und Phasen aus jährlichen und halbjährlichen Signalen zu erfassen. Für diese Aufgabe wird in dieser Arbeit die „singular spectrum analysis“ (SSA) als alternative Methode dargestellt. Im Gegensatz zu den üblichen modellbasierten Verfahren arbeitet die SSA modellunabhängig nur auf Grundlage der Daten. Verschiedene Freiheitsgrade in der SSA, wie zum Beispiel die Wahl der optimalen Fenstergröße, werden vor der Verwendung untersucht. Die Fähigkeit der SSA, saisonale Signale zu trennen, wird sowohl an der Bestimmung des Wasserstandes für den Urmia-See (Iran) als auch anhand der Zeitreihe der über dem Kongo-Becken gemittelten Massenänderungen demonstriert. Zusätzlich können mit SSA auch nichtlineare Trends und langfristige Oszillationen aus geodätischen Zeitreihen extrahiert werden.

Zweitens werden die Daten von GPS und GRACE unter besonderer Berücksichtigung der Filterung von GRACE-Daten verglichen. Drei Arten deterministischer Filter sowie zwei Arten stochastischer Filter werden untersucht und für die GPS-Stationen von zwei ausgewählten Regionen in Mitteleuropa und dem Amazonasgebiet gegenübergestellt. Der Vergleich bestätigt, dass keiner der Filter grundsätzlich den Anderen überlegen ist. Jedoch kann gezeigt werden, dass die stochastischen Filter im Allgemeinen besser abschneiden als die deterministischen Ansätze. Der DDK 1 Filter führt in Europa zu den besten Ergebnissen, während ein „Regularisierungsfilter“, der dem Konzept der DDK Filter nachempfunden ist, mit einem Regularisierungsparameter $\lambda = 4$ die besten Ergebnisse in für das Amazonasbecken liefert. Die Kombination aus einem isotropen Gaußfilter mit kleinem Glättungsradius, z. B. 300 km, und einem „De-striping“-Filter konnte als optimaler Filter bestätigt werden, solange nur deterministische Filter verwendet werden

Drittens werden nach einer Zusammenfassung der Deformationsmodelle auf verschiedenen räumlichen Skalen drei Methoden – zwei Arten von „half-space“-Ansätzen und die klassische Methode der Greenfunktionen – auf die räumlich hochauflösenden Daten der Überflutungen im Mississippi-Becken (2011) angewendet. Die Gleichwertigkeit der beiden „half-space“-Ansätze, einerseits der „point load approach“ und andererseits der „surface load approach“ werden für lokale Auflastdaten bestätigt. Aus Gründen der numerischen Effizienz

ist jedoch der „point load approach“ zu bevorzugen. Außerdem werden innerhalb des räumlich begrenzten Gebietes auch die Unterschiede zwischen den „half-space“-Ansätzen und die Methode der Greenfunktionen gegenübergestellt. Es wird gezeigt, dass die „half-space“-Ansätze größere Deformationen vorhersagen als die Greenfunktionen, wobei die Ergebnisse besser zu den Beobachtungen der 11 GPS-Stationen passen. Inzwischen können auch größere globale Auflasteffekte in den globalen hydrologischen Modellen, wie z. B. GLDAS und MERRA, gefunden werden. Daher wird eine vorherige Reduktion der Fernwirkung von Auflasteffekten empfohlen, ehe man eine lokale Krustenstruktur mit den „half-space“-Ansätzen erforscht.

Nicht zuletzt werden auch die Effekte der ortsabhängigen Greenfunktionen für die lokalen Auflastdaten studiert, wobei die beiden ortsabhängen Varianten der Greenfunktionen aus der lokalen Krustenstruktrur des REF Erdmodells mit den Modellen CRUST 1.0 bzw. CRUST 2.0 erzeugt werden. Im Vergleich zu den Greenfunktionen aus dem PERM Erdmodell wird ein relativer RMS der Differenzen von mehr als 5 % in der Vertikalkomponente und 25 % in der Horizonalkomponente beobachtet. Daraus kann man ablesen, dass die Greenfunktionen deutlich mehr Unsicherheiten zu den auflastinduzierten Deformationen beitragen, als dies bisher in der Literatur wahrgenommen wird.

List of Figures

List of Tables

List of Abbreviations

BIO	Biomass
CE	Center of solid Earth
CF	Center of Figure
CH	Center of surface Height figure
CL	Center of surface Lateral figure
CM	Center of Mass
CN	Center of Network
CSR	Center for Space Research
DEM	Digital Elevation Model
DLR	Deutsches Zentrum für Luft and Raumfahrt
ECCO	Estimating the Circulation & Climate of the Ocean
ECMWF	European Centre for Medium-Range Weather Forecasts
EMD	Empirical Mode Decomposition
ENVISAT	ENVIromental SATellite
EPN	EUREF Permanent Network
ESA	European Space Agency
EWH	Equivalent Water Height
FES2004	Finite Element Solutions 2004
GFZ	GeoForschungsZentrum
GGFC	Global Geophysical Fluids Center
GGOS	Global Geodetic Observing System
GIA	Glacial Isostatic Adjustment
GLDAS	Global Land Data Assimilation System
GMSL	Global Mean Sea Level
GNSS	Global Navigation Satellite System
GPS	Global Positioning System
GRACE	Gravity Recovery And Climate Experiment
GRGS	the Group de Recherche de Geodesie Spatiale
GRS80	Geodetic Reference System 80
GSHA	Global Spherical Harmonic Analysis
GSHS	Global Spherical Harmonic Synthesis
GW	Ground Water
ICA	Independent Component Analysis
ICGEM	International Centre for Global Earth Models

IERS	International Earth Rotation Service
IGS	International GNSS Service
IMF	Intrinsic Mode Function
ITG	Institute of Theoretical Geodesy, Bonn
ITRF	International Terrestrial Reference Frame
JPL	Jet Propulsion Laboratory
KBR	K-band ranging
MERRA	Modern-Era Retrospective Analysis for Research and Applications
MSSA	Multi-channel Singular Spectrum Analysis
NASA	National Aeronautics and Space Administration
NCEP	National Centers for Environmental Prediction
NGL	Nevada Geodetic Laboratory
NSE	Nash-Sutcliffe Efficiency
OBP	Ocean Bottom Pressure
OMCT	Ocean Model for Circulation and Tides
PCA	Principal Component Analysis
PEMC	Parametric Earth Model, Continental
PODAAC	Physical Oceanography Distributed Active Archive Center
PREM	Preliminary Reference Earth Model
RMS	Root Mean Square
SIRGAS	Geodetic Reference System for the Americans
SLR	Satellite Laser Ranging
SM	Soil Moisture
SNREI	Spherically symmetric, Non-Rotating, Elastic and Isotropic
SRTM	Shuttle Radar Topography Mission
SSA	Singular Spectrum Analysis
SSD	Singular Spectrum Decomposition
SWE	Snow Water Equivalent
SW	Surface Water
TWS	Total Water Storage
WGHM	WaterGAP Global Hydrology Model
WGS84	World Geodetic System 84
WRMS	Weighted Root Mean Square

Chapter 1

Introduction

1.1 Earth's elastic surface loading

THE Earth system with its atmosphere, ocean, continental hydrology, ice caps and its interior is subject to a multitude of dynamic processes. Mass variations and mass transports within the Earth system are happening at a broad variety of spatial and temporal scales and are driven by extensive interior and exterior forces. Fig. 1.1 displays all themes in terms of their field of Earth science. These geophysical processes cover from instantaneous to diurnal and to secular in terms of temporal scales, and from local, regional up to global in terms of spatial scales. They interact with each other and produce a series of consequences, e.g. crust deformation. To the interest of this thesis, we focus on mass variations from three geophysical processes, i.e. hydrology, atmosphere and ocean, which represent most significant mass changes in terms of the spatial and temporal scales shown clearly in Fig. 1.1.

Comparing to other surface mass loading like ice caps on secular time scales, these three surface mass loading sources present mostly on time scales ranging from monthly to annual and inter-annual. The resultant surface crust deformation accordingly behaves elastically with the same temporal resolutions. Thus, these three environmental surface loading components are called Earth's elastic surface loading here in this thesis. What's more, these three environmental loading components also contribute most signals in various satellite observations, for example, deformation observations from GPS (Global Positioning System) introduced in Section 1.2 and time-variable gravity measurements from GRACE (Gravity Recovery And Climate Experiment) presented in Section 1.3. The following will give a brief description of these three elastic surface loading components.

Hydrological water loading The water distribution within the global water cycle is a complex system and is the main driving force for life on the land masses. The whole hydrological cycle is composed of a series of water mass variations, which include evaporation from water surfaces and bare soil, evapotranspiration from vegetated land, transport of water vapour in the atmosphere, cloud droplet formation and cloud dynamics, the mechanisms leading to liquid and solid precipitation, the movement of water and change in soil moisture in the unsaturated soil including surface and river run-off, ground water flow (Rast et al., 2014). Owing to such a complex hydrological cycle system, water plays a fundamental role in shaping weather and climate.

Moreover, the hydrological cycle drives continental water to redistribute over the Earth's surface and it gives rise to a series of geophysical phenomena. One significant phenomenon due

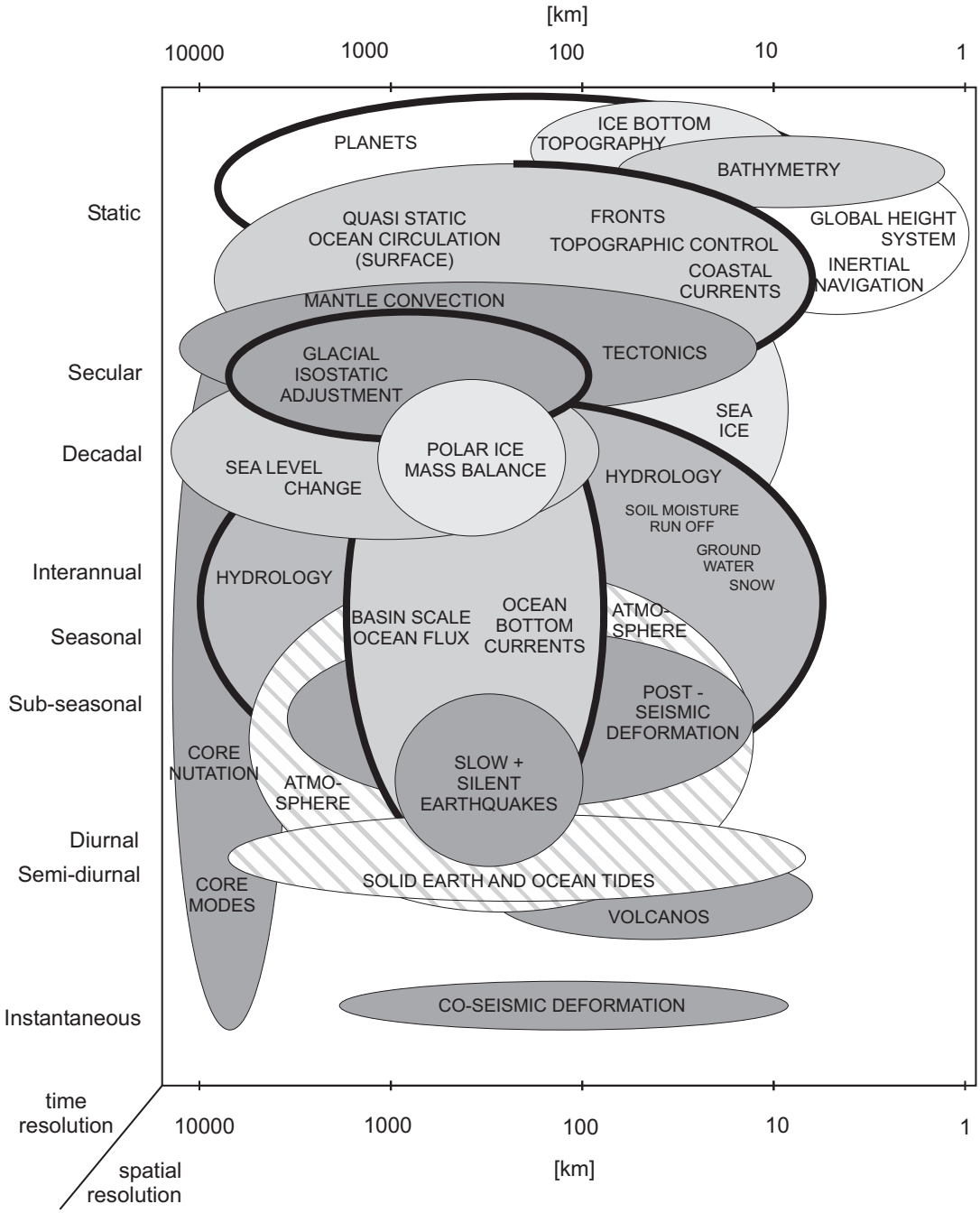

Figure 1.1: *Spatial and temporal scales of geophysical processes within the Earth system (courtesy: Sneeuw et al. (2005))*

to hydrological loading is crust deformation as discussed by van Dam et al. (2001). The predicted vertical displacements computed from hydrological models can reach up to 30 mm (van Dam et al., 2001) and show high correlation with observed displacements from GPS. Since then, the hydrological loading signals began to gain our interests in the spaceborne measurements. With the advent of satellite gravimetry, e.g. GRACE, hydrological loading signals could be retrieved at continental scales with unprecedented precision (Tapley et al., 2004) and studies of

the hydrological loading induced displacements multiplied using both GPS and GRACE techniques. Several studies have demonstrated the high agreement on the hydrological loading induced deformations between these two techniques (see Davis et al., 2004; van Dam et al., 2007; Tregoning et al., 2009; Tesmer et al., 2011; Fu et al., 2012, etc.).

Apart from the spaceborne measurements, several institutes provide operational hydrological models which are widely applied in hydrological loading related studies for mutual validation. Commonly used hydrological models are GLDAS (Global Land Data Assimilation System) (Rodell et al., 2004) , WGHM (WaterGAP Global Hydrology Model) (Döll et al., 2003) and MERRA (Modern-Era Retrospective Analysis for Research and Applications) land surface hydrology (Reichle et al., 2011). Hydrological products offered by these institutes are of different spatial and temporal resolutions, for example, 3-hourly and monthly products with both spatial resolutions of $0.25^\circ \times 0.25^\circ$ and $1^\circ \times 1^\circ$ from GLDAS. However, since they are models in essence, they are not consistent everywhere and suffer from large uncertainties. In addition, it has been demonstrated that no models is superior to others and performances of these models are region or basin dependent (Sneeuw et al., 2014; Lorenz et al., 2014).

Atmospheric mass loading Atmospheric mass loading, both tidal and non-tidal, has already been studied extensively since last century (see Spratt, 1982, etc.). Mass variations in the atmosphere affect both crust deformation and gravity changes at the Earth's surface (van Dam and Wahr, 1987; van Dam et al., 1994). Normally, effects due to the atmospheric mass loading are expected to be removed during the satellite data processing (Dach et al., 2011). For example, during the GPS data processing, the tidal atmospheric loading effects are well modeled and removed at the observation level by models recommended by IERS (International Earth Rotation Service) (Petit and Luzum, 2010). Likewise, in the GRACE data processing, an atmosphere dealiasing procedure, which expects to remove both tidal and non-tidal atmospheric loading effects, is required to better retrieve the hydrological information (e.g., Han et al., 2004).

However, for the non-tidal atmospheric loading effects, no operational models at the observational level are available yet for GPS data processing and this effect is normally removed by climate models after data processing. Several climate models are commonly used to predict the deformation, e.g. WGHM and NCEP (National Centers for Environmental Prediction) (Kalnay et al., 1996). As the atmosphere interacts closely with the ocean, an ocean response correction is required (van Dam et al., 2010). It is worth noting that care should be taken in the comparison of GPS and GRACE due to their unequal handling of the atmospheric mass loading effects and this point is also valid for oceanic mass loading. Specifically, it is emphasized in Section 4.3.

Oceanic mass loading Like the atmospheric mass loading, oceanic mass loading comprises tidal and non-tidal loading as well. Tidal oceanic loading effects are also well modeled using the ocean tide models, for example, FES2004 (Finite Element Solutions) model (Lyard et al., 2006) suggested by IERS. Thus, tidal oceanic loading effects could be eliminated at the observation level during the raw data processing. For the non-tidal oceanic loading effects, they are generally computed and removed by making use of ocean bottom pressure (OBP) products from the oceanic models, e.g. ECCO (Estimating the Circulation & Climate of the Ocean) (Williams and Penna, 2011; van Dam et al., 2012). Alternatively, displacement products due to

the above-mentioned non-tidal atmospheric and oceanic loading effects are publicly available from several organizations, e.g. the Global Geophysical Fluids Center (GGFC)[1].

In reality, the Earth's surface experiences the superposition of all loading effects. The elastic response of the solid Earth to surface load variations shows non-linear motions in different time scales ranging from long (inter-annual) to short (seasonal) and very short (daily, sub-daily) scale. These variations are detectable in geodetic observables, e.g. displacements observed by GPS (see Section 1.2) or derived from gravity spherical coefficients by GRACE (see Section 1.3).

1.2 The GPS technology and its applications

GPS has its root as a successor to military satellite positioning systems developed by the Department of Defense, USA, in 1960s (Evans et al., 2002). The GPS project was initialized in 1973 to overcome the limitations of those previous satellite positioning and navigation systems, e.g. needs for more accurate navigation in military and civilian sectors. The whole GPS system was designed based on the success of the Doppler technique by introducing the measurement of a biased range to the satellite, which remarkably improved the positioning precision in the meter level. By 1994, with the completion of a full constellation of 24 satellites, GPS became fully operational ensuring that users could see sufficient satellites (at least four) at any time, any where in the world. These 24 satellites are scattered in six evenly distributed orbital planes at an inclination angle of 55°. Thus, each orbital plane nominally contains four satellites. GPS signals are transmitted to an user's receiver at frequencies L1 = 1575.42 MHz, and L1 = 1227.60 MHz, which are encoded with the navigation message, e.g. orbit parameters. Via the navigation message, the receiver can obtain the satellite's coordinates (X_s, Y_s, Z_s) in the geocentric Cartesian coordinate system, i.e. WGS84 (World Geodetic System 84).

The basic principle of GPS positioning is trilateration, which requires minimally three ranges to three known points. In the case of GPS, the known points are the positions of the available satellites in the sky and the observed ranges are the distances between the GPS satellites and an user's GPS receiver, e.g. a fixed GPS site. GPS has two basic observables. One is code pseudorange, which measures the difference in time between the receiver's local clock and an atomic clock on board a satellite and multiplied by the speed of light to get the range, can readily provide us with a positioning precision of meters. The simplified observation equation to compute a GPS receiver's position (X_r, Y_r, Z_r) using pseudorange measurements is given by (see e.g. Kleusberg, 2009)

$$P = \rho + c(dt_r - dt_s) + d_I + d_T + \epsilon \,, \tag{1.1}$$

with

$$\rho = \sqrt{(X_r - X_s)^2 + (Y_r - Y_s)^2 + (Z_r - Z_s)^2} \,, \tag{1.2}$$

where P denotes the pseudorange observable from one GPS satellite and c is the light speed; dt_r and dt_s represent the receiver clock error and the satellite clock error, respectively; d_I is the ionospheric effect and d_T denotes the tropospheric effect; ϵ stands for remaining observation errors. Since the satellite clock error, the ionospheric and tropospheric effects are normally well modeled, the remaining unknown parameters are the receiver's position (X_r, Y_r, Z_r) and the receiver's clock error dt_r. Thus, a minimum of four satellites are required to constitute four equations like Eq. (1.1) to resolve the unknown parameters.

[1] http://geophy.uni.lu/

The other observable is carrier phase observation (ϕ), which measures the difference between the phase of the incoming carrier wave and the phase of a signal internally generated by the receiver. The corresponding observation equation is formed by (see e.g. Kleusberg, 2009)

$$\phi = \rho + c(dt_r - dt_s) - d_I + d_T + \lambda N + \epsilon \,, \tag{1.3}$$

where N is an integer phase ambiguity and λ denotes the wave length of the carrier. Measuring carrier phase is practically to measure the fractional phase (ϕ) and to keep tracking numbers (N) of the full carrier wave. Therefore, ambiguity resolution is essential to obtain the highest possible precision for geodetic applications using carrier phase observables. The fractional carrier phase (ϕ) can be observed by electronics with precision better than 1 % of the wavelength (19.0 mm for L1 and 24.4 mm for L2), which corresponds to the accuracy of a few millimeter level (Blewitt, 1989).

With the development of GPS, in 1994, the official organization – the International GPS Service (IGS, now renamed as International GNSS Service) was established (Beutler et al., 1994b). Since then, GPS had its fast development in 1990s toward high precision, which includes further refinement of tropospheric modeling (Davis et al., 1993), improved orbit models (Beutler et al., 1994a) and reference system conventions (McCarthy, 1996). In addition, data reprocessing of global GPS datasets began in earnest since the foundation of IGS and all levels GPS products, from raw observations to coordinate time series, are made publicly available by IGS since that.

With the further advancement of ambiguity resolution algorithms and background models, e.g. ionospheric and tropospheric delay models, station coordinate time series provided by the first IGS data reprocessing campaign, which contributed to ITRF2008 (International Terrestrial Reference Frame) (Altamimi et al., 2011), can reach a median repeatability of 4.7 mm in the vertical and 1.5 mm in the horizontal coordinates (Collilieux et al., 2011). Currently, the second IGS data reprocessing campaign contributing to the forthcoming ITRF2014 is under development. Additionally, the success of GPS has led to the development of similar systems and four positioning systems currently exist. Such multiple systems are generally referred to as GNSS (Global Navigation Satellite System).

Apart from IGS, other organizations or institutes, e.g. JPL (Jet Propulsion Laboratory) and NGL (Nevada Geodetic Laboratory) from America, also provide global continuous coordinate time series for public using state-of-the-art processing techniques. Furthermore, several regional GPS networks with dense coverage of stations, e.g. SIRGAS (Geodetic Reference System for the Americans) and EPN (EUREF Permanent Network), are operating their processing and combination centers to provide precise products for regional applications.

Thanks to those organizations or institutes, for more than two decades, a global network of GPS stations (see Fig. 1.2) has been providing us with continuous measurements of surface displacements. These coordinate time series have allowed us to monitor a variety of geophysical phenomena, such as tectonics, geodynamics, post-glacial rebound, post-seismic deformations (Herring, 1999). In addition, one more significant feature of the GPS time series is to help studying the surface mass loading phenomenon at global (e.g., van Dam and Wahr, 1987; van Dam et al., 2001), regional (e.g., Heki, 2001) and local scales (e.g., Bevis et al., 2004).

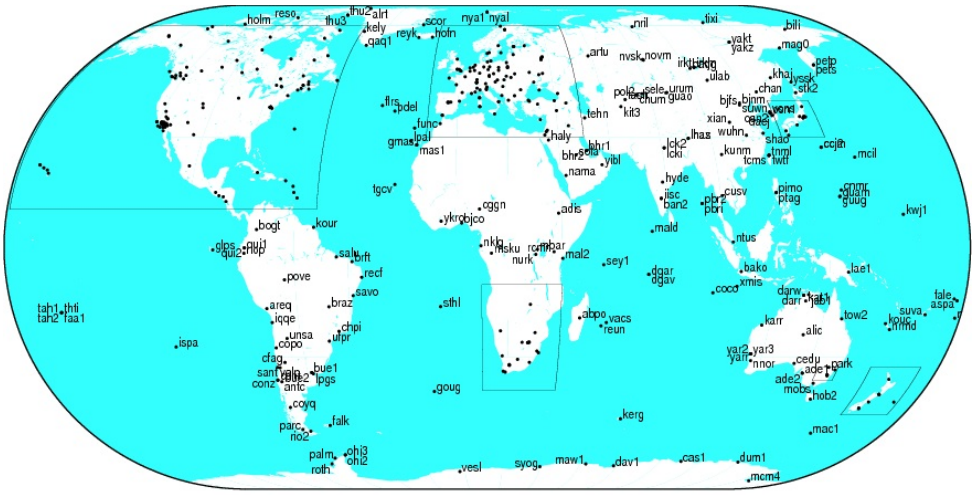

Figure 1.2: *A global network of* GPS *sites (courtesy:* IGS*).*

GPS for geophysics GPS contributes to geophysics through comparing the observed and modelled movement of the Earth's surface (Blewitt, 2007). The observed surface displacements represent the combination of a variety of geophysical phenomena with different temporal and spatial scales, which requires geophysics to be modelled as a whole. However, most geophysical phenomena are modelled separately in practice, such as ocean tidal models. GPS time series with different time length and resolution are required to explore different geophysical processes in terms of time resolution of the geophysical phenomena.

Short but high-sampling rate GPS data, for example 1 Hz GPS data, are utilized to study coseismic displacements (e.g., Larson et al., 2003), seismic waves (e.g., Nikolaidis et al., 2001), volcanism (e.g., Larson et al., 2001), which last from few seconds to few minutes. To investigate the tsunami loading, storm-surge loading and tidal loading effects, high-sampling rate GPS products with longer time span are processed and analyzed. Deformations due to the above-mentioned elastic surface mass loading, which normally have a seasonal signature, require low time resolution (daily or weekly) but relatively long GPS time series. For this type of GPS data with even longer time length, for example, more than 10 years, are used in long-time viscoelastic deformation studies, such ice sheet loading studies (e.g., Wahr et al., 2001). In addition, GPS time series with different time scales ranging from seconds to decades are appropriate for studying all phases of the earthquake cycle (e.g., Hammond, 2005).

In terms of signal composition buried in the GPS time series, e.g. linear trend and periodic seasonal signals, these components are normally of separate interests. For many applications, a mathematical model like Eq. (1.4) (Nikolaidis, 2002), is conventionally deployed to fit a discrete time series of the station's position.

$$y(t_i) = y_0 + vt_i + \sum_{k=1}^{q} a_k \sin(2\pi f_k t_i) + b_k \cos(2\pi f_k t_i) + \sum_{j=1}^{n_g} g_j H(t_i - T_{gj}) + \epsilon(t_i)\,, \qquad (1.4)$$

where t_i is the epoch of observation i in decimal year, y_0 is a constant initial offset, v is a constant velocity, a_k and b_k are the coefficients of periodic terms, f_k are the frequencies. The whole term $\sum_{j=1}^{n_g} g_j H(t_i - T_{gj})$ corrects for any number (n_g) of offsets with magnitudes g_j at epochs T_{gj}, and H denotes Heaviside step function. The last term $\epsilon(t_i)$ is the noise term, i.e. unmodelled signal

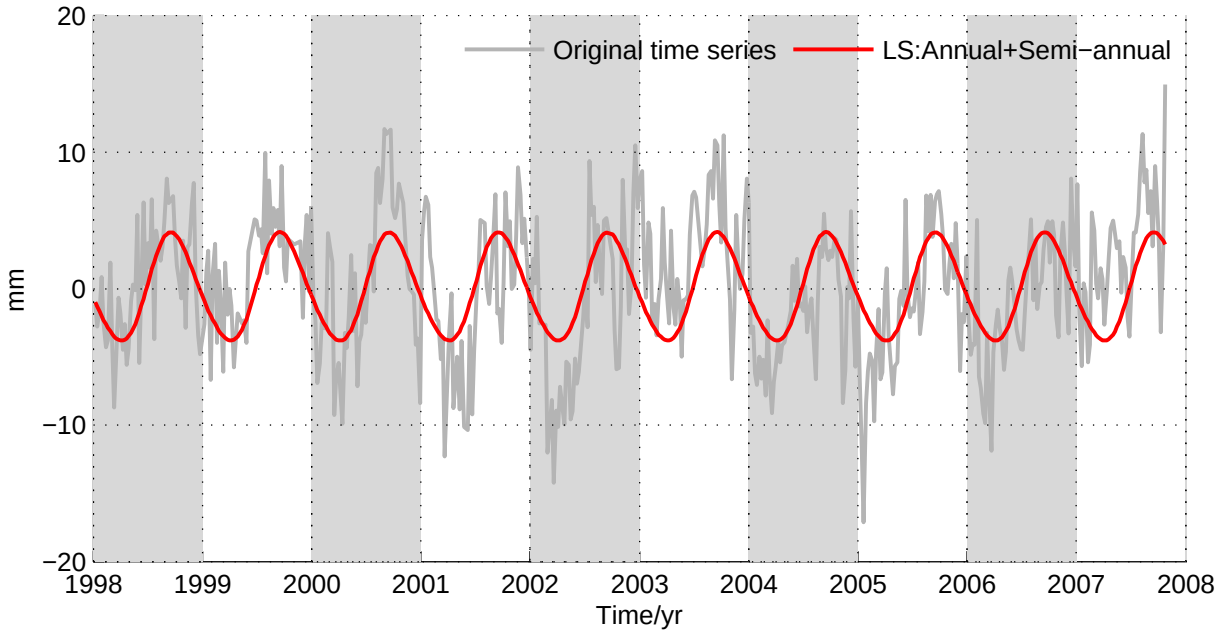

Figure 1.3: *Original height time series of station* WIS1 *and the* LS *fit.*

in Fig. 1.3. Most frequently a linear trend together with annual ($f_1 = 1$ cpy) and semi-annual ($f_2 = 2$ cpy) signals are resolved using the model of Eq. (1.4) (e.g., Zhang et al., 1997; Mao et al., 1999). It is worth noting that offsets due to equipment changes or earthquakes have significant effects on velocity estimation (Williams, 2003b). Detecting and removing offsets beforehand to obtain clean GPS time series is always an important procedure before further GPS time series analysis (Gazeaux et al., 2013). A typical detrended displacement time series recorded by GPS is shown in Fig. 1.3 with seasonal signals estimated using Eq. (1.4).

For those interested in plate-tectonic studies (e.g., Larson et al., 1997), the linear trend, i.e. estimation of station velocity v, is of key importance. While if the geophysical signals under investigation are seasonal in nature (Davis et al., 2012), then certainly the harmonic amplitudes (a_k and b_k) are interesting in their own right, and velocity term may be considered a nuisance parameter. For some applications it might be also valuable to investigate the post-fit residuals, i.e. $\epsilon(t_i)$, to study the environmental noise (e.g., Mao et al., 1999; Langbein, 2004), and this is in turn to better estimate the velocity term (Williams, 2003a).

GPS for hydrology Since the establishment of the GPS technology, it has been used to study the water vapor which is taken as unknown parameters during the GPS raw data processing (e.g., Tralli and Lichten, 1990). More recently, the GPS technology has also been applied to investigate other compartments of the hydrological cycle. For example, GPS signals are also used to measure surface soil moisture (e.g., Larson et al., 2008), snow depth (e.g., Larson and Small, 2013), as well as detecting hydrological loading information (e.g., van Dam et al., 2001; Davis et al., 2004; Tregoning et al., 2009). The hydrological loading information embedded in the displacement time series are in turn validated by the above-mentioned hydrological models (van Dam et al., 2001; Dill and Dobslaw, 2013) or GRACE observations at both global (van Dam et al., 2007; Tesmer et al., 2011) and regional scales (Fu et al., 2012). Apart from frequently used

vertical displacements, horizontal displacements are advantageous in locating the hydrological loading sources (Wahr et al., 2013; Fu et al., 2013).

More recently, the established fact that GPS time series contain hydrological information is heard around. GPS observations have also been applied as an independent tool to estimate terrestrial water storage variations at the global (e.g., Rietbroek et al., 2012, 2014), regional (e.g., Argus et al., 2014; Fu et al., 2014) or basin scales (e.g., Wang et al., 2013), based on the well-known loading theory (see Chapter 2 for more details). Furthermore, by comparing with climate indices, derived deformation from GPS has been regarded as an hydrological indicator of extreme hydrological events, e.g. droughts (Borsa et al., 2014; Chew and Small, 2014).

1.3 The GRACE mission and its applications

THE GRACE mission is a joint scientific satellite mission between the National Aeronautics and Space Administration (NASA) and Deutsches Zentrum für Luft and Raumfahrt (DLR) that has been measuring time-variation of the Earth's gravitational field since its launch on 2002 March 17 (Tapley et al., 2004). GRACE comprises two coplanar satellites (GRACE A and B, see Fig. 1.4) in a low, near circular, near polar orbit with an inclination of 89°, at an altitude of around 500 km, separated from each other by a distance of roughly 220 km. The mission measures variations of the Earth's gravity by tracking the inter-satellite range and range-rate between both satellites via a K-band ranging (KBR) system, which observes the distance between the twin satellites at micron meter level accuracy using carrier phase measurements at the K (26 GHz) and Ka (32 GHz) frequencies. In addition, both satellites are equipped with SuperSTAR accelerometers, GPS receivers, star cameras, and laser retro reflectors to complement the scientific sensor package.

From the so-called Level-1 data collected by these scientific instruments, monthly gravity fields are estimated in the form of corrections to a well-defined *a priori* background gravity model (e.g., Tapley et al., 2005). The monthly sampling rate has been selected in order to accumulate enough observations to provide a spatial resolution of about 400 km. Practically a trade-off in choosing the temporal sampling interval is made due to the fact that accumulating data over long time intervals improves spatial resolution, while decreasing temporal resolution (Cazenave and Chen, 2010).

The GRACE data are officially processed and provided by three science data centers, i.e. the GeoForschungsZentrum (GFZ) in Germany, the Center for Space Research (CSR) and the aforementioned JPL which are both located in USA. These products are presented in the form of spherical harmonics coefficients. Differences exist in the products among these three centers due to their different data processing strategies, which includes the background models used, the period over which orbits are integrated, weighting of the data, the maximum degree of the estimated gravity harmonics (see Bettadpur, 2012; Dahle et al., 2012; Watkins and Yuan, 2012). The latest version of products, i.e. RL05, has been released and providing since 2012, and the data from GFZ RL05 (Dahle et al., 2014) are used in the thesis, see data availability calendar in Fig. 1.5. Blank months indicate missing data, i.e. gaps. In addition, other groups provide the GRACE solutions at alternative sampling rates based on alternative approaches, for example, 10-day sampling rate products from GRGS (the Group de Recherche de Geodesie Spatiale) (Lemoine et al., 2007) and daily gravity field snapshot (Kurtenbach et al., 2009) from the Institute of Theoretical Geodesy (ITG) at the University of Bonn. It might be worth mentioning

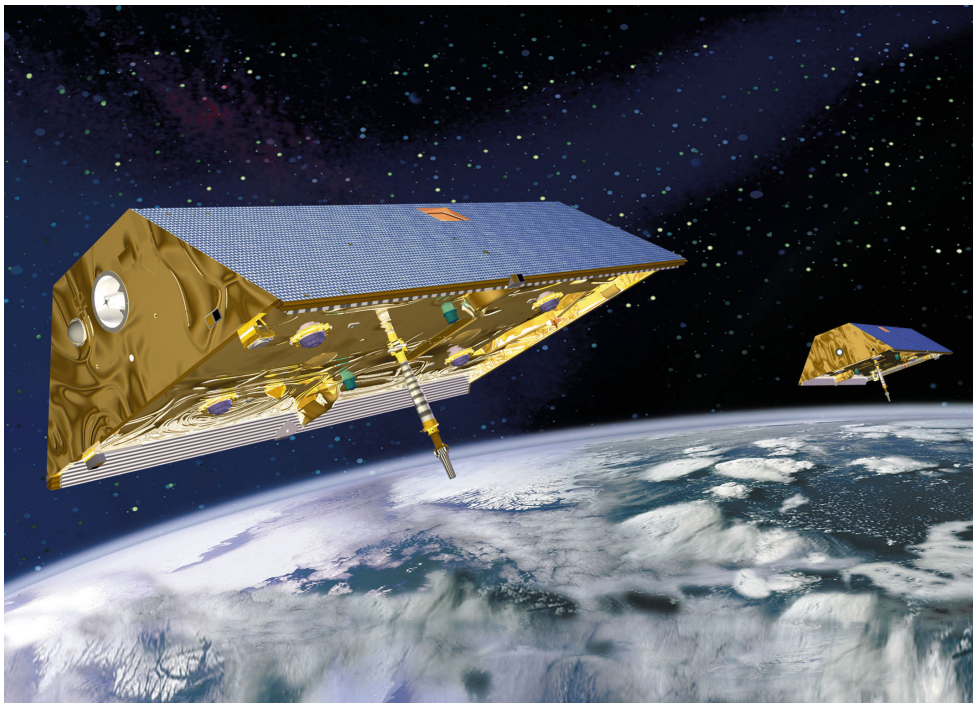

Figure 1.4: GRACE *satellites (courtesy:* NASA*)*

that all the aforementioned GRACE products are publicly available from ICGEM (International Centre for Global Earth Models) [2].

On the basis of these gravity products from the GRACE mission, GRACE has provided unique and valuable information on large-scale mass redistribution within the Earth system since its launch (Tapley et al., 2004). This has led to improved understanding of various mass fluxes like the hydrological cycle, mass balance of polar ice sheets, mountain glacier mass balance, sea level change and solid Earth processes. Among the applications of GRACE, it is particularly instrumental in closing the water budget because it offers us a homogeneous, global data source for total terrestrial water storage (TWS) changes (e.g., Lorenz et al., 2014). The theoretical background to infer TWS as well as deformation from GRACE is presented in Chapter 2. Note that, in addition to the spherical harmonic solutions, an alternative approach which was originally developed to study the gravity field of the moon, point masses or regional uniform mass concentrations, is adopted to derive regional mass anomalies directly from the Level-1 range rate data and it is commonly called the "mascon" approach (e.g., Rowlands et al., 2005).

Besides the complicated background theory, practical handling the GRACE data is also challenging. Two types of error sources exist requiring to be dealt with for its further applications (Wahr et al., 2006; Schmidt et al., 2008a). One type of errors is introduced during data processing either resulting from the GRACE measurements themselves or from the applied de-aliasing models. This type of errors is the so-called "noise" embedded in the delivered GRACE products, for example, the north-south stripes due to the orbit geometry of the GRACE mission (Swenson and Wahr, 2006). Several approaches have been developed to reduce the effects of noise in the GRACE data. One strategy is to convert the global spherical harmonics into local TWS time

[2] http://icgem.gfz-potsdam.de/ICGEM/

series and then average them over a large, pre-defined region, such as a basin. If the area is sufficiently large (larger than the spatial decorrelation scale of the noise), the noise will tend to cancel out and this concept was formulated into a basin averaging approach by Swenson and Wahr (2002), which is a common way of analyzing the GRACE data, especially in hydrological studies. Another commonly applied strategy to decrease the noise in the GRACE observations is filtering/smoothing the data, which could be implemented in both the spectral and the spatial domain. Descriptions of the most frequently applied filters, including deterministic filters and stochastic filters, are presented in Chapter 4.

Unfortunately, these two strategies aiming to reduce the first type of errors lead to the second type of errors, i.e. post-processing errors. Any type of filtering which reduces the first category of the GRACE noise will also reduce local signal amplitude (e.g., Chen et al., 2007a; Swenson and Wahr, 2011). In addition to the signal attenuation, both strategies will give rise to another problem, namely leakage effect, in a way that signal in neighboring areas will spill into the desired region, while part of the signal of interest will spread outside the desired region. Leakage is particularly severe in regions of high spatial variability in surface water storage patterns as well as coastlines where smoothing with ocean's signal significantly attenuates the apparent hydrological signal (Wouters et al., 2014). Several studies have been performed to account for the second type of errors (e.g., Wahr et al., 2007; Klees et al., 2007; Baur et al., 2009; Longuevergne et al., 2010; Landerer and Swenson, 2012) and the rescaling approach proposed by Wahr et al. (2007) appears to be the most common technique to remedy the signal loss.

After shortly introducing the mission design, the GRACE data and its practical handling, the following paragraphs aim to provide a brief literature overview of the applications of the GRACE mission.

GRACE for hydrology The GRACE mission was motivated to a large popularity in hydrology. Precise measurement of the Earth's time-varying gravitational field from the GRACE mission allow unprecedented tracking of the transport of mass across and underneath the surface of the Earth and give insight into secular, seasonal, and sub-seasonal variations in the global water supply. It is worth noting that GRACE measures vertically-integrated terrestrial water storage change and cannot separate contributions from individual stores, i.e. ground water (GW), near-surface and deep soil moisture (SM), surface water (SW), snow-water equivalent (SWE) and ice, and water in biomass (BIO), see Eq. (1.5), without other independent data.

$$\Delta\mathrm{TWS} = \Delta\mathrm{GW} + \Delta\mathrm{SM} + \Delta\mathrm{SW} + \Delta\mathrm{SWE} + \Delta\mathrm{BIO}\,. \tag{1.5}$$

ΔTWS derived from GRACE with respect to the mean field is particularly valuable in combination with *in situ* measurements for some of the terms on the right-hand side of Eq. (1.5). For example, several studies have demonstrated the abilities of GRACE for monitoring groundwater resources (e.g., Rodell et al., 2007, 2009). Alternatively, considering the causes of changes in TWS in a given area or basin, TWS change (dTWS) in unit time (dt) could be related to accumulated precipitation (P), evapotranspiration (E), and runoff (R):

$$\frac{d\mathrm{TWS}}{dt} = P - E - R\,. \tag{1.6}$$

As Eq. (1.6) describes the water mass balance within a certain region, it is normally used to close the water budget at basin scales and it is accordingly called the water mass balance equation

(Alsdorf et al., 2007; Cazenave and Chen, 2010; Riegger et al., 2012). On the one hand, based on Eq. (1.6), uncertainties of the GRACE data are able to be quantified since the right-hand side term $P - E - R$ could be estimated using the corresponding hydrological models and *in situ* measurements (e.g., Riegger et al., 2012). On the other hand, GRACE in turn could be the input measurements to infer some terms on right-hand side of Eq. (1.6), for example, estimating run-off R over gauged or ungauged basins (e.g., Syed et al., 2005; Sneeuw et al., 2014).

Certainly, the GRACE mission is remarkably beneficial to hydrologists who use TWS derived from GRACE for validating hydrological models or assimilating GRACE TWS into the hydrological models (e.g., Güntner, 2008; Eicker et al., 2014). Global or basin scale seasonal cycles in TWS from GRACE have been mostly investigated and compared with global hydrological models, and good agreements with models were demonstrated (e.g., Tapley et al., 2004; Schmidt et al., 2008b). Fig. 1.5 displays strong seasonal behavior in regions like the Amazon river basin with flooding normally starting in February or March and receding in June.

Likewise, these investigations using GRACE have been extended to infer climate variability, e.g. floods (e.g., Seitz et al., 2008; Chen et al., 2010; Creutzfeldt et al., 2012) and droughts (e.g., Long et al., 2013; Thomas et al., 2014), or even climate indices (e.g., Phillips et al., 2012; de Linage et al., 2013; Zhang et al., 2015).

GRACE for cryosphere The mass balance of the cryosphere is of considerable importance in the context of global warming and present-day sea level rise. Quantification of polar ice sheet and mountain glacier mass balance and their contribution to global sea level rise has long been a challenge due to the lack of *in situ* observations. Remote sensing data, for example elevation changes from satellite altimeters, have been applied to explore polar ice sheet mass balance. GRACE is providing the opportunity to study mass variations of the cyrosphere from a new perspective.

Since all right-hand terms except ΔSWE in Eq. (1.5) do not contribute to ΔTWS significantly with respect to ΔSWE in cryospheric regions, GRACE is able to offer us direct measurement of cryospheric mass changes, which has been demonstrated by a number of studies since its launch. These studies confirmed the continuous mass loss from Greenland (e.g., Velicogna and Wahr, 2006a; Baur et al., 2009; Harig and Simons, 2012) and Antarctica (e.g., Velicogna and Wahr, 2006b; Chen et al., 2009). Polar ice mass loss is also visible by carefully inspecting Fig. 1.5, which shows a clear mass loss during the GRACE era. Fig. 1.5 does not give a quantitative analysis which requires to further account for the above-mentioned GRACE errors, for example, errors due to choice of filters and leakage, as well as the GIA (glacial isostatic adjustment) effects. These errors and effects are the main causes of the significant variations among published results (e.g., Horwath and Dietrich, 2009).

Besides monitoring polar ice sheets, GRACE is able to provide unique estimates of mass rates of mountain glaciers in case that the signal is large enough (e.g., Tamisiea et al., 2005; Chen et al., 2006; Matsuo and Heki, 2010). For example, a number of studies demonstrated the mass loss of the Himalaya glaciers (e.g., Matsuo and Heki, 2010) and the Alaskan glaciers (e.g., Chen et al., 2006).

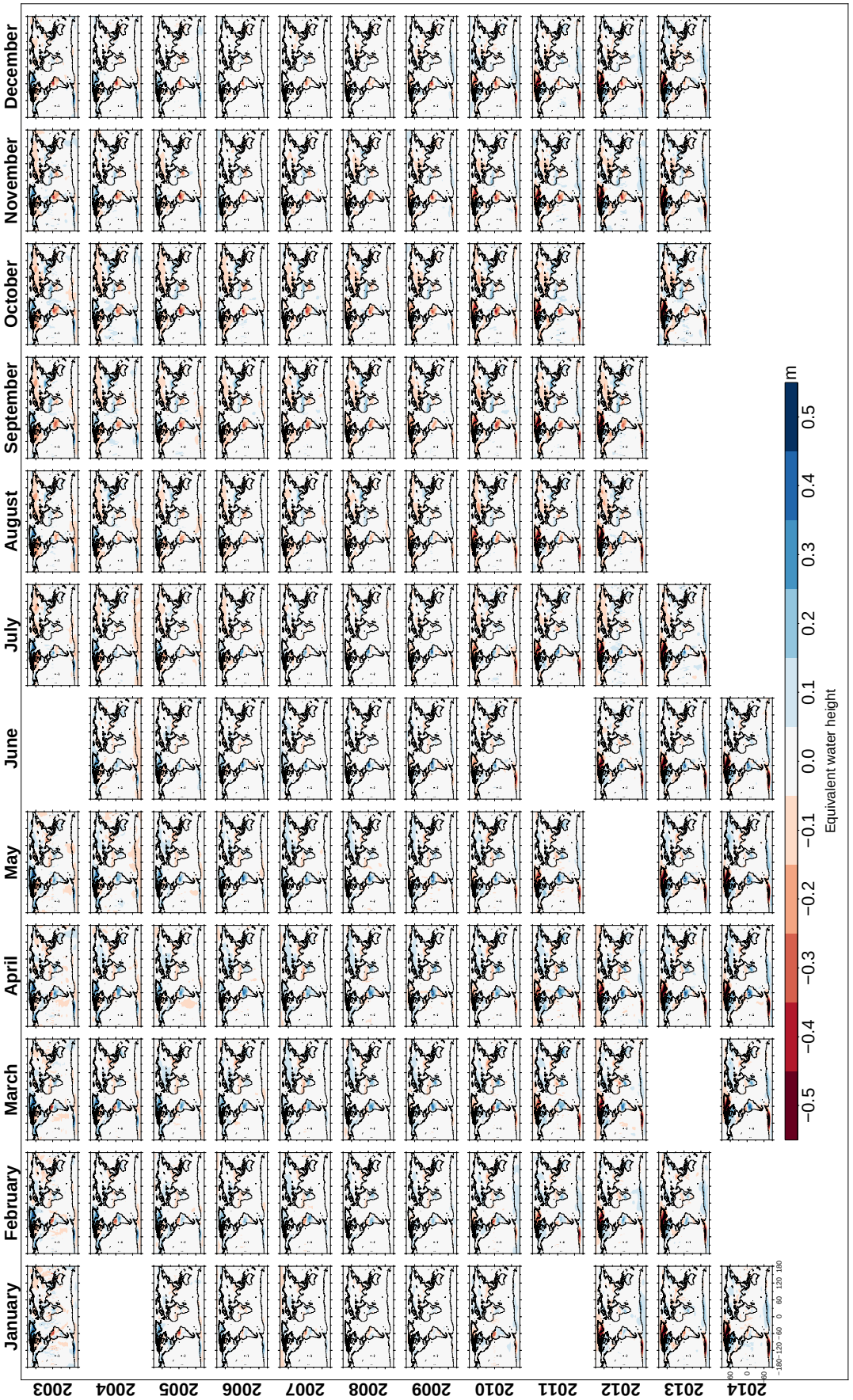

Figure 1.5: *The calendar of the available* GRACE *data from* GFZ

GRACE for ocean and sea level rise Water flux into and out of ocean causes its mass change, which could be detected by the GRACE twin satellites flying over the vast ocean. GRACE, since its launch, allows us for the first time to directly observe the global mass variation and its contribution to sea level change (e.g., Chambers et al., 2004).

GRACE contributes to the oceanic studies from both its time-mean and time-variable components (Wouters et al., 2014). The combination of the mean mass change from GRACE with sea surface height from satellite altimetry determines the dynamic ocean topography (e.g., Chambers et al., 2004; Lombard et al., 2007). GRACE also helps to study the global mean sea level (GMSL) which consists of the mass component and the thermosteric component, and to close the sea level budget (e.g., Willis et al., 2008). The time-variable mass component observed by GRACE contributes to quantify certain aspects of regional ocean dynamics, e.g. low-frequency variations in ocean bottom pressure (OBP) (e.g., Chambers and Willis, 2008, 2009), which are particularly troublesome to measure or model (Wouters et al., 2014).

GRACE for solid Earth The afore-mentioned extraordinary contributions of GRACE focus on the hydrosphere, cryosphere as well as ocean, which represent the mass redistribution of water within a thin layer at the Earth's surface. Besides these applications, GRACE also opens us a window for probing into the Earth's interior where the mean density is about five times as large as that of water, and therefore GRACE is particularly sensitive to mass flux inside the Earth. Studies of this aspect mainly go to investigate GIA effects, coseismic and postseismic deformation.

GIA follows the melting of past ice loads and leads to secular deformation of the Earth's surface as well as secular gravity field changes, which are measured by GRACE. The spatial GIA pattern was firstly analyzed in the GRACE dataset for 2002 to 2005 by (Tamisiea et al., 2007), followed by (Paulson et al., 2007) who first applied GRACE to refine GIA modeling and constrain upper and lower mantle viscosity. In line with them, several studies take advantage of GRACE for GIA modeling and in turn apply GIA corrections to better quantify ice mass loss over the cryospheric region (e.g., van der Wal, 2009; Steffen et al., 2010).

Moreover, GRACE is also applied in combination with the aforementioned GPS to estimate the short-term solid Earth deformations caused by variations in global and local hydrological loading (e.g., Davis et al., 2004; van Dam et al., 2007). These loading induced deformations normally represent strong seasonal behavior and the high agreement between GPS and GRACE has been validated (e.g., Tregoning et al., 2009; Tesmer et al., 2011; Fu et al., 2012). This thesis also studies the comparison between GPS and GRACE but with a focus on the effects of GRACE data filtering.

In addition to the long-term trend signal and seasonal signals in GRACE, abrupt jumps in the gravity field due to earthquakes could be recorded by GRACE as well. For example, Han et al. (2006) utilized raw Level-1 GRACE satellite range and range-rate observations to determine the gravity change due to the earthquake. Several other studies followed in this direction and demonstrated the unique value of GRACE in exploring both coseismic and postseismic deformation from major earthquakes (e.g., Chen et al., 2007b; De Viron et al., 2008; Han et al., 2010, 2011).

As described above, GRACE has remarkably improved our understanding of mass fluxes within Earth's near-surface fluid envelopes since its launch. Unfortunately, GRACE will end its mis-

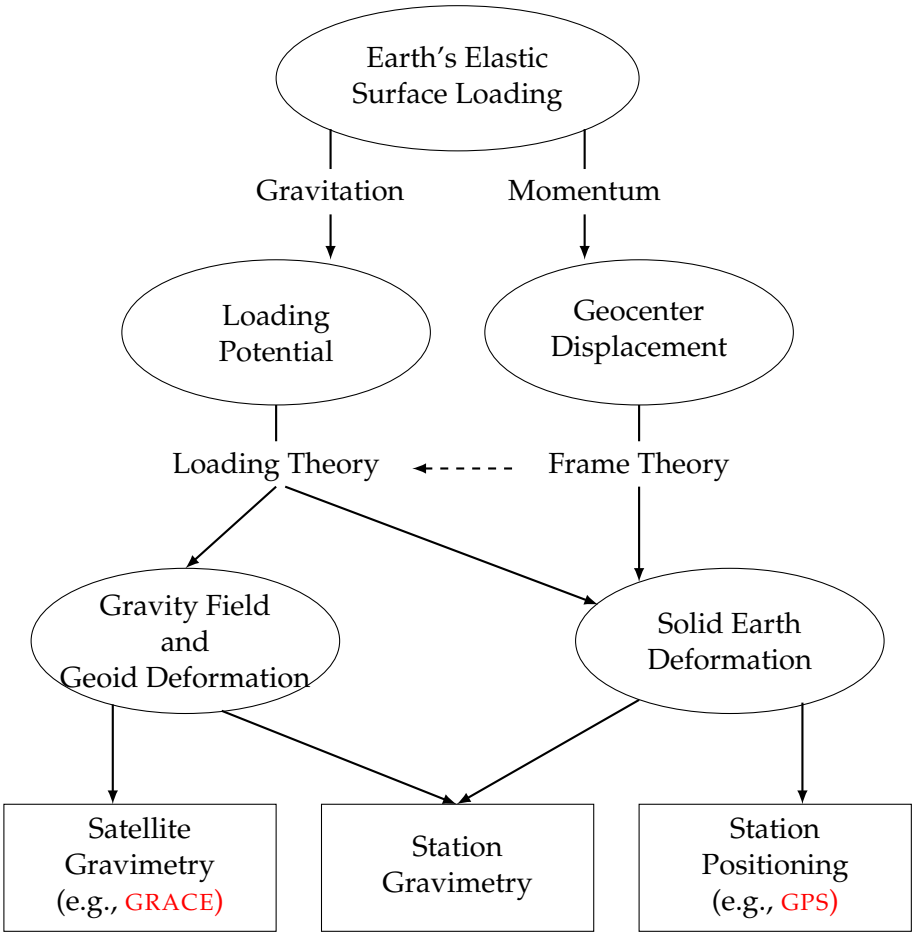

Figure 1.6: *The relationship between the Earth's surface elastic loading, the* GPS *technology and the* GRACE *mission (see also Blewitt, 2003). Geophysical phenomena are represented in ellipses and observation types are illustrated in rectangles. Theoretical relationships and physical principles are connected by arrows. The arrows indicate the direction leading toward the computation of measurement models.*

sion soon. However, as its successor, the GRACE follow-on mission (Flechtner et al., 2014b) is scheduled to be launched in 2017 to continue the mission of GRACE.

1.4 Motivation

THE above three sections describe the Earth's surface elastic loading, the GPS technology and the GRACE mission. Strong relationships exist among one another and Fig. 1.6 represents the derivation from the Earth's elastic surface loading leading to measurements. Certainly inverse derivation from measurements to surface loading is possible. Regarding the two measurement types used in this thesis, GRACE satellites directly sense the gravitational effect of surface loading changes, whereas GPS observations are linked to surface loading changes through surface deformation. Nevertheless, both techniques could be connected theoretically by the well-known loading theory. Numerous studies focus on the forward and backward relationships in Fig. 1.6 so as to investigate one or another, e.g. the aforementioned application

of GRACE for hydrology. Following the relationships in Fig. 1.6, the thesis aims to advance the relevant studies involving surface loading, GPS and GRACE from the following three aspects.

1. The first aspect involves the seasonality characteristics of the elastic surface loadings and their corresponding records from spaceborne techniques, e.g. GPS and GRACE. Seasonal signals are conventionally retrieved based on models with constant amplitudes and phases. However, in reality, true seasonal signals are not constant from year to year. Few studies made endeavors to solve the problem with model based approaches (e.g., Davis et al., 2012). This thesis tries to attack this problem with an alternative approach named singular spectrum analysis (SSA) which is a non-parametric approach and independent of models.

2. Secondly, as presented in Fig. 1.6, GPS and GRACE are theoretically related and several studies focused on comparing the common surface loading signals, especially hydrological signals, recorded by both techniques (e.g., Davis et al., 2004; van Dam et al., 2007). However, these studies neglect the importance of GRACE data filtering and they seem to randomly choose the Gaussian filter with a smoothing radii around 500 km. King et al. (2006) investigated the effects of the Gaussian filter using different smoothing radii when comparing GPS and GRACE. However, except the Gaussian filter, other filters like both deterministic filters and stochastic filters exist and play important roles in GRACE data filtering for different purposes. This thesis contributes to this aspect by comparing GPS and GRACE with a special focus on the effects of different filters. Both deterministic filters and stochastic filters are applied and compared in this thesis.

3. Last but not least, inferring deformation from global surface loads is based on the loading theory, i.e. the Green functions , which depend on the Earth model. The current commonly used Earth model in the Green function approach is the Preliminary Reference Earth Model (PREM) (Dziewonski and Anderson, 1981), which is laterally homogeneous and isotropic over the globe. The computed deformation depends solely on the spherical distance between the load and the computation point. However, it is reasonable to expect that the Earth's crust responds to its surface load varying inhomogeneously and anisotropically. Bevis et al. (2012) pointed out that it is probably inappropriate to use elastic-loading Green functions based on PREM, or any other radially symmetric, whole-earth model. By using a local high spatial resolution load dataset, we investigate the effects of different location-dependent, e.g. site dependent Green functions, with respect to the isotropic Green functions. In addition, we compare the two approaches in modeling deformation in a local area, i.e. comparison of the global Green function approach and the half-space approach.

1.5 Outline

In line with these three aspects, the thesis is organized as follows. Chapter 2 presents in detail the theoretical relationships shown in Fig. 1.6, e.g. the loading theory as well as the reference frame theory, which lays a solid theoretical foundation for the coming chapters. Chapter 3 firstly provides the methodology of SSA and several aspects relating to its application. This is followed by three examples which demonstrate the capabilities of SSA for extracting time-variable signals from geodetic time series. Chapter 4 targets to investigate the effects of different filters on the comparison of GPS and GRACE. Commonly used deterministic filters and

stochastic filters are introduced in this chapter. Comparisons over two study areas are presented. Chapter 5 provides a detailed investigation of site and area dependent Green function approach. In addition, two approaches to modeling deformation in the local area are presented and compared with respect to the Green function approach. Lastly in this chapter, an empirical Green function approach is discussed as well. Finally, conclusions and outlook are given in Chapter 6.

Chapter 2

Gravity and loading theory

THE geographical distribution of atmospheric, oceanic and hydrological masses varies in time and this in turn changes the external gravity field and the geometrical shape of the Earth. The mass variations, gravity changes and displacements on the Earth's surface are therefore intrinsically connected to each other and they also become measurable with modern space and terrestrial geodetic techniques at global, regional as well as local scales.

This chapter is dedicated to present the theoretical relationships between surface mass variations, gravity changes and the associated displacements, which lays a solid foundation for the practical analysis and comparison of different types of observations in the following chapters. It should be mentioned that the notation used in this chapter follows mostly Farrell (1972) and Sneeuw (2006). It might be worth noting that the term "the Green function" is used in this thesis instead of the commonly used "the Green's function" due to the English grammatical issue, see the example about Stokes in geodesy (Featherstone and Vaníek, 1996).

2.1 From geopotential to surface mass variation

A point mass m at $\mathbf{x}'$ within the whole Earth system, including the atmosphere and the oceans, generates a gravitational acceleration at $\mathbf{x}$:

$$\mathbf{g}(\mathbf{x}) = -\frac{Gm(\mathbf{x}-\mathbf{x}')}{|\mathbf{x}-\mathbf{x}'|^3}\,, \tag{2.1}$$

where G is the gravitational constant. For a continuous mass density $\rho(\mathbf{x}')$, integrating over $\mathbf{x}'$ obtains:

$$\mathbf{g}(\mathbf{x}) = -\int_\Omega \frac{G\rho(\mathbf{x}')(\mathbf{x}-\mathbf{x}')}{|\mathbf{x}-\mathbf{x}'|^3} d^3\mathbf{x}'\,, \tag{2.2}$$

where Ω consists of volume mass elements $d\mathbf{x}'$ inside the Earth system. The gravitational potential is then defined as

$$\nabla\phi(\mathbf{x}) = \mathbf{g}(\mathbf{x})\,. \tag{2.3}$$

Accordingly, the scalar field $\phi(\mathbf{x})$ has the form

$$\phi(\mathbf{x}) = \int_\Omega \frac{G\rho(\mathbf{x}')}{|\mathbf{x}-\mathbf{x}'|} d^3\mathbf{x}'\,. \tag{2.4}$$

Eq. (2.4) represents the gravitational potential both inside and outside of the Earth's surface. For all the mass beyond the Earth's surface, e.g. the hydrosphere, the gravitational potential satisfies the Laplace equation:

$$\nabla^2\phi(\mathbf{x}) = 0\,. \tag{2.5}$$

Solving Eq. (2.5) using spherical coordinates r (radial distance), λ (spherical longitude) and θ (spherical co-latitude), the analytical solution can be expressed in terms of spherical harmonic expansions (Heiskanen and Moritz, 1967; Sneeuw, 2006):

$$\phi(r,\theta,\lambda) = \frac{GM}{R}\sum_{n=0}^{\infty}\left(\frac{R}{r}\right)^{n+1}\sum_{m=0}^{n}P_{nm}(\cos\theta)(C_{nm}\cos m\lambda + S_{nm}\sin m\lambda)\,, \tag{2.6}$$

where R denotes the mean radius of the Earth and M is the total mass of the Earth. The dimensionless coefficients C_{nm} and S_{nm} describe the gravitational potential field of the exterior Earth in terms of the spectral degree n and order m. P_{nm} represents the associated Legendre functions of the 1^{st} kind. In practice, Eq. (2.6) is assumed to be band-limited, so the upper limit (infinity) is accordingly replaced by an upper-bound $N_{\max}$.

For the purpose of handling Eq. (2.6) conveniently in numerical sense (Lambeck, 1988), P_{nm}, C_{nm} and S_{nm} are conventionally fully normalized, e.g. GRACE gravity spherical harmonic coefficients, which makes

$$\bar{P}_{nm} = N_{nm}P_{nm}\,, \tag{2.7a}$$

$$\bar{C}_{nm} = \frac{C_{nm}}{N_{nm}}\,, \tag{2.7b}$$

$$\bar{S}_{nm} = \frac{S_{nm}}{N_{nm}}\,, \tag{2.7c}$$

with the normalization factor

$$N_{nm} = \sqrt{(2-\delta_{m,0})(2n+1)\frac{(n-m)!}{(n+m)!}}\,, \tag{2.8}$$

where $\delta_{m,0}$ is called Kronecker delta, which is 1 if $m = 0$ and 0 otherwise. In the normalization and band-limited case Eq. (2.6) can be also written as

$$\phi(r,\theta,\lambda) = \frac{GM}{R}\sum_{n=0}^{N_{\max}}\left(\frac{R}{r}\right)^{n+1}\sum_{m=0}^{n}\bar{P}_{nm}(\cos\theta)(\bar{C}_{nm}\cos m\lambda + \bar{S}_{nm}\sin m\lambda)\,. \tag{2.9}$$

In addition to the gravitational potential, the rotation of the Earth with an angular speed ω will give rise to another potential, i.e. a centrifugal potential ϕ_c written in spherical coordinates

$$\phi_c(r,\theta,\lambda) = \frac{1}{2}\omega^2 r^2\sin^2\theta\,. \tag{2.10}$$

The combination of the gravitational potential and the centrifugal potential obtains the gravity potential W, which is

$$W = \phi + \phi_c\,. \tag{2.11}$$

It is imperative to note that the gravity potential W can also be expressed in terms of a normal potential term U and a disturbing potential term T. The normal potential is an ellipsoidal

approximation, e.g. GRS80 (Geodetic Reference System 80), to the real gravity potential. Besides, the normal potential is defined following several properties (Heiskanen and Moritz, 1967; Sneeuw, 2006) and therefore time-invariant. The disturbing potential is defined as $T = W - U$. In the light of Bruns's equation (Heiskanen and Moritz, 1967), one may relate the geoid N to the disturbing potential T

$$N = \frac{T}{\gamma}\,, \tag{2.12}$$

where γ is the associated normal gravity acceleration. The geoid is an equipotential surface coinciding with the mean ocean surface of the Earth if the oceans and atmosphere were in equilibrium, and extending through the continents.

With the advent of the new era of gravity satellite missions, spherical harmonic coefficients $\bar{C}_{nm}$ and $\bar{S}_{nm}$ can be retrieved with temporal resolution of one month or below and spatial resolution of up to $N_{\max} = 120$ (Kusche, 2010). Nevertheless, it is still impossible to uniquely determine the mass distribution within the Earth system as an infinite number of mass distributions generate the same external gravity potential field. This leaves us to make physically plausible assumptions to link the gravity to mass distribution. A common assumption is to concentrate the mass distribution in a thin layer of thickness H at the Earth's surface with $(n+2)H/R \ll 1 \quad \text{for} \quad n \ll N_{\max}$ (Wahr et al., 1998), see Fig. 2.1. In other words, under the assumption, we are aiming at the mass distribution, especially mass variations, around the geoid N. In addition, this thin layer must be thick enough to include those portions of the atmosphere, oceans, ice caps, and below-ground water storage with significant mass fluxes and the thin layer is of the order of 10-15 km (Wahr et al., 1998).

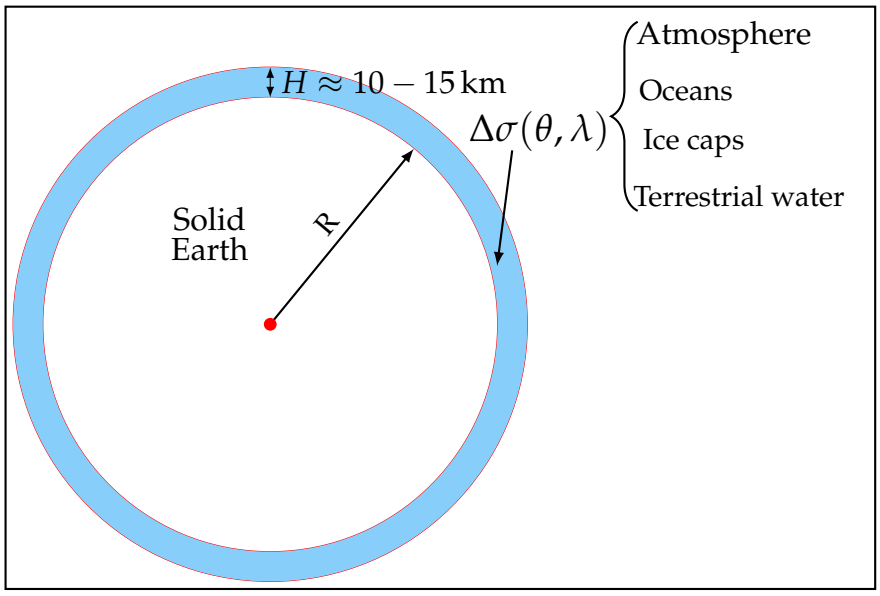

Figure 2.1: *A simple sketch of the spherical think layer around the Earth's geoid.*

The mass redistribution within the thin spherical layer causes correspondingly the gravity changes as well as the geoid changes ΔN. Note that the contribution to the geoid changes originates from not only the direct gravitational attraction of the surface mass variation but also the additional part due to the deformation of the solid Earth caused by the loading ef-

fects of the surface mass. To put it another way, the light blue part in Fig. 2.1 which loads and deforms the solid Earth will induce the additional part to the changes of the geoid.

Practically, e.g. for the GRACE satellite mission, instead of removing the normal potential U from the full potential W, a long-term (multi-year) mean gravity potential field $\tilde{W}$ is adopted to obtain the time variable part of the disturbing potential ΔT. Note that $\tilde{W}$ comprises both the normal potential and the mean disturbing potential. Therefore, ΔT indicates also the time-variable part of the full gravity field in the form of

$$\Delta T(r,\theta,\lambda) = \frac{GM}{R}\sum_{n=0}^{N_{\max}}\left(\frac{R}{r}\right)^{n+1}\sum_{m=0}^{n}\bar{P}_{nm}(\cos\theta)(\Delta\bar{C}_{nm}\cos m\lambda + \Delta\bar{S}_{nm}\sin m\lambda)\,, \tag{2.13}$$

where $\Delta\bar{C}_{nm}$ and $\Delta\bar{S}_{nm}$ are spherical harmonic coefficients with respect to their long-term mean. With the spherical approximation $\gamma = \frac{GM}{R^2}$ at the surface, the geoid changes can be represented as

$$\Delta N(\theta,\lambda) = \frac{\Delta T}{\gamma} = R\sum_{n=0}^{N_{\max}}\sum_{m=0}^{n}\bar{P}_{nm}(\cos\theta)(\Delta\bar{C}_{nm}\cos m\lambda + \Delta\bar{S}_{nm}\sin m\lambda)\,. \tag{2.14}$$

Eq. (2.14) describes the geoid variations in terms of the changes of the gravity potential. However, the ultimate goal is to further establish the relationship with the surface mass variations. To fulfill the goal, it is also necessary to expand the surface mass variation in spherical harmonics manner. Within the thin spherical shell, instead of using the volume mass density ρ, surface mass density σ (see Fig. 2.1), which is defined as mass/area (kg/m^2), is conventionally utilized. Therefore, the surface mass density changes can be represented as (Wahr et al., 1998)

$$\Delta\sigma(\theta,\lambda) = R\rho_{\mathrm{w}}\sum_{n=0}^{\infty}\sum_{m=0}^{n}\bar{P}_{nm}(\cos\theta)(\Delta\bar{C}^{\sigma}_{nm}\cos m\lambda + \Delta\bar{S}^{\sigma}_{nm}\sin m\lambda)\,, \tag{2.15}$$

where ρ_{w} denotes the density of water, and $\Delta\bar{C}^{\sigma}_{nm}$ and $\Delta\bar{S}^{\sigma}_{nm}$ are fully normalized dimensionless spherical harmonic coefficients representing surface mass density. To distinguish from the above-mentioned gravity spherical harmonic coefficients $\Delta\bar{C}_{nm}$ and $\Delta\bar{S}_{nm}$, a superscript $^{\sigma}$ is marked in $\Delta\bar{C}^{\sigma}_{nm}$ and $\Delta\bar{S}^{\sigma}_{nm}$. According to Wahr et al. (1998), the relationship between them is formulated as

$$\begin{Bmatrix}\Delta\bar{C}^{\sigma}_{nm}\\ \Delta\bar{S}^{\sigma}_{nm}\end{Bmatrix} = \frac{\rho_{\mathrm{e}}}{3\rho_{\mathrm{w}}}\frac{2n+1}{1+k'_n}\begin{Bmatrix}\Delta\bar{C}_{nm}\\ \Delta\bar{S}_{nm}\end{Bmatrix}, \tag{2.16}$$

where ρ_{e} is the average density of the Earth and k'_n describes the loading Love numbers which will be explained in detail in Section 2.2.1. Substituting Eq. (2.16) in Eq. (2.15) gives

$$\Delta\sigma(\theta,\lambda) = \frac{R\rho_{\mathrm{e}}}{3}\sum_{n=0}^{N_{\max}}\frac{2n+1}{1+k'_n}\sum_{m=0}^{n}\bar{P}_{nm}(\cos\theta)(\Delta\bar{C}_{nm}\cos m\lambda + \Delta\bar{S}_{nm}\sin m\lambda)\,. \tag{2.17}$$

Eq. (2.17) allows us to retrieve the surface mass density changes by means of the changes in gravity, i.e. $\Delta\bar{C}_{nm}$ and $\Delta\bar{S}_{nm}$. Note that the surface mass density changes are usually further expressed in equivalent water height Δh via dividing by ρ_{w}, i.e. $\Delta h = \Delta\sigma/\rho_{\mathrm{w}}$. Appendix A gives the practical procedure to compute the equivalent water height from the GRACE products.

The above procedure which synthesizes the spherical harmonic basis functions with the gravity spherical coefficients to obtain certain quantities, e.g. the surface mass densities here, is called global spherical harmonic synthesis (GSHS). Conversely, if the surface density changes are given, the derivation shown above can also be implemented reversely. Starting from Eq. (2.15),

the spherical harmonic coefficients $\Delta\bar{C}^{\sigma}_{nm}$ and $\Delta\bar{S}^{\sigma}_{nm}$ are obtained by a so-called global spherical harmonic analysis (GSHA) formulation (Sneeuw, 1994)

$$\begin{Bmatrix} \Delta\bar{C}^{\sigma}_{nm} \\ \Delta\bar{S}^{\sigma}_{nm} \end{Bmatrix} = \frac{1}{4\pi R\rho_{\mathrm{w}}} \iint \Delta\sigma(\theta,\lambda)\bar{P}_{nm} \begin{Bmatrix} \cos(m\lambda) \\ \sin(m\lambda) \end{Bmatrix} d\Omega \,. \tag{2.18}$$

Applying Eq. (2.16) inversely together with Eq. (2.18) yields the gravity spherical harmonic coefficients and other quantities, like the potential field and the geoid changes are consequently retrieved.

In this section, the relationship between the surface mass variations and the gravity changes has been established. Since the Earth is not rigid, the surface mass loaded on the surface of the solid Earth causes deformations elastically or visco-elastically. The elastic deformations are induced primarily by the fast changing loads, e.g. the redistribution of hydrological, atmospheric and oceanic masses, while the visco-elastic deformations are caused by the slow changing loads, e.g. glacier mass variations. This thesis will focus on the former deformations and the relationship between the gravity changes and the elastic displacements will further be formulated in the next section.

2.2 Elastic response to the Earth's surface loads

2.2.1 Elastic loading Love numbers and Green functions

SEVERAL types of Love numbers exist in practice. The Love h and k, and Shida l numbers were firstly introduced by Love (1909) and Shida and Matsuyama (1912), respectively. They were used to characterize the Earth's response to the potential or force without loading the surface of the Earth, such as the external tidal potential. For describing the response to the surface load, e.g. terrestrial water load, another type of Love numbers distinguished by a superscript prime, i.e. h', l' and k', were adopted (Munk and MacDonald, 1960), which are normally called loading Love numbers (Farrell, 1972). A further category of Love numbers, shear Love numbers, denoted by h'', l'' and k'', were also defined to represent the deformations arising from horizontal frictional forces exerted on the Earth's surface by winds or ocean currents (Lambeck, 1988). Different types of Love and Shida numbers are summarized in Table 2.1. In the case of the loading Love numbers, elastic loading Love numbers and viscoelastic loading Love numbers are used in the literature to depict the reaction of the Earth's interior to the fast changing and slow changing surface loading processes, respectively. In this thesis, the primary concentration lies on the elastic loading Love numbers since the fast changing loading process will be investigated here.

The elastic loading Love numbers is computed by integrating the equations of motion, the stress-strain relationship and Poisson equation inside the Earth, from the center to the surface using a spherical Earth model, e.g. the Preliminary Reference Earth Model (PREM) (Dziewonski and Anderson, 1981). The equations of motion (Eq. (2.19a)) as well as the Poisson equation (Eq. (2.19b)) are linearized and formulated as (Farrell, 1972)

$$\nabla\cdot\boldsymbol{\tau} - \nabla(\rho g\mathbf{s}\cdot\mathbf{e}_{\mathbf{r}}) - \rho\nabla\phi + g\nabla\cdot(\rho\mathbf{s}\mathbf{e}_{\mathbf{r}}) = 0\,, \tag{2.19a}$$

$$\nabla^2\phi = -4\pi G\nabla\cdot(\rho\mathbf{s})\,, \tag{2.19b}$$

Table 2.1: *Three different types of Love and Shida numbers.*

Type of Love numbers	Notation	Cause	Reference
Tidal Love and Shida numbers	h, k, l	forces without loading the Earth, e.g. tide	(Love, 1909) (Shida and Matsuyama, 1912)
Load Love numbers	h', l', k'	direct load on Earth's surface, e.g. water load	(Munk and MacDonald, 1960)
Shear Love numbers	h'', l'', k''	horizontal frictional forces, e.g. winds or ocean currents	(Lambeck, 1988)

where $\boldsymbol{\tau}$ is the incremental stress tensor, ρ and g are the unperturbed density and gravitational acceleration, $\mathbf{s}$ is the displacement vector, ϕ is the perturbed gravitational potential, $\mathbf{e_r}$ denotes the unit vector of the vertical component. In Eq. (2.19a), the first term describes the contribution of the stresses, the second term refers to the change in density, the third term represents self-gravitation, implying the change in gravity and the last term stands for the advection of the hydrostatic pre-stress. It should be noted that the last term in Eq. (27) in (Farrell, 1972) is missing here since we are dealing with the elastic loading process (Kusche, 2010).

Supposing a spherically symmetric Earth model with certain boundary conditions at the surface, the solutions of Eq. (2.19a) and Eq. (2.19b) can be transformed and expressed as

$$\mathbf{s} = \sum_{n=0}^{\infty} \left(U_n(r) P_n(\cos\psi)\mathbf{e_r} + V_n(r) \frac{\partial P_n(\cos\psi)}{\partial \psi} \mathbf{e_v} \right) , \tag{2.20a}$$

$$\phi = \sum_{n=0}^{\infty} \Phi_n(r) P_n(\cos\psi) , \tag{2.20b}$$

where U_n, V_n and Φ_n are transformed variables indicating vertical displacements, tangential displacements and potential, respectively. $\mathbf{e_v}$ denotes the unit vector of the horizontal component. Note that we use ψ here instead of θ which was used by Farrell (1972) to indicate the spherical distance.

With further simplifications applied, the transformed variables can be further related to the elastic loading Love numbers (see details in (Farrell, 1972))

$$\begin{bmatrix} U_n(r) \\ V_n(r) \\ \Phi_n(r) \end{bmatrix} = W(r) \begin{bmatrix} h'_n(r)/g \\ l'_n(r)/g \\ k'_n(r) \end{bmatrix} , \tag{2.21}$$

where $W(r)$ stands for the potential induced by the point mass. Since we evaluate the loading-induced displacements at the Earth's surface, $r = R$ is accordingly applied in Eq. (2.21) which makes

$$W(r = R) = \frac{gR}{M} . \tag{2.22}$$

Eq. (2.21) defines the loading Love numbers and clearly tells that h'_n, l'_n and k'_n describe vertical and horizontal displacements and potential, respectively. Solving and integrating Eq. (2.21) from the inner Earth to the surface gives the set of loading Love numbers which are based on the given Earth model. A practical numerical computation guide of the loading Love numbers is shown in (Gegout et al., 2010).

The elastic loading Love numbers are exemplarily shown in Fig. 2.2. When considering the loading Love numbers, special attention should be paid to the degree-0 and degree-1 terms. The degree-0 term is usually not given, e.g. Table A2 in (Farrell, 1972). This is due to the fact that degree-0 load does not exist and the total mass is conserved within the Earth system. The degree-0 term is also absent in Fig. 2.2. The degree-1 term is intrinsically linked to geocenter motion and the reference frame (Blewitt, 2003), which can be seen from Fig. 2.2 and will be explained in more detail in Section 2.3.

Derivation of the loading Love numbers is the first step to estimate the Earth's response to the surface load. Furthermore, Longman (1962) introduced the elastic Green functions which represent the loading Love numbers in the spatial domain and essentially reflect the impulse response of the Earth to its elastic surface loading. As this thesis focuses only on the displacements, the derivation of the vertical and horizontal displacements are therefore only given here. Other Green functions, e.g. for gravity, are detailed in (Longman, 1963) and (Farrell, 1972).

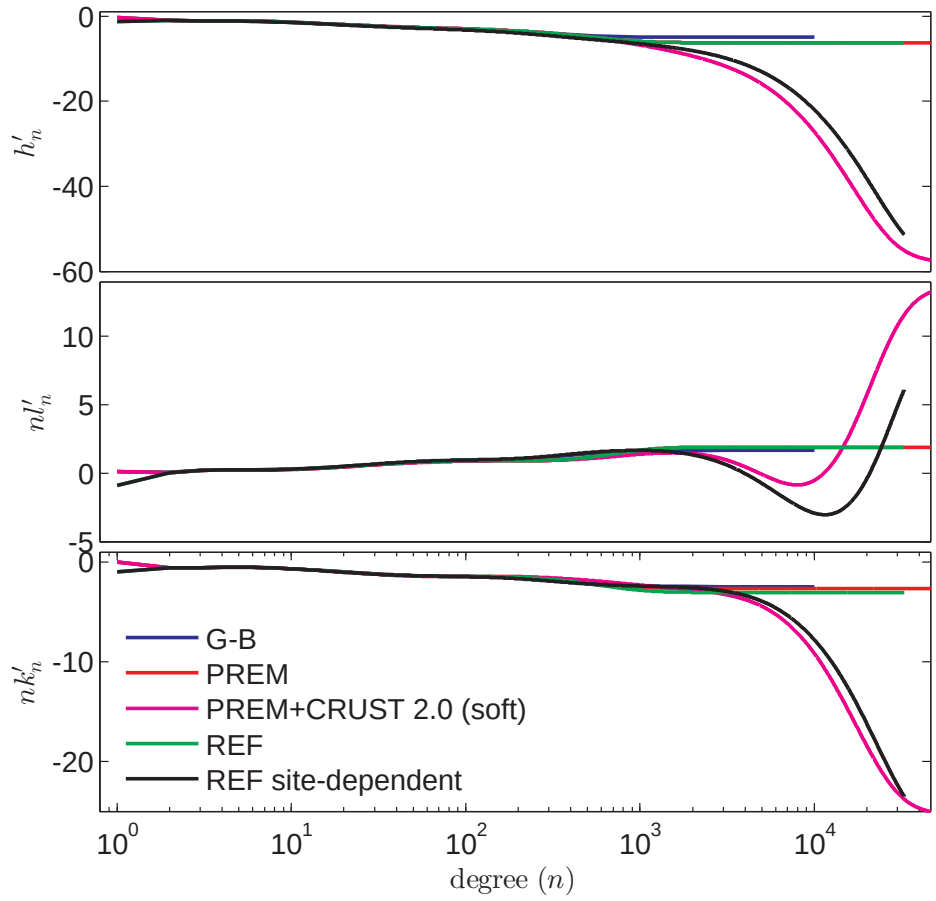

Figure 2.2: *Five different sets of elastic loading Love Numbers come from five different Earth models: 1) Gutenberg-Bullen (Farrell, 1972); 2)* PREM *(Dziewonski and Anderson, 1981); 3) a modified* PREM *with crustal structures adapting from* CRUST 2.0 *model (Wang et al., 2012) 4)* REF *(Kustowski et al., 2008) 5)* REF *model with a site-dependent setting (Gegout, 2013). The elastic loading Love numbers for* G-B *model are obtained from (Farrell, 1972) and these for* PREM, PREM+CRUST 2.0 *(soft) are obtained from (Wang et al., 2012). The* REF *and its site-dependent Love numbers are provided by Gegout (2013) [personal communication]. It is worth mentioning that the first three sets of loading Love numbers differ from the last two sets also in the reference frame issues which are noticeable in the degree-1 term.*

Substituting Eq. (2.21) and Eq. (2.22) into Eq. (2.20a), one can obtain the elastic Green functions for the vertical (u) and horizontal (v)displacements evaluated at the Earth's surface

$$G_u(\psi) = \frac{R}{M}\sum_{n=0}^{\infty} h'_n P_n(\cos\psi)\,, \tag{2.23a}$$

$$G_v(\psi) = \frac{R}{M}\sum_{n=1}^{\infty} l'_n \frac{\partial P_n(\cos\psi)}{\partial\psi}\,. \tag{2.23b}$$

The procedure of deriving the elastic Green functions starts by summing Eq. (2.23a) and Eq. (2.23b) from 0 to infinity. However, in practice, the elastic loading Love numbers are given only up to a limited degree, for instance up to degree 10 000 in (Farrell, 1972). As shown in Fig. 2.2, h'_n, nl'_n and nk'_n illustrate an asymptotic behavior with degree n becoming large and Eq. (2.24) was consequently defined by Farrell (1972)

$$\lim_{n\to\infty}\begin{bmatrix} h'_n \\ nl'_n \\ nk'_n \end{bmatrix} = \begin{bmatrix} h'_\infty \\ l'_\infty \\ k'_\infty \end{bmatrix}\,. \tag{2.24}$$

Several tricks have been investigated to accelerate the convergence of Eq. (2.23a) and Eq. (2.23b) (e.g., Farrell, 1972; Francis and Dehant, 1987; Guo et al., 2004; Wang and Wang, 2007). Among those tricks, the so-called Kummer transformation was mostly applied to make use of Eq. (2.24). Accordingly, Eq. (2.23a) and Eq. (2.23b) can be transformed to

$$G_u(\psi) = \frac{Rh'_\infty}{M}\sum_{n=0}^{\infty} P_n(\cos\psi) + \frac{R}{M}\sum_{n=0}^{\infty}(h'_n - h'_\infty)P_n(\cos\psi)\,, \tag{2.25a}$$

$$G_v(\psi) = \frac{Rl'_\infty}{M}\sum_{n=1}^{\infty}\frac{1}{n}\frac{\partial P_n(\cos\psi)}{\partial\psi} + \frac{R}{M}\sum_{n=1}^{\infty}\frac{(nl'_n - l'_\infty)}{n}\frac{\partial P_n(\cos\psi)}{\partial\psi}\,. \tag{2.25b}$$

Using the asymptotic values for h'_n and nl'_n, the term $h'_n - h'_\infty$ and $nl'_n - l'_\infty$ turn zero above a certain high degree $N_{\max}$. The first terms in both Eq. (2.25a) and Eq. (2.25b) are evaluated exactly with the help of expressions from Singh and Ben-Menahem (1968), see Eq. (2.26)

$$\sum_{n=0}^{\infty} P_n(\cos\psi) = \frac{1}{\sin(\psi/2)}\,, \tag{2.26a}$$

$$\sum_{n=1}^{\infty}\frac{1}{n}\frac{\partial P_n(\cos\psi)}{\partial\psi} = -\frac{\cos(\psi/2)\,[1+2\sin(\psi/2)]}{\sin(\psi/2)\,[1+\sin(\psi/2)]}\,. \tag{2.26b}$$

Substituting Eq. (2.26) into Eq. (2.25a) and Eq. (2.25b) yields

$$G_u(\psi) = \frac{Rh'_\infty}{2M\sin(\psi/2)} + \frac{R}{M}\sum_{n=0}^{N_{\max}}(h'_n - h'_\infty)P_n(\cos\psi)\,, \tag{2.27a}$$

$$G_v(\psi) = -\frac{Rl'_\infty}{2M}\frac{\cos(\psi/2)\,[1+2\sin(\psi/2)]}{\sin(\psi/2)\,[1+\sin(\psi/2)]} + \frac{R}{M}\sum_{n=1}^{N_{\max}}\frac{(nl'_n - l'_\infty)}{n}\frac{\partial P_n(\cos\psi)}{\partial\psi}\,. \tag{2.27b}$$

Eq. (2.27a) and Eq. (2.27b) represent the expressions to derive the vertical and horizontal elastic Green functions out of the elastic loading Love numbers. The derived elastic loading Green function coefficients are displayed in Fig. 2.3. As clearly illustrated in the Fig. 2.3, one significant characteristic of the Green functions is that the relative influence of a load falls off with the increasing spherical distance ψ. To be more precise, the load affects strongly in the near field, i.e. $\psi < 0.1°$, and less in the far field beyond.

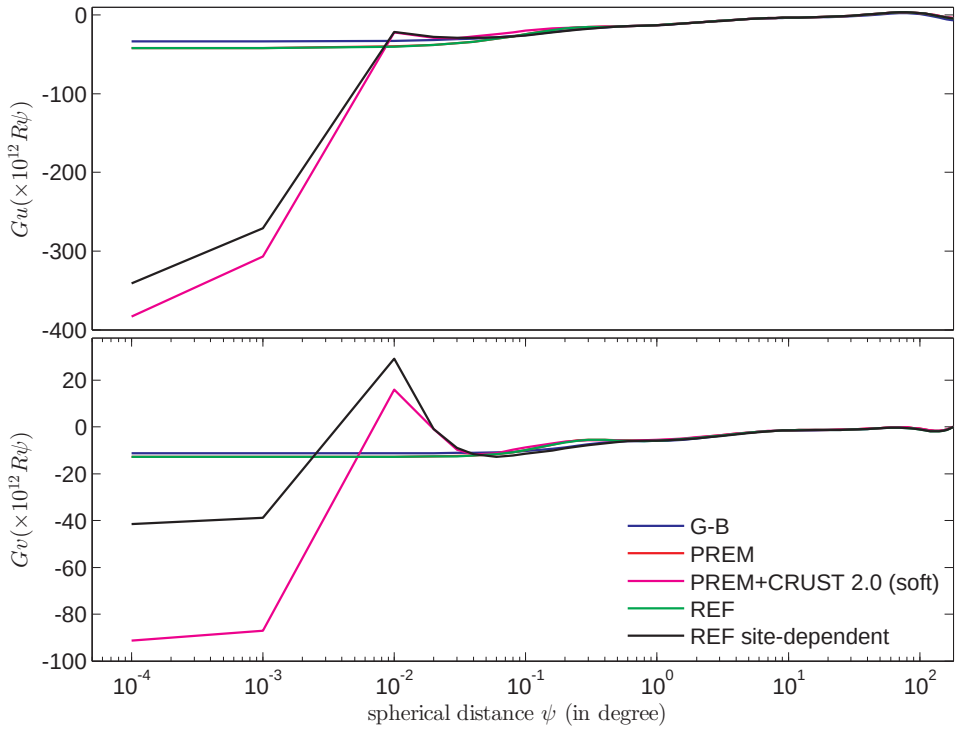

Figure 2.3: *Corresponding elastic Green functions to the loading Love numbers shown in Fig. 2.2.*

Meanwhile, it is worth noting that Eq. (2.27a) and Eq. (2.27b) represent the class of the elastic Green functions for a spherically symmetric, non-rotating, elastic and isotropic (SNREI) model of the Earth which depends on the spherical distance (ψ) only. This class of the elastic Green functions is particularly popular among the current loading-related studies due to the simplifications of the given Earth model, especially the Green functions based on the PREM (van Dam and Wahr, 1987; van Dam et al., 2001, 2010). However, in reality, the solid Earth is neither spherically symmetric nor purely elastic or isotropic. What is more, it also rotates in space. Even though these effects are generally thought to produce negligible uncertainties under current understanding of the Earth (Métivier et al., 2005), issues such as anisotropy, lateral heterogeneities or visco-elasticity give rise to increasing concern over recent years. For instance, van Dam et al. (2003) pointed out the importance of both the Earth models and the theoretical part for dealing with issues like lateral heterogeneities in future studies. Other studies, e.g. Latychev et al. (2005), have already made attempts to include lateral heterogeneities in the Earth model for the viscoelastic loading case.

One more issue to be emphasized here is that differences in the mechanical properties, e.g. lithospheric properties, of the Earth model would result in differences in the estimated displacements due to the same amount of the surface loads. Plag et al. (1996) found that differences in the lithospheric properties of the PREM model and the PEMC (parametric

Earth model, continental; Dziewonski et al. (1975)) model caused differences in the vertical displacement of up to 20 % and in the horizontal displacement of up to 40 % in the near field of the load but identical responses for the far field. In addition, insufficiencies of the popular PREM model which has a globally averaged crust and its potential effects are pointed out lately (e.g., van Dam et al., 2003; Bevis et al., 2012). Adaption of the relatively high resolution crust model, e.g. CRUST 1.0 (Laske et al., 2013), into the PREM or other Earth models to account for the inhomogeneous crust structure is under investigation (Wang et al., 2012; Gegout, 2013; Dill et al., 2015). The effects in the displacement field due to the inhomogeneous crust structures will be studied in detail in Chapter 5 at the local scale using a local load dataset.

2.2.2 Convolution in the spatial domain

THE elastic Green functions describe the impulse response of the Earth to a point load at a certain spherical distance ψ. To compute the loading-induced displacements due to surface loads spreading over a vast area, a spatial convolution is required. Supposing we evaluate the deformations at any point P with colatitude θ_P and longitude λ_P due to the surface mass load at point Q with colatitude θ_Q and longitude λ_Q which can be represented by Eq. (2.15), convolving the load mass and the elastic Green functions leads to

$$d_u(\theta_P,\lambda_P) = R^2 \iint_\Omega G_u(\psi_{PQ})\Delta\sigma(\theta_Q,\lambda_Q)d\Omega\,, \tag{2.28a}$$

$$d_v(\theta_P,\lambda_P) = R^2 \iint_\Omega G_v(\psi_{PQ})\Delta\sigma(\theta_Q,\lambda_Q)d\Omega\,, \tag{2.28b}$$

where $d\Omega = \sin\theta_Q d\theta_Q d\lambda_Q$ and $R^2 d\Omega$ gives the surface area of the corresponding surface load.

Decomposing the horizontal displacement into the north and east component using the azimuth α of the direction from the loading point Q to the computation point P, i.e. vector $\overrightarrow{QP}$ in Fig. 2.4, yields

$$d_n(\theta_P,\lambda_P) = -R^2\cos\alpha \iint_\Omega \Delta\sigma(\theta_Q,\lambda_Q)G_v(\psi_{PQ})d\Omega\,, \tag{2.29a}$$

$$d_e(\theta_P,\lambda_P) = -R^2\sin\alpha \iint_\Omega \Delta\sigma(\theta_Q,\lambda_Q)G_v(\psi_{PQ})d\Omega\,. \tag{2.29b}$$

Eq. (2.28a), Eq. (2.29a) and Eq. (2.29b) describe convolution in the spatial domain and we normally refer to this approach as the Green function approach. Although the equations above are shown in a continuous manner at a global scale, the numerical computation is conducted in a discrete way and these equations are also suitable for a regional or local area (e.g., Elósegui et al., 2003). This is a significant advantage of the Green function approach over the spherical harmonic approach (see Section 2.2.3) if we are interested in geographically restricted loads.

A comparison of vertical deformations determined for 4 different sets of Green functions (one set based on the Gutenburg-Bullen A Earth model (Farrell, 1972), three other sets based on PREM but computed by different groups) was performed by van Dam et al. (2003). Differences resulting from the two Earth models were always less than 0.04 mm and it was concluded that the choice of the elastic loading Love numbers (as long as they are for a SNREI model) will not have a significant influence on the estimated loading effects.

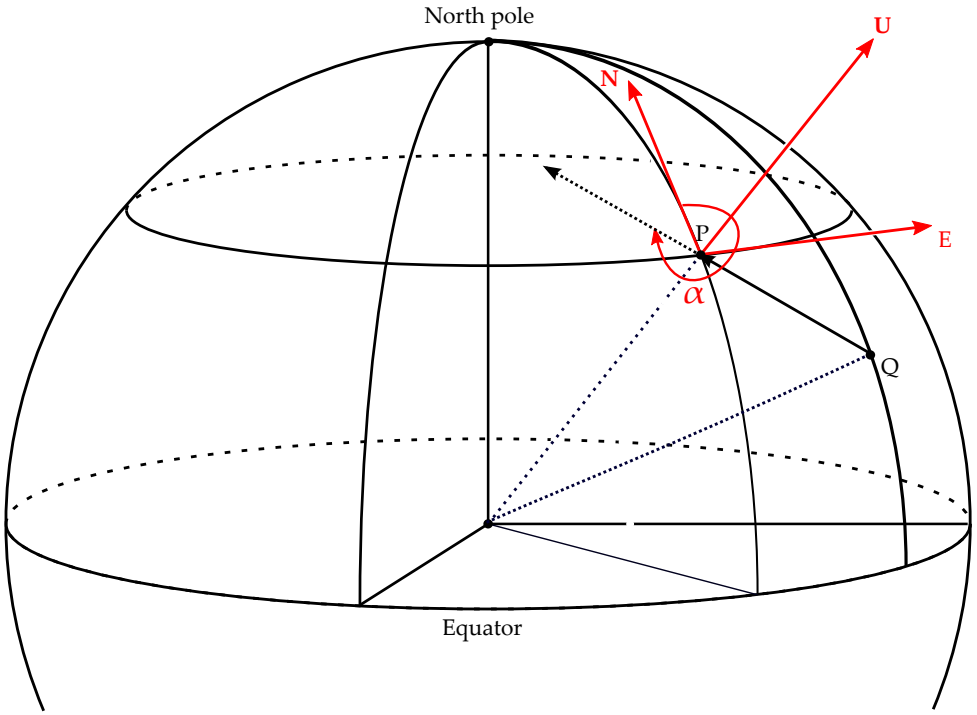

Figure 2.4: *Sketch of decomposing the horizontal displacement into the north and east component.*

2.2.3 Convolution in the spectral domain

As described in Section 2.1, at the global scale, the surface mass changes can be represented in terms of spherical harmonics, which makes it possible to implement the convolution procedure of Eq. (2.28a), Eq. (2.29a) and Eq. (2.29b) in the spectral domain. Computation in the spectral domain is especially convenient for the case of the GRACE products which are delivered in the form of the normalized gravity spherical harmonic coefficients. This subsection deals with the detailed derivation from the Green function approach to the spectral approach.

The derivation starts firstly with the vertical direction. Applying the addition theorem

$$P_n(\cos\psi_{PQ}) = \frac{1}{2n+1}\sum_{m=0}^{n}\bar{P}_{nm}(\cos\theta_P)\bar{P}_{nm}(\cos\theta_Q)\cos m(\lambda_P-\lambda_Q)\,, \tag{2.30}$$

to Eq. (2.23a) gets

$$G_u(\psi_{PQ}) = \frac{R}{M}\sum_{n=0}^{\infty}\frac{h'_n}{2n+1}\sum_{m=0}^{n}\bar{P}_{nm}(\cos\theta_P)\bar{P}_{nm}(\cos\theta_Q)\cos m(\lambda_P-\lambda_Q)\,, \tag{2.31}$$

which is now inserted in Eq. (2.28a) together with Eq. (2.15) and Eq. (2.18), which obtains

$$\begin{aligned} d_u(\theta_P,\lambda_P) = \frac{R^3}{M}\iint\Delta\sigma(\theta_Q,\lambda_Q)\sum_{n=0}^{\infty}\frac{h'_n}{2n+1}\sum_{m=0}^{n}(&\bar{P}_{nm}(\cos\theta_P)\bar{P}_{nm}(\cos\theta_Q)\cos m\lambda_P\cos m\lambda_Q \\ &+\bar{P}_{nm}(\cos\theta_P)\bar{P}_{nm}(\cos\theta_Q)\sin m\lambda_P\sin m\lambda_Q)d\Omega \end{aligned}$$

$$
\begin{aligned}
&= \frac{R^3}{M}\sum_{n=0}^{\infty}\frac{h'_n}{2n+1}\sum_{m=0}^{n}\iint \Delta\sigma(\theta_Q,\lambda_Q)(\bar{P}_{nm}(\cos\theta_P)\bar{P}_{nm}(\cos\theta_Q)\cos m\lambda_P\cos m\lambda_Q \\
&+ \bar{P}_{nm}(\cos\theta_P)\bar{P}_{nm}(\cos\theta_Q)\sin m\lambda_P\sin m\lambda_Q)d\Omega \\
&= \frac{R^3}{M}\sum_{n=0}^{\infty}4\pi R\rho_{\mathrm{w}}\frac{h'_n}{2n+1}\sum_{m=0}^{n}(\bar{P}_{nm}(\cos\theta_P)\cos m\lambda_P\Delta\bar{C}^{\sigma}_{nm} \\
&+ \bar{P}_{nm}(\cos\theta_P)\sin m\lambda_P\Delta\bar{S}^{\sigma}_{nm}) \\
&= \frac{3R\rho_{\mathrm{w}}}{\rho_{\mathrm{e}}}\sum_{n=0}^{\infty}\frac{h'_n}{2n+1}\sum_{m=0}^{n}(\bar{P}_{nm}(\cos\theta_P)\cos m\lambda_P\Delta\bar{C}^{\sigma}_{nm} \\
&+ \bar{P}_{nm}(\cos\theta_P)\sin m\lambda_P\Delta\bar{S}^{\sigma}_{nm}) \,. \qquad (2.32)
\end{aligned}
$$

Applying the relationship (Eq. (2.16)) between the surface density spherical harmonic coefficients and the gravity spherical harmonic coefficients to the above derivation yields the vertical displacement due to surface mass changes

$$
d_u(\theta_P,\lambda_P) = R\sum_{n=1}^{\infty}\frac{h'_n}{1+k'_n}\sum_{m=0}^{n}\bar{P}_{nm}(\cos\theta_P)(\Delta\bar{C}_{nm}\cos m\lambda_P + \Delta\bar{S}_{nm}\sin m\lambda_P) \,. \qquad (2.33)
$$

Expressions for the horizontal components can be obtained by the similar derivation as the vertical component. The detailed derivations for the north and east components are presented in Appendix B and we simply show the resultant formulas here, see Eq. (2.34a) and Eq. (2.34b),

$$
d_n(\theta_P,\lambda_P) = -R\sum_{n=1}^{\infty}\frac{l'_n}{1+k'_n}\sum_{m=0}^{n}\frac{\partial\bar{P}_{nm}(\cos\theta_P)}{\partial\theta_P}(\Delta\bar{C}_{nm}\cos m\lambda_P + \Delta\bar{S}_{nm}\sin m\lambda_P) \,, \qquad (2.34a)
$$

$$
d_e(\theta_P,\lambda_P) = \frac{R}{\sin\theta}\sum_{n=1}^{\infty}\frac{l'_n}{1+k'_n}\sum_{m=0}^{n}\bar{P}_{nm}(\cos\theta_P)m(-\Delta\bar{C}_{nm}\sin m\lambda_P + \Delta\bar{S}_{nm}\cos m\lambda_P) \,. \qquad (2.34b)
$$

Eq. (2.34a), Eq. (2.34b) together with Eq. (2.33) represent the convolution in the spectral domain in terms of gravity spherical harmonic coefficients, especially convolving with the GRACE products (e.g., Davis et al., 2004; van Dam et al., 2007). This approach is accordingly called the spherical harmonic approach. It might be interesting to mention that if the surface displacements are also expanded into the spherical harmonics in terms of the vertical and horizontal directions, one-to-one correspondence between these deformation spherical harmonics and the gravity spherical harmonics could also be established (Blewitt, 2003; Kusche, 2010). Summarizing Eq. (2.16), Eq. (2.32) and Eq. (2.33), we can easily obtain the spectral relationship between vertical displacements ($\Delta\bar{C}^{u}_{nm}$, $\Delta\bar{S}^{u}_{nm}$), surface mass density changes ($\Delta\bar{C}^{\sigma}_{nm}$, $\Delta\bar{S}^{\sigma}_{nm}$) and gravity changes ($\Delta\bar{C}_{nm}$, $\Delta\bar{S}_{nm}$)

Similar relationship can be obtained for the horizontal component ($\Delta\bar{C}^{v}_{nm}$, $\Delta\bar{S}^{v}_{nm}$) if we derive the north and east component as a whole. The only difference from the vertical component is to replace Love number h'_n with l'_n (Blewitt, 2003; Kusche, 2010; Rietbroek, 2014) and we therefore do not repeat here.

As demonstrated above, the Green function spatial approach and the spherical harmonic spectral approach are mathematically equivalent when the degree n goes to infinity. Nevertheless,

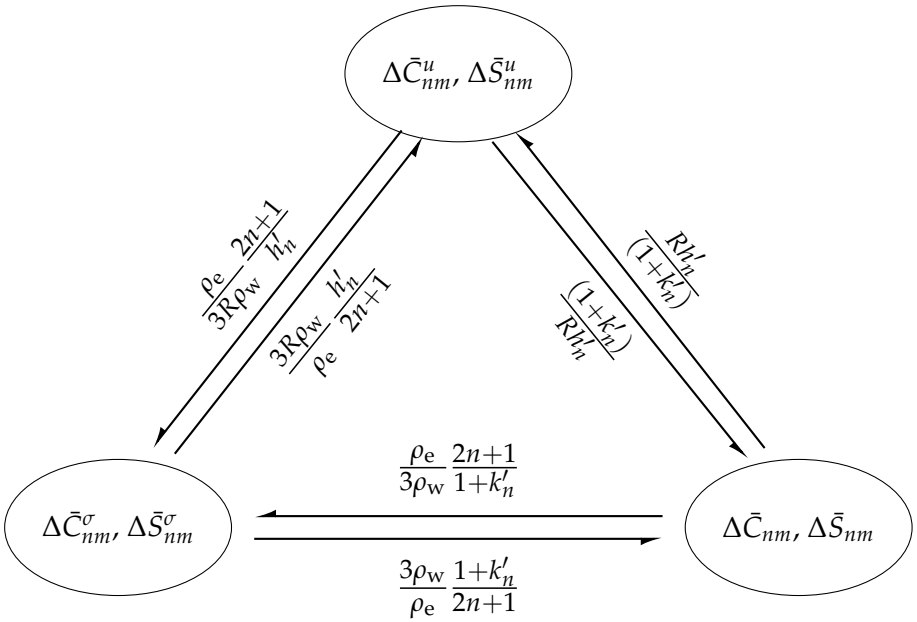

Figure 2.5: *Spectral relationship between vertical displacements, surface mass density changes and gravity changes.*

in practice, the spherical harmonics approach truncates at, e.g. degree 90 for the GRACE products RL05 from GFZ, whereas the Green function approach develops till degree 10000 when we compute the Green function coefficients (see Eq. (2.27a) and Eq. (2.27b)). These truncations will therefore cause differences between the two manners practically and these differences will be quantified below with real data.

Fig. 2.6 compares between the two approaches using the GRACE RL05 products from GFZ (Dahle et al., 2014). The loading Love numbers are settled in the CF reference frame (see Section 2.3 for details). The three-dimensional displacements over 914 GPS stations with both approaches are evaluated. In the Green function approach, loads on a $0.5^\circ \times 0.5^\circ$ grid over the globe are computed following the procedure described in Appendix A (we receive almost the same results if we use smaller grids).

The root mean square (RMS) of the differences between the two approaches in each component are shown in Fig. 2.6. The average RMS of the differences over 914 GPS stations for the north, east and up component is 0.04 mm, 0.04 mm and 0.05 mm, respectively. The comparison indicates that the differences are quite small in the practical application over the globe. With respect to the GPS noise level, these differences can be neglected and either approach produces satisfactory results.

In addition, from the computational efficiency point of view, the spherical harmonic approach is more efficient than the Green function approach if we deal with the data in the form of spherical harmonics. Therefore, the spherical harmonic approach will be applied in Chapter 4 when we compare GPS and GRACE. However, when we face the regional or local load data or the data not in spherical harmonics, the Green function approach is recommended rather than the spherical harmonic approach. For example, the Green function approach will be deployed in Chapter 5 to handle the local load data.

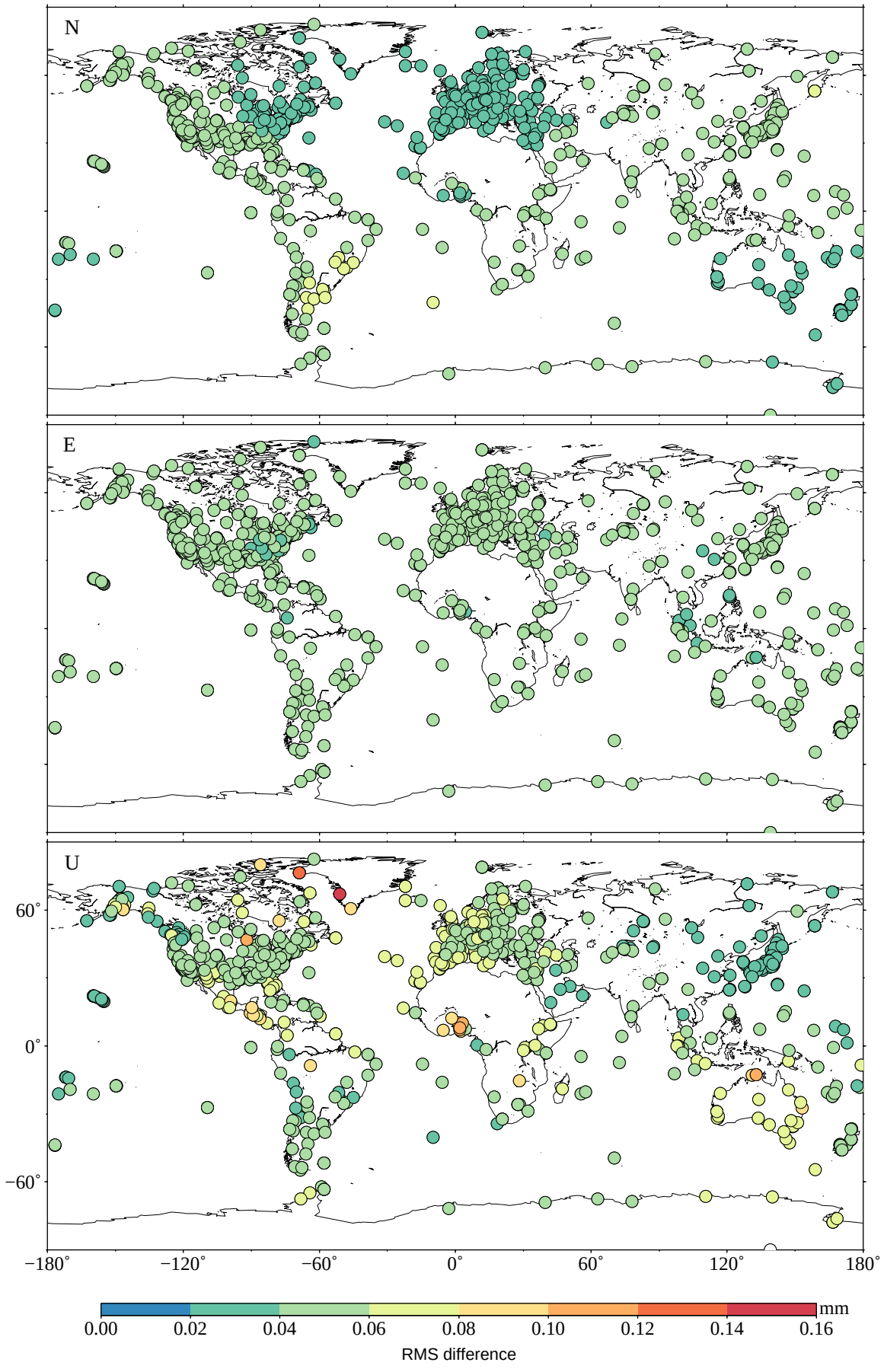

Figure 2.6: *The* RMS *of difference between the Green function approach and the spherical harmonic approach over 914* GPS *sites.*

2.3 Reference frame theory

In terms of the loading theory described in the last section, surface displacements caused by the mass redistribution are a vector field (see Eq. (2.20a)), which depends on both physical deformation and the corresponding reference frames. Interpretation of the surface displacements requires a terrestrial reference frame defined consistently with the dynamics of loading, namely, a clear description of the dynamic relationship between the Earth's surface and the frame origin at some defined center of the Earth. In particular, in the era of a variety of satellite missions, a proper definition of reference frames is of great significance when handling the spaceborne measurements together with the ground-fixed observations.

To this end, Blewitt (2003) proposed the concept of the so-called "isomorphic frames" which indicates a class of reference frames with dynamically consistent kinematic interpretations of the Earth's deformation field. This set of reference frames consist of current most used reference frames in geodesy, which are distinguished by the definition of the origin of the reference frames. These frequently used isomorphic frames are the Center of Mass of the Solid Earth (CE) frame, the Center of Mass of the Earth System (CM) frame, and the Center of Surface Figure (CF) frame. One exaggerated illustration of these frames is shown in Fig. 2.7. Specifically, the Center of the Network (CN) frame is shown in the figure to demonstrate that the CF frame is the expansion of the CN frame to covering the whole globe. It should be mentioned that other isomorphic reference frames, for example the Center of Surface Lateral Figure (CL) frame and the Center of Surface Height Figure (CH) frame, are also used in the literature but not in this thesis.

The driving force of introducing the concept of isomorphic frames is intimately related to the degree-1 load. Therefore one important feature of the isomorphic frames is that the transformation between them can be accordingly linked to the loading theory and can be easily implemented by altering only the degree-1 loading Love numbers. Higher degree loading Love numbers will remain unchanged.

This section will give a brief description of the CE, CM and CF frames and their mutual transformations. Detailed explanation of these reference frames and the derivation of their mutual relationships can be found in the literature (e.g., Trupin et al., 1992; Greff-Lefftz and Legros, 1997; Dong et al., 1997; Blewitt, 2003; Wu et al., 2012; Rietbroek, 2014).

Center of Mass of the Solid Earth (CE) As illustrated in Fig. 2.7 (a), the CE frame indicates the frame whose origin is assigned to the center of the solid Earth. Its origin will be altered whenever the barycenter of the surface load changes. The CE frame is also a natural frame for calculating the dynamics of solid Earth deformation and to compute the loading Love numbers. Most of the published loading Love numbers are given in the CE frame, for instance the loading Love numbers given by Farrell (1972). As specified by Blewitt (2003), one major drawback of the CE frame is that its coordinate origin can not be measured directly. This feature prevents its further practical application. In the literature the relative motion between CE and CM is commonly referred to as *geocenter vector* (Dong et al., 1997). Nevertheless, practically, CE is replaced by CF in the determination of the geocenter motion since the CF frame closely approximates the CE frame, see Fig. 2.7 (d). According to Blewitt (2003), the trajectories of CE and CF coincide to within 2% of their magnitudes, i.e. relative difference between $k_1'^{\mathrm{CE}}$ and $k_1'^{\mathrm{CF}}$, for the Gutenberg-Bullen Earth model and 3% for PREM (Rietbroek, 2014).

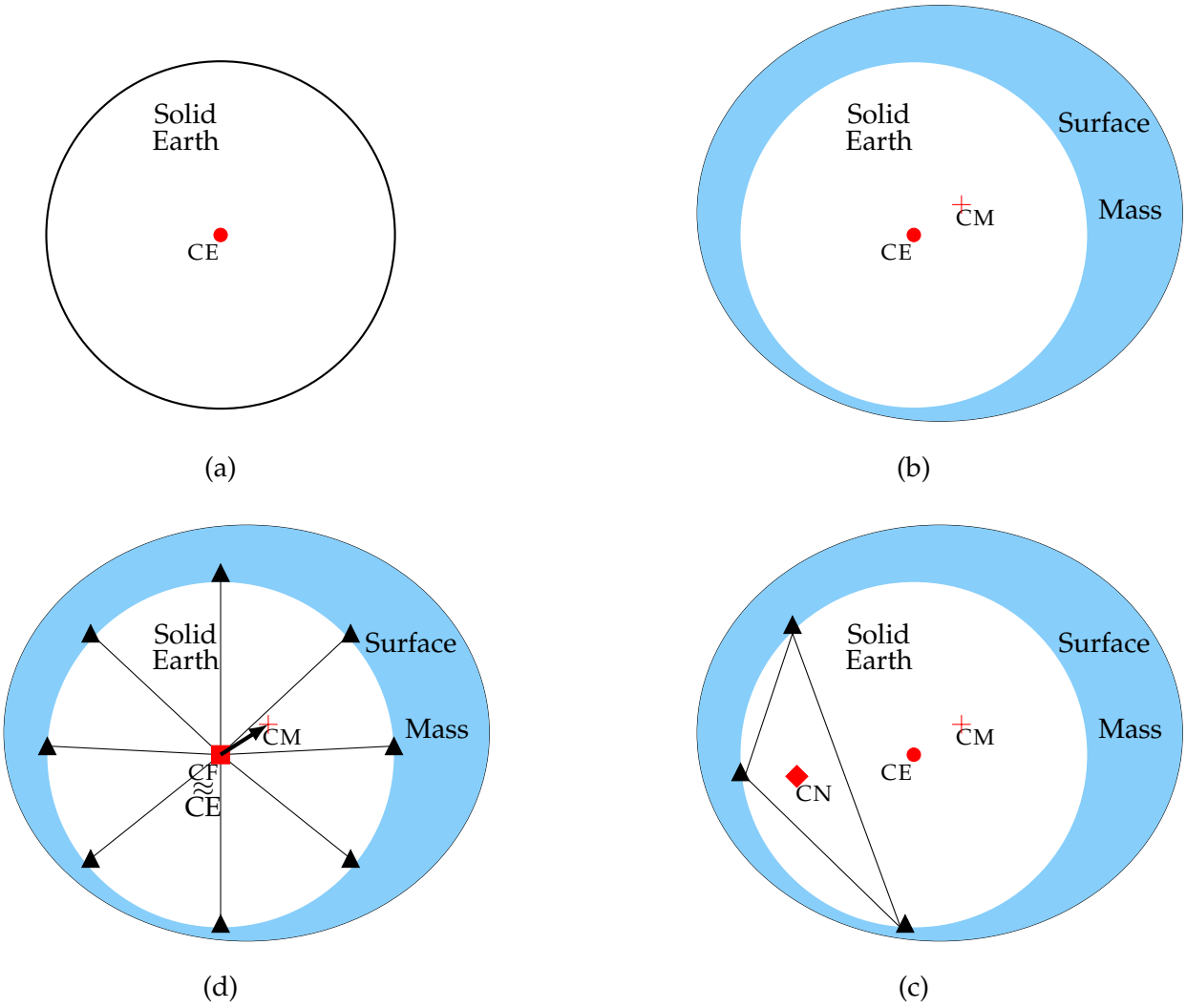

Figure 2.7: *The clockwise sketches illustrate the different geodetic reference frames used in satellite geodesy. Subfigure (a) shows the Center of the solid Earth (CE) and subfigure (b) illustrates the Center of the Earth system (CM), which includes the solid Earth and its surface mass. Subfigure (c) and (d) display the Center of Network (CN) and the Center of Figure (CF), respectively. In essence, CF is the one extreme example of CN with a globally and uniformly distributed tracking stations. Subfigure (d) also presents the vector pointing from the origin of CF to the origin of CM and the time evolution of this vector is called geocenter motion.*

Center of Mass fo the Earth System (CM) Different from the CE frame, the origin of the CM frame is defined as the center of mass of the entire Earth system, including the solid Earth and its fluid envelope, see Fig. 2.7 (b). According to Petit and Luzum (2010), CM is used to describe Earth's motion in inertial space and is therefore referred to as the geocenter. CM also serves as the orbital center for all Earth satellites and it is a natural choice of the reference frame for spaceborne measurements. In addition, the coordinate origin of the International Terrestrial Reference System (ITRS) is theoretically defined at the long-term mean of CM (Petit and Luzum, 2010).

The coordinate of CM in a chosen coordinate system, e.g. CE, can also be represented directly by the degree-1 gravity spherical harmonics as

$$\boldsymbol{X}_{\mathrm{CM}}^{\mathrm{CE}} = \sqrt{3}R \begin{bmatrix} \bar{C}_{11} \\ \bar{S}_{11} \\ \bar{C}_{10} \end{bmatrix}_{\mathrm{CE}} , \tag{2.35}$$

where the degree-1 spherical harmonic coefficients are generated in the chosen coordinate system, e.g. CE here.

As satellites fly around CM and can not sense the motion of CM, the degree-1 gravity spherical harmonics in the spaceborne products are normally zero or missing. For example, the degree-1 coefficients in the GRACE gravity spherical harmonics do not exist. This phenomenon accordingly indicates that the GRACE products are generated in the CM frame.

Center of Surface Figure (CF) Following the definition of Trupin et al. (1992), Dong et al. (1997) and Blewitt (2003), CF is defined geometrically as the geometric center of an infinite series of points which distribute uniformly over the surface of the Earth. The CF frame can be realized by a sufficiently dense global coverage of geodetic stations and it is consequently a natural reference frame choice for ground-fixed measurements, e.g. GPS station coordinate time series.

Theoretically, the origin of the CF frame is defined such that the integral of the surface deformation field over the entire globe is zero (Blewitt, 2003). It is also interpreted in another way that the position of CF located in the CE frame can be computed by integrating the deformation field $\mathbf{s}$ over the whole surface of the Earth (Wu et al., 2012; Rietbroek, 2014), which implies

$$\boldsymbol{X}_{\mathrm{CF}}^{\mathrm{CE}} = \frac{1}{4\pi} \iint_{\Omega} \mathbf{s}(\theta, \lambda) \sin\theta d\theta d\lambda \, . \tag{2.36}$$

According to Eq. (2.36), the origin of the CF frame can further be related to the vertical and horizontal spherical harmonics (see Eq.(2.41) in (Rietbroek, 2014)) as well as possibly to the surface density spherical harmonics.

Several definitions of the geocenter vector exist in the literature (e.g., Trupin et al., 1992; Dong et al., 1997; Blewitt, 2003; Wu et al., 2012). Following the definition of the geocenter vector in the IERS convention (Petit and Luzum, 2010), translation of CM with respect to CF is referred as the geocenter vector $\boldsymbol{X}_{\mathrm{CM}}^{\mathrm{CF}}$ (Wu et al., 2012), which is approximately here $\boldsymbol{X}_{\mathrm{CM}}^{\mathrm{CE}} - \boldsymbol{X}_{\mathrm{CF}}^{\mathrm{CE}}$ as CE closely coincides with CF, see Fig. 2.7 (d). In this case, the geocenter vector tightly corresponds to the above-mentioned degree-1 gravity spherical harmonic coefficients. In practice, if one wants to interpret a result, which is produced in the CF frame, in the CM frame, the geocenter vector should be removed. One should be cautious that the description here is opposite to that in Blewitt (2003) where geocenter vector is defined in a reverse way.

Practically, the geocenter motion time series is provided either in the form of the Cartesian coordinates $\boldsymbol{X}_{\mathrm{CM}}^{\mathrm{CF}}$ (Cheng et al., 2013) or in terms of the degree-1 spherical harmonics (Swenson et al., 2008). They can be readily translated to each other by Eq. (2.35).

Transformation between the isomorphic reference frames Several reference frames exist in use in geodesy and it is of central importance to confirm that the datasets at hand are in the same reference frame. Reference frame consistency is the first step to compare different types of observations or derived results. Taking station displacements for instance, the station deformation computed in the CM frame can be easily transformed and interpreted to be in the CF frame by adding the geocenter vector. Instead, this procedure can be done by calculating the station deformation directly in the CF frame, which consequently corresponds to the transformation of the reference frame before computation. Since the cause of the isomorphic reference frames is due to the degree-1 load, the transformation of the reference frames is accordingly transferred to a transformation of the degree-1 loading Love numbers between different isomorphic reference frames (Blewitt, 2003).

Following the work done by Trupin et al. (1992) and Dong et al. (1997), Blewitt (2003) listed the transformation of the degree-1 loading Love numbers from the CE frame to other isomorphic reference frames. Further, Rietbroek (2014) presented the mutual transformations of the isomorphic reference frames, e.g. transformation from the reference frame A to B, which are of the form as follows

$$h_1'^B = h_1'^A - \alpha^{A\to B}\,, \tag{2.37a}$$
$$l_1'^B = l_1'^A - \alpha^{A\to B}\,, \tag{2.37b}$$
$$1 + k_1'^B = 1 + k_1'^A - \alpha^{A\to B}\,, \tag{2.37c}$$

with

$$\alpha^{A\to \mathrm{CM}} = 1 + k_1'^A\,, \tag{2.38a}$$
$$\alpha^{A\to \mathrm{CF}} = \frac{h_1'^A + 2l_1'^A}{3}\,, \tag{2.38b}$$
$$\alpha^{A\to \mathrm{CE}} = k_1'^A\,. \tag{2.38c}$$

The transformation of the degree-1 loading Love numbers starts normally from the CE frame in which the loading Love numbers are normally produced. Given the degree-1 loading Love numbers listed in Farrell (1972), transferring to the CF frame will be

$$h_1'^{\mathrm{CF}} = h_1'^{\mathrm{CE}} - \frac{h_1'^{\mathrm{CE}} + 2l_1'^{\mathrm{CE}}}{3} = -0.290 - \frac{-0.290 + 2\times 0.113}{3} = -0.268\,, \tag{2.39a}$$
$$l_1'^{\mathrm{CF}} = l_1'^{\mathrm{CE}} - \frac{h_1'^{\mathrm{CE}} + 2l_1'^{\mathrm{CE}}}{3} = 0.113 - \frac{-0.290 + 2\times 0.113}{3} = 0.134\,, \tag{2.39b}$$
$$1 + k_1'^{\mathrm{CF}} = 1 + k_1'^{\mathrm{CE}} - \frac{h_1'^{\mathrm{CE}} + 2l_1'^{\mathrm{CE}}}{3} = 1.021\,. \tag{2.39c}$$

After transformation of the degree-1 loading Love numbers, the convolution in either the spatial domain (see Section 2.2.2) or the spectral domain (see Section 2.2.3) can be implemented in the respective reference frame.

Considering the datasets used in this thesis, the mutual relationship between the data and the corresponding reference frames could be summarized in Fig. 2.8. The GRACE and GPS data are provided in the CM and the CF reference frames, respectively, and the difference between them is the geocenter vector. According to Fig. 2.8, two ways exist to keep the reference frame

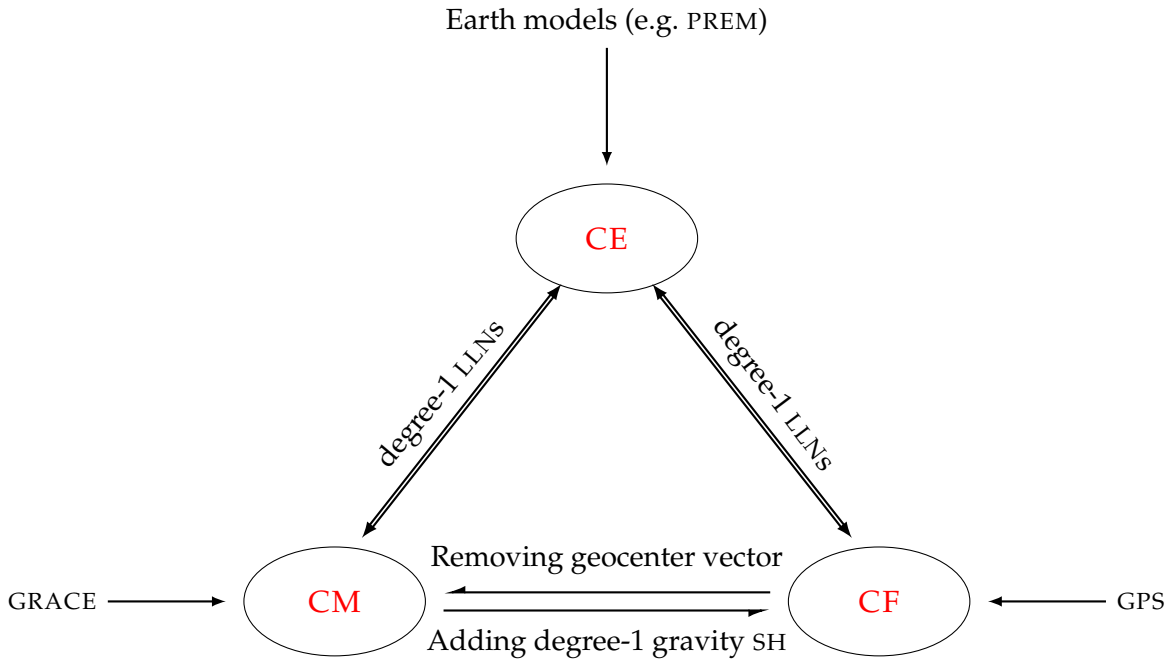

Figure 2.8: *Mutual relationships between* CE, CM *and* CF, *with connection to the Earth models, the* GRACE *and* GPS *datasets, respectively.*

consistent before comparing and analyzing the GRACE and GPS data. One way is that adding the degree-1 gravity spherical harmonic coefficients to the GRACE products and subsequently being convolved in the spectral domain with the loading Love numbers from the CF frame will result in the displacements in the CF frame. This procedure is most frequently applied in the literature (see Davis et al., 2004; Tregoning et al., 2009; Fu et al., 2012, etc.). Conversely, the other way is to remove the geocenter motion time series from the GPS data which will correspond to a result in the CM frame. This manner is also used in the literature (see van Dam et al., 2007; Tesmer et al., 2011).

Chapter 3

Singular spectrum analysis for modeling geodetic time series

3.1 Motivation

OVER the last two decades, investigation of surface mass loading via space-geodetic techniques has shown that many of the mass fluxes display a seasonal behavior, especially a composition of annual plus semiannual signals (Blewitt et al., 2001; van Dam et al., 2001; Dong et al., 2002). Much attention has been given to separate these periodic signals from other signals in the geodetic time series, e.g. linear or nonlinear trends. Conventionally, these seasonal signals are modeled by sums of sinusoids with annual plus semiannual cycles using the classical least squares estimation approach. However, only constant amplitudes and phases can be obtained in this parametric approach. In reality, true seasonal signals are not constant from year to year. For example, water storage changes show strong peaks due to floods or droughts. Recently, several studies have endeavored to determine the time-varying periodic variations using non-parametric approaches (e.g. Freymueller, 2009; Tesmer et al., 2009; Chen et al., 2013) or model based approaches (e.g. Davis et al., 2006; Bennett, 2008; Davis et al., 2012). Among them, Chen et al. (2013) successfully applied singular spectrum analysis (SSA) to time-variable seasonal signals modeling for GPS time series. Comparing to the least squares as well as the Kalman filtering approach (Davis et al., 2012), SSA shows both its advantages and disadvantages (Chen et al., 2013, 2015)

In geodesy, data-driven methods, such as Empirical Orthogonal Function (EOF)/Principal Component Analysis (PCA) and Independent Component Analysis (ICA), are of significant interests because of their parameter free and straightforward implementation characteristics. These approaches are normally used to smooth or model multivariate geodetic time series, e.g. multivariate GPS time series (Dong et al., 2006) and GRACE gravity spherical harmonic coefficients (e.g., Rangelova et al., 2007; Frappart et al., 2011; Forootan and Kusche, 2012; Rangelova et al., 2012). To be more precise in those applications, Dong et al. (2006) applied PCA to remove the common mode errors from regional spatial GPS time series and Rangelova et al. (2007, 2012) used PCA and M-SSA (multi-channel singular spectrum analysis) respectively to investigate the main time-variable mass variations from GRACE data. In comparison to these approaches, SSA, as a special case of M-SSA, is designed to analyze univariate time series. This feature facilitates its application to univariate geodetic time series, for example, single-coordinate GPS time series (Chen et al., 2013), basin averaged equivalent water height time series from GRACE (Swenson and Wahr, 2002) or even water level variations from Satellite Altimetry (Tourian et al., 2015).

As an extension of (Chen et al., 2013), this chapter is dedicated to extend the application of SSA to other univariate geodetic time series. In addition to extracting seasonal signals, other features of SSA, e.g. non-linear trend extraction, will also be investigated. Few aspects related to the application of SSA will be discussed as well.

3.2 Methodology

SSA has the same origin as PCA which are both based on the Karhunen-Loève theory of random fields and of stationary random processes (Ghil et al., 2002). The key idea in both approaches is to identify the main patterns of the variability included in the data, along with decreasing order of the associated variance. The idea is implemented by diagonalizing the corresponding covariance matrix.

SSA is designed for univariate time series and it can be extended to multivariate time series, resulting in multi-channel SSA (M-SSA). As a natural extension of SSA, M-SSA allows in the same way as SSA to decompose the given time series into its spectral components. However, in contrast to SSA, M-SSA has advantages of extracting common information from any given multivariate time series. For instance, application of M-SSA to GRACE gravity spherical harmonic coefficients takes both spatial and temporal correlations embedded inside the data into account (Rangelova et al., 2012). PCA is actually a special case of the M-SSA when no time lags are introduced.

SSA therefore is a data-driven method that uses univariate data to extract information from short and noisy time series without prior knowledge of the dynamics affecting the time series. An important feature of SSA is that obtained trends are not necessary linear and extracted oscillations can be amplitude and phase modulated. A number of authors have given thorough descriptions of this technique (e.g., Broomhead and King, 1986; Vautard and Ghil, 1989; Vautard et al., 1992; Plaut and Vautard, 1994; Allen and Robertson, 1996; Ghil et al., 2002). In the following, we briefly summarize their contributions and outline the main steps of the SSA algorithm.

The starting point of SSA is to embed a time series $(x_i, 1 \leq t \leq N)$ into a trajectory matrix D by sliding a M-point window. The dimension of the trajectory matrix is $N' \times M$, where $N' = N - M + 1$. The trajectory matrix D has the form

$$D = \begin{pmatrix} x_1 & x_2 & x_3 & \cdot & \cdots & x_M \\ x_2 & x_3 & x_4 & \cdot & \cdots & \cdot \\ x_3 & x_4 & x_5 & \cdot & \cdots & \cdot \\ \cdot & x_5 & x_6 & x_7 & \cdots & \cdot \\ \vdots & \vdots & \vdots & \vdots & \vdots & \vdots \\ \cdot & \cdot & \cdot & \cdot & \cdot & x_{N-1} \\ x_{N'} & \cdot & \cdot & \cdot & x_{N-1} & x_N \end{pmatrix} . \tag{3.1}$$

The covariance matrix is then formed by

$$C_{\mathrm{BK}} = \frac{1}{N'} D^T D \, . \tag{3.2}$$

As this way of constructing the covariance matrix was originally proposed by Broomhead and King (1986), known for BK algorithm, we call the covariance matrix as C_{BK}. An alternative way to computing the covariance matrix C is called VG algorithm (proposed by Vautard and Ghil (1989)), which is based on the lagged-covariance matrix of the process x_i. The average of x_i is removed and the series is normalized by its standard deviation. With a maximum lag (or window size) M, the matrix C_{VG} has a Toeplitz structure, i.e., constant diagonals corresponding to equal lags:

$$C_{VG} = \begin{pmatrix} c_0 & c_1 & c_2 & \cdot & \cdots & c_{M-1} \\ c_1 & c_0 & c_1 & \cdot & \cdots & \cdot \\ c_2 & c_1 & c_0 & \cdot & \cdots & \cdot \\ \cdot & c_2 & c_1 & c_0 & \cdots & \cdot \\ \vdots & \vdots & \vdots & \vdots & \vdots & \vdots \\ \cdot & \cdot & \cdot & \cdot & \cdot & c_1 \\ c_{M-1} & \cdot & \cdot & \cdot & c_1 & c_0 \end{pmatrix}, \tag{3.3}$$

where entries c_j, $0 \leq j \leq M-1$, is the covariance of x at lag j. Its unbiased estimates are:

$$c_j = \frac{1}{N-j} \sum_{i=1}^{N-j} x_i x_{i+j}, \qquad 0 \leq j \leq M-1\,. \tag{3.4}$$

The similarities and differences between BK algorithm and VG algorithm in computing the covariance matrix have been discussed by Allen and Smith (1996) and Ghil and Taricco (1997). Both algorithms lead to a symmetric covariance matrix C. However, the VG approach has the advantage of better noise reduction when applied to short time series with respect to the BK approach (Ghil et al., 2002). In this chapter, we apply the VG approach to compute the covariance matrix C.

The second step is eigenvalue decomposition of C yielding eigenvalues λ_k and eigenvectors (also called EOFs) E_j^k of this matrix, which are sorted in descending order of λ_k, where indices j and k vary from 1 to M. The kth principal component is

$$a_i^k = \sum_{j=1}^{M} x_{i+j} E_j^k, \qquad 0 \leq i \leq N-M\,. \tag{3.5}$$

Finally, each component of the original time series identified by SSA can be reconstructed, with the kth reconstructed component (RC) series given by Vautard et al. (1992)

$$x_i^k = \begin{cases} \frac{1}{i} \sum_{j=1}^{i} a_{i-j}^k E_j^k & 1 \leq i \leq M-1 \\ \frac{1}{M} \sum_{j=1}^{M} a_{i-j}^k E_j^k & M \leq i \leq N-M+1 \\ \frac{1}{N-i+1} \sum_{j=i-N+M}^{M} a_{i-j}^k E_j^k & N-M+2 \leq i \leq N\,. \end{cases} \tag{3.6}$$

SSA typically decomposes a time series into RCs that are nearly periodic with periods less than M and one or two RCs containing variations in the time series with periods greater than M.

According to Plaut and Vautard (1994), harmonic oscillations can be identified in terms of the three fundamental properties of SSA: (1) two consecutive eigenvalues are nearly equal; (2) the two corresponding time sequences described by EOFs are nearly periodic, with the same period and in quadrature, namely, EOFs of the same frequency but with phase shift by 90°; (3) the associated PCs are in quadrature.

3.3 Aspects of application of SSA

Choice of lag-window size *M* Implementing the SSA technique, a key procedure is the proper choice of lag-window size M, which defines the spectral resolution of the algorithm, i.e., the ability to distinguish between two spectral peaks. There is no universal rule for the selection of the window size M. Nevertheless, due to the symmetry of the covariance matrix, one needs always to make $M \leq N/2$.

In addition to this basic rule, a number of empirical suggestions from other studies are given as follows. For example, according to Vautard et al. (1992), M can not be either too large or too small. If M is too small, the coarse resolution may cause several neighboring peaks in the spectrum of signal to coalesce. On the contrary, large M values will split the peak into several components with neighboring frequencies and weaken the capability of isolating peaks at frequencies lower than the resolution $1/M$, i.e., periods larger than M. Vautard et al. (1992) therefore suggested SSA succeeds in distinguishing oscillations with periods between $M/5$ and M. Moreover, when choosing the lag-window size, Ghil et al. (2002) proposed to balance two considerations: quantity of information extracted versus the degree of statistical confidence in that information. The former requires as wide a window as possible, i.e. a large M, while the latter requires as many repetitions of the features of interest as possible, i.e., as large a ratio N'/M as possible. Golyandina and Zhigljavsky (2013) also recommended to select a window size that makes M/T an integer if we have a good knowledge of the period T of the signals. In other words, it is advantageous to choose M to be an integer multiple of the period T. This is particularly useful for geodetic time series in which seasonal signals are always of much significance.

In the geodetic field, Rangelova et al. (2012) applied a three-year window (156 weeks) to retrieve long-term changes together with seasonal variations from weekly GRACE solutions. For the case of weekly GPS time series, annual and semi-annual signals are currently of most interests and Chen et al. (2013) confirmed window sizes of two or three years to be suitable for most of GPS time series. Nevertheless, depending on the composition of signals, window sizes of four years or even five years are also possible for few cases (Chen et al., 2015).

Recently, a mathematical way of selecting window length, which statistically test the convergence of the autocovariance function, is proposed by Khan and Poskitt (2012). However, in the geodetic field, our main interests focus on extracting annual and semi-annual signals and we therefore only follow the empirical rules rather than try the newly proposed mathematic method to determine the window length. Generally, trial and error experience is recommended in order to select the optimal window size.

Separability of signals Golyandina et al. (2001) introduced the concept of separability of components of time series using SSA when the composition of signals are complicated with several approximate frequencies. The so-called **w**-correlation between the RCs are computed so as to define whether a weak separability or strong separability exists. Strong separability or even exact separability is desirable in practice although this does not always occur. In reality, an approximate separability can be more frequently obtained (Golyandina and Zhigljavsky, 2013).

According to Golyandina and Zhigljavsky (2013), the **w**-correlation between two RCs is mathematically defined as

$$\rho^w(\mathrm{RC}^1, \mathrm{RC}^2) \stackrel{\text{def}}{=} \frac{(\mathrm{RC}^1, \mathrm{RC}^2)_w}{\|\mathrm{RC}^1\|_w \|\mathrm{RC}^2\|_w}, \tag{3.7}$$

with

$$(\mathrm{RC}^1, \mathrm{RC}^2)_w \stackrel{\text{def}}{=} \sum_{i=1}^{N} w_i x_i^1 x_i^2. \tag{3.8}$$

RC^1 and RC^2 is called **w**-orthogonal if $(\mathrm{RC}^1, \mathrm{RC}^2)_w = 0$. The weight w_i in Eq. (3.8) denotes the frequency of the element x_i from the original time series appearing in the trajectory matrix D in Eq. (3.1) and w_i is defined as

$$w_i = \begin{cases} i & \text{for} \quad 1 \le i < \min(M, N') \\ \min(M, N') & \text{for} \quad \min(M, N') \le i < \max(M, N') \\ N - i + 1 & \text{for} \quad N - M + 2 \le i \le N\,. \end{cases} \tag{3.9}$$

Two RCs are approximately separable if $\rho^w(\mathrm{RC}^1, \mathrm{RC}^2) \simeq 0$. Fig. 3.1 presents the **w**-correlation of RCs from the water level time series in Section 3.4.1 which clearly shows different separabilities using the respective window sizes. The separabilities are weaker using the 3-year window size than with the other two window sizes, especially in the first ten RC modes. Comparing to the top and the middle row, the strong separabilities in the first six RCs using the 5-year window size are desirable and these six modes are proved to be important signals in Section 3.4.1. As strong or exact separabilities are preferable in practice, the **w**-correlation analysis can help us to determine the optimal window size and categorize the component groups in a way.

Unevenly sampled time series Two situations exist in the case of unevenly sampled time series. One is the case of irregular sampling, e.g. water level time series from satellite altimetry (e.g., Tourian et al., 2015) while the other is the evenly sampling but with missing data, e.g. daily or weekly GPS time series (Dow et al., 2009). In order to apply SSA, the former case requires to resample the data into regular sampling. For the latter case, one solution is to fill the gaps using interpolation techniques and apply SSA afterwards. An alternative approach is suggested by Schoellhamer (2001). He used a modified singular spectrum analysis algorithm to obtain spectral estimates from records with a large fraction of missing data and the modified algorithm is implemented as follows. An over-bar in the following notation indicates that the series either contains missing data or is calculated from a series that contains missing data. First, the lagged autocorrelation is computed by ignoring any pair of data points with a missing value.

$$\bar{c}_j = \frac{1}{N_l} \sum_{l \le N-j} \bar{x}_l \bar{x}_{l+j}, \qquad 0 \le j \le M - 1\,, \tag{3.10}$$

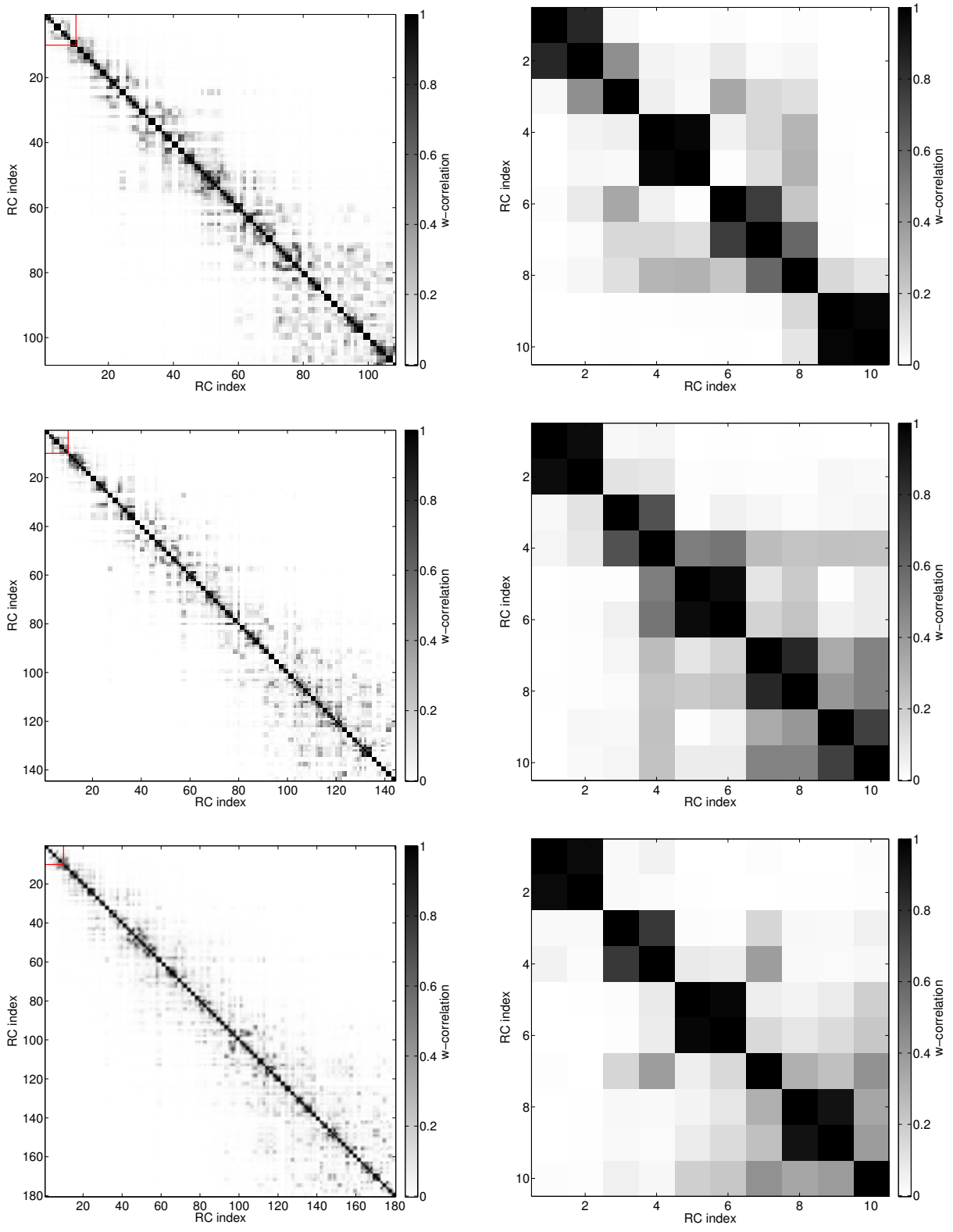

Figure 3.1: *w-correlation analysis of the water level time series using a 3-year window size ($M = 108$, top row), a 4-year window size ($M = 144$, middle row) and a 5-year window size ($M = 180$, bottom row). The first ten* RCs *for each window size which are indicated by the red boxes are shown on the right column.*

where N_l are pairs with no missing data. The lagged covariance matrix C_{VG} is then formed in the same way as Eq. (3.3) using $\bar{c}_j$. Eigenvalue decomposition is applied to C_{VG} and eigenvectors are obtained subsequently. Note that the eigenvectors contain no missing data. Computation of the k^{th} principal component ignores missing data points

$$\bar{a}_i^k = \frac{M}{N_l} \sum_{l \leq M} \bar{x}_{i+l} \bar{E}_l^k, \qquad 0 \leq i \leq N - M\,. \tag{3.11}$$

If $N_l \leq fM$, where $f \in [0,1]$ is introduced that represents a specified fraction of allowable missing data points within a given window size M, then $\bar{a}_i^k$ is given a missing value. The final reconstruction step is implemented in the same manner as SSA and if any PC value in the sum is missing, then the RC value will accordingly be missing.

This technique has been applied successfully in GPS time series with missing data (Chen et al., 2013). In the case of monthly GRACE derived total water storage time series, Schoellhamer's approach will also be applied instead of interpolation.

Centering the time series Centering the time series, i.e. subtracting the mean, is one simple but non-trivial step in the course of operating SSA. This step is also important for other spectral decomposition methods, e.g. PCA (Rangelova et al., 2007), which ensures the first principal component describing the direction of maximum variance. This simple preliminary process of the data is justified by Miranda et al. (2008) who demonstrated the necessity of a zero mean to find a basis minimizing the mean square error of the approximation of the data. Thus the mean of the time series is always removed before the SSA analysis is performed in the following section.

3.4 Application of SSA to geodetic time series

SSA has been demonstrated to be useful in various fields, e.g. climate science, meteorology and geophysics (Golyandina and Zhigljavsky, 2013). Basic SSA can be used for several purposes, e.g. non-linear trend extraction, separating amplitude-modulated periodicities and smoothing. Extension of SSA are possible for time series gap-filling (Kondrashov and Ghil, 2006), forecasting (Marques et al., 2006) as well as other applications (Golyandina and Zhigljavsky, 2013).

In geodesy, the application of SSA is relatively new. Rangelova et al. (2012) investigated the capabilities of M-SSA for extracting the main periodic and non-periodic variabilities from weekly GRACE data which demonstrated the potentialities of SSA. A further application of SSA is provided by Chen et al. (2013) who applied SSA successfully to GPS time series for modeling the time-variable seasonal signals. As an extension of these contributions, this section endeavors to investigate the potential application of SSA to other geodetic time series, e.g. lake level time series from satellite altimetry (Section 3.4.1) and basin aggregated total water storage time series from GRACE (Section 3.4.2).

3.4.1 Lake level time series

THE lake level time series used in this subsection comes from Tourian et al. (2015) which was derived for monitoring the desiccation of Lake Urmia. Lake Urmia is a dischargeless salt lake located in northwestern Iran between the two Iranian provinces of East and West Azerbaijan. Over the past decade, it is suffering from severe decline of lake surface area as well as water level (Tourian et al., 2015). Nowadays, various space-borne techniques, such as satellite altimetry, are employed to observe its changes.

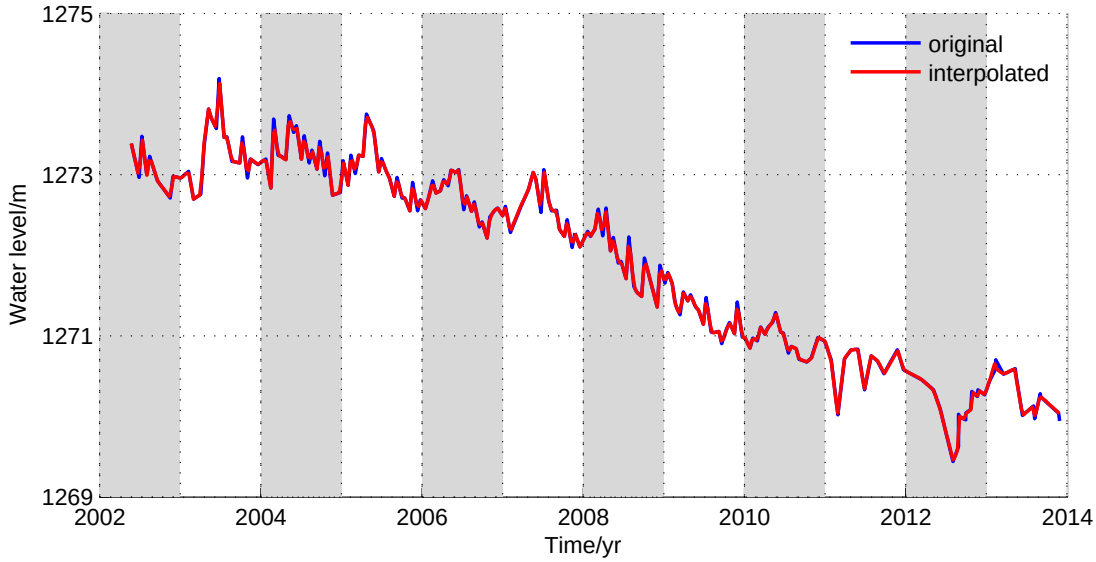

Figure 3.2: *The observed water level time series of Lake Urmia (Tourian et al., 2015) and the interpolated time series.*

The water level data used here spanning from 2002.4 to 2013.9 was derived from three different satellite altimetry orbit configurations launched by European Space Agency (ESA), namely, ENVISAT (ENVIromental SATellite), EVISAT extended and CryoSat-2. Each satellite orbit configuration has its own sampling rate, for example, a 35-day repeat period for ENVISAT and a 30-day repeat cycle for ENVISAT extended. In addition, both descending and ascending tracks were used to derive lake level changes. All these factors make the whole dataset into an irregularly sampled time series (Tourian et al., 2015). Thus, it is necessary to resample the data and it is accordingly interpolated with the piecewise cubic spline interpolation into time series with a 10-day sampling interval. The original water level time series and the interpolated one are shown in Fig. 3.2 which display a very clear non-linear trend together with different periodicities and noise. The following analysis will show capabilities of SSA to capture the non-linear trend and separate the oscillations.

Based on the experiences from Chen et al. (2013) as well as the **w**-correlation analysis shown in Fig. 3.1, a 5-year window size ($M = 180$) is selected and applied. In terms of the methodology presented in Section 3.2, the corresponding plots of eigenvalues and eigenvalue spectrum are firstly shown in Fig. 3.3. It is shown in Fig. 3.3 that the long term trend signal appears in the first four modes which dominate the whole data and correspond to up to 92.5 % of the total variance. Annual signals appear in the fifth and sixth modes corresponding only up to 1.85 % energy and no significant semi-annual signals occur in the time series.

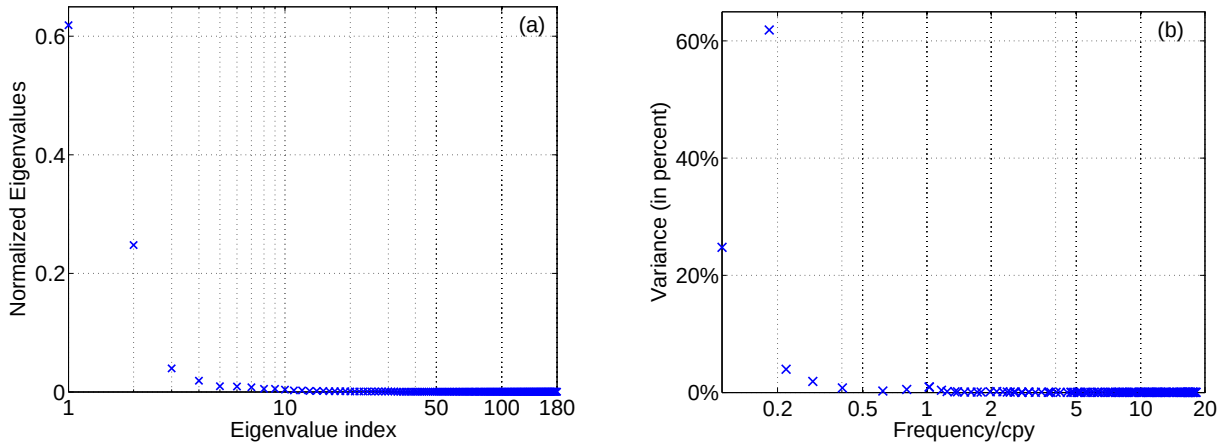

Figure 3.3: *(a) Eigenvalues from eigenvalue decomposition of the covariance matrix; (b) eigenvalues versus the dominant frequency associated with their corresponding* EOFs.

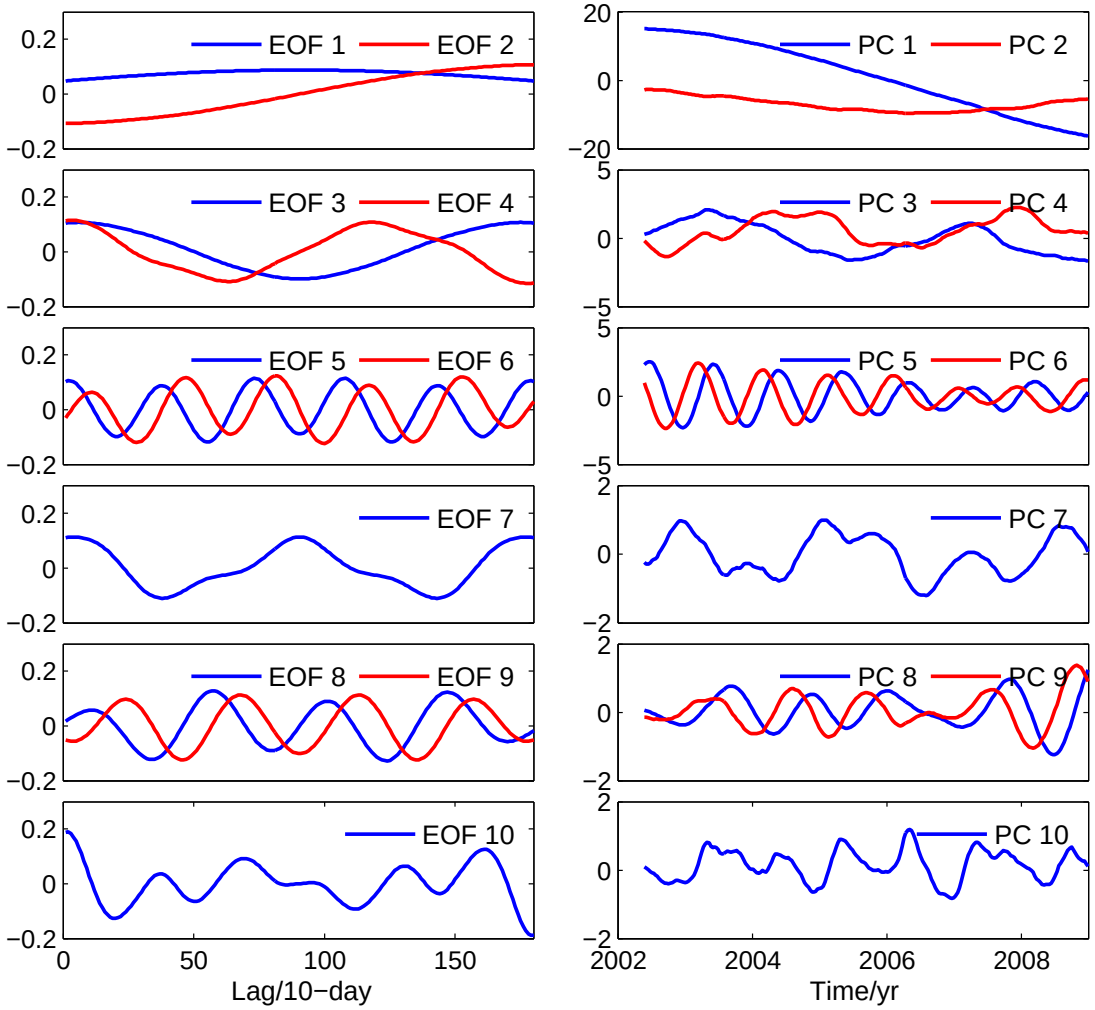

Figure 3.4: *The first 10* EOFs *and* PCs *are grouped in terms of the eigenspectrum.*

According to the eigenspectrum shown in Fig. 3.3 as well as suggestions by Plaut and Vautard (1994), corresponding EOFs (E matrix in Eq. (3.5)) and PCs (a matrix in Eq. (3.5)) are grouped and shown in Fig. 3.4. The first four modes clearly illustrate the long-term trends with different frequencies and the fifth and sixth modes correspond to the annual signals. The latter four modes correspond to other irregular oscillations with no origins to our knowledge which might be due to colored noise (Allen and Smith, 1996).

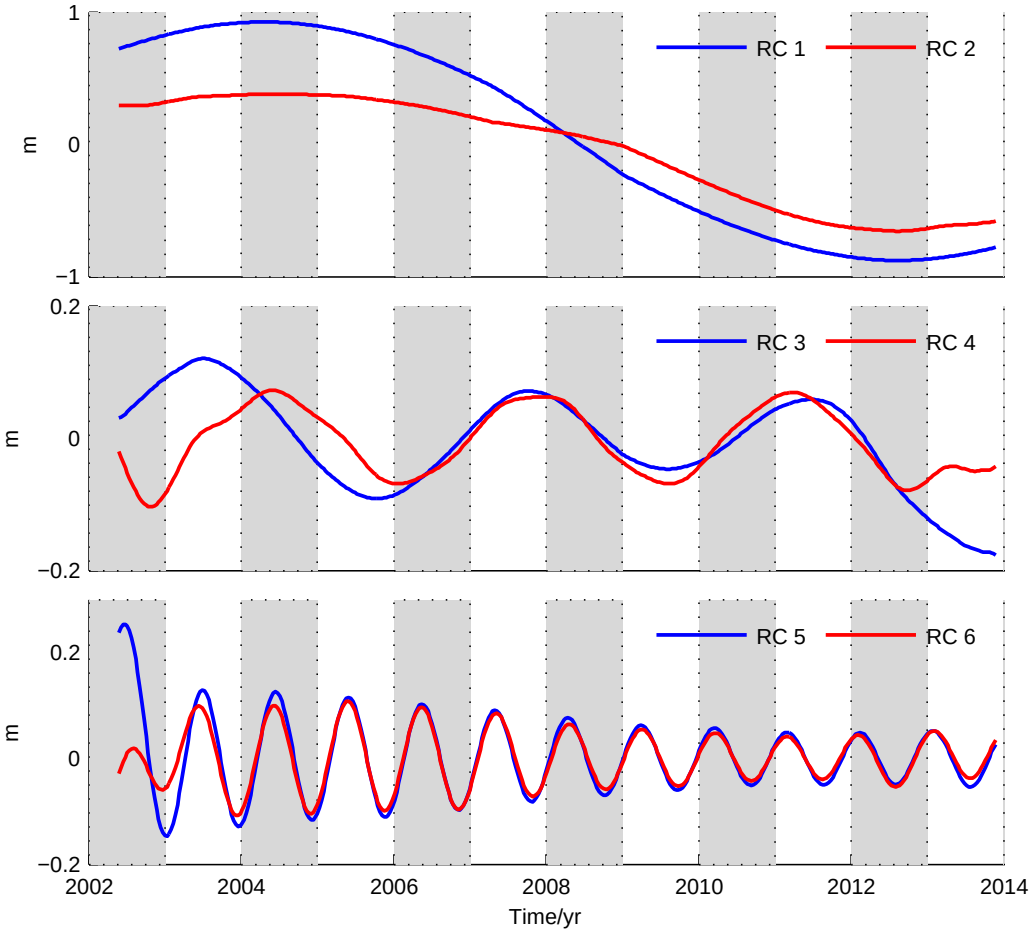

Figure 3.5: *The first six reconstructed components.*

In terms of variance contributions, the first six modes contribute up to 94.35 % of the total variance and therefore these first six modes are reconstructed and displayed in Fig. 3.5. The first two RCs clearly display the long-term trend while the third and fourth RCs seem to show two long-term oscillations with a period around 4 years which deserve a further investigation of their origin. However, this further investigation is out of the scope of this section. The amplitude modulated annual signals are obviously represented with decreasing amplitudes which might be caused by the desiccation of Lake Urmia (Tourian et al., 2015).

Fig. 3.6 shows the summation of the first six RCs with respect to the original time series. The blue curve in Fig. 3.6 fits the original time series very well capturing both the non-linear trend as well as the periodic signals. Furthermore, it is also found that the red curve representing the long-linear trend follows the whole time series closely, which demonstrates the ability of SSA to separate the long-term trend from the periodic variabilities and noise.

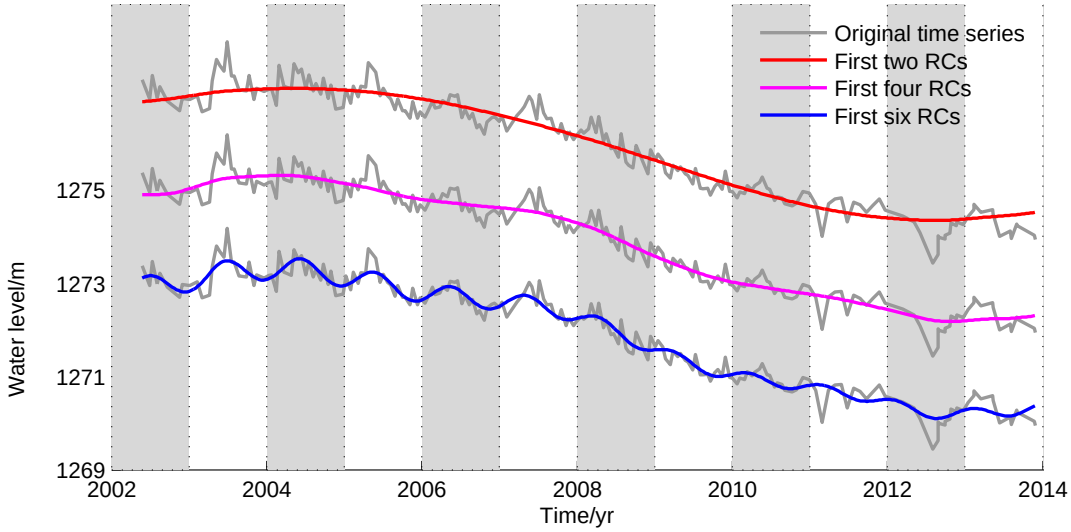

Figure 3.6: *Comparison of* RCs *with respect to the original time series. Plots with magenta and red curves are shifted for plotting purposes.*

SSA is not compared with other mode-based techniques, e.g. the classical least squares method and the Kalman filter approach (Davis et al., 2012; Chen et al., 2013), due to the existence of the non-linear trend which is hard to be represented by a simple mathematic model. Nevertheless, future work will focus on this aspect to compare SSA with other potential techniques or to examine the significance of those captured signals using, for example, Monto-Carlo SSA (Allen and Smith, 1996).

3.4.2 Basin averaged equivalent water height time series

WITH the advent of the GRACE mission, equivalent water height (EWH) time series, especially area or basin averaged ones, are of remarkable interest for geodesists to study hydrological loading processes (Tapley et al., 2004). These time series normally display a strong seasonal signal together with a linear or non-linear trend depending on location (e.g., Baur, 2012; Rangelova et al., 2012). It is always of central importance to separate these components so as to facilitate the understanding of their origins (see Rangelova et al., 2007; Schmidt et al., 2008b; Frappart et al., 2011; Davis et al., 2012; Baur, 2012; Rangelova et al., 2012). In particular, Rangelova et al. (2012) demonstrated the usage of M-SSA combined with a 700 km Gaussian filter on the weekly GRACE gravity spherical harmonic coefficients to derive basin averaged seasonal total water storages. This subsection aims to show an alternative procedure which applies SSA to extract non-linear and seasonal signals from the basin averaged total water storage time series.

It is worth mentioning that, before performing SSA, we firstly follow the steps described in Appendix A to estimate the equivalent water height and then compute the basin averages using the approach given by Swenson and Wahr (2002) to obtain the basin scale equivalent water height time series. The Congo basin which is located in west equatorial Africa with a basin size of 3693×10^3 km^2 is adopted here as an example. To be more detailed in the procedure of deriving the equivalent water height time series, the combination of the destriping filter

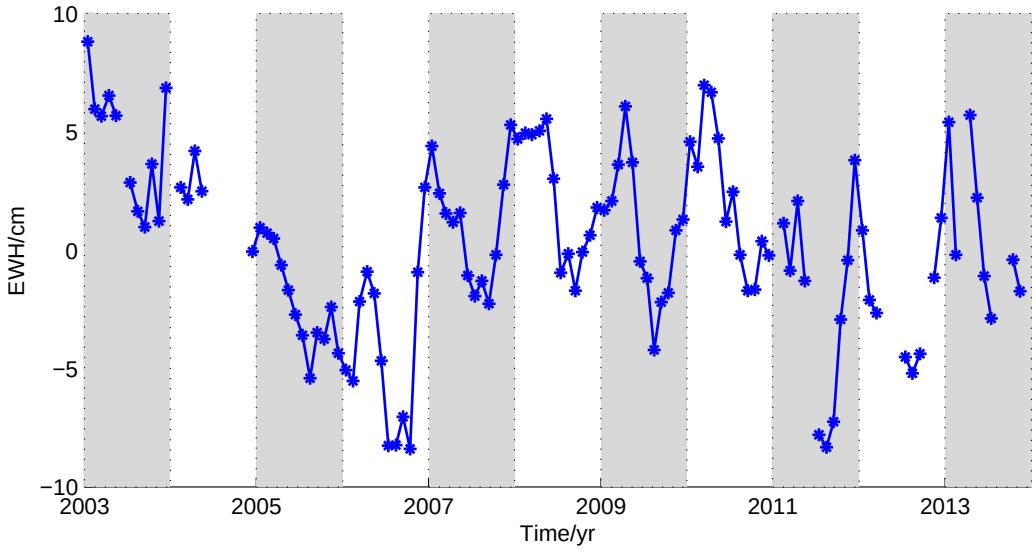

Figure 3.7: *The derived equivalent water height time series of the Congo Basin.*

(Swenson and Wahr, 2006) and a 500 km Gaussian filter (Jekeli, 1981) is applied to the monthly GFZ RL 05a spherical harmonic coefficients (Dahle et al., 2014). The months with regularized solutions, e.g. June to November in 2005, are removed so that a few gaps exist in the time series, see Fig. 3.7.

As mentioned before, Schoellhamer (2001)'s approach is used here for dealing with gaps in the course of the SSA analysis. Via the **w**-correlation analysis, a window size of 5-year is deployed here in this example and the corresponding eigenvalue spectrum and the **w**-correlation plots are shown in Fig. 3.8. It is evident from Fig. 3.8 that both the **w**-correlation and the eigenspectrum indicate five pairs of oscillations from the first ten modes. The corresponding EOFs and PCs displayed in Fig. 3.9 further support the analysis.

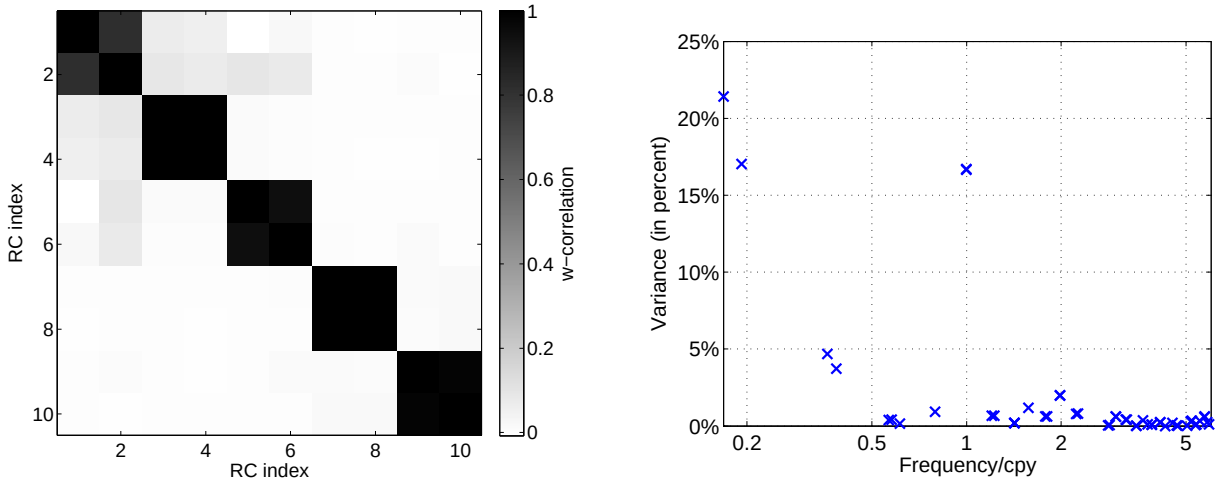

Figure 3.8: *Left: the **w**-correlation; Right: the eigenspectrum indicating the eigenvalues versus the dominant frequency associated with their corresponding* EOFs.

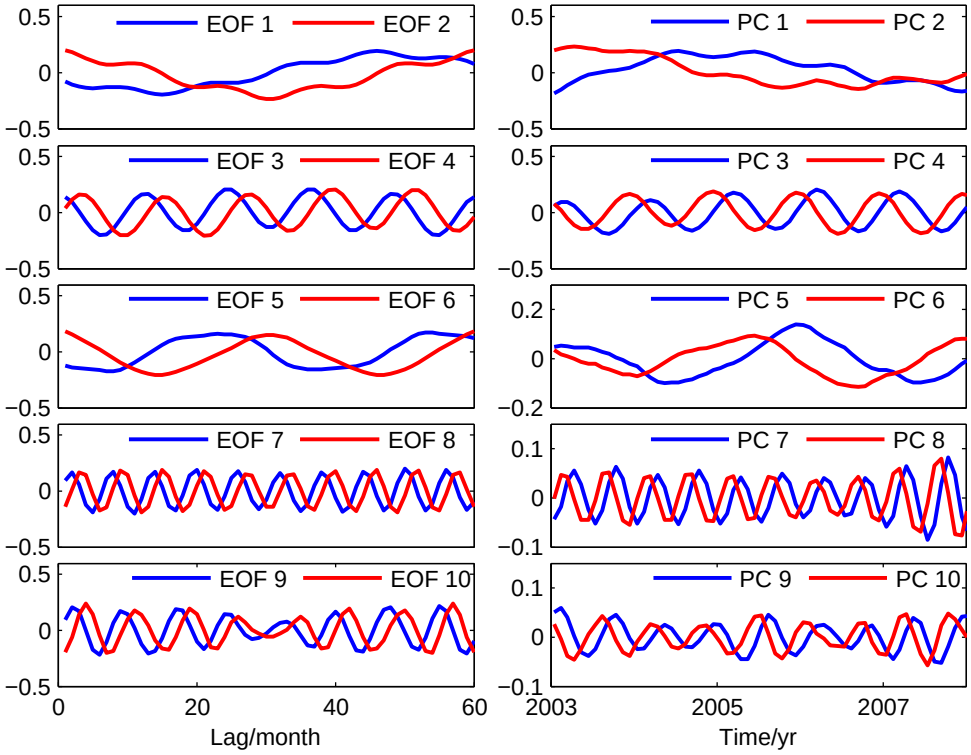

Figure 3.9: *The first 10* EOFs *and* PCs *are grouped in terms of the eigenspectrum.*

Clearly shown in Fig. 3.9, long-term trends appear in the first two modes and strong annual signal patterns (see also, Crowley et al., 2006) occur in the third and fourth components. From the eigenspectrum in Fig. 3.8, these four modes dominate the whole time series contributing up to 71.8 % in terms of variance. Inter-annual patterns (a 3-year cycle) which were also seen by Schmidt et al. (2008b) and Rangelova et al. (2012) are observed in the fifth and sixth modes with a contribution of 8.4 % variance. The same finding as Schmidt et al. (2008b) for the Congo basin here is that semi-annual signals do not play a significant role contributing only 4.0 % variance. An approximate 1.5-year oscillation pattern also appears in the ninth and tenth modes which requires further investigation of its origin.

Fig. 3.10 shows the corresponding reconstructed components with a more clear view of the long-term trend and the different periodicities. The comparison of the reconstructed components with respect to the derived equivalent water height is displayed in Fig. 3.11. The blue curve consists of the first eight RCs with a contribution of 84.2 % ot the total variance and it fits the original time series closely with a correlation of 0.9. The red curve indicating the non-linear trend also sees the minimum and the peak which were also shown in Rangelova et al. (2012). By a careful visual inspection, the pattern shown in Fig. 3.11 has significant similarities with the Figure 9 (b) shown in Rangelova et al. (2012), which in a way verifies the analysis presented here.

The above analysis confirms that gaps are not a problem in the SSA analysis and the modified SSA algorithm proposed by Schoellhamer (2001) could adequately handle time series with missing data. Nevertheless, it is worth pointing out that SSA fails to capture few peaks of the equivalent water height time series in Congo. This might be a potential weakness of SSA.

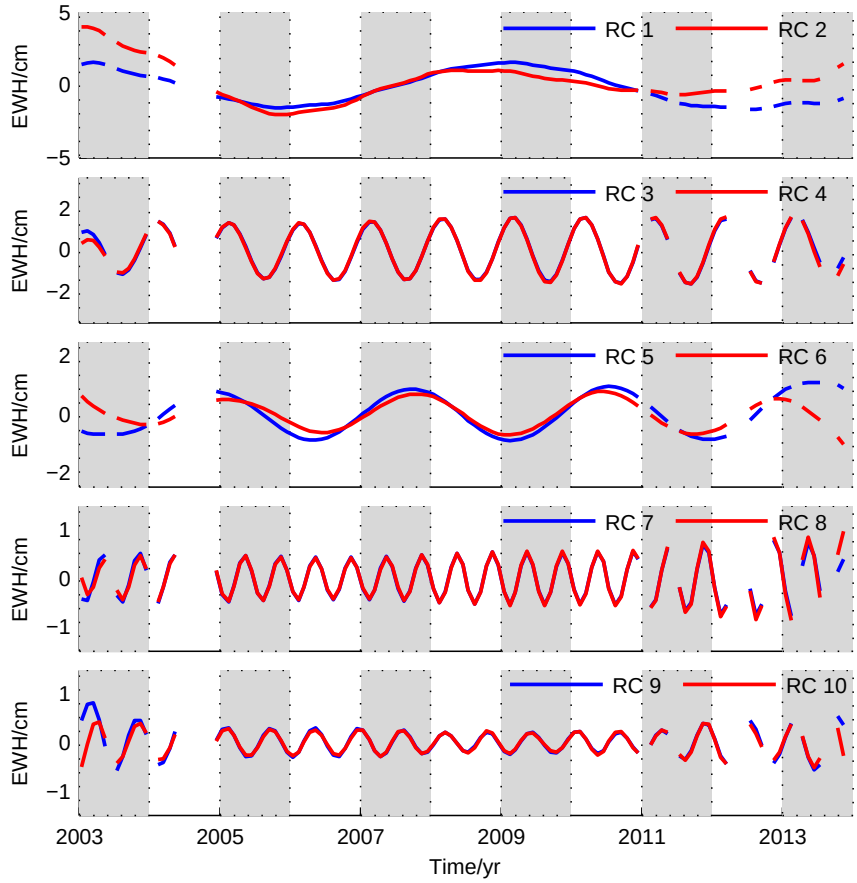

Figure 3.10: *The first ten reconstructed components of the equivalent water height time series from the Congo basin.*

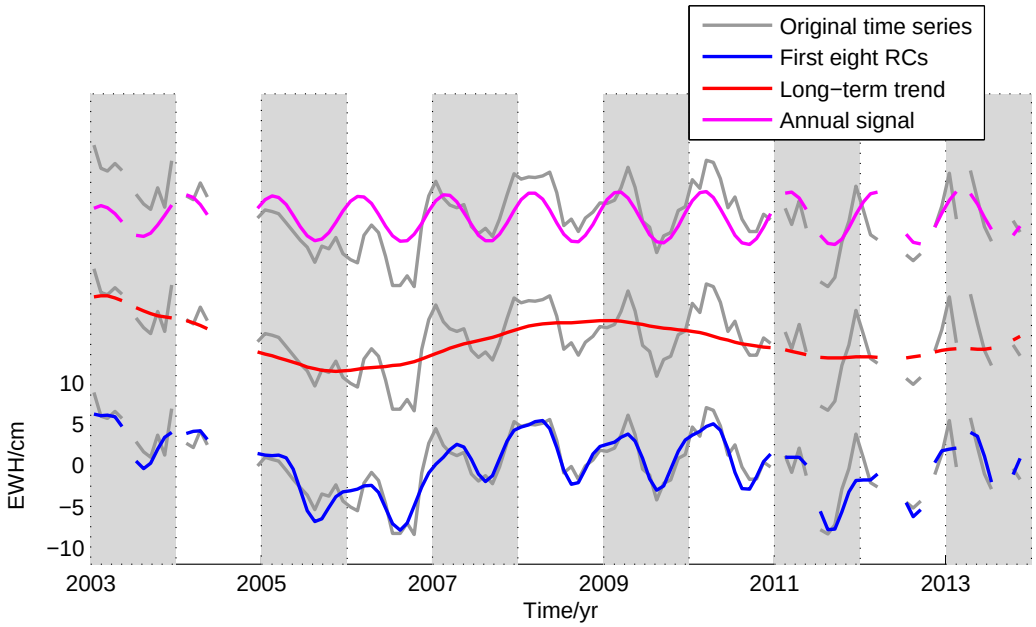

Figure 3.11: *Comparison of* RCs *with respect to the original time series in the Congo basin. Plots with magenta and red curves are shifted for plotting purposes.*

3.5 Discussion and summary

THIS chapter discusses the methodology as well as the application of SSA in the lake level time series and the basin averaged equivalent water height time series. A clear long-term trend together with other periodic variabilities, e.g. annual variations, exist in both exemplary time series. By applying SSA to both time series, it is demonstrated that SSA has the ability to extract both long-term variations as well as the periodic oscillations.

As mentioned before, the window size is a key parameter in SSA. With the help of the **w**-correlation analysis, a 5-year window size which is found to be the optimal window size, is applied in both examples. It should be mentioned that the same window size in time does not necessarily correspond to the same M in samples because the number of M depends on the sampling rate as well. For instance, in the case of the water level time series, $M = 180$ (out of 421 samples) is adopted while $M = 60$ (out of 131 samples) is used in the second example. Large window sizes used here support the description stated in (Golyandina and Zhigljavsky, 2013) that separating long-term trend from oscillations requires large window sizes. The choices of window size here also follow the recommendation by Golyandina and Zhigljavsky (2013) to make M/T an integer since we know that annual signals are always significant in geodetic time series.

SSA is not compared to the model-based approaches here because the comparison has been done in Chen et al. (2013). The conclusions presented there certainly apply here. For instance, comparing to the Kalman filtering approach, SSA can avoid the complication of assuming the noise processes that affect the time series. Model-independence and data-driven are the most significant features of SSA.

However, its merits also lead to its drawbacks that the whole SSA analysis in this chapter does not include any uncertainty estimation or statistical significance test. This means that we cannot obtain a quantitative evaluation of the analysis. A significance test is required after the analysis, especially in the presence of colored noise. Performing Monte-Carlo significance test in the course of implementing SSA in the future might possibly help us to assess the significance of the detected periods, for example, the 1.5-year cycle detected in the second example. In a way, Monte-Carlo SSA can serve as a potential detector of unknown periods against the correlated errors (Allen and Robertson, 1996; Schmidt et al., 2008b).

Chapter 4

Hydrological loading induced vertical displacements from GPS and GRACE

4.1 Motivation

OVER the last decade, the gravity field satellite mission GRACE has been proved successful in monitoring surface mass variations (e.g., Tapley et al., 2004). GRACE-derived spherical harmonic coefficients can be converted to several other physical quantities for geophysical studies, e.g. equivalent water height and deformation (e.g., Wahr et al., 1998; Davis et al., 2004). However, the absence of a truth dataset for the GRACE results poses challenges in the validation process. Measurements from other satellite techniques or from Earth models are therefore employed to validate or complement GRACE. The GNSS technique, which directly measure the crust deformation, is strongly connected to the GRACE mission.

Through the past few years, both GPS and GRACE have been employed together to study changes of the Earth's shape due to surface mass loading, especially hydrological loading (e.g., Davis et al., 2004; van Dam et al., 2007; Tregoning et al., 2009). With the advancement of background models in both GPS and GRACE data processing, the agreement between GPS and GRACE signals were significantly improved (e.g., Tregoning et al., 2009; Tesmer et al., 2011). Nevertheless, remaining error sources still affect the consistency between the two techniques. GRACE data filtering is among one of them (Tesmer et al., 2011), which can remarkably affect the derived surface displacements with respect to their noisiness, as well as regional systematic patterns.

In the GRACE community, several filters were designed to reduce the systematic noise of the GRACE data and enhance the signal-to-noise ratio. Various filtering schemes were investigated and compared for different purposes (King et al., 2006; Werth et al., 2009; van der Wal, 2009; Steffen et al., 2010; Scheller, 2012; Belda et al., 2015). For example, Werth et al. (2009) evaluated the performances of six types of filters from a hydrological perspective and Scheller (2012) conducted another detailed comparison of several types of filters for a regional freshwater fluxes system study using GRACE in Siberia. In addition, van der Wal (2009) and Steffen et al. (2010) compared different types of filters when applying GRACE to investigate the glacial isostatic adjustment. These filtering comparisons in the literature indicate the central importance of filtering and it is also concluded that no single filter produces consistent good performances for all studies.

In comparison to GPS observed deformation, the commonly used way of filtering GRACE gravity models in previous studies is mostly making use of the isotropic Gaussian filter of a given

half-width (Jekeli, 1981). For instance, King et al. (2006) investigated the choice of optimal Gaussian smoothing radii for temporal GRACE gravity solutions and validated with vertical displacements measured using a global GPS network of 63 sites. They concluded that optimum smoothing radii were ∼500 km for continental sites in terms of correlations between GPS observed and GRACE-derived vertical displacements. At the global scale, van Dam et al. (2007) applied the isotropic Gaussian filter with a radius of 500 km while Tesmer et al. (2011) decreased the radius to 400 km to balance between minimizing the GRACE errors and avoiding the signal loss for better interpretation. In comparison with GPS at the regional scale, Khan et al. (2010) utilized the isotropic Gaussian filter with a smoothing radius of 250 km for the GRACE products from CSR over Greenland while Fu et al. (2013) applied the isotropic Gaussian filter with a radius of 350 km in the Amazon region. It seems that the optimal smoothing radius of the isotropic Gaussian filter is not fixed. How will the different smoothing radii affect the GRACE-derived vertical displacements? This question will be answered in this chapter?

Besides the isotropic Gaussian filter, anisotropic Gaussian filter (Han et al., 2005), destriping filter (Swenson and Wahr, 2006), and stochastic filters (e.g., Kusche, 2007) are designed to minimize systematic errors in GRACE. Those filters are immensely used in GRACE filtering for hydrological purposes while they are hardly applied in the case of comparison with GPS. In this sense, the choice of optimum Gaussian smoothing radii or even choice of optimum filters is not settled yet.

In addition, as time elapses, the procedure to generate the gravity spherical harmonic coefficients is improved and the latest GRACE products, e.g. Release 05 (RL05), have been released by different data processing agencies in 2012. The new releases are less contaminated by noise than previous solutions due to the improvement of raw data processing. Therefore the associated filter choices might be changed accordingly comparing to other studies who used the old releases (van Dam et al., 2007). To investigate the impact of filtering on the GRACE-derived vertical displacements, the GPS observations from Europe and South America are selected for two reasons: 1) both regions have relatively dense GPS station coverage; 2) Europe represents an area where the hydrological signal is low while South America stands for an area where strong mass variation happens. Using the latest GRACE RL05 data from GFZ (Dahle et al., 2014) and the improved GPS time series from IGS (Collilieux et al., 2011) and the SIRGAS network (Sánchez et al., 2013), we revisit the idea of King et al. (2006) by including more filters in addition to the isotropic Gaussian filter.

4.2 GRACE data filtering

In general, the filters used in the GRACE community can be categorized into two types: deterministic filters and stochastic filters. In deterministic filter design the impulse response of the filter function is pre-defined, which implicitly means that the frequencies that possess signal and the frequencies that are dominated by noise are pre-defined. This further implies that one must have a certain idea about the signal and noise content of the frequencies. Jekeli (1981) presents some of the most commonly used filters in gravity field determination, and of those filters the Gaussian averaging function is the one chosen here. In addition, this study also uses the anisotropic Gaussian filter of Han et al. (2005) and the destriping filter of Swenson and Wahr (2006).

Stochastic filtering, unlike deterministic filtering, utilizes the behavior of signal and noise described by their respective covariances to filter out noise. The stochastic filters that this study has used for processing the GRACE are the DDK filter described in Kusche (2007) and the regularization filter (Lorenz, 2009; Devaraju et al., 2012) which follows the basic principle of the DDK filter. However, the regularization filter differs from the DDK filter in two aspects, which are the ways of constructing the noise and signal covariances. Section 4.2.2 details the DDK filter approach as well as the the regularization filter approach and their differences.

4.2.1 Deterministic filters

Isotropic Gaussian filter Smoothing the gravity field on the sphere using the isotropic Gaussian filter was first formulated by Jekeli (1981) in physical geodesy. The isotropic Gaussian filter smooths a signal by attenuating the power of high-frequencies which are represented as high degree and order spherical harmonic coefficients in the gravity field. In terms of Jekeli (1981), the Gaussian window function between two points $P(\theta, \lambda)$ and $P'(\theta', \lambda')$ on the sphere follows

$$W^{\mathrm{G}}(\psi) = e^{-b(1-\cos\psi)}, \quad b > 0 \quad \text{and} \quad 0 \leq \psi \leq \pi, \tag{4.1}$$

where b is a dimensionless parameter characterizing the smoothing process and ψ is the spherical distance between P and P' on the sphere. Applying Eq. (4.1) over the whole sphere, the smoothing kernel in the spatial domain becomes

$$W^{\mathrm{G}}(\psi) = \frac{e^{-b(1-\cos\psi)}}{1 - e^{-2b}}\,, \tag{4.2}$$

with

$$b = \frac{\ln(2)}{1 - \cos(\frac{r}{R})}\,, \tag{4.3}$$

where $r = R\psi$ denotes the *half-width radius* parameter i.e. the distance on the Earth's surface at which $W(\psi)$ has dropped to half its value at $\psi = 0$. The parameter r is commonly used to indicate the level of the Gaussian smoothing.

In the spectral domain, Wahr et al. (1998) presented the recursive form of computing the smoothing coefficients W_l:

$$\begin{aligned} W_0^{\mathrm{G}} &= 1\,, \\ W_1^{\mathrm{G}} &= \tfrac{1+e^{-2b}}{1-e^{-2b}} - \tfrac{1}{b}\,, \\ W_{l+1}^{\mathrm{G}} &= -\tfrac{2l+1}{b} W_l^{\mathrm{G}} + W_{l-1}^{\mathrm{G}}\,, \quad l \geq 1\,. \end{aligned} \tag{4.4}$$

According to Eq. (4.2) and Eq. (4.4), an important feature of the above Gaussian filter is *isotropy*, i.e. the weighting structure of the smoothing kernel is directional invariant. The smoothing coefficients in the spectral domain are only degree-dependent and are therefore location-independent in the spatial domain.

Anisotropic Gaussian filter (Han Filter) Due to the fact that noise, existing in the GRACE spherical harmonic coefficients, varies with both degree and order, Han et al. (2005) proposed a Gaussian-based anisotropic averaging approach. The smoothing kernel is constructed as

$$\begin{aligned} W_{lm}^{\mathrm{H}} &= W_{l}^{\mathrm{G}}(r_{\frac{1}{2}}(m)) \,, \\ \text{with} \quad r_{\frac{1}{2}}(m) &= \tfrac{r_1 - r_0}{m_1} m + r_0 \,, \end{aligned} \tag{4.5}$$

where r_0 and r_1 are the averaging radii, respectively, applied for zonal harmonics ($m = 0$) and for order m_1 harmonics ($m = m_1$). In the case of $r_0 = r_1$, Eq. (4.5) becomes the isotropic Gaussian smoothing operator with the smoothing radius of r_1.

The merit of the Han filter lies in its *anisotropic* characteristic i.e. the weighting structure of the smoothing kernel is directional variant, which behaves both degree and order dependent in the spectral domain (W_{lm}^{H}). In the spatial domain, the averaging resolution depends on r_0 in latitude direction and r_1 and m_1 in longitude direction. Normally, r_1 is fixed to be twice of r_0, which produces a better resolution in latitude direction than the isotropic Gaussian filter (Lorenz, 2009).

Within the anisotropic filter group, it might be interesting to mention that another non-isotropic filter called Fan filter (Zhang et al., 2009) was also used by researchers (Belda et al., 2015). The Fan filter is a 2-D double filter consisting of a low-pass along the degree l (the same as the conventional isotropic filter) simultaneously with a low-pass along the order m, whose contour projection onto the (l, m)-plane is fan-shaped.

Destriping filter Swenson and Wahr (2006) observed the presence of long, linear, north-south striped phenomena in the unsmoothed GRACE data, which correspond to a correlation in the spectral domain between even and odd degrees for spherical harmonic coefficients of a particular order. To remove the correlated errors, Swenson and Wahr (2006) proposed a destriping filter (or decorrelation filter) by fitting and removing a low order polynomial in a moving window of half-width w centered on the degree l for a particular order m:

$$C_{lm}^{\mathrm{ds}} = \sum_{i=0}^{p} Q_{lm}^{i} l^{i}, \tag{4.6}$$

where C_{lm}^{ds} is the destriped spherical harmonic coefficients; Q_{lm}^{i} is the degree i coefficient of the polynomial fit; p is the order of the polynomial. Note that Eq. (4.6) for C_{lm} is also valid for S_{lm}. The polynomial coefficients are obtained by least-squares according to

$$Q_{lm}^{i} = \sum_{j=0}^{p} \sum_{\substack{n=l-w/2 \\ n\text{: even or odd}}}^{l+w/2} L_{ij}^{-1} n^{j} C_{nm} \,, \tag{4.7}$$

with

$$L_{ij} = \sum_{\substack{n=l-w/2 \\ n\text{: even or odd}}}^{l+w/2} n^{i} n^{j} \,. \tag{4.8}$$

The summation process over degree n in Eq. (4.7) is done separately for odd and even degrees; that is, if l is odd, then only odd degrees n are summed, and likewise when l is even. It is worth

mentioning that a much more detailed implementation of the algorithm, which is written in algebraic form, can be found in Devaraju (2015).

Variations in the implementation of the destriping filter exist for different purposes. The cut-off degree l, the degree p of polynomial fit and the window size w can be varied based on the order and on the error pattern (Duan et al., 2009). For example, Chen et al. (2007b) applied the destriping filter with a setting of the cut-off degree $l = 6$ and the polynomial degree $p = 3$, which was denoted as P3M6, for investigating the ability of GRACE to detect coseismic and postseismic deformation from the Sumatra-Andaman earthquake. Whereas Chambers (2006) used the cut-off degree $l = 8$ and the polynomial degree $p = 7$ for evaluation of GRACE RL02 products over the ocean. Based on the previous studies, Duan et al. (2009) proposed to determine the cut-off degree l and the window size w in terms of the error patterns provided by the processing centers. Very recently, Belda et al. (2015) updated the configuration of the destriping parameters for the global application for GRACE RL05 monthly solutions.

4.2.2 Stochastic filters

UNLIKE the deterministic filters, the stochastic filters are designed to filter the GRACE gravity spherical harmonic coefficients using the *a prior* information about the unfiltered coefficients. For instance, Sasgen et al. (2006) presented a filter using the idea behind the Wiener filter, which tries to minimize the difference between the filtered signal and a desired output signal. Implementation of this filter requires prior knowledge about the desired signal which, however, does not exist in the case of GRACE signals, and Sasgen et al. (2006) utilized the characteristics of the GRACE spherical harmonic coefficients to approximate the signal variance. Tracking back to the least-squares estimation of the GRACE spherical harmonic coefficients, Kusche (2007) proposed to smooth and constrain the noisy GRACE signal within the concept of a *Bayesian type regularization* (Koch and Kusche, 2002). Kusche et al. (2009) simplified the approach of Kusche (2007) by applying a block diagonal instead of a full synthetic error covariance matrix which was mapped from the GRACE twin-satellite orbital pattern and resulted in the so-called *DDK filter*. Note that in (Kusche, 2007) and (Kusche et al., 2009), the signal variance used is derived from geophysical models and the synthetic error covariance matrix obtained based on the GRACE orbit of August 2003 is the same for the entire time series.

In a variation of the approach of Kusche (2007) and Kusche et al. (2009) but unlike them, Lorenz (2009) implemented an approach using different strategies to deal with the error covariance and the signal covariance, which was further extended by Devaraju et al. (2012). Here we denote the stochastic filter developed by Lorenz (2009) and Devaraju et al. (2012) as the *Regularization filter*. The details about the DDK filter and the Regularization filter are introduced below.

DDK filter In matrix notation, the DDK filter can be written as:

$$\mathbf{x}' = \mathbf{W}\mathbf{x}\,, \tag{4.9}$$

with the filter matrix $\mathbf{W}$:

$$\mathbf{W} = (\mathbf{N}^{-1} + \alpha\mathbf{S}^{-1})^{-1}\mathbf{N}^{-1}\,, \tag{4.10}$$

where vectors $\mathbf{x}'$ and $\mathbf{x}$ denote the filtered and unfiltered Stokes coefficients, respectively, and $\mathbf{N}$ is the approximate block-diagonal GRACE error covariance matrix and $\mathbf{S}$ is a diagonal degree

dependent signal covariance estimated from geophysical models. The degree of smoothing is controlled by the regularization parameter α. The strongest smoothing corresponds to the parameter $\alpha = 10^{14}$, denoted as DDK 1, while the parameter $\alpha = 10^{11}$, which is called DDK 5, produces the weakest smoothing. According to Börgens and Eicker (2014), it is impossible to find the one-to-one correspondence between the Gaussian smoothing radii and the different DDK filters, but only in terms of different characteristics, such as *attenuation*. In this thesis, the DDK filtered datasets are downloaded directly from the ICGEM website.

Regularization filter Within the concept of regularizing the GRACE normal equation proposed by Kusche (2007), Lorenz (2009) implemented the stochastic filtering in a similar way but differing from that by

1. instead of using the invariant error covariance matrix, Lorenz (2009) simulated a full error covariance matrix for each month according to the energy balance approach (see Eq. 4.2.1 in Lorenz (2009));
2. instead of constraining the smoothing using the same power-law signal covariance model derived from the geophysical models, Lorenz (2009) utilized a Kaula-type rule estimated from the monthly GRACE coefficients as the stochastic constraint.

Note that though we use different notations here, Lorenz (2009) fundamentally follows Kusche (2007) closely. Likewise, in algebraic form, the regularization filter can be formulated as:

$$\mathbf{x}' = (\mathbf{P}_{\mathrm{G}}^{i} + \lambda \mathbf{P}_{\mathrm{K}})^{-1} \mathbf{P}_{\mathrm{G}} \mathbf{x} \,, \tag{4.11}$$

where $\mathbf{P}_{\mathrm{G}}^{i}$ is the inverse of the simulated error covariance matrix for the month i and $\mathbf{P}_{\mathrm{K}}$ denotes the inverse of the signal variance matrix derived from the Kaula-type rule of the GRACE coefficients; λ determines the degree of smoothing. Unlike from the parameter α used by Kusche (2007), the regularization parameter λ ranges in theory from 0 to ∞. Higher values indicate stronger smoothing.

In more details, $\mathbf{P}_{\mathrm{K}}$ is computed according to Eq. (4.12)

$$\mathbf{P}_{\mathrm{K}} = \mathbf{Q}_{\mathrm{K}}^{-1} = \begin{pmatrix} \mathbf{K}^{\mathrm{C}} & 0 \\ 0 & \mathbf{K}^{\mathrm{S}} \end{pmatrix}^{-1} \,, \tag{4.12}$$

with

$$K_{lm} = \frac{\sigma_l^2}{2l+1}, \quad l = m, m+1, ..., L, \quad m = 0, 1, ..., L \,, \tag{4.13}$$

where σ_l^2 denotes the signal degree variances estimated by fitting a power law to the pure signal degree variances of the monthly GRACE coefficients (see more details in Section 4.1 in (Lorenz, 2009)). Thus, K_{lm} represents the signal variance per coefficient. Specifically, the weight matrix $\mathbf{P}_{\mathrm{K}}$ is invariant for the entire period.

Devaraju et al. (2012) and Sneeuw et al. (2014) further developed the regularization filter by introducing the characteristics of cyclo-stationarity, buried in the monthly GRACE products, into the regularization process. As a consequence, the weight matrix $\mathbf{P}_{\mathrm{K}}$ varies for each calendar month. It is worth mentioning that the regularization parameter λ was optimally computed using variance component estimation in (Lorenz, 2009) while in (Devaraju et al., 2012) and

(Sneeuw et al., 2014), λ can be adapted based on trial and error, behaving similarly as the different DDK filters.

Table 4.1 summarizes the differences between different stochastic filters. i indicates the sampling month of the GRACE solutions and j indicates the calendar month ranging from 1 to 12.

Table 4.1: *Different settings for stochastic filters*

Method	Filter
Wiener filter	$\frac{S}{S+N}$
DDK filter	$\frac{N^{-1}}{N^{-1}+\alpha S^{-1}}$
Regularization filter	$\frac{P_{\mathrm{G}}^{i}}{P_{\mathrm{G}}^{i}+\lambda P_{\mathrm{K}}^{j}}$

Other than the filters which are introduced above in detail, other filters which are designed for specific purposes or for specific regions exist in the literature. For example, the Empirical Orthogonal Function (EOF) approach is applied to extract the principle components from the GRACE monthly solutions which can serve as a filtering tool (e.g., Schrama et al., 2007; Rangelova et al., 2007), and Klees et al. (2008) introduced an anisotropic, non-symmetric (ANS) filter which they claimed to be the optimal filter for the GRACE signals. The ANS filter makes use of the noise and the full signal variance-covariance matrix to tailor the filter to the error characteristics of a particular monthly solution and it can be considered as an extended version of Kusche (2007). Davis et al. (2008) presented a statistical filtering approach utilizing a parameterized model for the temporal evolution of the GRACE coefficients.

Table 4.2: *Settings of five categories of filters we used. In the destriping filter, l and m refer to the starting degree and order.*

Filter type	Variable parameter	Reference
Isotropic Gaussian filter	$r_g = 200, 250, 300, 350, 400, 450,$ 500, 600, 800 ,1000 km	(Jekeli, 1981)
Anisotropic Gaussian filter	$r_0 = r_g, r_1 = 2 \times r_0$	(Han et al., 2005)
Destriping filter	$p = 2, l = m = 8$	(Swenson and Wahr, 2006)
DDK filter	$\alpha = 10^{14}, 10^{13}, 10^{12}, 5 \times 10^{11}, 10^{11}$	(Kusche, 2007)
Regularization filter	$\lambda = 0.5, 1, 2, 3, 4, 5, 6, 7, 8, 9, 10$	(Kusche, 2007; Lorenz, 2009; Devaraju et al., 2012)

Certainly, several other filters are not listed here and a thorough evaluation of all possible filters is not straightforward. Thus the filters which are commonly used are selected in this chapter for comparison and they are presented in Table 4.2. Throughout this chapter, the following abbreviations are used for the deterministic filters in the tables and figures: IG (isotropic Gaussian

filter), AG (anisotropic Gaussian filter), IGD (isotropic Gaussian filter combined with the destriping filter), AGD (anisotropic Gaussian filter combined with the destriping filter). It should be noted that the combination of the destriping filter with the isotropic or anisotropic Gaussian filter is conducted by applying the destriping first.

4.3 Datasets and their inconsistencies

4.3.1 GPS time series

THE weekly GPS height time series from Collilieux et al. (2011), which preserves crustal deformation information in the position time series, especially at the seasonal timescale, are utilized and the same sites in Europe as used in (van Dam et al., 2007) are selected for the comparison over this area. A total of 40 sites are chosen for the comparison, see Fig. 4.1, and 13 exemplary GPS height time series are shown in Fig. 4.2. It is evident that GPS height time series from this area present similar seasonal behavior except MORP, which does not show clear annual and semi-annual signals. In addition, GPS sites from Eastern Europe show relatively stronger seasonal signals than GPS sites from the west, for example, POLV, located in Poltava, Ukraine. This phenomenon is also seen in the forthcoming analysis from GRACE. As both solutions from Europe and the SIRGAS GPS network described below are weekly solutions, they are therefore averaged into monthly time series to be consistent with the GRACE monthly solutions.

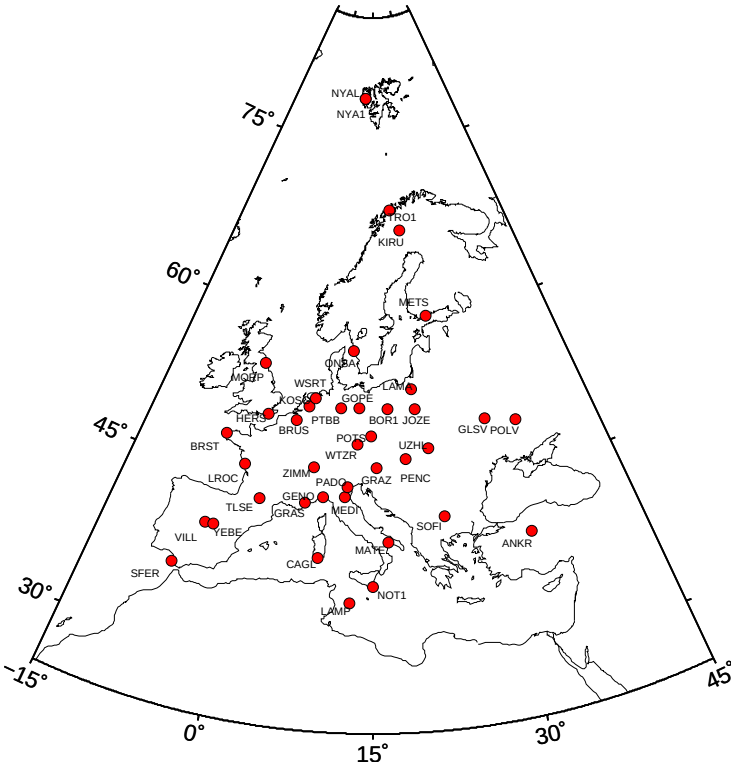

Figure 4.1: *Distribution of the selected 40* GPS *sites from Europe.*

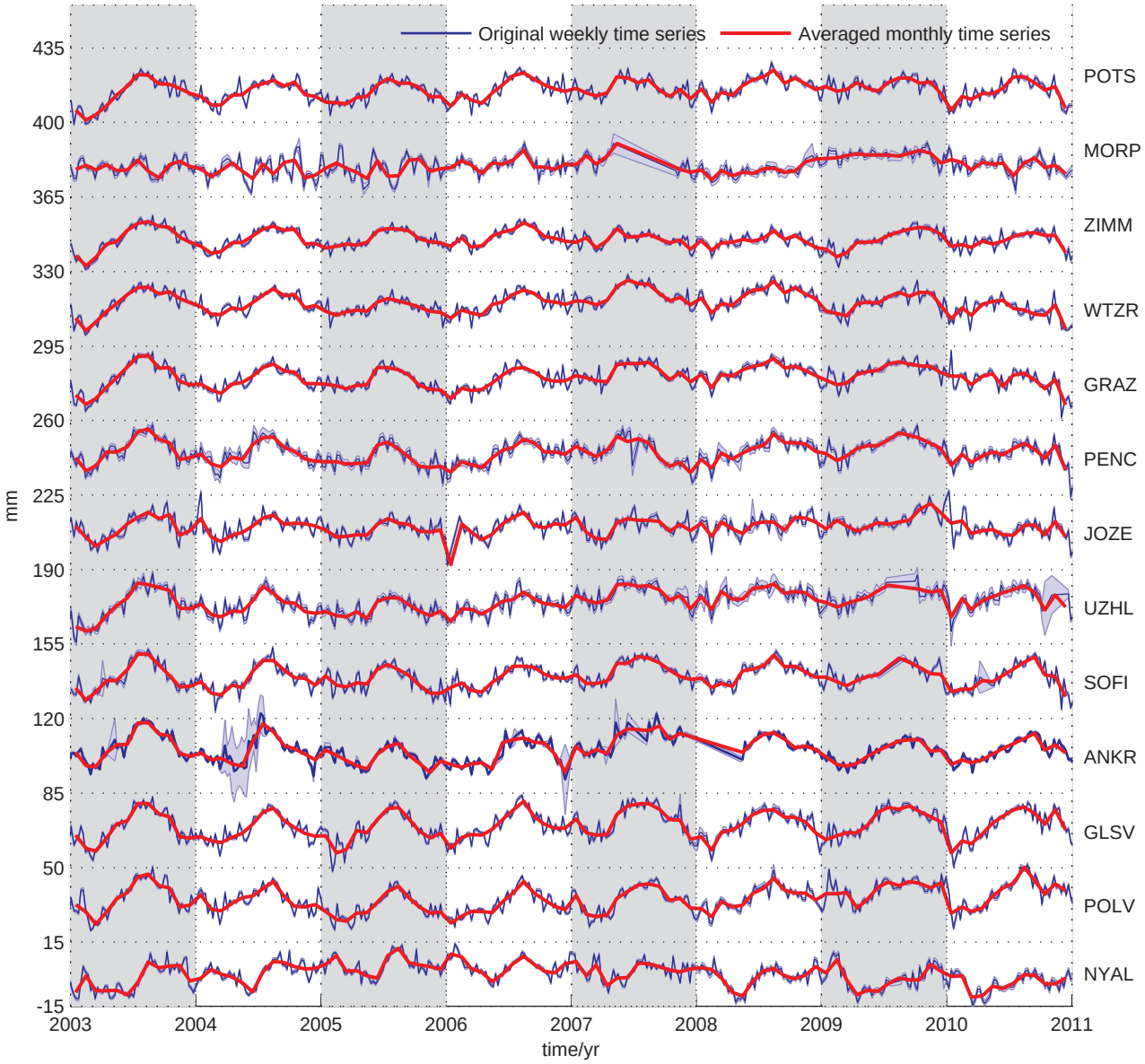

Figure 4.2: *Exemplary* GPS *height time series from Europe. In the figure, except* NYAL, GPS *height time series of the rest stations are shifted for plotting purposes. Shaded areas are error bounds of each original weekly time series.*

For the comparison over the Amazon area, the GPS time series from SIRGAS GPS network, which is processed by DGFI (German Geodetic Research Institute), are used. The whole SIRGAS GPS network, see Fig. 4.3, comprises 58 IGS global stations and other SIRGAS-CON regional stations, which makes up to around 300 stations in total up to now. The time series utilized in this comparison are the latest multi-year solution SIR11P01 (Sánchez and Seitz, 2011; Sánchez et al., 2013) and the detailed computation procedure is described in (Sánchez and Seitz, 2011). The final residual time series out of this multi-year solution are cleaned and detrended weekly solutions spanning from 2000 to 2011.29 when the IGS08 reference frame was introduced.

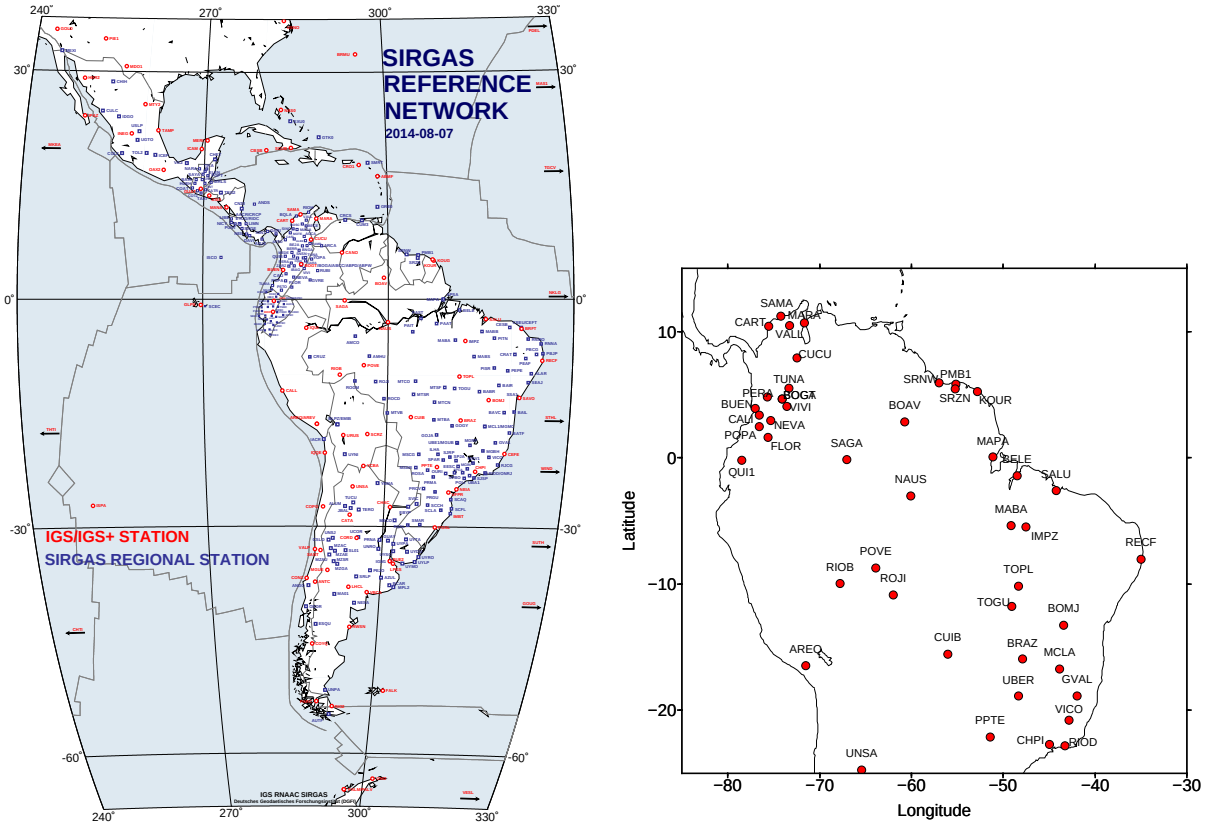

Figure 4.3: *Map of the* SIRGAS GPS *network (courtesy:* www.sirgas.org*) and distribution of the selected 46* GPS *sites from this regional* GPS *network.*

To compare with GRACE in this area, GPS stations with time series which overlap with the GRACE time frame more than three years are selected. As this study focuses on hydrological signals, the stations which are not located inside or around the Amazon basin and its nearby basins are ruled out. Eventually 46 stations out of 228 stations are used in the comparison, see Fig. 4.3. A few time series are shown in Fig. 4.4 as examples. Since the SIRGAS GPS network is under development, time series length from SIRGAS varies among the GPS sites.

Relative to GPS height time series from Europe, seasonal signals are much stronger in the SIRGAS network because significant water mass variations are happening in and around the Amazon area. For example, NAUS (located in Manaus, Brazil) displays a peak-to-peak 40 mm annual oscillation with an exception in 2009 when a severe flood happened (Chen et al., 2010). In addition to seasonal behavior, stations like BOGA (located in Bogota, Columbia) also show a clear non-linear trend signal.

4.3.2 GRACE products

THE GRACE GSM RL05a product from GFZ (Dahle et al., 2014) is used for the following reasons. Firstly, as reported by Tesmer et al. (2011), the GRACE datasets from GFZ, CSR and JPL did not show significant systematic differences. Secondly, compared to the GRACE related

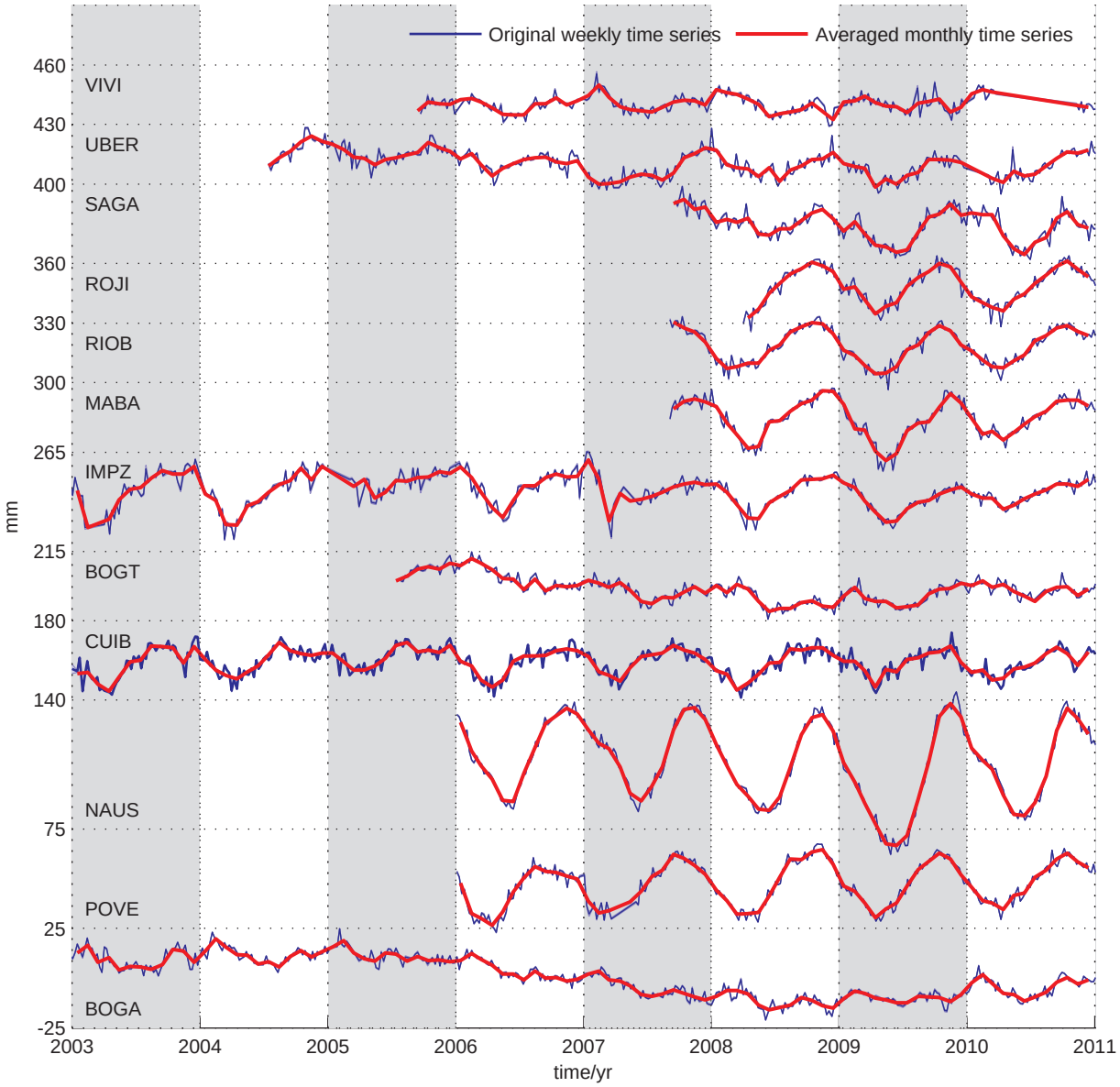

Figure 4.4: *Exemplary time series from* SIRGAS. *In the figure, except* BOGA, GPS *height time series of the rest stations are shifted for plotting purposes.*

products from CSR and JPL, GFZ provides better metadata, e.g. the calibrated standard deviations of the Stokes coefficients, which are used in the regularization filtering.

Before deriving displacements from the GRACE data, the C_{20} term is replaced in the GRACE GSM data using the product from Cheng et al. (2011). The resultant monthly GRACE GSM Stokes coefficients are then filtered using the deterministic filters and the regularization filter tabulated in Table 4.2. The DDK filtered datasets are downloaded directly from the ICGEM website. Note that the C_{20} term in the DDK filtered datasets are replaced as well before deriving the displacements for comparison.

4.3.3 Inconsistencies between GPS and GRACE

As discussed in the previous chapters, GPS and GRACE observe two fundamentally different quantities and they both experience totally different data processing procedures. Several issues exist in reality affecting the agreement between GPS and GRACE. For example, van Dam et al. (2007) and Tesmer et al. (2011) mentioned possible error sources in both GPS and GRACE which could probably influence the consistencies. To be more precise, van Dam et al. (2007) pointed out possible error sources from the GPS part, e.g. atmospheric mismodelling, bedrock thermal expansion, monument thermal expansion, phase center modeling and common orbital errors. Tesmer et al. (2011) also attributed disagreements in part to GRACE, e.g. external C_{20} term used in GRACE, GRACE data filtering and atmospheric and oceanic dealiasing models. Apart from these possible errors, however, two fundamental issues should be resolved before comparing GPS and GRACE: 1) the reference frame issue; 2) the atmospheric loading and non-tidal oceanic loading issue. These two issues are not dealt consistently in GPS and GRACE products and they should be corrected in those solutions before comparison.

Reference frame issue Several reference frames exist in use in geodesy and they have been discussed in Section 2.3. From there we know that the resultant GPS data stay in the CF reference frame while GRACE GSM products lie in the CM frame. Besides, translation of the reference frame from one to another is essentially linked to the translation of the degree-1 terms. As GRACE does not sense the geocenter motion, the degree-1 terms in the GRACE GSM gravity monthly solutions are set to zero. To keep GPS and GRACE consistent in the reference frame, several ways were adopted in the literature. However, in essence, the rule is to change from one into the other, that is to say, we either change GPS from the CF frame into the CM frame or the other way around.

Davis et al. (2004) firstly started to compare the displacements observed by GPS and derived from GRACE. They added the $l = 1$ contribution to the deformation inferred from GRACE, which was followed by Nahmani et al. (2012). Whilst van Dam et al. (2007) corrected the reference frame issues by removing the displacements due to the degree-1 effects from GPS (see Fig. 2.8) and this approach was also applied by Tesmer et al. (2011). It should be noted that the displacements computed by van Dam et al. (2007) and Tesmer et al. (2011) were simply an average of the X, Y, Z components from a global GPS network. Apparently, this way is not suitable for a regional GPS network study, e.g. the GPS network in Europe and the SIRGAS network used in this chapter. Alternatively, Tregoning et al. (2009) directly restored the degree-1 Stokes coefficients from Munekane (2007). Fu et al. (2012) followed Tregoning et al. (2009) but with the degree-1 Stokes coefficients obtained from Swenson et al. (2008). In theory, all the above-mentioned approaches should be able to maintain the consistency in the reference frame issues. However, different approaches using different datasets will certainly cause differences.

Here we conduct one experiment regarding the frame issue. Two geocenter motion datasets, which are provided in coordinates sensed by Satellite Laser Ranging (SLR) (Cheng et al., 2013) and in the degree-1 Stokes coefficients delivered by Swenson et al. (2008), are applied. One is to follow van Dam et al. (2007) but using the degree-1 displacements computed from Cheng et al. (2013) and the other way is to follow Fu et al. (2012). We find that the latter way provides slightly better but negligible consistencies than the former way in both two study areas. Thus, the degree-1 coefficients from Swenson et al. (2008) are restored back to the GRACE GSM data

to be consistent with the GPS time series in the CF reference frame in the forthcoming comparisons.

Non-tidal atmospheric and oceanic loading effects Since a key geoscience application of GPS time series is to monitor non-tidal loading effects, those effects are accordingly fully retained in the GPS products. However, during the GRACE data processing, the non-tidal variabilities in the atmosphere and oceans are removed using the background atmospheric and oceanic models. For example, de-aliasing product AOD1B RL05, delivered by GFZ, is derived in a combination of the ECMWF (European Centre for Medium-Range Weather Forecasts) operational atmospheric fields and the baroclinic ocean model OMCT (Ocean Model for Circulation and Tides) driven with the same atmospheric fields. Therefore, displacements derived from GRACE GSM gravity coefficients are not accordant with the GPS time series if the non-tidal atmospheric and oceanic effects are not resolved.

In the literature, several scenarios were adopted to restore consistency. For example, van Dam et al. (2007) reduced the non-tidal atmospheric and oceanic effects from the GPS data using the displacements computed from the AOD1B products while other studies, e.g. Tesmer et al. (2011) and Fu et al. (2012), they added the AOD1B products back to the GRACE GSM gravity fields. Essentially, consistency is kept in either cases.

It is worth noting that S1/S2 atmospheric pressure tidal loading are normally not resolved either during the GPS data processing, for example, the multi-year solution SIR11P01 used later. According to Flechtner et al. (2014a), signals from atmospheric tides are also fully retained in the AOD1B products. By adding back the AOD1B products, both tidal and non-tidal atmospheric loading effects are consistent in the GPS and GRACE datasets. In addition, the AOD1B products require no additional filtering process when using with the GSM monthly gravity products which is recommended by Flechtner et al. (2014a).

4.4 Metrics for performance evaluation

TO evaluate the comparison between the GPS observed displacements and the GRACE derived deformations, especially the performances of different filtering schemes, correlation coefficient, WRMS reduction (van Dam et al., 2007; Tregoning et al., 2009) along with Nash-Sutcliffe efficiency (Nash and Sutcliffe, 1970) are adopted here for evaluation.

Correlation coefficient It measures the similarity of two time series by

$$r = \frac{\sum_{i=1}^{n} (h_i^{\mathrm{GPS}} - \bar{h}_i^{\mathrm{GPS}})(h_i^{\mathrm{GRACE}} - \bar{h}^{\mathrm{GRACE}})}{\sqrt{\sum_{i=1}^{n} (h_i^{\mathrm{GPS}} - \bar{h}^{\mathrm{GPS}})^2} \sqrt{\sum_{i=1}^{n} (h_i^{\mathrm{GRACE}} - \bar{h}^{\mathrm{GRACE}})^2}} . \tag{4.14}$$

As it is well known, the correlation coefficient is sensitive to phases of two time series but insensitive to their amplitude differences. This characteristic normally leads us to apply other evaluation criteria along with the correlation coefficient.

WRMS reduction This metric is applied frequently in the comparison of GPS and GRACE (e.g., van Dam et al., 2007; Tregoning et al., 2009; Tesmer et al., 2011). It evaluates the agreement between GPS and GRACE by comparing the WRMS of the GPS displacements before and after removing the GRACE predicted deformations. The WRMS reduction is given by Eq. (4.15). Comparing to the correlation coefficient, WRMS reduction takes both phase and amplitude information into account. Note that the weight in computation of the WRMS reduction is adopted from the formal error information from GPS (e.g., van Dam et al., 2007; Tesmer et al., 2011). As such, it does not take the error information from GRACE into account. From an error propagation point of view, it is improper. However, this is the common way applied in statistical analysis when comparing GPS and GRACE and we therefore follow this manner here as well.

$$reduction = \frac{\mathrm{WRMS}\left[h_i^{\mathrm{GPS}}\right] - \mathrm{WRMS}\left[h_i^{\mathrm{GPS}} - h_i^{\mathrm{GRACE}}\right]}{\mathrm{WRMS}\left[h_i^{\mathrm{GPS}}\right]} . \tag{4.15}$$

Several studies have emphasized the strong agreement between the GPS-observed and the GRACE-derived height deformations at the seasonal frequency, especially annual signals (e.g., Davis et al., 2004; van Dam et al., 2007; Tesmer et al., 2011). To evaluate the impact of the GRACE filtering on the seasonal signals, a WRMS reduction ratio at the seasonal frequency level is defined according to Eq. (4.16) (e.g., Fu et al., 2012).

$$ratio_{\mathrm{reduction}} = \frac{\mathrm{WRMS}\left[h_i^{\mathrm{GPS}}\right] - \mathrm{WRMS}\left[h_i^{\mathrm{GPS}} - h_{\mathrm{fit},i}^{\mathrm{GRACE}}\right]}{\mathrm{WRMS}\left[h_i^{\mathrm{GPS}}\right] - \mathrm{WRMS}\left[h_i^{\mathrm{GPS}} - h_{\mathrm{fit},i}^{\mathrm{GPS}}\right]} , \tag{4.16}$$

where $h_{\mathrm{fit},i}^{\mathrm{GRACE}}$ and $h_{\mathrm{fit},i}^{\mathrm{GPS}}$ are derived annual and semi-annual variations from GRACE and GPS, respectively. In theory, a value of 1 indicates perfect agreement between the GPS observed and GRACE-derived seasonal displacements.

It is worth mentioning that annual and semi-annual variations entering into Eq.(4.16) in the following two case studies are derived simply using the least squares estimation rather than the SSA approach. The reasons are twofold: one is simply because the least squares approach is more straightforward than SSA in the case of computing statistic metrics; the other is to be easy for cross-comparison with other studies.

Nash-Sutcliffe efficiency (NSE) NSE coefficient is a statistical indicator widely used in the field of hydrology to evaluate the performace of simulated time series against observations, which is calculated by

$$\mathrm{NSE} = 1 - \frac{\sum_{i=1}^{n} (h_i^{\mathrm{GPS}} - h_i^{\mathrm{GRACE}})^2}{\sum_{i=1}^{n} (h_i^{\mathrm{GPS}} - \bar{h}^{\mathrm{GPS}})^2} . \tag{4.17}$$

Adapting NSE to the evaluation here, the simulated time series is replaced by the derived displacements from the filtered GRACE data. NSE is a conservative quantity and it is highly sensitive to the information including phase, amplitude and mean. The value of NSE ranges from $-\infty$ to 1, where a value of 1 indicates a perfect match between the observed GPS displacement and the derived displacement from GRACE.

Notes on the interpretation of figures To better display the performances of all filtering schemes in a very condensed way, the figure styles from Lorenz et al. (2014) are adopted here, cf. Figs. 4.6, 4.8, 4.10, 4.15, 4.17 and 4.19. These figures are interpreted in the following way: the upper part of these figures collects the values of the performance metrics into a matrix, where each cell indicates the individual performance of a single station under one specific filtering scheme. To put it another way, each row of the matrix represents an overview of the performance of different filtering schemes over one single station while each column depicts the behavior of one single filtering scheme over all the considered stations. The grey scales displayed in these figures have been designed in such a manner that darker grey values illustrate better performance and lighter grey values accordingly describe poorer performance.

The lower part, i.e. the histograms, summarizes each column of the matrix by sorting the performance metric values into the predefined intervals. The length of each grey scale interval in the histograms indicates the number of GPS sites categorized into that specific interval.

The color legends in these figures describe different types of filters. The green color and purple color group denote the deterministic filters and the color from light to dark indicates different smoothing radii tabulated in Table 4.2 from 200 km to 1000 km. The red color group indicates the DDK filter and the color from light to dark indicates the DDK filter from DDK 1 to DDK 5, which means from strong smoothing to weak smoothing. The blue color group correspondingly denotes the regularization filter and the color from light to dark indicates the parameter λ from 0.5 to 10, which inversely means from weak smoothing to strong smoothing.

Along with the statistic charts and histograms, mean statistics are computed and presented in Figs. 4.7, 4.9 and 4.11 for the Europe area, and Figs. 4.16, 4.18 and 4.20 for the Amazon area. For comparison, we use two x-axes and two y-axes to evaluate each mean performance metric for all filters in one figure: one axis in black indicates the deterministic filter group and the axes in blue displays the stochastic filter group. Note that mean statistics of the DDK filter are plotted in a way using the regularization parameter $\lambda = 1, 2, 3, 4, 5$ from the regularization filter to indicate the corresponding DDK filter indexes.

4.5 Case study I: the Europe area

We commence the comparison in the Europe area, where a relatively dense GPS network exists. Relatively weak mass variations are seen in this area and the resultant displacements are accordingly low. Fig. 4.5, which presents the estimated annual vertical amplitudes from the GRACE GSM dataset using different filtering schemes as well as the corresponding correlations with observed displacements from GPS. Each row represents one specific type of filter and columns from left to right indicate smoothing from weak to strong of each filter. Inspection of the figure shows that the maximum annual amplitude are less than 6 mm for all filtering schemes and various spatial patterns are also obviously displayed. These patterns distinctly show that stronger surface mass variations happen in the eastern Europe where less GPS stations exist. This phenomenon is observed as well by the correlation metric shown in Fig. 4.5. In Europe, the GPS sites mostly scatter in the western or central part, where the correlations show mostly between 0.6 and 0.8.

Examination of the figure tells evidently that weak smoothing preserves more detailed features than strong smoothing comparing the subplots in the left column with that in the right

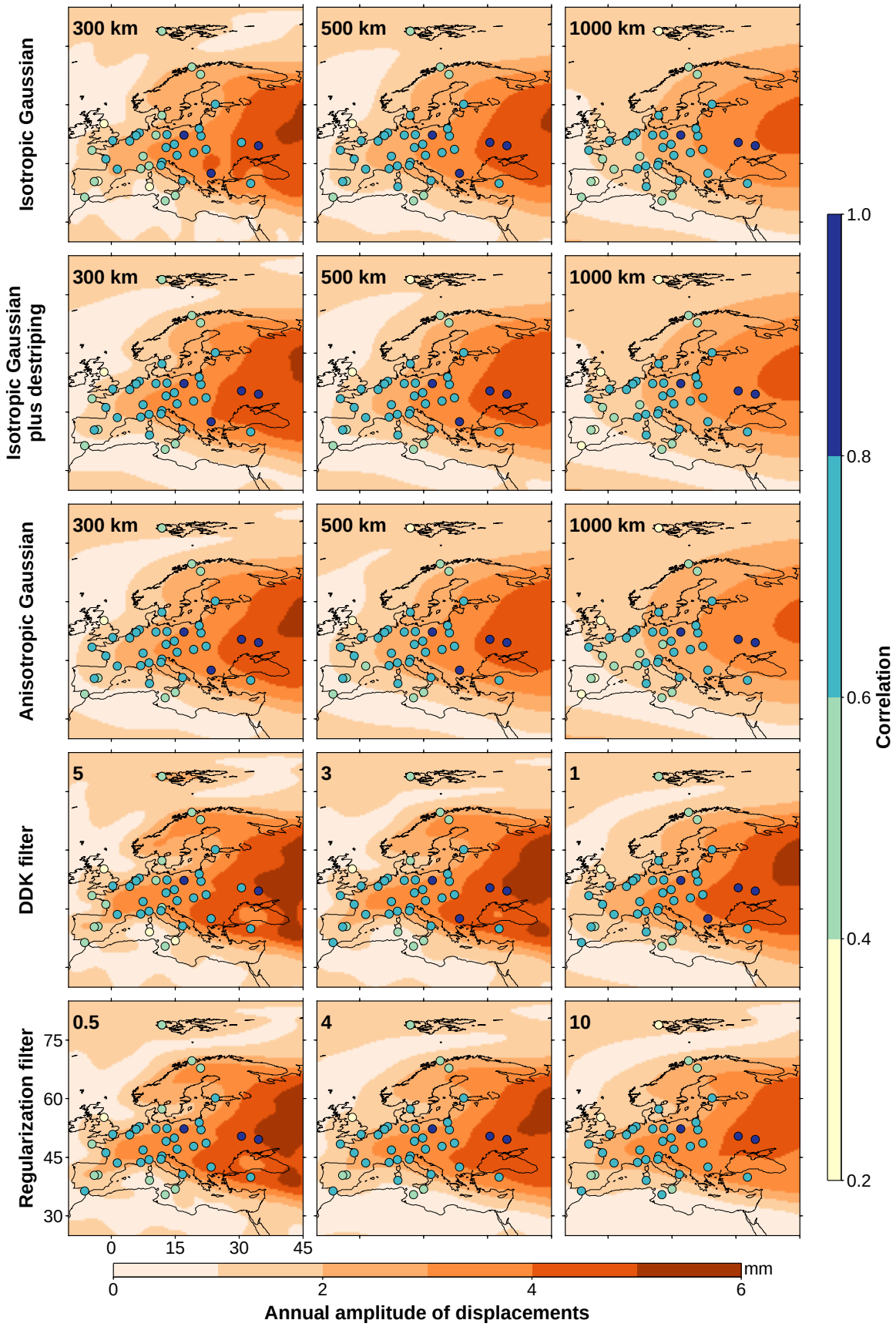

Figure 4.5: *Annual amplitudes of the computed vertical displacements from the* GRACE GSM *dataset using different filtering schemes. Colored dots indicate correlations between observed displacements from* GPS *and* GRACE*-derived deformations using corresponding filter schemes in Europe.*

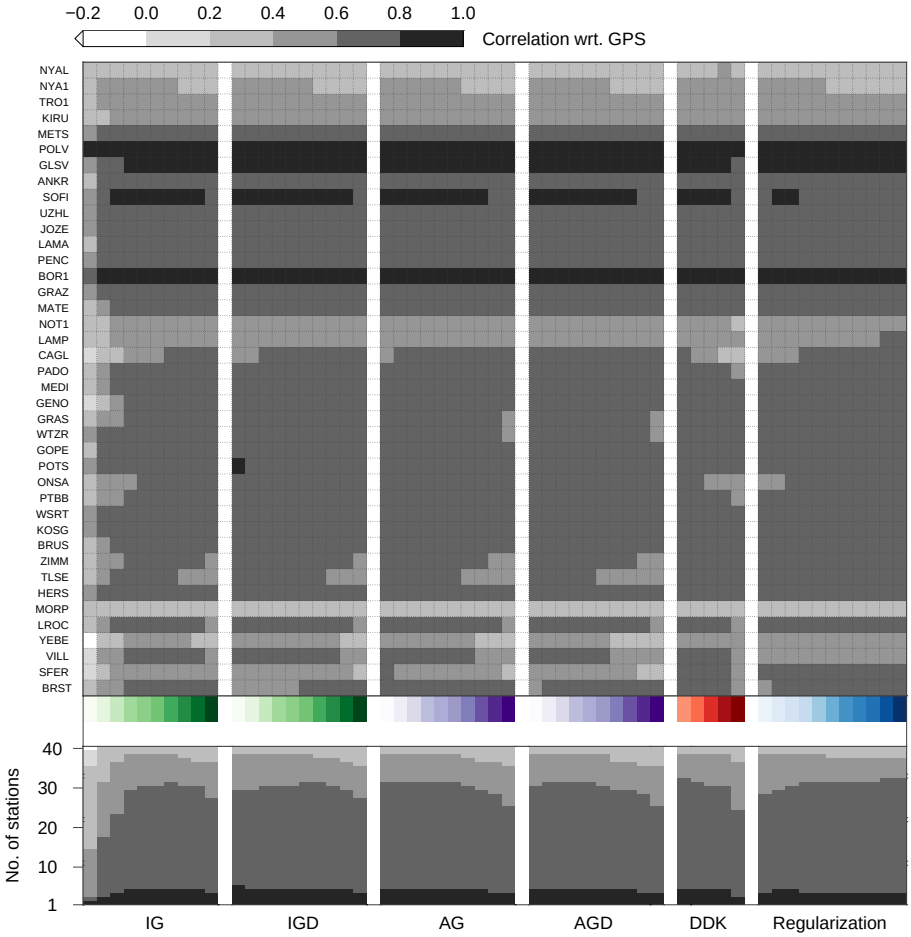

Figure 4.6: *Correlation coefficients for the 40 stations located in Europe between the displacements observed by* GPS *and derived from* GRACE *using different filtering schemes. A description on reading the figure is given in Section 4.4*

.

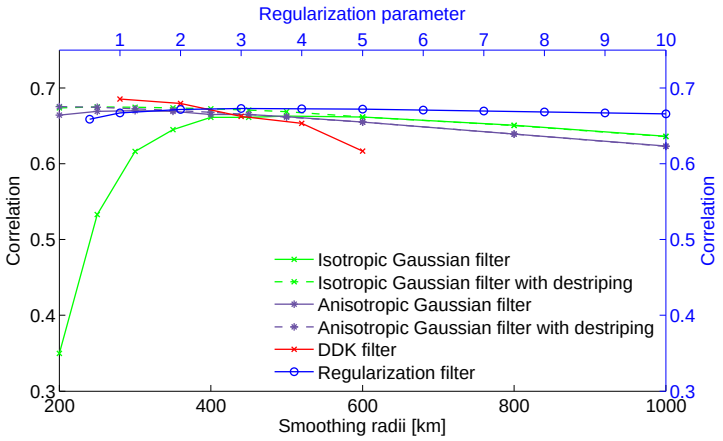

Figure 4.7: *Mean correlations over 40 stations for different filtering schemes. Axis with black color indicates the deterministic filter with different smoothing radii and axis with blue color denotes the stochastic filters. Specifically,* DDK *filters in short black curve are plotted with indexes from 1 to 5 using the regularization parameter λ from the regularization filter.*

column in Fig. 4.5. Using the destriping filter in a combination with the Gaussian filter removes more details comparing the first and the second row. Furthermore, it is clear that the effects of the destriping filter becomes weak when the smoothing radius of the Gaussian filter becomes large. Careful inspection of the second and the third row, it is interesting to find that the anisotropic filter acts similarly as the destriping filter with an additional Gaussian filter of the same smoothing radius.

Comparing the stochastic filters (the fourth and the fifth row) with the deterministic filters, different spatial patterns are visible in Fig. 4.5. Clearly, the stochastic filters provide more sophisticated spatial patterns and more details are kept. An elaborate look at the subplots of the stochastic filters, especially DDK 3, DDK 5 and the regularization filter of 0.5, spatial patterns in these subplots follow quite well the coastlines. This might be due to the external regularization information. For example, geophysical models are involved in the regularization process of the DDK filter (Kusche, 2007; Kusche et al., 2009). According to Kusche et al. (2009), DDK 1 and DDK 3 correspond to Gaussian filters with smoothing radii of 530 km and 240 km, respectively. However, in terms of the visual inspection of the subplots, DDK 1 seems to retain finer scale features than the Gaussian filter with a smoothing radius of 500 km and this point is also held for DDK 3.

As the regularization filter follows the same principle of the DDK filters, the last two rows present quite similar spatial distributions, for example, DDK 3 and the regularization filter of 0.5 (the comparability between them will be demonstrated later). According to Lorenz et al. (2014)[personal communication], the parameter λ around 4 in the regularization filter group generally provides the best performance from a global hydrological view.

All three performance metrics are shown in matrix charts, histograms and curve plots from Fig. 4.6 to Fig. 4.11. The performance metric shown in Fig. 4.6 provides an overview of the correlation between all derived displacements from GRACE under different filtering schemes and the observed displacements from GPS. Correlations higher than 0.6 are observed for most of stations in the upper part of Fig. 4.6 and the phenomena are also witnessed in the lower part of the figure. In particular, four stations (POLV, GLSV, SOFI, BOR1) which are located closer to western Europe present correlations higher than 0.8, see also Fig. 4.5. These high correlations indicate the strong correlations in hydrological loading signals observed by both GPS and GRACE.

In contrast to correlation, the WRMS reduction matrix shown in Fig. 4.8 displays relatively low values which are probably due to the low surface mass variations in Europe. Nevertheless, it might be worth mentioning that, as compared to van Dam et al. (2007) which showed only 10 out of 51 sites got positive WRMS reduction, all 40 sites used in this study have received a positive WRMS reduction, see Fig. 4.8. The result shown in this study is also slightly better than that found in (Tregoning et al., 2009) which showed the WRMS in 32 out of 36 sites to decrease. The improvement in WRMS reduction is likely to be a consequence of improved GPS and GRACE data processing strategies.

NSE, as a metric similar to WRMS reduction, shows quite a similar pattern in Fig. 4.10. All 40 stations in Europe can reach positive NSE values and it accordingly means the derived displacements from GRACE are at least better than the mean values estimated from GPS. Depending on the particular filter around half the number of stations can obtain NSE values bigger than 0.5 and only one station, POLV, receives a NSE value higher than 0.75.

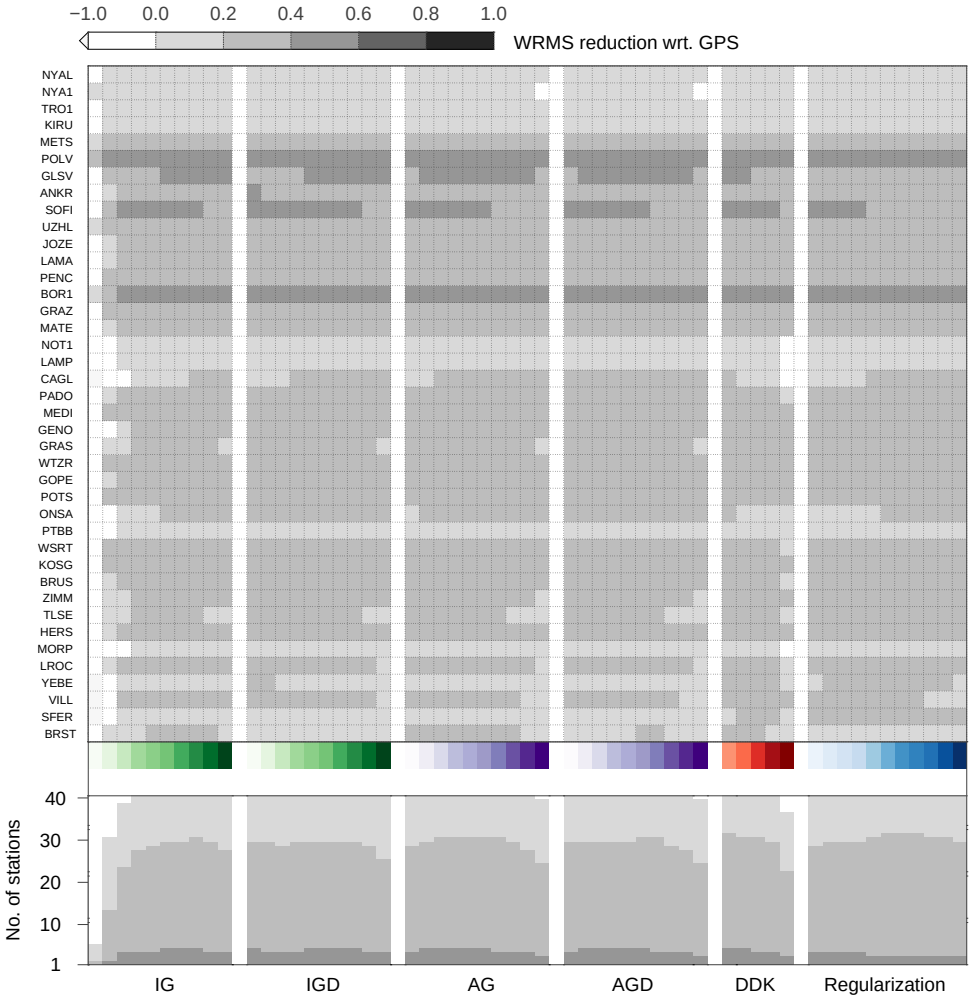

Figure 4.8: *The same as Fig. 4.6 but for* WRMS *reduction.*

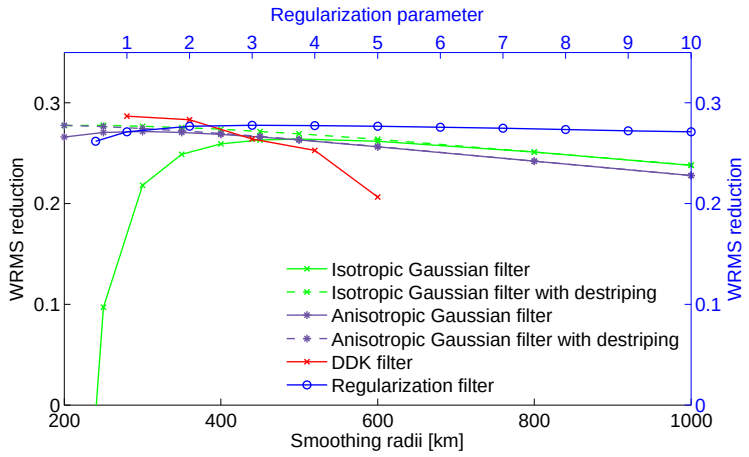

Figure 4.9: *The same comparison as Fig. 4.7 but for* WRMS *reduction.*

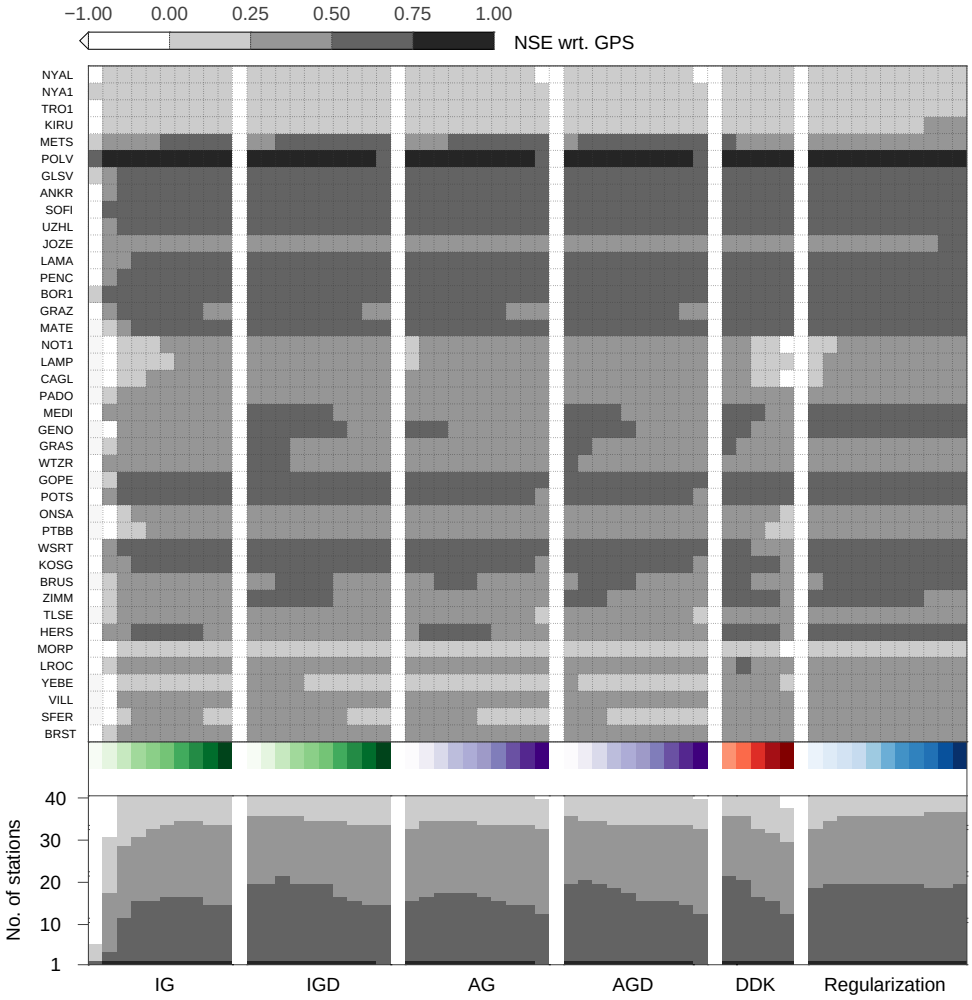

Figure 4.10: *The same as Fig. 4.6 but for* NSE.

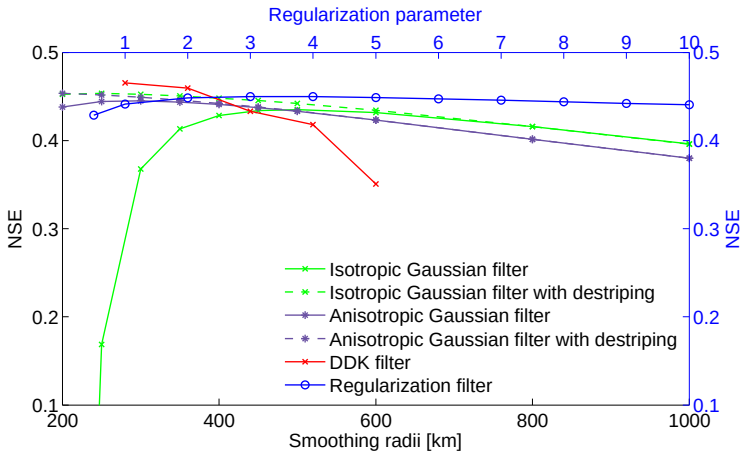

Figure 4.11: *The same comparison as Fig. 4.7 but for* NSE.

Inspection of all three metrics shown in Fig. 4.6, Fig. 4.8 and Fig. 4.10, no single filter is found to demonstrate consistent better results than all other filters over all stations. In the deterministic filter group, inspecting both Fig. 4.6 and Fig. 4.7, it is interesting to find that the isotropic Gaussian filter demonstrates its best performance with the smoothing radius around 500 km. The other two metrics shown later confirm this behavior and this makes us arrive at the same conclusions as King et al. (2006) that there is no benefit using larger than 500 km smoothing radii for the sites in Europe if only the isotropic Gaussian filtering is applied.

When combining the isotropic Gaussian filter with the destriping filter, all performance metrics, see figures from Fig. 4.6 to Fig. 4.11, illustrate the benefit of the destriping filter, which significantly improves the statistics, especially at smoothing radii lower than 400 km. These figures also tell us that there is no meaning in combining the destriping and the isotropic Gaussian filter at smoothing radii higher than 600 km. The power of the isotropic Gaussian filter with a high smoothing radius conceals the effect of the destriping filter and this is demonstrated both in the spatial map (see Fig. 4.5) and the site-to-site comparison. In comparison with the isotropic Gaussian filter with a smoothing radius of 400 km used by Tesmer et al. (2011) and 500 km used by van Dam et al. (2007), the isotropic Gaussian filters with low smoothing radii associated with the destriping filter demonstrates its better performances in terms of all three metrics.

The performance of the anisotropic Gaussian filters in association with or without the destriping filter are depicted in Fig. 4.6 and Fig. 4.7. No prominent improvements are found over different smoothing radii. This is also in agreement with the performance metrics of WRMS reduction and NSE shown in figures from Fig. 4.8 to Fig. 4.11. Only minor advantages of combining the destriping filter to the anisotropic Gaussian filter are found at smoothing radii lower than 400 km. In view of all three performance metrics, a conclusion can be drawn that it makes no sense to combine the anisotropic Gaussian filter and the destriping filter to smooth the GRACE data when comparing with GPS. In addition, the anisotropic Gaussian filter group combined with or without the destriping filter do not display better results in comparison with the isotropic Gaussian filter group combined with the destriping filter.

Summarizing the performance analysis within the deterministic group, the isotropic Gaussian filter with low smoothing radii, e.g. 300 km, in a combination with the destriping filter is recommended for the GPS stations in Europe. This filtering option will be further compared with the stochastic filters.

In the DDK filter group, mean value curves of all three metrics show a sharp and monotonous decrease with increasing indexes. The DDK 1 filter, i.e. the strongest smoothing in the DDK filter group, is superior to other DDK filters in Europe. This phenomenon is also evident in the metrics as well as the histograms shown in Figs. 4.6, 4.8 and 4.10. In view of the annual vertical displacements shown in Fig. 4.5, it is also found that the higher spatial resolutions in grids estimated from the DDK 5 filter do not help to improve the metric statistics between the GPS-observed and the GRACE-derived vertical displacements. This is due to the fact that GPS measurements are point samples and the agreement between the GPS observed and the GRACE-derived vertical deformations depends highly on the distribution of the GPS sites. This fact is also supported in the other study area presented in Section 4.6.

The differences in the regularization filter group are not so prominent as in the DDK filter group. Nevertheless, the best performance in this group appears at the regularization parameter around 4 (see metric charts, histograms and mean value curves) which corresponds to the

best regularization parameter from the global hydrological view (Lorenz et al., 2014). Comparing the two types of stochastic filters, the regularization filter shows slightly worse correlation, WRMS reduction as well as NSE values than the DDK 1 and DDK 2 filters while better than the other three DDK filters, which could be observed in all the three metrics shown from Fig. 4.6 to Fig. 4.11. Summarizing the performance analysis within the stochastic filter group, the DDK 1 filter outperforms ohter stochastic filters in Europe.

Considering the performance of the deterministic filters versus the stochastic filters, generally speaking, the stochastic filters outperform the deterministic filters, especially the DDK 1 filter. This conclusion is supported by all three metrics shown in the figures from Fig. 4.6 to Fig. 4.11 as well as Table 4.3.

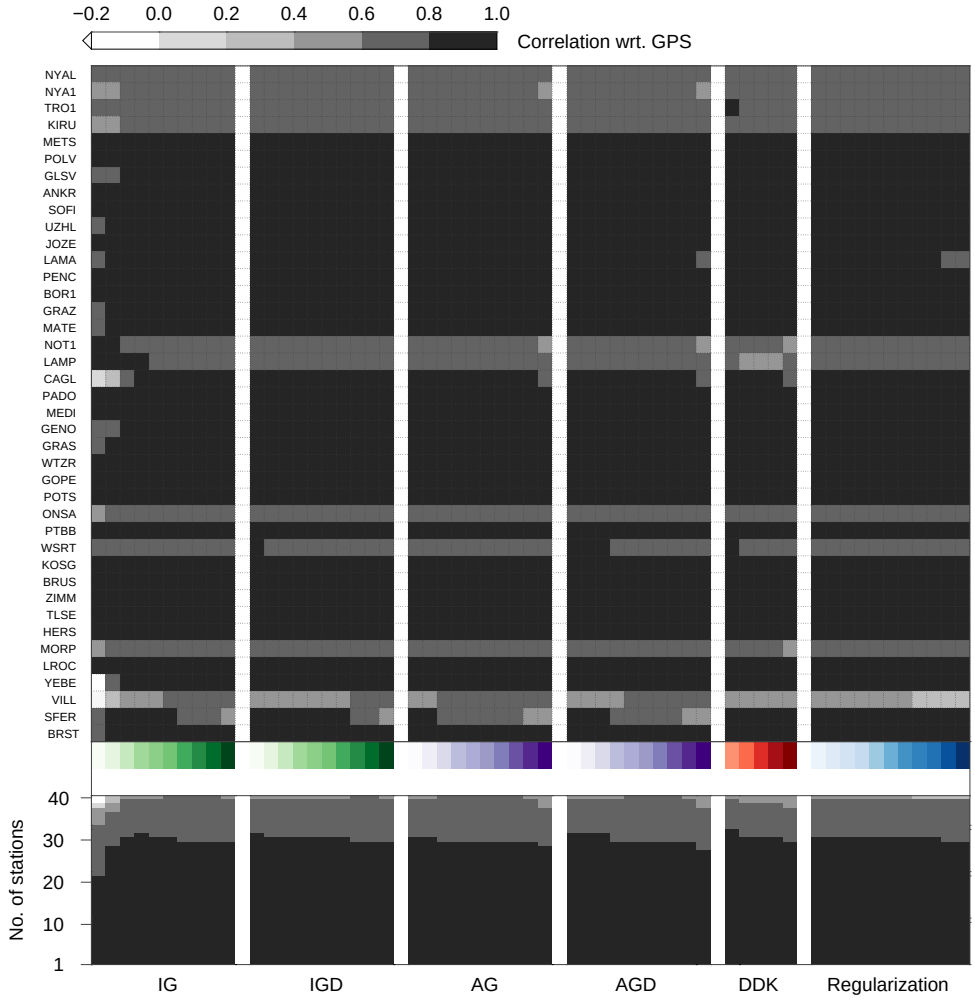

Figure 4.12: *The same as Fig. 4.6 but for correlation at the seasonal signal level.*

Seasonal signals The agreement at the seasonal level between displacements observed by GPS and derived from GRACE has already been demonstrated by a number of studies. As shown in Fig. 4.2, evident seasonal signals are observed in the Europe area. We now look into the effects of different filtering schemes on the agreement between them at the seasonal level using the correlation and the WRMS reduction ratio. In analogy to Fig. 4.6 and Fig. 4.8, the

correlation and WRMS reduction ratio at the seasonal level are shown in Fig. 4.12 and Fig. 4.13, which observe significant improvements in both correlation and WRMS reduction ratio between GPS and GRACE at the seasonal signal level utilizing all filtering schemes. The improvements are also recorded in terms of mean values which are tabulated in Table 4.3. To get unbiased mean values in WRMS reduction, MORP is excluded due to the insignificant seasonal signal and it is also the only site which gets decreased in WRMS reduction ratio at the seasonal level. MORP, located in Morpeth, United Kingdom, is close to the coast and it probably experiences less displacements due to water mass variations than non-tidal ocean mass variations. In addition, the non-tidal oceanic loading generally contributes insignificant at annual periods (Nordman et al., 2009; Tesmer et al., 2011). This phenomenon is also seen in the forthcoming study area, the Amazon area, where most stations lie along the coast.

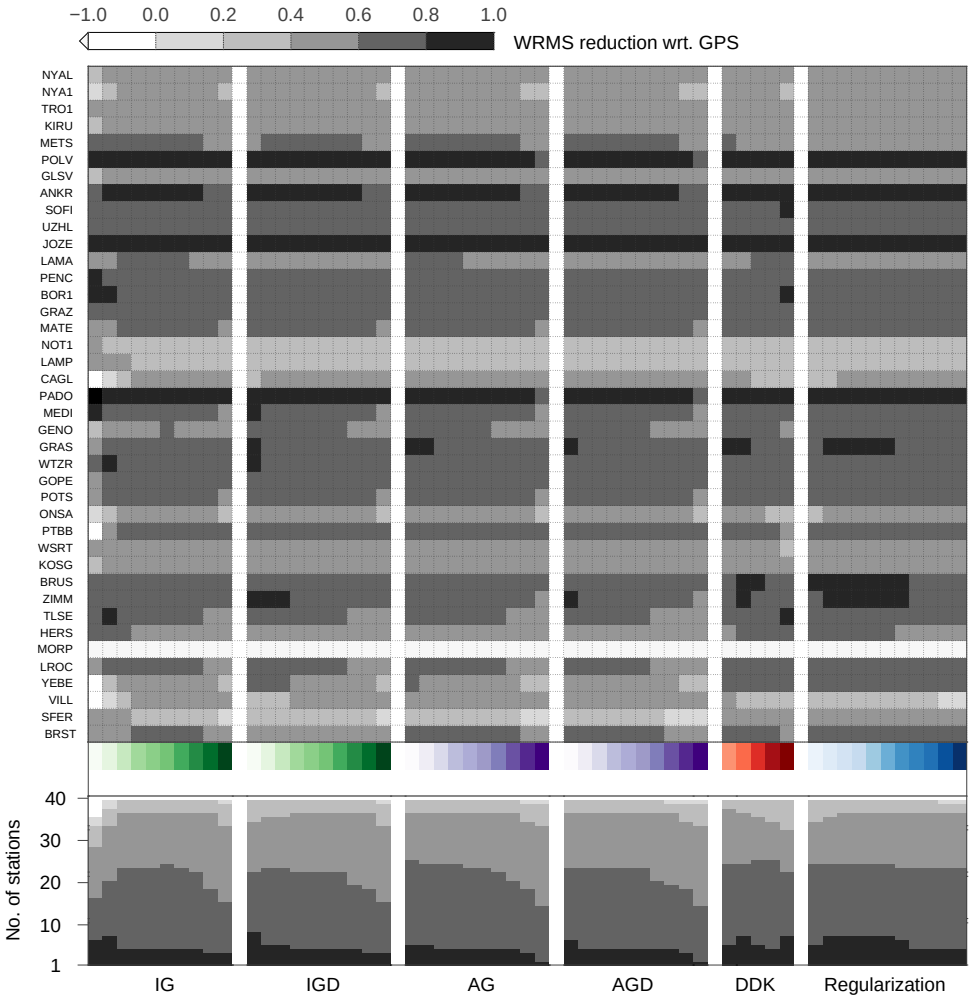

Figure 4.13: *The same as Fig. 4.6 but for* WRMS *reduction ratio at the seasonal signal level.*

The improvements shown here were also found and documented in (Tesmer et al., 2011) on usage of the mean annual signals. The high agreement on the seasonal level between GPS and GRACE indicates the possibility of using the GRACE-derived seasonal displacements to remove effects of the seasonal signals buried in the GPS time series on estimating the linear velocity (Fu et al., 2012), or on the global and regional reference frame issues (Zou et al., 2013).

Table 4.3: *Mean performance measures of the selected best filtering schemes from the deterministic filter group and the stochastic filter group on the monthly time series and the annual signals.*

Filtering scheme selection	monthly time series			seasonal signals	
	correlation	WRMS reduction [%]	NSE	correlation	WRMS reduction ratio [%]
IG 400	0.66	25.9	0.43	0.86	63.0
IG 500	0.66	26.4	0.44	0.86	63.0
IGD 300	0.67	27.7	0.45	0.86	63.6
AG 300	0.67	27.1	0.45	0.86	63.8
DDK 1	**0.69**	**28.7**	**0.47**	**0.87**	**65.2**
DDK 3	0.66	26.4	0.43	0.85	63.7
DDK 5	0.62	20.6	0.35	0.82	61.6
Regularization filter 0.5	0.66	26.2	0.43	0.85	63.8
Regularization filter 4	0.67	27.7	0.45	0.85	64.2

As shown in Table 4.3, in the deterministic filter group, the isotropic Gaussian filter of the smoothing radius 300 km combined with the destriping filter shows somewhat the same performance with the anisotropic Gaussian filter on both the monthly time series and the seasonal signal level, which are better than the isotropic Gaussian of the smoothing radius 500 km. In the stochastic filter group, DDK 1 filter performs best not only on the monthly time series but also on the seasonal signals. Among the stochastic filter group, DDK 5 is the worst which has already been demonstrated in the previous analysis. The performance of the regularization filter of the factor 4 is between that of the DDK 1 and the deterministic filters. It is further proved that the performance of the regularization filter of the factor 0.5 is close to that of DDK 3 filter in Europe.

4.6 Case study II: the Amazon area

THE other study area to illustrate the effects of GRACE data filtering is the Amazon area, located in the South America. The Amazon river basin experiences the most significant water mass variabilities in the world which are observed by GRACE (Tapley et al., 2004; Chen et al., 2010). The severe water variations in turn result in remarkable elastic surface displacements which are recorded by GPS (Davis et al., 2004; Bevis et al., 2005; Sánchez and Seitz, 2011; Sánchez et al., 2013; Fu et al., 2013). For instance, the displacement at NAUS shown in Fig. 4.4 shows a 40 mm peak-to-peak fluctuations. Fig. 4.14 displays the derived annual amplitudes of the vertical displacements over the Amazon basin and its nearby areas. The corresponding correlations with observed displacements from GPS are also shown in Fig. 4.14.

Similar analysis of Fig. 4.5 regarding different filtering schemes can also be applied here in Fig. 4.14. As opposed to Fig. 4.5, stronger displacements with an amplitude up to 22 mm are represented due to the strong terrestrial water changes. In particular, spatial distributions with weak filtering schemes, e.g. left column in Fig. 4.14, illustrate a center area where the most significant displacements happen around the NAUS station, which could be observed from the correlation metric as well. This center area is located in the city of Manaus, where the Rio

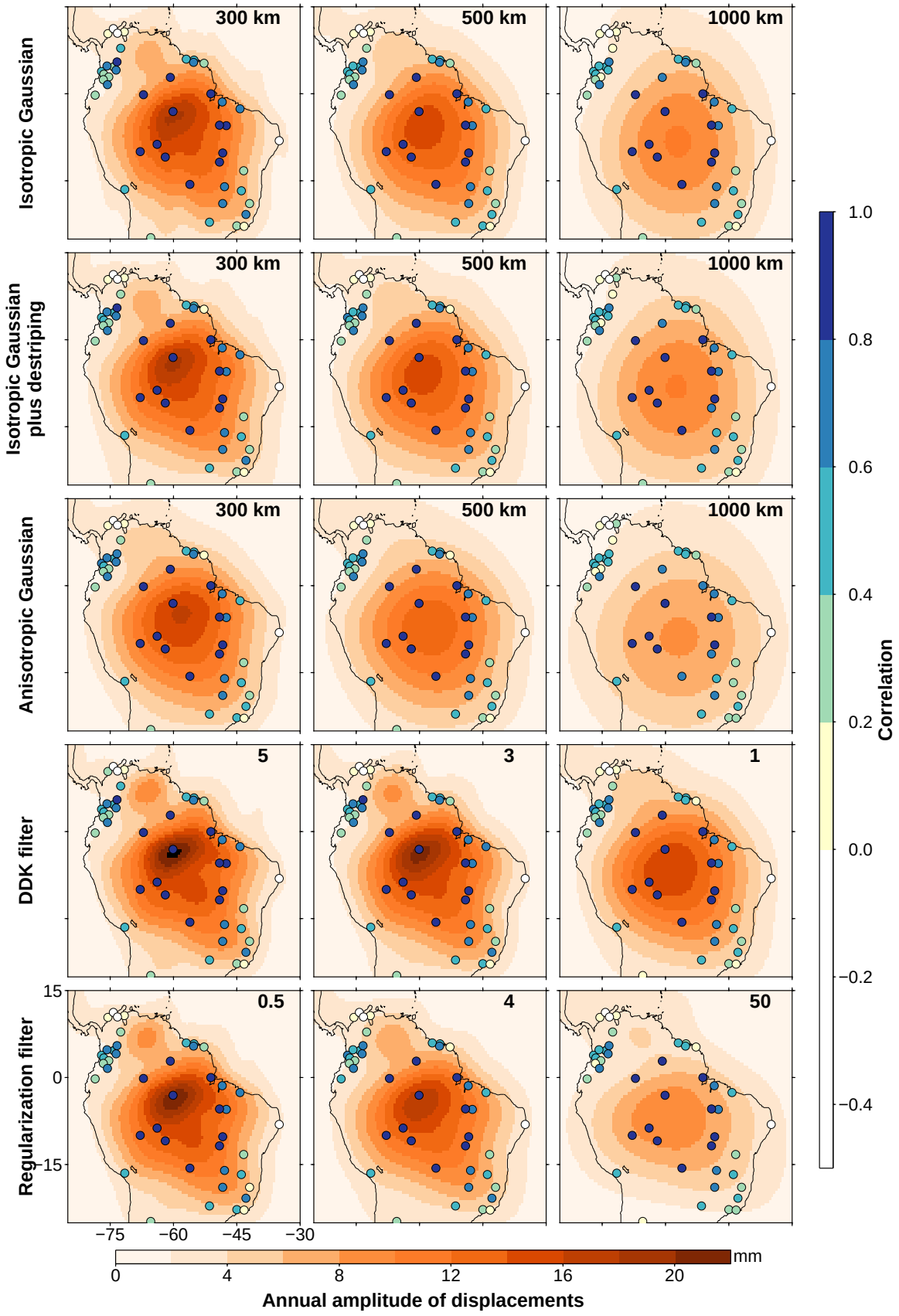

Figure 4.14: *The same as Fig. 4.5, but for the Amazon area.*

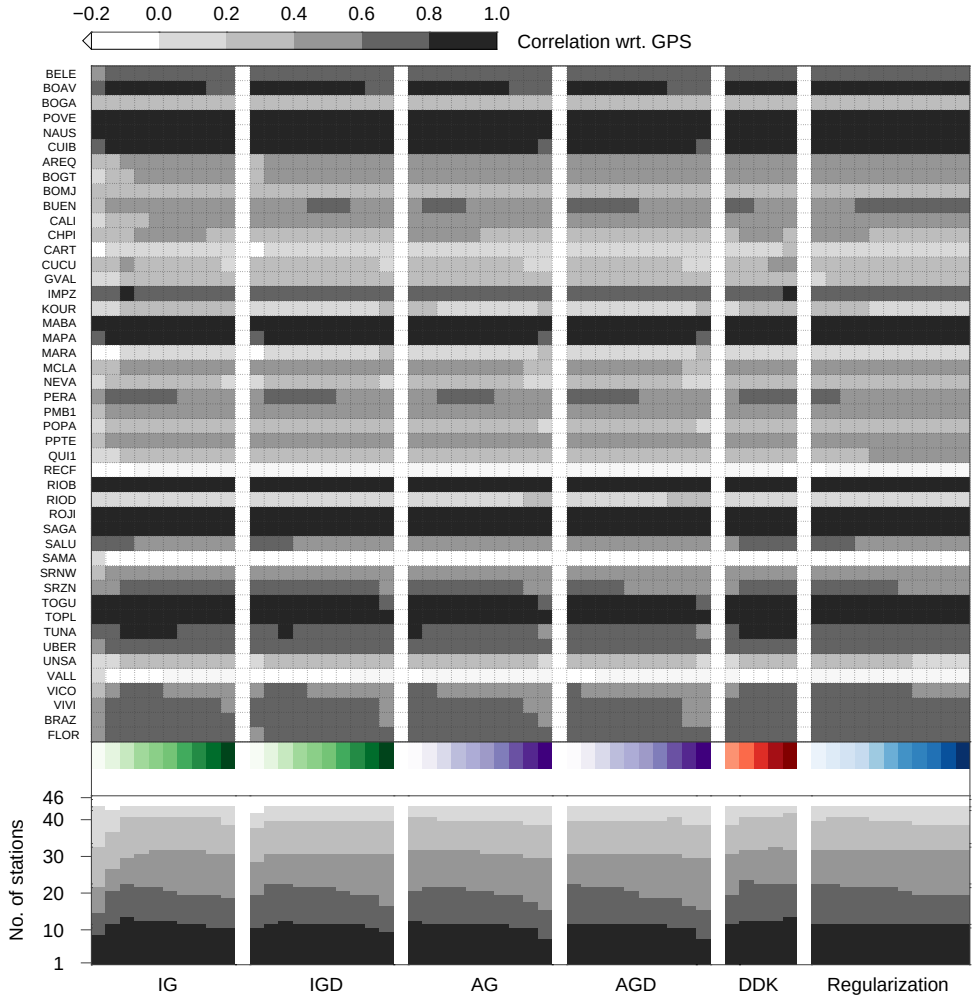

Figure 4.15: *Correlation coefficients for the 46 stations located in the Amazon area between the displacements observed by* GPS *and derived from* GRACE *using different filtering schemes. A description on reading the figure is given in Section 4.4*

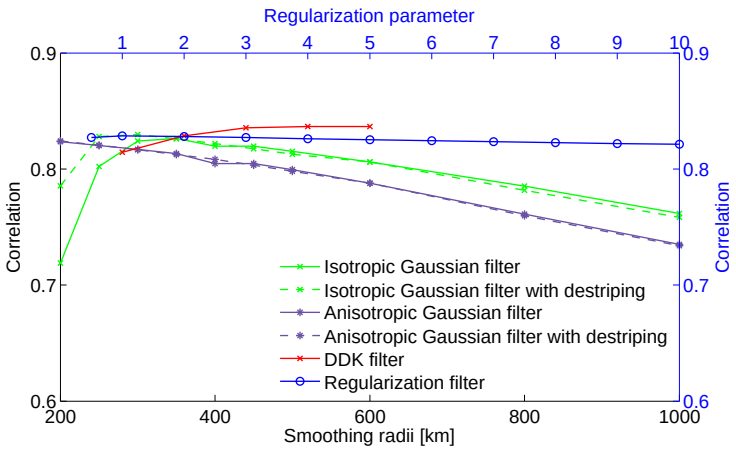

Figure 4.16: *Mean correlations over 16 stations for different filtering schemes. Axis with black color indicates the deterministic filter with different smoothing radii and axis with blue color denotes the stochastic filters. Specifically,* DDK *filters in short black curve are plotted with indexes from 1 to 5.*

Negro flows into the Amazon river. Significant water changes in this center area have been documented in other studies (Chen et al., 2010; Fu et al., 2013) as well. Strong smoothing, especially the deterministic filtering using high smoothing radii, produces spatial maps shifting this center area southward, which is obviously unrealistic.

Similar to the analysis in Europe, all three performance metrics are displayed in metrics charts, histograms and curve plots from Fig. 4.15 to 4.20. In terms of the correlation statistics, 11 stations have correlations over 0.8 and these stations are mostly located far away from the coast. Meanwhile, three stations (RECF, VALL, SAMA) which are located close to the coastline present negative correlations. The histograms shown in the lower part of Fig. 4.15 tell that around 35% of stations show correlations less than 0.4. Comparing the correlation statistics in the Amazon area with that in Europe, we have more stations with high correlation but also more stations with low correlations even negative correlations. The reason for more stations with high correlations is probably due to the strong mass variations around the Amazon area and the reason for more stations with low correlations is possibly because of the fact that more stations lie close to the coast. Bad correlations at the GPS sites close to the coastline are found in other studies which are possibly affected by non-tidal oceanic loading effects (King et al., 2006; Nordman et al., 2009; Tesmer et al., 2011) or even spurious long-period signals due to unmodeled short-periodic displacements (Penna et al., 2007).

The upper part in Fig. 4.17 depicts the WRMS reduction matrix presenting relatively bad results with around 20 stations in negative reduction which are shown in the histograms as well. These stations are scattered along the coastlines. Five GPS sites (BOAV, POVE, NAUS, RIOB, ROJI) display WRMS reductions higher than 0.5 under most of the filtering schemes. Specifically, the grey scale legend in this figure is designed to highlight the highest reduction appears at NAUS which presents 70% WRMS reduction using the DDK 5 filter. This is consistent with the spatial distribution map in Fig. 4.14. Fig. 4.19 presents the NSE statistics showing similar maps with the WRMS reduction. Depending on filters, six stations (BOAV, POVE, NAUS, MABA, RIOB, ROJI) display NSE values larger than 0.75 whilst 19 stations out of 46 show negative NSE values.

Concerning the filter comparison over this study area, careful inspection of three performance metric maps allows us to make the same conclusion as the Section 4.5 that no single filtering scheme can provide consistent better performances than other filtering schemes. Fig. 4.16, Fig. 4.18 together with Fig. 4.20 illustrate the mean performances in terms of correlation, WRMS reduction and NSE separately over 16 stations. These 16 stations are chosen in order to avoid biased statistics due to those coastal stations. The 16 stations are: BOAV, POVE, NAUS, CUIB, BOGT, IMPZ, MABA, PERA, RIOB, ROJI, SAGA, TOGU, TOPL, TUNA, UBER and VIVI. In view of the histograms in Figs. 4.15, 4.17 and 4.19, these stations possess good correlations ($\geq$ 0.6), WRMS reduction higher than 0.1 and NSE values bigger than 0.25.

In the deterministic filter group, in terms of correlation in Fig. 4.15, the isotropic Gaussian filter displays its best performance at smoothing radius 350 km and the advantage of combining the destriping filter is again demonstrated here at low smoothing radii, which is also proved in the other two performance metrics. When combining the destriping filter with the isotropic Gaussian filter, the same optimal smoothing radius as in Europe, i.e. 300 km, is reached here in the Amazon area as well. Fig. 4.15 also depicts the useless of applying the isotropic Gaussian filter with high smoothing radii. In contrast to the isotropic Gaussian filter group, the anisotropic Gaussian filter group shows inferior correlations even at low smoothing radii in either cases with or without associating the destriping filter. This is again accordant to the other two performance metrics shown in Fig. 4.18 and Fig. 4.20.

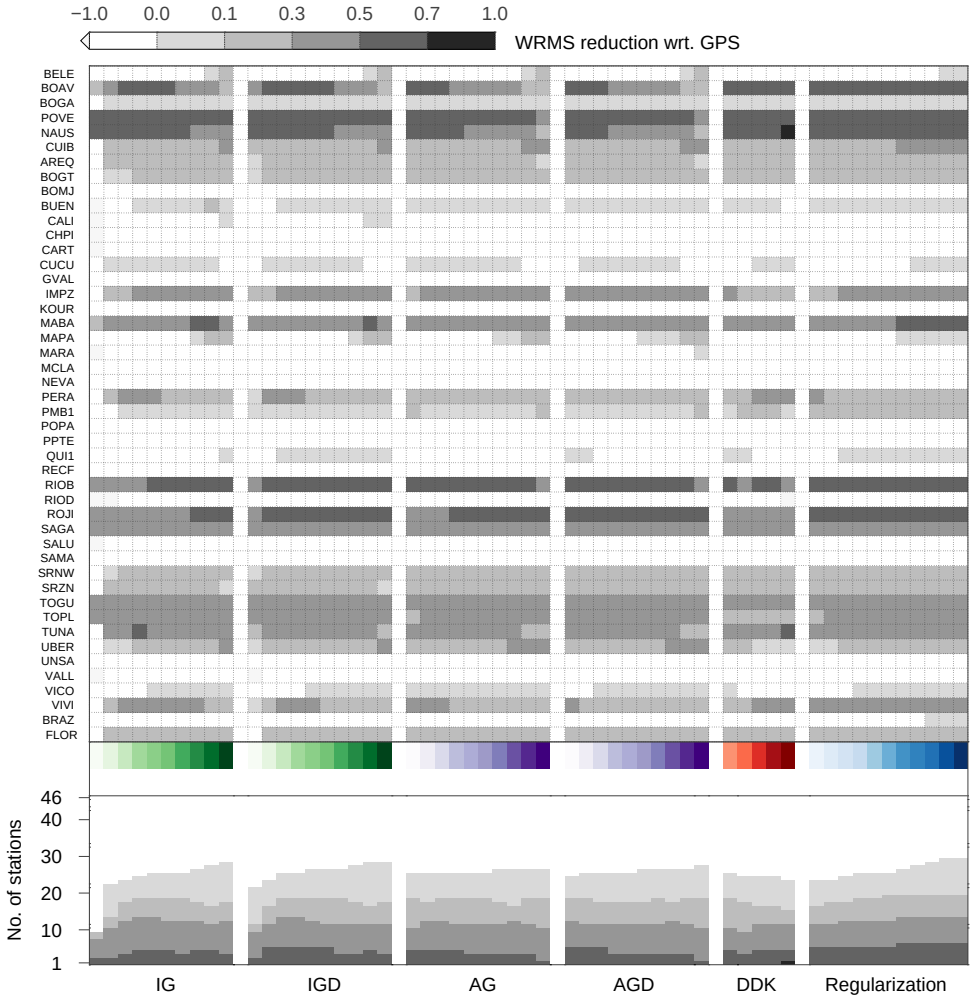

Figure 4.17: *The same as Fig. 4.15, but for* WRMS *reduction in the Amazon area.*

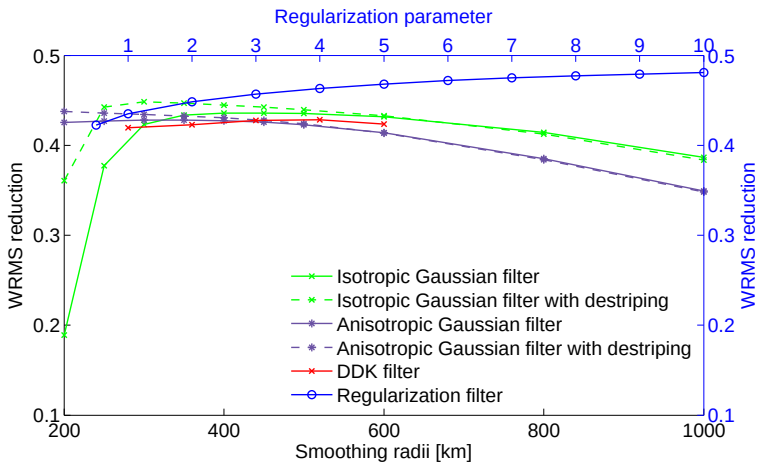

Figure 4.18: *The same comparison as Fig. 4.16 but for* WRMS *reduction.*

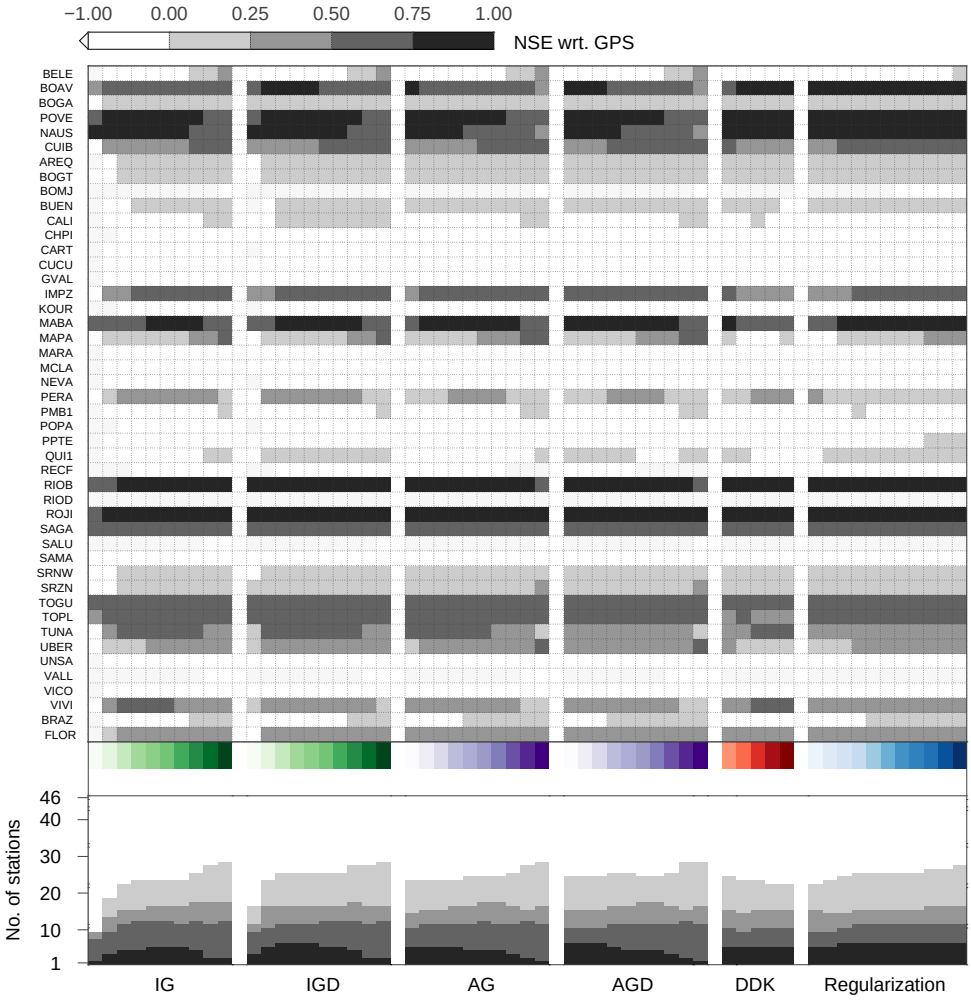

Figure 4.19: *The same as Fig. 4.15, but for* NSE *in the Amazon area.*

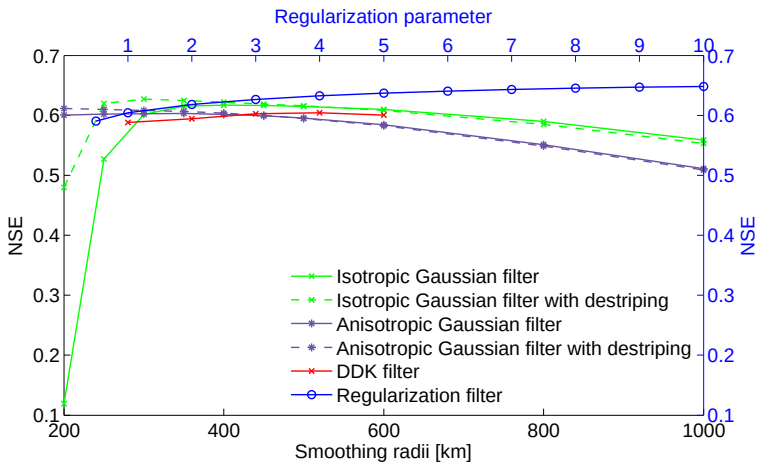

Figure 4.20: *The same comparison as Fig. 4.16 but for* NSE.

Fig. 4.18 shows the mean WRMS reduction curves and the isotropic Gaussian filter achieves its best performance at smoothing radius 500 km, which is in agreement with the analysis in Europe. The combination of the isotropic Gaussian filter using smooth radius of 300 km with the destriping filter stands out of the isotropic Gaussian filter group again in terms of the WRMS reduction, which is also superior to the anisotropic Gaussian filter group. The analysis is held for the NSE metric shown in Fig. 4.20 which convey similar information.

Summarizing the comparison between the isotropic and anisotropic Gaussian filter groups in the Amazon area, it leaves us to draw the same conclusion as in Europe that the isotropic Gaussian filter with a smoothing radius 300 km in association with the destriping filter is the optimal option in the deterministic group. This might indicate this option could be extended to be applied at global scale.

In the DDK filter group, weaker smoothing (DDK 5) provides better correlations whilst they show quite flat curves in terms of the WRMS reduction and NSE metrics. As for the regularization filter, a straight horizontal line is observed in correlation while for both the WRMS reduction and NSE curves, they increase with the regularization parameter up to $\lambda = 50$ which is certainly unrealistic (see subplot in Fig. 4.14). Nevertheless, as opposed to the DDK filter, the regularization filter with the parameter around $\lambda = 4$ which is the best option from the global hydrological view (Lorenz et al., 2014) already outperforms the DDK filters in terms of the WRMS reduction and NSE metrics.

With respect to the deterministic filters, the DDK filters (except the DDK 1) do provide higher correlations but they perform poor in the WRMS reduction and NSE metrics, while the regularization filter ($\lambda \geq 4$) showcases better performances in all three metrics. The regularization parameter of 4 is selected in this filter group by a balance of the performance metrics and the signal preservation. Less filtering is always preferable on the condition that good achievements have been reached.

Summarizing the performance statistics of the deterministic and stochastic filters in the Amazon area, the derived displacements from GRACE using the stochastic filter again could provide better agreements with respect to the displacements observed by GPS. In particular, the regularization filter with $\lambda = 4$ is opted for the best filter scenario in this area and this choice is strongly supported by the statistics shown in the figures.

Seasonal signals The seasonal signals are investigated in the same manner as in the Europe area. As expected, correlations and the WRMS reduction ratio at the seasonal level are immensely improved. Shown in Fig. 4.21 the number of stations with correlation higher than 0.8 increases from 11 to 26. The mean correlations of the considered 16 stations are enhanced as well, see Table 4.4. However, the three stations (RECF, SAMA, VALL) which have negative correlations in Fig. 4.15 are still not improved.

The WRMS reduction ratio at the seasonal level shown in Fig. 4.22 displays similar behavior as the correlation and these stations which show negative reductions in Fig. 4.17 still present negatives in Fig. 4.22. Nevertheless, the considered 16 stations display significant improvements, see Table 4.4. The number of stations with the WRMS reduction ratio bigger than 70% jump from only 1 GPS site (NAUS) up to 20 GPS stations. This means four stations, which are not counted for calculating the mean statistics, are also increased in terms of the seasonal WRMS

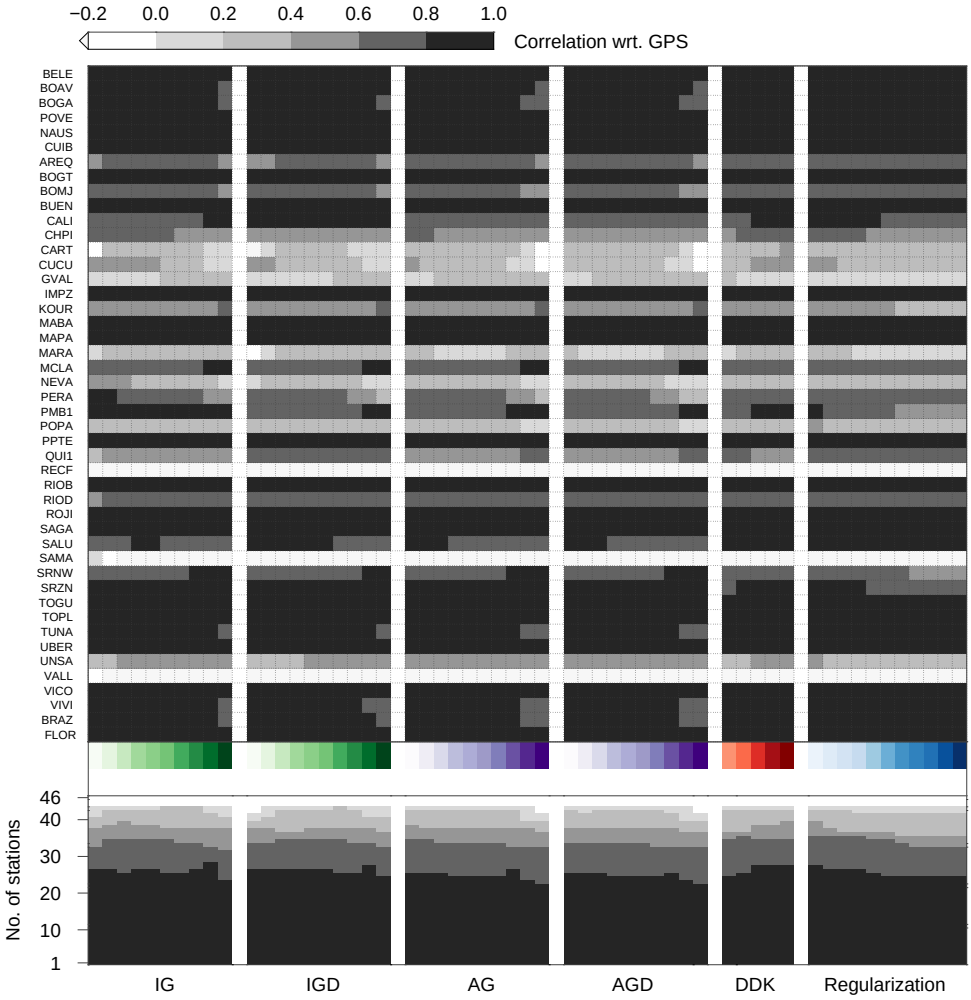

Figure 4.21: *The same as Fig. 4.15 but for correlation at the seasonal signal level.*

Table 4.4: *Mean performance measures of the selected best filtering schemes from the deterministic filter group and the stochastic filter group on the monthly time series and the annual signals over the considered 16 stations.*

Filtering scheme selection	monthly time series			seasonal signals	
	correlation	WRMS reduction [%]	NSE	correlation	WRMS reduction ratio [%]
IG 400	0.82	43.5	0.62	0.95	76.6
IG 500	0.82	43.5	0.62	0.94	75.2
IGD 300	0.83	44.8	0.63	0.95	75.1
AG 300	0.82	42.8	0.60	0.94	75.1
DDK 1	0.81	41.9	0.59	0.93	71.8
DDK 3	**0.84**	42.8	0.60	0.95	74.4
DDK 5	**0.84**	42.4	0.60	**0.96**	75.6
Regularization filter 0.5	0.83	42.3	0.59	**0.96**	75.3
Regularization filter 4	0.83	**46.3**	**0.64**	0.95	**79.7**

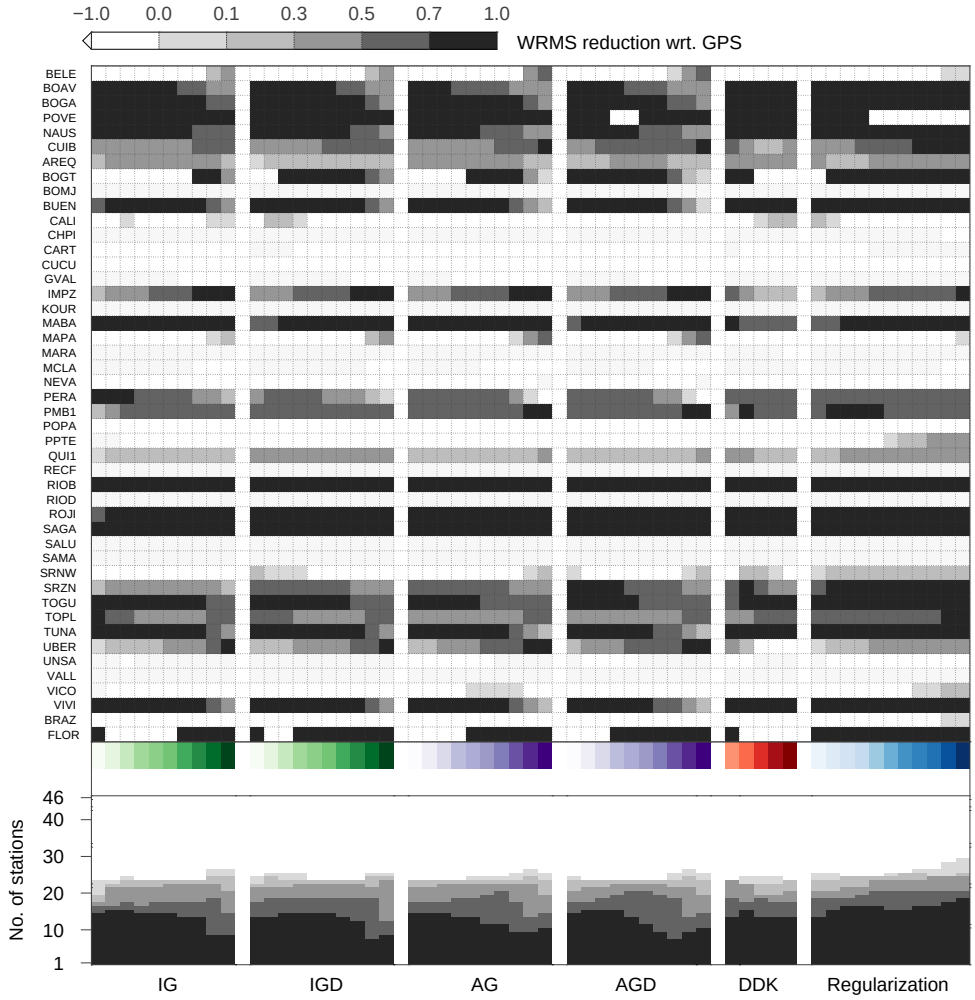

Figure 4.22: *The same as Fig. 4.15 but for* WRMS *reduction ratio at the seasonal signal level.*

reduction ratio. These statistics indicate the strong agreements between the GPS observed displacements and the estimated deformations from GRACE at the seasonal level in the Amazon area. However, attentions should be paid on selecting the stations properly to make use of the seasonal displacements derived from GRACE for additional purposes, e.g. the aforementioned regional reference frame issue (Zou et al., 2013).

In addition, statistics shown in Table 4.4 confirms the conclusion of the best filter in the Amazon area. The regularization filter with $\lambda = 4$ outperforms other filtering schemes in both the monthly time series and the seasonal signals.

4.7 Discussion and summary

THIS chapter investigates the hydrological loading induced displacement signal observed by GPS and derived from GRACE, with an emphasis on the impact of GRACE data filtering. Several types of commonly used filters were analyzed and their performances by utilising two

GPS datasets from two study areas, i.e. the Europe area and the Amazon area. Strong correlations between GPS and GRACE are obtained in both areas. In Europe, all considered 40 GPS sites have observed positive WRMS reduction with respect to previous studies (e.g., van Dam et al., 2007; Tregoning et al., 2009) which is a consequence of improved GPS and GRACE data. In the Amazon area, high correlations, WRMS reductions and NSE values are observed in the GPS sites located in the central Amazon area. While for the sites located close to the coast, poor statistics are shown possibly in part due to the high impact of non-tidal oceanic loading effects, which are not accounted for in the GPS time series. The non-tidal oceanic loading induced displacements computed over 46 GPS sites in the Amazon area using the ECCO model show a mean RMS value of 0.36 mm. What's more, GRACE senses less hydrological loading information close to the coastline that the inland, which could also be attributed to poor statistics for stations close to the coast.

At the seasonal level, the agreements between GPS and GRACE are significant in both areas which might indicate the potential usage of the GRACE derived displacements for correcting hydrological loading signals buried in the GPS time series.

Concerning the effects of different filtering schemes used in this chapter, like other studies regarding GRACE filtering comparison (e.g., Werth et al., 2009; Steffen et al., 2010), no single filtering scheme can produce consistent good results over the two different study areas. In view of single GPS site, different filtering schemes can produce significant differences, for example, different DDK filters can produce a difference up to 19% at NAUS in terms of the WRMS reduction value. The differences will be even larger when comparing among all the considered filters. However, it is not possible to tune filtering schemes for each site separately. Considering the mean performances, the used filters do not produce as big differences as single GPS station. Nevertheless, the optimal filters for both areas are obtained and several common features of filters for the two study areas are observed.

In the deterministic filter group, we arrive at the same conclusion as King et al. (2006) that a smoothing radius around 500 km reaches best performance if only the isotropic Gaussian filter is applied. However, this is not true when combined with the destriping filter. The advantage of combining the destriping filter with the isotropic Gaussian filter is demonstrated in both study areas. It is highly recommended to use the Gaussian filter with a low smoothing radius, e.g. around 300 km, combined with the destriping filter, which produces consistent good results in both the Europe area and the Amazon area with respect to other deterministic filtering scenarios. The performance of the anisotropic Gaussian filter decreases with increasing the smoothing radius. Besides, the anisotropic Gaussian filter only shows its better performance as opposed to the Gaussian filter at low smoothing radii. However, this point is not held when they are combined with the destriping filter. In view of the performance of all deterministic filters, the study concludes the optimal filtering scheme in this filter group is the combination of the Gaussian filter of a low smoothing radius with the destriping filter.

In the stochastic filter group, the DDK 1 filter displays better performance in the Europe area while the regularization filter of $\lambda = 4$ stands out in the Amazon area. These two filter schemes outperform other filters respectively in the two study areas. It is shown that the performance of the DDK filters depends on the study area. The DDK 1 and DDK 2 which show good performances in the Europe area turn out to be inferior to other DDK filters in the Amazon area. While in the regularization filter group, the parameter $\lambda = 4$ turns out to produce consistently better and reliable results.

In view of both the deterministic filters and the stochastic filters, the stochastic filter generally demonstrates better performance in both study areas.

It is worth mentioning that the DDK 5 filter produces the highest spatial resolution deformation maps in both study areas. However, the high spatial resolution in grids does not help to improve the consistency between the GPS-observed and the GRACE-derived vertical displacements. We attribute this phenomenon to the fact that GPS measurements are point samples while GRACE provides low spatial resolution products, which leads to the agreement between the GPS-observed and the GRACE-derived vertical deformations depending highly on the distribution of the GPS sites.

In conclusion, the study in this chapter presents results and experiences regarding evaluating different filtering schemes when comparing GPS and GRACE, which could serve as a reference for future studies concerning GPS and GRACE comparison. In addition, the GRACE follow-on mission, which is simply a copy of the GRACE mission, is planned to be launched in 2017 (Sheard et al., 2012; Flechtner et al., 2014b). The conclusions and experiences obtained from the study in this chapter could be possibly applied in the products delivered by the GRACE follow-on mission in the future.

Chapter 5

Site dependent modeling of load induced displacements

5.1 Motivation

As introduced in the previous chapters, the redistribution of atmospheric, oceanic and hydrological masses on the Earth's surface varies in time and this in turn loads and deforms the surface of the solid Earth. The Earth responds to its environmental loadings elastically at different time scales, from monthly to inter-annual (van Dam et al., 2001; Dong et al., 2002). It also manifest spatially at global (Blewitt et al., 2001), regional (Heki, 2001) and local scales (Bevis et al., 2004). Loading induced deformations can either be measured directly by GPS or be theoretically derived from GRACE (Davis et al., 2004) or loading models (Farrell, 1972; van Dam et al., 2001).

At global or regional scales, deformations estimated from mass changes are normally implemented in terms of the well-known Green function approach based on the PREM model (see Chapter 2 for more details). PREM is homogeneous and isotropic over the globe which leads to the derived deformation depending solely on the spherical distance between the load and the computation point. However, it is reasonable to expect that the Earth's crust responds to its surface load inhomogeneously and anisotropically. Bevis et al. (2012) pointed out it is probably inappropriate to use elastic-loading Green functions based on PREM, or any other radially symmetric, whole-earth model, in order to invert the crustal displacements observed by GNET (Greenland GPS Network) for the spatial variation of surface load changes in Greenland. Using an Earth model with modified crust structure given by CRUST 2.0, Wang et al. (2012) found larger deformations than three other spherically symmetric models for the very near field ($< 0.1^{\circ}$). In line with them, several other studies also modified the local crust structure in terms of the crust models and estimated the deformation with the corresponding adapted Green functions due to ice sheet loading (Nielsen et al., 2013), ocean tidal loading (Arnoso et al., 2013) or surface water loading (Dill et al., 2015).

In the era of various modern space geodetic observation techniques, Gross et al. (2009) puts forward the requirement of high accuracy of the Global Geodetic Observing System (GGOS) for the scientific and societal users, e.g. accuracy of less than 1 mm in terms of 3-D displacements. Certainly, corresponding displacement modeling due to elastic surface loading should meet this requirement as well. Several factors contribute to the uncertainties of modeled displacements (Petrov and Boy, 2004) and uncertainty due to the Green function coefficients is one of them (van Dam et al., 2003; Petrov and Boy, 2004). This chapter aims to investigate this aspect using different types of the Green function coefficients.

At the local scale, the Green function approach is also applicable. For example, Elósegui et al. (2003) applied the Green function approach to a $2^\circ \times 1.5^\circ$ area near Great Salt Lake, Utah. Furthermore, within a limited spatial extent, other valuable tools which neglect the curvature and the topography of the Earth were presented as an elastic half-space approach (Boussinesq, 1885; Love, 1929; Farrell, 1972). Farrell (1972) presented Green functions for both the half-space model as well as the spherical Earth model. However, only the Green function for the spherical Earth model is well-known and widely used while the Green function for the half-space model based on the assumption of point load is seldom touched even in the case of a local scale, for instance, the example of Elósegui et al. (2003). Nevertheless, a small number of studies applied the local Green function approach practically. For example, Memin et al. (2009) utilized this approach to model deformation owing to ice thinning in the Mont Blanc massif (Mer de Glace, Talèfre, Leschaux) and in Svalbard (Norway) in the Arctic.

Beyond the point load assumption, Becker and Bevis (2004) developed the theory of and provided explicit expressions for the displacements generated in a semi-infinite half-space by uniform surface pressure (surface load) applied over a rectangular region. More generalized expressions for an arbitrary polygonal region were contributed by D'Urso and Marmo (2013). Utilizing the elastic half-space approach, Bevis et al. (2005) obtained a fairly good fit to the vertical displacement records at the geodetic GPS station located in the city of Manaus (Brazil). More recently, Steckler et al. (2010) and Amosu et al. (2012) applied the explicit expressions from (Becker and Bevis, 2004) and modeled the Earth's crustal elastic deformations due to the continental water loading in Bangladesh and along the Mississippi river so as to determine Young's modulus, respectively.

In addition to these geophysically based approaches, Seitz and Krügel (2009) proposed an empirical Green function approach which substitutes the original Green functions with a simple exponential function fitting. This approach considers the crustal inhomogeneities and behaves like a site-dependent or region-dependent Green function approach.

As described above, several approaches regarding deformation modeling exist in the literature for various spatial scales. This chapter targets to evaluate these approaches within a local region using a high-spatial resolution local load dataset provided by Amosu et al. (2012). Firstly, fundamental theory about the half-space approach will be introduced. This is followed by the comparison of the displacements modeled from the common Green function approach and two half-space approaches. In addition, we will examine the effects of site-dependent Green function coefficients in deformation modeling. The empirical Green function approach proposed by Seitz and Krügel (2009) will be investigated as well in this chapter.

5.2 Modeling deformation in the half-space

THE elastic half-space approach originated from Boussinesq (1885), who expressed displacements and stresses at any point within the half-space as the various spatial derivatives of elastic potential functions. Explicit expressions for the deformations and stresses due to a specific shape and form were developed subsequently by many researchers (e.g., Boussinesq, 1885; Love, 1929; Farrell, 1972). Among them, load shapes of point load and rectangular load are popular and applied in practice (e.g., Bevis et al., 2005; Memin et al., 2009; Steckler et al., 2010). Farrell (1972) presented the solutions due to a point load and Love (1929) derived explicit representations for the stresses due to a vertical uniform surface pressure applied within

a rectangular region. Becker and Bevis (2004) revisited Love's problem (Love, 1929) and provided the corresponding analytical solutions for the displacements due to a rectangular load. Following Becker and Bevis (2004), D'Urso and Marmo (2013) derived a more generalized solution for computing the displacements within a homogeneous, elastic half-space induced by an arbitrary polygonal load.

In the elastic half-space approach, estimated displacements depend not only on the load but also on the geological structure of the loaded area, that is, Láme constants (λ and μ) or Young's modulus E and Poisson's ratio ν instead. They have the mutual relationship

$$\lambda = \frac{E \times \nu}{(1+\nu)(1-2\nu)}\,, \tag{5.1a}$$

$$\mu = \frac{E}{2(1+\nu)}\,. \tag{5.1b}$$

The following subsections will briefly present the basic theory of the two half-space approaches. It should be mentioned that, in the following approaches, we will always consider the vertical axis (z) to be directed downwards so that unloading will mainly induce a negative vertical displacement.

5.2.1 Point load

THE loading theory presented in Section 2.2 is the solution to Boussinesq (1885) provided by Farrell (1972) based on a realistic spherical, non-rotating, elastic and isotropic Earth model. Meanwhile, Farrell (1972) presented the answer to Boussinesq (1885) in a homogeneous elastic half-space. By neglecting the Earth's curvature in a homogeneous half-space, the static displacement vector $\mathbf{s}$ satisfies the elastic equilibrium equation

$$\sigma\nabla(\nabla\cdot\mathbf{s}) - \mu\nabla\times(\nabla\times\mathbf{s}) = 0\,, \tag{5.2}$$

with $\sigma = \lambda + 2\mu$. Let g_0 be the norm of a unit force exerted vertically at the Earth's surface by the unit mass point. Farrell (1972) solved Eq. (5.2) in the cylindrical coordinate system (r, θ, z) centered at the application point of the force (see Eq. (10) in (Farrell, 1972)). By neglecting the topography of the Earth, i.e. $z = 0$, the analytical solutions of the horizontal and vertical displacements are correspondingly written as (Memin et al., 2009; Chanard et al., 2014)

$$u_r(R,0) = -\frac{g_0}{4\pi R\eta} = -\frac{g_0}{2\pi R}\frac{(1+\nu)(1-2\nu)}{E}\,, \tag{5.3a}$$

$$u_z(R,0) = \frac{g_0}{4\pi R\mu}\frac{\sigma}{\eta} = \frac{g_0}{\pi R}\frac{1-\nu^2}{E}\,, \tag{5.3b}$$

where $\eta = \lambda + \mu$ and R indicates the distance between the observation point and the mass force point. By symmetry, $u_\theta = 0$ and all components of surface displacements are independent of θ. In practice, the same convolution process as the global Green function approach is implemented to evaluate the displacements. To differentiate from the widely applied global Green function approach, this approach is normally called the Green function approach for the half-space (e.g., Pinel et al., 2007).

Eq. (5.3) indicates that the displacements depend not only on the distance between the load point and the computation point but also the geological structure of the loaded region. On the one hand, providing we have the knowledge of the geological parameters beforehand, Eq. (5.3) could be utilized to predict the deformation due to local elastic surface loading (e.g., Pinel et al., 2007; Memin et al., 2009; Zhao et al., 2014). On the other hand, if we possess the observed deformation of the loaded region, it is plausible to probe the geological settings underneath the loaded area.

It is worth mentioning that, since a point load is a mathematical idealization, these studies using the point load approach normally took the load in the shape of a disc (Pinel et al., 2007) or a square (Memin et al., 2009; Zhao et al., 2014) as point load. In this chapter, we take the square shape load as point load in comparison with the surface load approach described below.

5.2.2 Surface load

In addition to the point load, Love (1929) presented the solution to Boussinesq (1885) in the stress field due to a rectangular pressure field, but not in the displacement field. In line with them, Becker and Bevis (2004) revisited Boussinesq's problem and referred the solutions due to the surface rectangular load to Love's problem.

In the framework of Love (1929) and Becker and Bevis (2004), the rectangular region, where the uniform pressure P is applied, is defined by $-a \leq x \leq a$, $-b \leq y \leq b$ at the surface ($z = 0$) of a semi-infinite solid (see Fig. 5.1), where z is positive downward so that points in the solid have $z \geq 0$. The distance between the point (x, y, z) within the solid and the point $(x', y', 0)$ on the plane boundary is denoted as r with

$$r^2 = \Delta x^2 + \Delta y^2 + z^2 \,, \tag{5.4}$$

where $\Delta x = x' - x$, $\Delta y = y' - y$ and $r > 0$.

The horizontal displacements u_x and u_y, and the vertical displacement u_z generated by this applied pressure are given by

$$u_x = -\frac{1}{4\pi}\left(\frac{1}{\lambda+\mu}\frac{\partial \chi}{\partial x} + \frac{z}{\mu}\frac{\partial V}{\partial x}\right) \,, \tag{5.5a}$$

$$u_y = -\frac{1}{4\pi}\left(\frac{1}{\lambda+\mu}\frac{\partial \chi}{\partial y} + \frac{z}{\mu}\frac{\partial V}{\partial y}\right) \,, \tag{5.5b}$$

$$u_z = \frac{1}{4\pi\mu}\left(\frac{\lambda+2\mu}{\lambda+\mu}V - z\frac{\partial V}{\partial z}\right) \,, \tag{5.5c}$$

and

$$\chi = \int_{-a}^{a}\int_{-b}^{b} P \log(z+r) dx' dy' \,, \tag{5.6}$$

is Boussinesq's 3-D logarithmic potential, and

$$V = \int_{-a}^{a}\int_{-b}^{b} \frac{P}{r} dx' dy' \,, \tag{5.7}$$

is the Newtonian potential of a surface distribution.

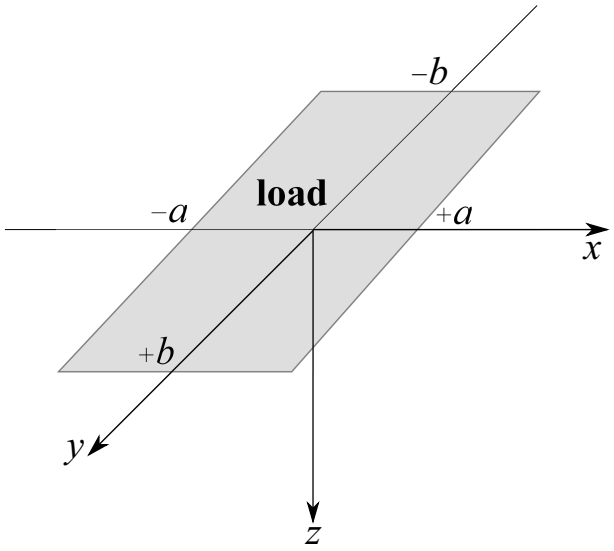

Figure 5.1: *Half-space model with the uniform rectangular load applied at the surface of a semi-infinite elastic solid.*

An elaborate derivation of the solutions to Eq. (5.5) was provided by Becker and Bevis (2004). Here we just summarize the final analytical solutions which could be implemented numerically for evaluating the horizontal and vertical displacements. The corresponding horizontal displacements u_x and u_y are

$$u_x = -\frac{P}{4\pi}\left[\frac{1}{\lambda+\mu}(J_2 - J_1) + \frac{z}{\mu}\log\left(\frac{\Delta x + r_{20}}{\Delta y + r_{10}}\right)\right]_{y'=-b}^{y'=b}, \tag{5.8a}$$

$$u_y = -\frac{P}{4\pi}\left[\frac{1}{\lambda+\mu}(K_2 - K_1) + \frac{z}{\mu}\log\left(\frac{\Delta x + r_{02}}{\Delta y + r_{01}}\right)\right]_{x'=-a}^{x'=a}, \tag{5.8b}$$

where J_1, J_2, K_1, K_2, r_{01}, r_{02}, r_{10} and r_{20} are functions of x, y, z, a and b (see Becker and Bevis (2004) for more details). The respective vertical displacement is

$$u_z = \frac{P}{4\pi\mu}\left[\frac{\lambda+2\mu}{\lambda+\mu}(L_1 - L_2) + z\left\{\operatorname{atan}\frac{(a-x)\Delta y}{z r_{01}} + \operatorname{atan}\frac{(a+x)\Delta y}{z r_{02}}\right\}\right]_{x'=-a}^{x'=a}, \tag{5.9}$$

where L_1 and L_2 are also functions of x, y, z, a and b. Eq. (5.8) and Eq. (5.9) are implemented numerically in this chapter using the local load data [1]. In practice, the same consideration as the point load is made here that the topography of the Earth is ignored and therefore the terms including z vanish.

Comparing to the point load approach, the surface load approach seems to be more complicated in terms of numerical computation. Nevertheless, the surface load approach has been applied in several studies to probe the local geological structure of the Earth (e.g., Bevis et al., 2005; Steckler et al., 2010; Amosu et al., 2012). In addition, to our knowledge, it seems no studies have discussed and compared the two manners in their studies and we will quantify the difference between them with real data in Section 5.4, which might serve as a reference for readers.

[1] Implementation is done based on Matlab code which could be available on request from Becker and Bevis (2004)

5.3 Site-dependent and area-dependent Green function coefficients

SINCE the SNREI Earth model, e.g. PREM, has its limitations, there is an increasing concern about modifying the SNREI models using the crust models, e.g. CRUST 2.0 (Bassin et al., 2000) or TEA12 (Tesauro et al., 2012), to obtain site-dependent or area-dependent Green function coefficients. Except for the PREM model, other Earth models are utilized to produce loading Love numbers and Green function coefficients and they are: iasp91 (Kennett and Engdahl, 1991), ak135 (Kennett et al., 1995), ak135f (Montagner and Kennett, 1996) and REF (Kustowski et al., 2008).

We list a collection of up-to-date site-dependent or area-dependent Green function coefficients in Table 5.1. In particular, site-dependent loading Love numbers and their corresponding Green function coefficients derived using the REF model with modified crust structure from CRUST 1.0 and CRUST 2.0 were obtained upon request from Gegout (2013). We use these Green functions in Section 5.4.4 to investigate their effects in displacement modeling in a local area.

Table 5.1: *Different types of site-dependent or grid-dependent Green function coefficients.*

Coefficient type	Characteristic	Reference
PREM+CRUST 2.0	one set coefficient for the whole Earth	(Wang et al., 2012)
iasp91+CRUST 2.0	one set coefficient for the whole Earth	
ak135+CRUST 2.0	one set coefficient for the whole Earth	
REF+CRUST 2.0	site-dependent	(Gegout, 2013)
REF+CRUST 1.0	site-dependent	
ak135f+CRUST 2.0	site-dependent	
ak135f+CRUST 1.0	site-dependent	
PREM+TEA12	grid-dependent ($1^\circ \times 1^\circ$)	(Dill et al., 2015)

5.4 Case study: the lower Mississippi river

5.4.1 Study area and dataset

THE study area in this section is located along the lower Mississippi river with the region spanning from -91.5° to -88.7° in latitude and from 35° to 37.5° in longitude, in central USA, see Fig. 5.2. A complicated geological structure exists here with the Mississippi embayment and the Reelfoot fault scarp. In addition, the famous Madrid seismic zone is also located underneath this region (Smalley et al., 2005).

The dataset used in this section consists of the load data and displacement time series recorded by GPS, which are provided by Amosu et al. (2012). Here a brief introduction of the datasets is given. Both datasets were sampled daily in 2011 from day 1 to day 365. In particular, during April and May in 2011, a severe flood happened along the Mississippi river. The daily GPS data of eleven continuous GPS stations from the GPS array for Mid-America (GAMA) were processed which provided results in the ITRF2008 reference frame. The daily load data were computed

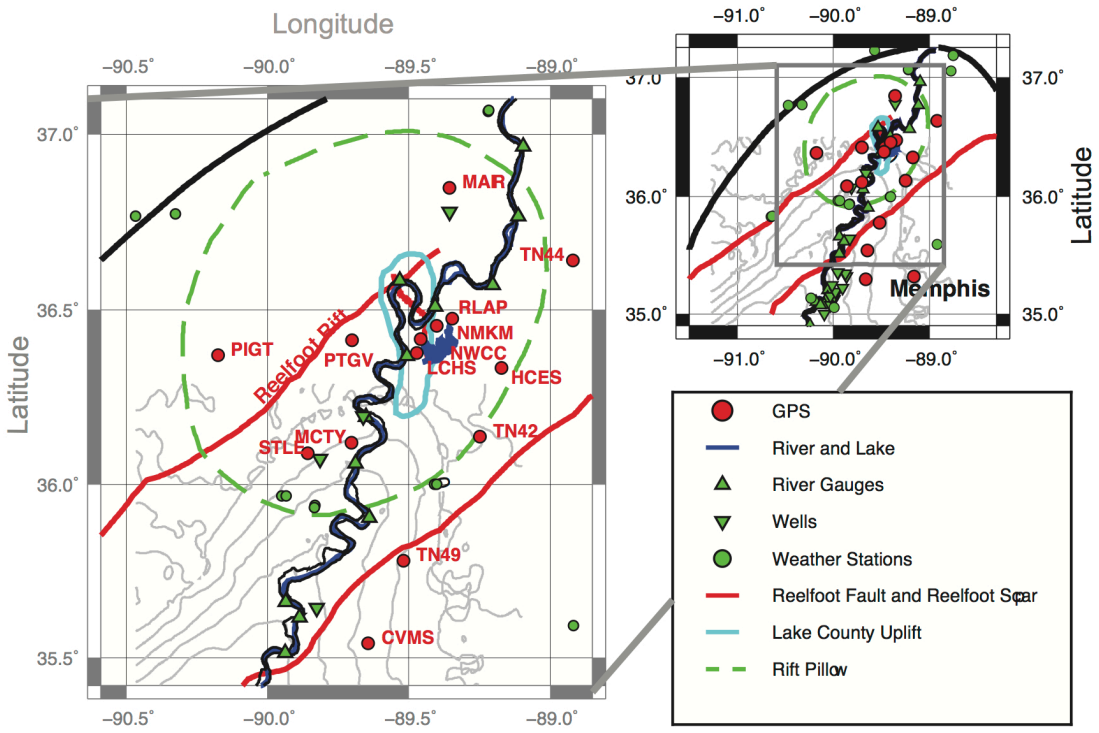

Figure 5.2: *Map of the study area: lower Mississippi river region (courtesy: Adewale M. Amosu from* CERI*, University of Memphis). The geological structures, such as the Mississippi embayment (heavy black line), are shown. Wells, river gauges, and weather stations which contribute to the load, are illustrated as well.* GPS *sites which document the observed displacements are denoted in red circles.*

using the daily river/lake gauges, well data and atmospheric pressure data (see Fig. 5.2) following the same strategy as Steckler et al. (2010). By deploying the 3-arcsecond DEM (Digital

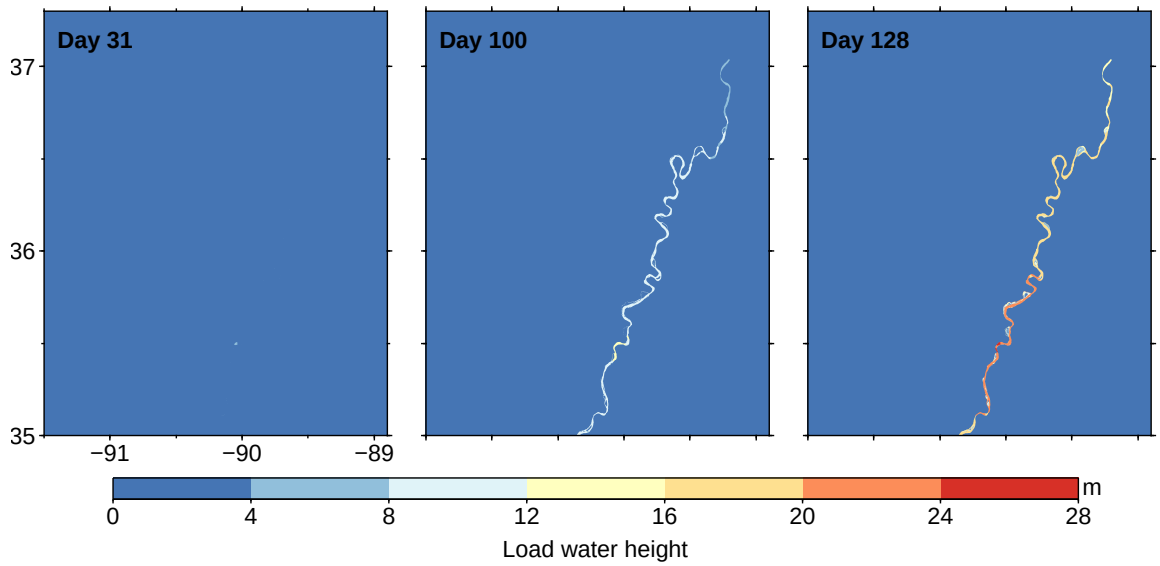

Figure 5.3: *Load water height for day 31 (no flood), day 100 (medium flood) and day 128 (peak of flood)*

Elevation Model) from the SRTM (Shuttle Radar Topography Mission) data, the load data were resampled into a high spatial resolution of $3'' \times 3''$. The load data in equivalent water height for day 31 (no flood), day 100 (medium) flood and day 128 (peak of flood) are shown in Fig. 5.3. A significant load of up to 26 m is observed when the flood happened.

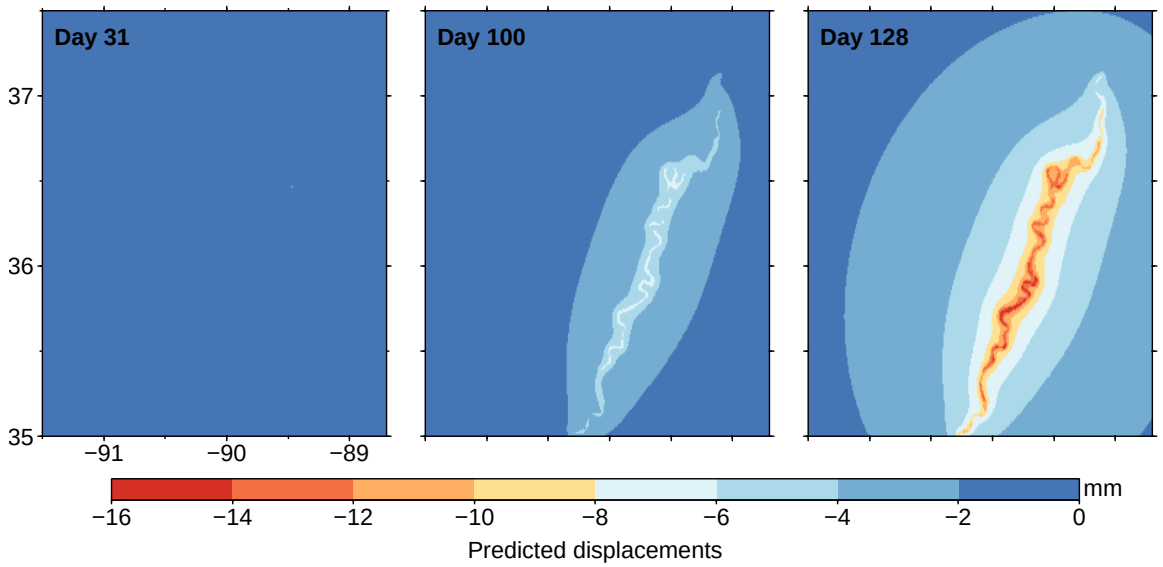

Figure 5.4: *Predicted vertical displacements for day 31 (no flood), day 100 (medium flood) and day 128 (peak of flood), using the half-space approach with $E = 140$ GPa.*

Since our aim is to evaluate different approaches in modeling the deformation within a local region, we rely on obtained Young's modulus E around 140 GPa. Note that the other parameter, Poisson's ratio, is normally set to 0.25 (Bevis et al., 2005; Steckler et al., 2010). The corresponding predicted displacements using the half-space approach for days 31, 100 and 128, are displayed in Fig. 5.4. Heavy load corresponds to large displacements up to 16 mm beneath the river and its surroundings.

5.4.2 Point load versus surface load

USING the $3'' \times 3''$ resolution load dataset, we apply the point load approach and the surface load approach to compute the displacements at 11 GPS stations. Note that the $3'' \times 3''$ load is considered as the point load and applied using Eq. (5.3a) and Eq. (5.3b). The comparison between them is displayed with one exemplary GPS site in Fig. 5.5. Other GPS sites show a very similar behavior.

Clearly, the two approaches produce quite close displacements with differences in the level of 10^{-3} mm in vertical component and 10^{-4} mm in horizontal component, which are negligible in practice. In terms of computational efficiency, the point load approach is more efficient than the surface load approach; that is, under the same computation environment (Matlab 2013a installed in Windows 7 with the processor Inter Core i5-3740 and the RAM of 8 GB), time consumption for the point load approach is around 327 seconds while the surface load approach requires around 10772 seconds. The longer time required for the surface load approach is due

to the complicated numerical computation using Eq. (5.8) and Eq. (5.9), which needs to evaluate several subfunctions, e.g. J_1 and J_2. The comparison shown here indicates the advantage of the point load approach against the surface load approach in practical use. We therefore recommend to utilize the point load approach in practice for the case of the half-space deformation modeling. This point load approach will be used in the forthcoming comparison.

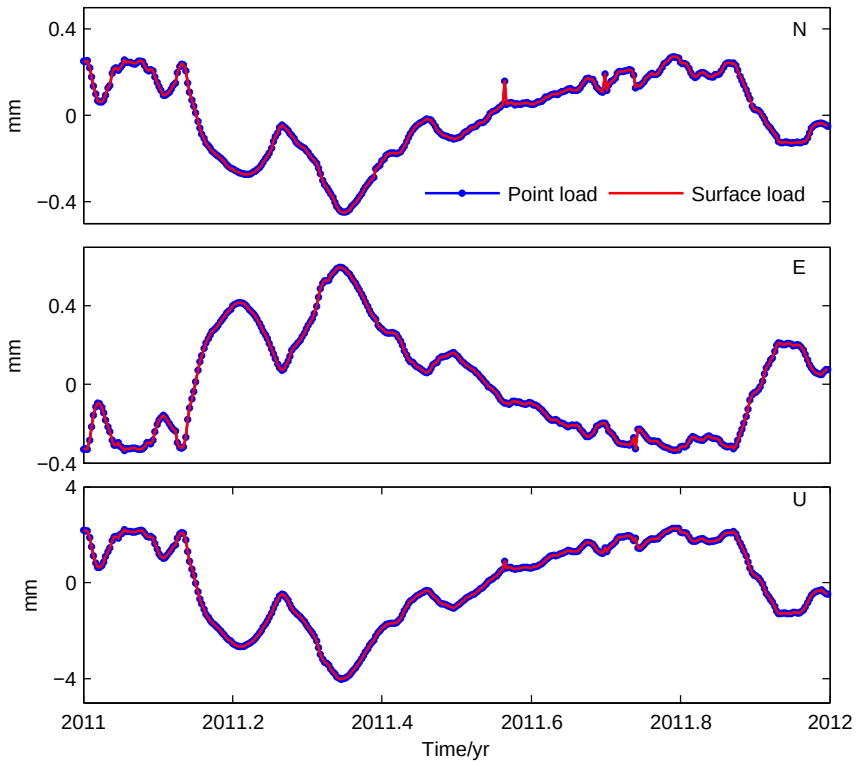

Figure 5.5: *Comparison of the point load approach and the surface load approach at* GPS *site* PTGV.

5.4.3 Global Green function approach versus half-space approach

In addition to the half-space approach approach, using the same load data, we also apply the classic Green function approach at these GPS sites. To complement the analysis, we include two hydrological models into the comparison as well: MERRA-B (Reichle et al., 2011) and GLDAS-1 (Noah 2.7) (Rodell et al., 2004), which are used to model displacements due to the global continental water loading. The temporal resolution for the two models we used are hourly and 3-hourly, respectively, and the corresponding spatial resolution are $1/2^\circ \times 2/3^\circ$ and $0.25^\circ \times 0.25^\circ$. Using the Green function approach, the displacements at the 11 GPS stations from the two hydrological models and the local high-resolution load data are evaluated.

Here we choose the Green function based on PREM in the CF frame to keep consistency between the estimated displacements and the observed GPS height deformations. Due to the fact that the local load data does not include the water components of soil moisture and snow water equivalent, the local area is not excluded in the computation of the displacements from the hydrological models.

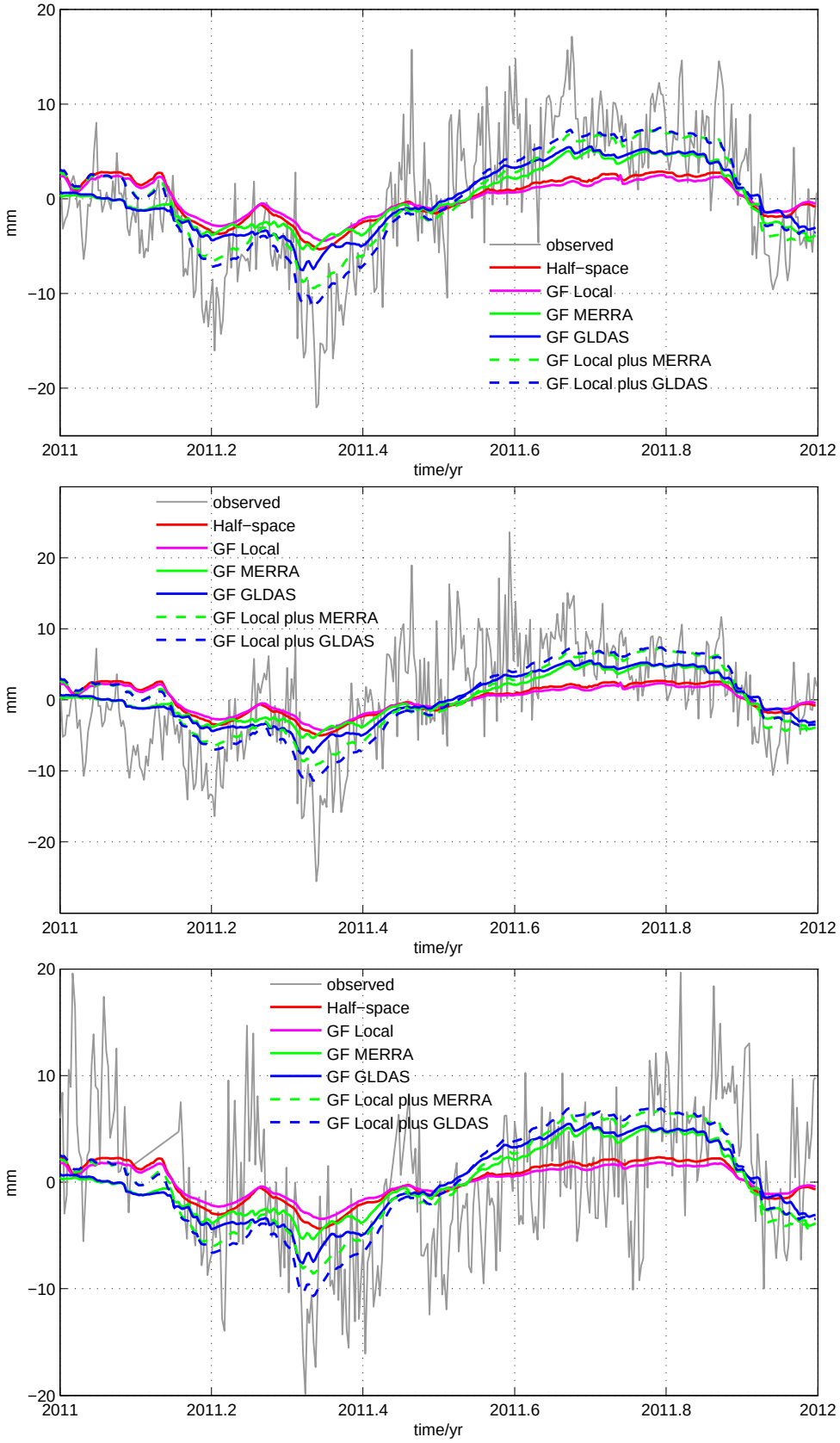

Figure 5.6: *The observed vertical displacements from* GPS *and the predicted deformations at* NWCC *(top),* NMKM *(middle) and* RLAP *(bottom). Abbreviations, e.g.* GF Local*, stand for using the Green function approach with respective load datasets. These abbreviations are used in Figs. 5.7, 5.8,5.9 and Table 5.2 as well.*

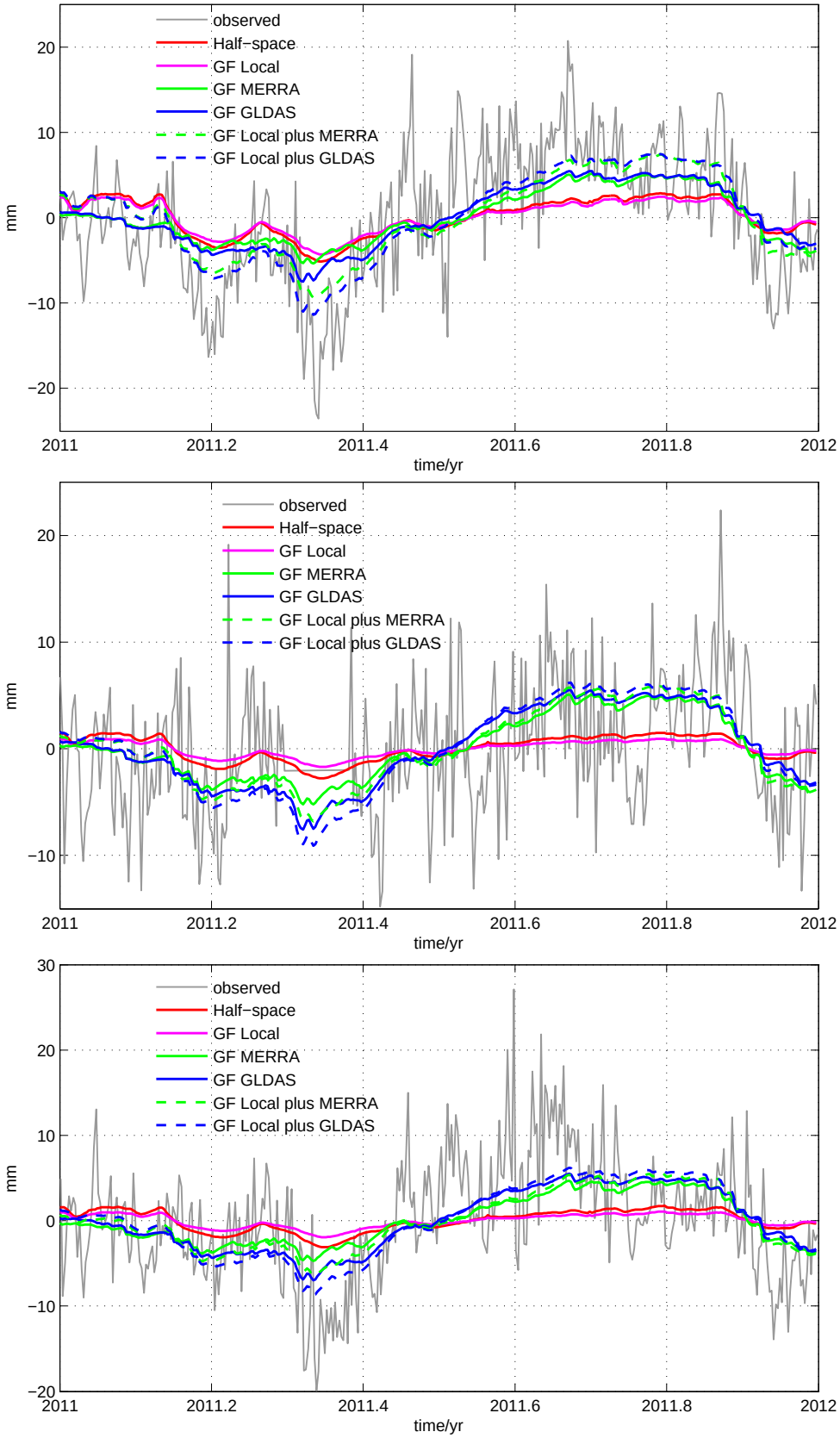

Figure 5.7: *The observed vertical displacements from* GPS *and the predicted deformations at* LCHS *(top),* HCES *(middle) and* CVMS *(bottom).*

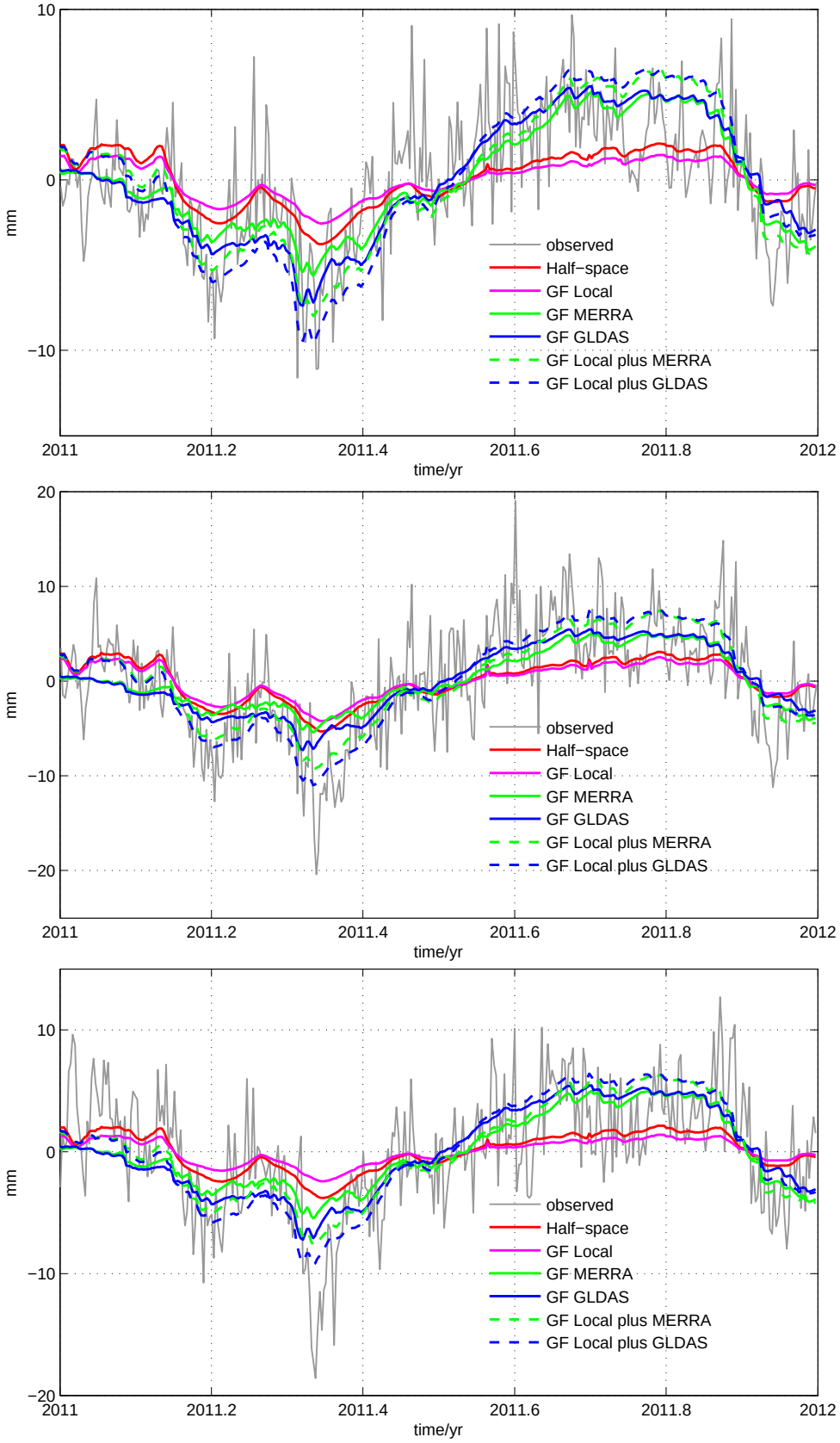

Figure 5.8: *The observed vertical displacements from* GPS *and the predicted deformations at* PTGV *(top),* MCTY *(middle) and* STLE *(bottom).*

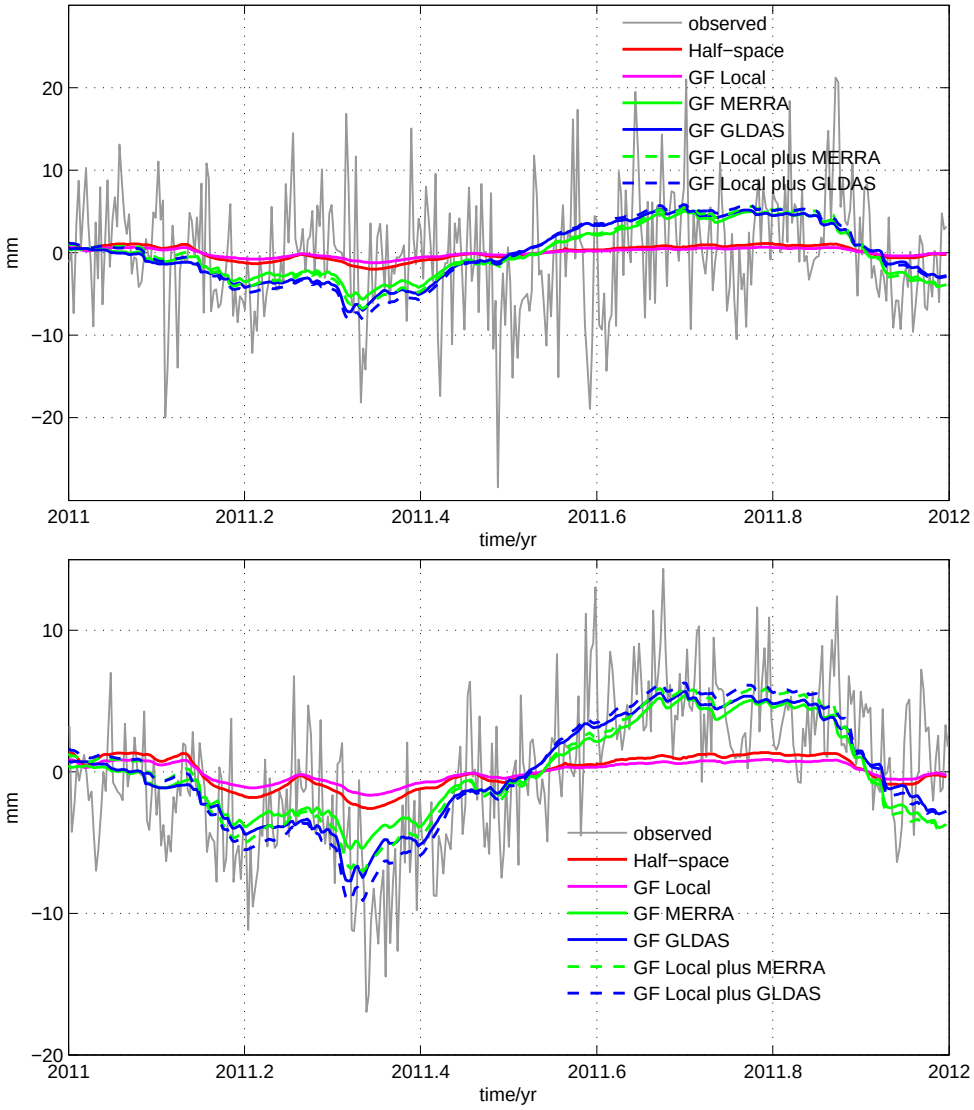

Figure 5.9: *The observed vertical displacements from* GPS *and the predicted deformations at* PIGT *(top) and* MAIR *(bottom).*

Figs. 5.6, 5.7, 5.8 and 5.9 present the comparison at all considered 11 GPS sites. With only the local load data involved, it is interesting to find that the vertical deformations derived from the elastic half-space approach and the Green function approach follow each other quite well. The former predicts obviously larger displacements than the latter. It indicates that, within a limited spatial extent, the elastic half-space approach seems to be more effective than the Green function approach. However, the predicted vertical deformations from the two methods fail to fit the observed GPS time series very well, especially during both the flood and the rebound periods. The modeled vertical displacements from the two hydrological models tell us that the GPS stations are also affected by the global, i.e. far field, water loading effects (van Dam et al., 2001). Nevertheless, the elastic half-space approach which neglects the curvature and the topography of the Earth is unable to model the global loading effects from hydrology, atmosphere and ocean.

Table 5.2: *The* NSE *values of the predicted displacements with respect to the observed* GPS *time series.*

GPS sites	HS Local	GF Local	GF MERRA	GF GLDAS	GF Local + MERRA	GF Local + GLDAS
total period						
CVMS	0.16	0.11	0.31	0.37	0.35	**0.38**
MAIR	0.25	0.17	0.48	**0.52**	0.50	**0.52**
MCTY	0.41	0.35	0.47	0.52	**0.57**	**0.57**
NWCC	0.38	0.32	0.51	0.57	0.65	**0.68**
PIGT	**0.05**	0.03	0.02	-0.05	0.00	-0.07
PTGV	0.37	0.29	**0.47**	0.44	0.36	0.28
RLAP	**0.24**	0.20	0.18	0.19	0.22	0.20
STLE	0.37	0.26	0.42	0.42	**0.47**	0.44
HCES	0.07	0.05	**0.13**	0.08	0.10	0.04
NMKM	0.24	0.20	0.36	0.41	0.40	**0.42**
LCHS	0.32	0.27	0.43	0.48	0.55	**0.57**
flood period						
CVMS	-0.08	-0.26	0.05	0.22	0.21	**0.31**
MAIR	-0.28	-0.80	0.13	0.21	**0.27**	0.25
MCTY	0.03	-0.16	0.02	0.20	**0.45**	0.44
NWCC	-0.52	-0.76	-0.46	-0.13	0.28	**0.42**
PIGT	**0.04**	0.03	-0.13	-0.32	-0.21	-0.42
PTGV	0.20	-0.04	**0.30**	0.21	0.25	-0.08
RLAP	-0.12	-0.15	-0.01	0.04	-0.08	-0.13
STLE	0.06	-0.17	0.24	0.31	**0.40**	0.36
HCES	**0.05**	0.02	-0.14	-0.39	-0.06	-0.22
NMKM	-0.16	-0.28	-0.11	0.03	0.22	**0.24**
LCHS	-0.27	-0.43	-0.24	-0.02	0.29	**0.37**

Inspection of Figs. 5.6, 5.7, 5.8 and 5.9, two exceptional GPS sites are observed. One is PIGT, which is the farthest away from the Mississippi river, showing pretty flat signal during the flood period. Neither the local data nor the models can predict displacements fitting well to the observed deformation at PIGT. The other is HCES which contains a big gap during the flood, decreasing the statistical performance in Table 5.2.

A statistical analysis of the the performance of the two approaches and the two hydrological models is implemented with NSE (see Section 4.4). NSE values can range from $-\infty$ to 1 and an efficiency of 1 corresponds to a perfect match of the predicted deformations to the observed displacements in this context. In addition, NSE values larger than zero indicate statistical consistency. To facilitate the comparison, we evaluate the NSE values during the total period of 2011 and the flood period (day 50 to day 150), respectively. The result is shown in Table 5.2.

The statistical result further confirms the previous analysis. At all 11 GPS stations we studied, either during the total period or only the flood period, the predicted deformations from the elastic half-space approach agree better with the observed GPS time series than the estimated displacements from the Green function approach. The statistical result also demonstrates the effects of the global water loading, which delivers even better agreements than the local load data. On the condition of models only, the modeled displacements from GLDAS fit the obser-

vations marginally better than those from MERRA at more than half of the stations. In the case of combining the models with the local data, GLDAS gives also better performance with respect to MERRA at most of the stations during the whole period and comparable performance during the flood period. Comparing to the modeled displacements from the elastic half-space approach as well as other combinations, the combination of the local data with the GLDAS model using the Green function approach also shows a superior performances.

Steckler et al. (2010) mentioned that, for loads beyond Bangladesh, the elastic half-space approach may not be adequate and a spherical Earth model may be necessary. To some extent, our study confirms this assumption. Considering the quite large displacements predicted from the global terrestrial water loading models, a pre-reduction of global water loading effects might help to determine the geological settings, i.e. Young's modulus, more precisely via the elastic half-space approach.

The question remains also how large area the half-space approach can be applied. Steckler et al. (2010) applied the half-space approach in Bangladesh of an area of $5^\circ \times 6^\circ$ and Bevis et al. (2005) deployed it in the Amazon region with an even bigger extent of $10^\circ \times 10^\circ$. Chanard et al. (2014) argued the inappropriateness of the half-space approach with respect to the Green function approach when they applied them to probe the crustal structure around the Himalaya region with an area covering $40^\circ \times 60^\circ$. On this aspect, further studies are required to investigate the proper maximum area that the half-space approach can be utilized.

5.4.4 Isotropic Green functions versus site-dependent Green functions

To investigate effects of elastic loading Love numbers (LLNs), we use one reference LLNs based on the REF model and two sets of the site-dependent LLNs provided by Gegout (2013). The site-dependent LLNs are derived from a combination of CRUST 1.0 or CRUST 2.0 with a REF Earth model. We denote the LLNs and the GFs derived from the combination of CRUST 1.0 and CRUST 2.0 with the REF model as CRUST_1 and CRUST_2, respectively. Fig. 5.10 presents examples of the site-dependent LLNs and their corresponding Green function coefficients at NWCC.

In terms of LLNs, since both the PREM and REF are SNREI Earth models, the difference between them is negligible (less than 1 %) (Gegout, 2013). While by modifying the local crustal rheology of the REF model with the crust models, it can cause small differences at large scales around 10 % for low degree less than 100; large uncertainties around 30 % at medium scales with degree from 100 to 1000 and significant differences at local scales for degrees over 1000. Differences in LLNs are accordingly propagated to the site-dependent Green function coefficients, which represent the Earth's structure as if the local crustal characteristics extend over the whole globe (Wang et al., 2012; Gegout, 2013; Dill et al., 2015). Compared to the GFs derived from the PREM model and the REF model, CRUST_1 and CRUST_2 influence mainly the displacement pattern in the very near field of the load source ($\psi < 0.1^\circ$). While in the far field, the GFs derived on the basis of PREM seem to produce larger deformations with respect to the two site-dependent sets of GFs.

Fig. 5.11 illustrates the predicted displacements using four sets of GFs. As expected, differences between two SNREI models are small and we do not show them here so as to focus on comparison between PREM and the two modified models. With the local load data, the deformations computed with CRUST_1 and CRUST_2 are slightly larger than those calculated with

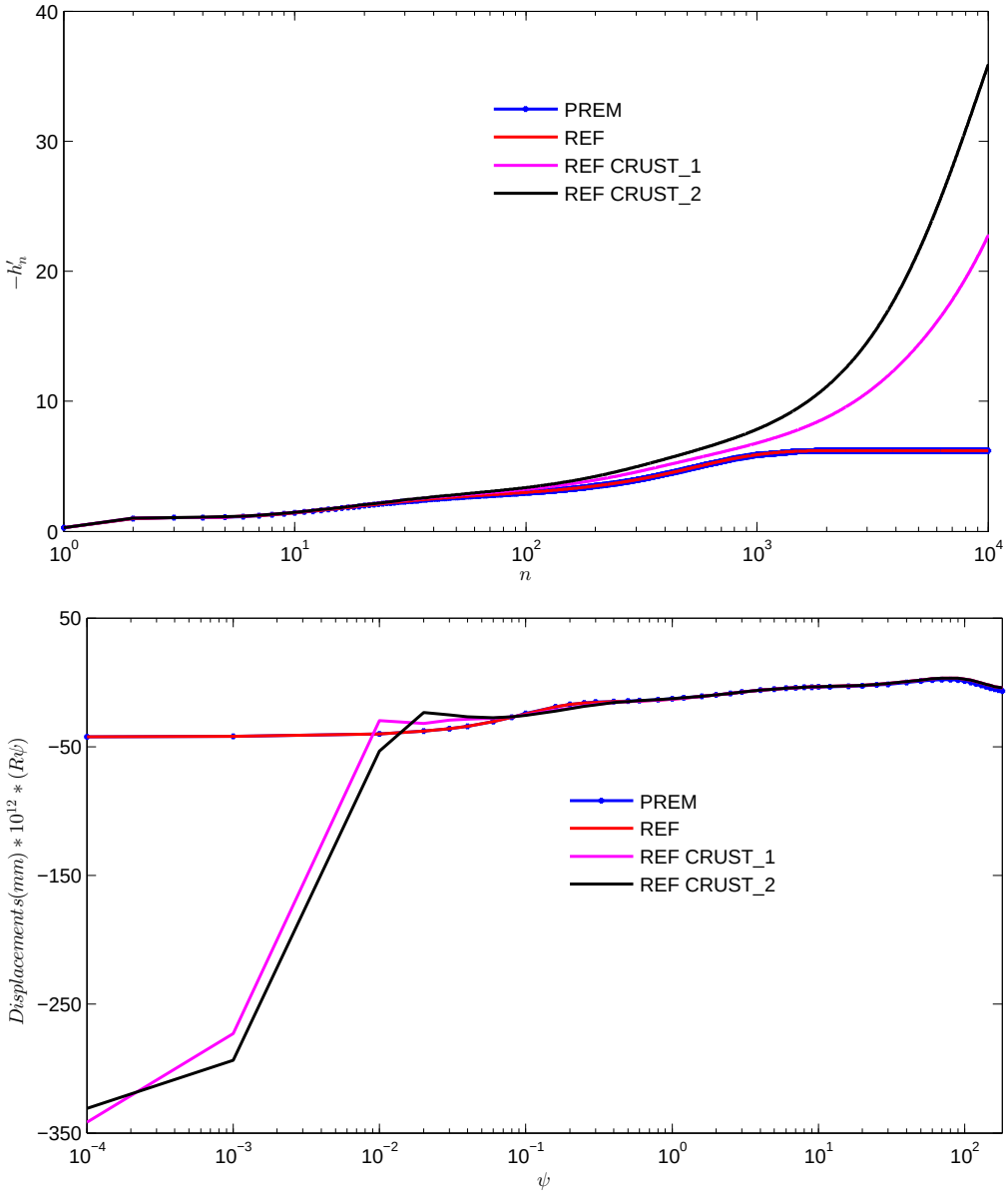

Figure 5.10: *Loading Love Numbers from* PREM, REF, REF *with modified crust from* CRUST *1.0 and* REF *with modified crust from* CRUST *2.0 and their corresponding Green function coefficients at* NWCC.

REF and PREM, which makes us arrive at the same findings as Wang et al. (2012). However, these differences are not obviously distinguishable in Fig. 5.11 as the absolute differences are too small to be seen with the total deformations. To this end, statistical analysis of these differences in the north, east and vertical components are evaluated individually using four metrics including maximum and minimum differences, RMS of the differences and relative RMS of the differences with respect to PREM. The statistical results are tabulated in Tables 5.3, 5.4 and 5.5. In the north component, the maximum absolute differences are 0.14 mm appearing at CVMS and MAIR for CRUST_1 and 0.18 mm at NWCC for CRUST_2. In the east component, slightly larger maximum absolute differences are observed with respect to that in the north component, which are 0.26 mm at PTGV for CRUST_1 and 0.30 mm at LCHS for CRUST_2. The highest

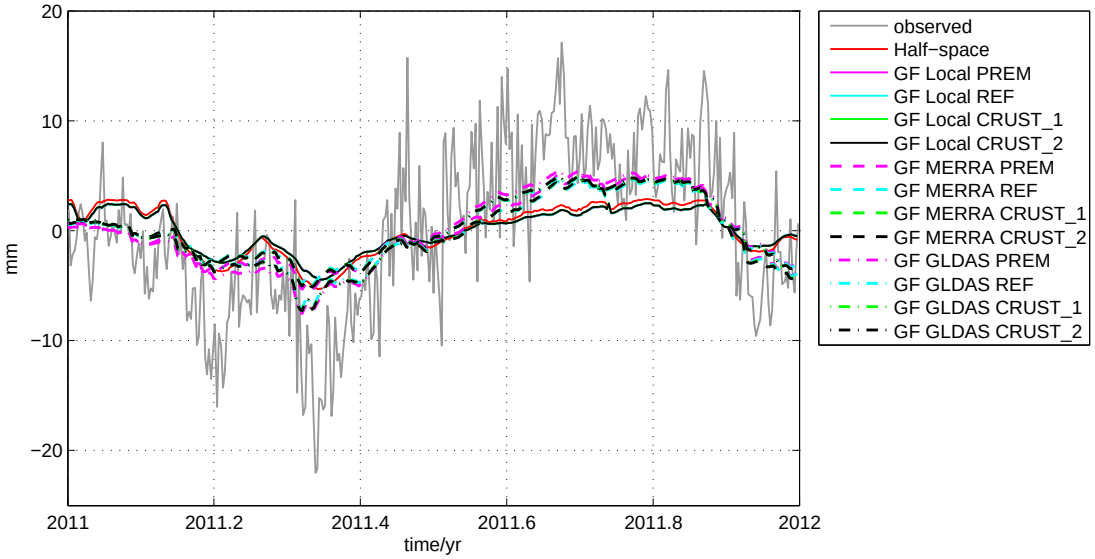

Figure 5.11: *The vertical displacements computed from the local load and models with site-dependent Green function coefficients at* NWCC.

maximum absolute differences for both CRUST_1 and CRUST_2 are seen in the vertical component, 0.38 mm and 0.56 mm, respectively, at the same site PTGV. The absolute differences are not significant and the average RMS of differences between the predicted deformations at 11 GPS stations are no bigger than 0.1 mm in all three components. This is due to the fact that the predicted displacements using only the local load data are relatively small by the global Green function approach. For example, based on PREM, maximum absolute displacements are 0.7 mm, 1.3 mm and 7.5 mm in the north, east and vertical components, respectively.

However, if we look at the relative RMS, big values are found for the north and east components with averages of 25.7 % and 37.8 % for CRUST_1, 31.0 % and 52.0 % for CRUST_2. In the vertical component, the relative RMS values are smaller with averages of 5.6 % for CRUST_1 and 6.6 % for CRUST_2. The averages of the relative RMS values are quite in agreement with that in (Dill et al., 2015) who applied their grid-dependent Green function coefficients to predict deformations due to the global hydrological and atmospheric loading.

Petrov and Boy (2004) analyzed the global error budget of evaluating the atmospheric pressure loading induced displacements and attributed less than 2 % uncertainties to the Green functions. However, the comparisons shown here demonstrate that the site-dependent Green function coefficients can contribute more than 5 % uncertainties in evaluating deformations due to environmental loading, which is also indicated by Dill et al. (2015).

Utilizing the MERRA model and the GLDAS model, the GFs derived from CRUST_1 and CRUST_2 produce less displacements than those from PREM due to being less effective in the far field. To predict higher displacements, the combination of the site-dependent GFs with the GFs derived from PREM is advisable. For instance, Nielsen et al. (2013) applied the GFs from a site-dependent Earth model in the Jakobshavn Isbræ area in Greenland and the GFs from PREM outside of the area.

It is worth mentioning that, in the Green function approach, the displacement is proportional to the magnitude of the loaded pressure as well. In this section, the load data we used were

Table 5.3: *Differences of displacements predicted by the site-dependent* GFs *with respect to that from* PREM *in the north component.*

GPS sites	REF with CRUST 1.0				REF with CRUST 2.0			
	max [mm]	min [mm]	RMS [mm]	Relative RMS [%]	max [mm]	min [mm]	RMS [mm]	Relative RMS [%]
CVMS	**0.14**	0.00	0.06	24.8	0.15	0.00	0.06	25.9
MAIR	0.00	**-0.14**	**0.07**	20.9	0.00	-0.14	0.07	20.8
MCTY	0.01	-0.01	0.01	2.4	0.17	0.00	0.09	43.0
NWCC	0.03	-0.01	0.01	3.0	-0.01	**-0.18**	**0.11**	32.5
PIGT	0.00	-0.02	0.01	35.2	0.00	-0.01	0.01	62.6
PTGV	0.01	-0.09	0.04	15.9	0.01	-0.08	0.04	14.9
RLAP	0.09	0.00	0.04	31.1	0.10	0.00	0.04	33.8
STLE	0.00	-0.11	0.05	31.1	0.00	-0.12	0.05	33.8
HCES	0.10	0.00	0.05	123.0	0.12	0.00	0.05	145.8
NMKM	0.04	-0.02	0.01	4.8	-0.01	-0.17	0.10	35.0
LCHS	0.09	0.00	0.05	31.5	0.11	0.00	0.06	39.1

Table 5.4: *Differences of displacements predicted by the site-dependent* GFs *with respect to that from* PREM *in the east component.*

GPS sites	REF with CRUST 1.0				REF with CRUST 2.0			
	max [mm]	min [mm]	RMS [mm]	Relative RMS [%]	max [mm]	min [mm]	RMS [mm]	Relative RMS [%]
CVMS	-0.01	-0.22	0.10	38.8	-0.01	-0.25	0.11	43.4
MAIR	0.10	0.00	0.04	79.6	0.11	0.00	0.05	94.7
MCTY	0.06	0.00	0.03	6.4	0.01	-0.14	0.07	14.5
NWCC	-0.01	-0.08	0.04	8.9	0.03	-0.01	0.02	3.8
PIGT	0.05	0.00	0.02	9.4	0.04	0.00	0.02	7.9
PTGV	**0.26**	0.02	**0.13**	31.0	0.28	0.02	0.13	33.0
RLAP	-0.02	-0.18	0.10	17.1	-0.02	-0.14	0.08	14.5
STLE	0.25	0.01	0.12	31.8	0.27	0.01	0.13	34.0
HCES	-0.01	-0.17	0.08	25.1	-0.01	-0.17	0.08	25.8
NMKM	-0.01	-0.12	0.05	7.3	0.17	-0.02	0.10	14.4
LCHS	0.00	-0.03	0.01	2.50	**0.30**	-0.01	**0.15**	28.6

calculated only along the river which means the loaded area is quite small (see Fig. 5.3). To test the sensitivity of the site-dependent LLNs to the magnitude of the given load, we increase the amplitude of the load data simply by 10 times, the consequent average RMS of differences is proportionally up to 1.1 mm. The absolute differences between the modeled deformations can reach up to 2.6 mm at STLE during the flood period. In a sense, the site-dependent LLNs and GFs are generated to account for such differences. It is also reasonable to imagine that the effects of the site-dependent LLNs and GFs will be amplified with more load data involved.

Table 5.5: *Differences of displacements predicted by the site-dependent* GFs *with respect to that from* PREM *in the vertical component.*

GPS sites	REF with CRUST 1.0				REF with CRUST 2.0			
	max [mm]	min [mm]	RMS [mm]	Relative RMS [%]	max [mm]	min [mm]	RMS [mm]	Relative RMS [%]
CVMS	-0.01	-0.27	0.12	8.6	-0.01	-0.31	0.14	9.6
MAIR	-0.01	-0.24	0.11	9.0	-0.01	-0.28	0.13	10.5
MCTY	0.01	-0.01	0.04	1.3	0.17	0.00	0.03	1.0
NWCC	0.05	-0.05	0.03	0.7	0.07	-0.03	0.03	0.9
PIGT	0.00	-0.03	0.01	1.6	0.00	-0.02	0.01	1.1
PTGV	-0.03	**-0.38**	**0.19**	9.2	-0.04	**-0.56**	**0.27**	13.4
RLAP	-0.02	-0.31	0.15	5.7	-0.02	-0.36	0.18	6.6
STLE	-0.01	-0.37	0.17	9.2	-0.01	-0.43	0.20	11.0
HCES	-0.01	-0.19	0.09	6.9	-0.01	-0.22	0.10	7.9
NMKM	0.05	-0.07	0.03	1.0	0.07	-0.06	0.04	1.1
LCHS	0.01	-0.08	0.04	1.2	0.02	-0.04	0.02	0.7

5.5 An empirical Green function approach

APART from these loading theory based approaches, Seitz and Krügel (2009) proposed one empirical Green function approach which replaces the classical Green function coefficient curve (Eq. (2.23a)) with an exponential function

$$F(\psi_{PQ}) = 10^{-17} a e^{-b\psi_{PQ}} , \tag{5.10}$$

where parameter a is related to the density ρ_Q of the loaded grid cell and parameter b corresponds to the mean density ρ_M of the surrounding grids, see Fig. 5.12. Different parameters a and b allow us to account for regional discrepancies of crustal densities. In other words, different groups of a and b correspond to different Green functions in the respective region. In a way, this approach works as a site-dependent or region-dependent Green function approach.

By substituting Eq. (2.23a) with Eq. (5.10) in Eq. (2.28a), the vertical displacement within a regional area could be written in a discrete way as

$$d_u(P) = \sum_{\substack{k=1 \\ \psi_{PQ_k} < dist}}^{N} 10^{-17} q_{Q_k} A_{Q_k} a_{ik} e^{-b_{ik}\psi_{PQ_k}} , \tag{5.11}$$

where q_{Q_k} is mass surface density with unit of kg/m^2 and A_{Q_k} represents the area of the grid cell k. The parameters a_{ik} and b_{ik} indicate the values of a and b for the specific loaded grid cell k. The summation will be implemented within all cells whose distances away from the computation point P are less than the predefined distance threshold $dist$. $dist = 10^\circ$ was assumed in (Seitz and Krügel, 2009).

On the basis of Eq. (5.11), the parameters a_{ik} and b_{ik} are able to be estimated using the loading models and displacements from a global coverage of GPS sites in the framework of least squares adjustment. Before starting inversion, predefining the parameters a_{ik} and b_{ik} is necessary and this process has been done in consideration of crustal inhomogeneities by deploying

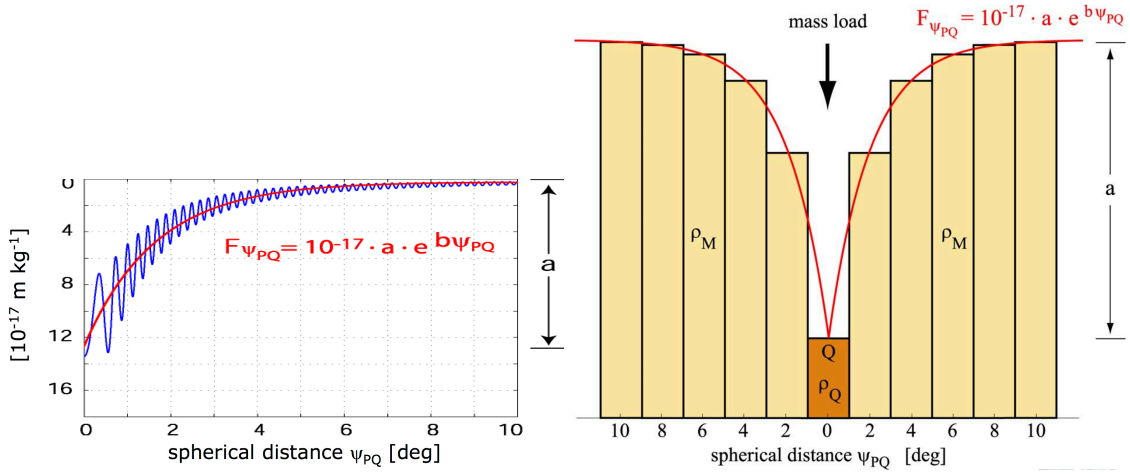

Figure 5.12: *Left: an exponential function fits to the classical Green function approach; Right: basic principle of the empirical Green function approach (courtesy: Seitz and Krügel (2009))*

the CRUST 2.0 model in (Seitz and Krügel, 2009). The mean crustal densities are evaluated at each grid cell by averaging densities from crustal layers of soft and hard sediment, upper, middle and lower crust. Grid cells with the same mean crust density will share the same values for a value. It should be mentioned that, since b is related to the mean density of the surrounding cells, the mean density of the cells within the distance $dist$ around a certain cell is computed which leads to b parameters fewer than a. In (Seitz and Krügel, 2009), seven a and five b parameters were estimated for the whole Earth, see Table 1 in (Seitz and Krügel, 2009).

From the methodology of Seitz and Krügel (2009), this empirical site-dependent Green function approach was deliberately designed for global determination of the parameters a and b based on the crust models. However, Galván et al. (2015) might have applied this approach in an improper manner who estimated the parameters a and b for each GPS site separately in South America using GRACE as input load. To converge in the least squares inversion process, Galván et al. (2015) required to apply regularization.

For validation, we implement this point-wise approach like Galván et al. (2015) for the station NAUS in South America using GRACE and GPS described in Section 4.3. Instead of least squares inversion, we search the parameters a and b in the potential range indicated by Seitz and Krügel (2009) to obtain the minimal RMS value of the difference between the predicted by Eq. (5.11) and the observed displacement by GPS. The possible combinations of a and b are shown in Fig. 5.13. Large, curved and extended a, b parameter domain with equivalent RMS values exist. LS-inversion for a and b is an ill-posed problem and regularization will lead to a result, but not necessarily an appropriate result. To some extent, Fig. 5.13 implies inappropriateness of applying this empirical Green function approach in the way of Galván et al. (2015). In the case of global inversion like Seitz and Krügel (2009), several GPS stations will constrain the same a or b, thereby converging at certain values.

In addition, comparing to the classical Green function approach, this approach does not depend on any Earth models but only on the crust models to predefine the parameters a and b, which could in a way account for the crust's anisotropy. As discussed in Seitz and Krügel (2009), one possible disadvantage of this approach might be that it does depend on the loading models to invert the parameters a and b. Significant uncertainties exist in these models (see

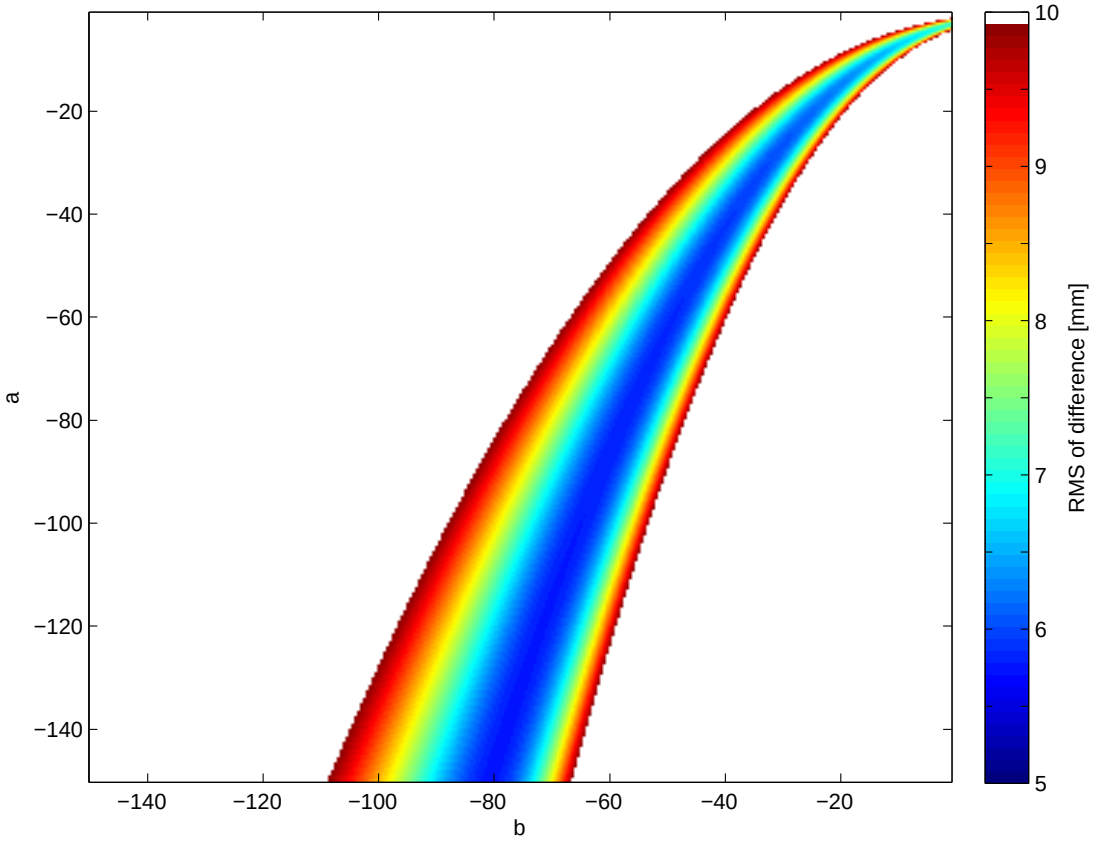

Figure 5.13: *Possible combinations of the parameter a and b at* NAUS

e.g., Petrov and Boy, 2004; Lorenz et al., 2014) which could accordingly result in uncertainties in the estimated a and b. Nevertheless, this site-dependent Green function approach provides us an alternative way to predict the displacements due to Earth's surface loading.

5.6 Discussion and summary

ENVIRONMENTAL loading varies spatially and temporally and it in turn loads and deforms the surface of the solid Earth. This chapter focuses on investigating the currently available approaches which are applied to model the loading induced displacements. The half-space approach and the classic Green function approach are studied and compared using a local high resolution load dataset along with two hydrological models. In addition, an empirical Green function approach is analyzed as well.

In terms of the half-space approach, the equivalence of the point load approach and the surface load approach is demonstrated with real data. Considering the computational efficiency, we recommend to use the point load approach in practice. Comparing the global Green function approach with the half-space approach within a limited spatial extent, the half-space approach provides clearly better performance. However, they both fail to fit the observed displacements recorded at the 11 GPS sites if only the local load data is considered. This is probably due to neglecting the global load outside of the study region. As analyzed, a pre-reduction of the

global environmental loading effects might be helpful in precise determination of the geological structure using the half-space approach.

Regarding the site-dependent Green functions, they do not provide significant absolute differences due to the limited loaded extent with respect to the SNREI-derived Green functions. However, they do produce big differences in terms of the relative RMS. These relative differences indicate that the site-dependent Green functions could contribute more uncertainties to the estimated displacements, i.e. more than 5 %, which was less than 2 % reported by Petrov and Boy (2004). Further comparisons using all up-to-date site-dependent or grid-dependent Green functions will be done in future to evaluate their effects at global scales.

Lastly, the methodology of the empirical Green function proposed by Seitz and Krügel (2009) is discussed and one improper application of this site-dependent Green function approach is pointed out. Maybe the application by Galván et al. (2015) was improper indeed. But in the future we will have more loading data/models and probably denser GNSS networks, so the empirical Green function method must be investigated in future. In addition, it might be interesting to compare with the grid-dependent Green functions derived by Dill et al. (2015) as well.

Chapter 6

Conclusions and outlook

6.1 Conclusions

THE redistribution of atmospheric, oceanic and hydrological masses on the Earth's surface varies in time and this in turn loads and deforms the surface of the solid Earth. Analyzing environmental loading signal and modeling its induced elastic displacements is of ultra importance for explaining a series of geophysical phenomena. This thesis starts with introducing the theoretical relationship between surface mass variation, gravity changes and elastic surface displacements. Particularly, derivations from the spatial Green function approach to the spectral spherical harmonic approach are presented. The two approaches are proved to be equivalent theoretically and practically. Based on the well-established loading theory, this thesis utilizes two different space-borne measurements, i.e. station displacements recorded by GPS and gravity changes in the form of spherical harmonics from GRACE, along with other environmental loading data to contribute to the field from the following three aspects.

Time-variable geodetic seasonal signals modeling Recently, as opposed to seasonal signals with constant amplitudes and phases, an increasing concern regarding the time-variable seasonal signals is observed. Several approaches were proposed to retrieve the time-varying annual and semi-annual signals. However, most of them are model-dependent, e.g. the Kalman filtering based approach (Davis et al., 2012). In this thesis, one data-driven approach, namely, singular spectrum analysis (SSA), is introduced into this field. Through applying SSA to the water level time series of Lake Urmia from satellite altimetry and the basin averaged equivalent water height time series in the Congo basin from GRACE, SSA is demonstrated to be a viable tool in analyzing and modeling the time-variable seasonal signals buried in various geodetic time series.

In addition, several aspects of applying SSA are discussed in this thesis. Among them, one key parameter in SSA, i.e. window size M, is investigated with the above-mentioned geodetic time series. It is shown that the w-correlation analysis is helpful in determining the optimal window size. A window size of 5-year is selected to be optimal for both two types of signals.

Apart from separating time variable seasonal signals, SSA is proved to be able to extract the long-term trend signals as well. In the example of water level time series of Lake Urmia, a clear long-term trend signal is observed and extracted as the first two principal components, which follows the original time series closely.

Optimal filtering on GRACE with respect to GPS GRACE data filtering is always of significant importance in practice. King et al. (2006) investigated the optimal filtering on GRACE within the isotropic Gaussian filtering group in a comparison with GPS. This thesis revisits the idea of King et al. (2006) by including more filters into comparison. In addition to the isotropic Gaussian filter, other two deterministic filters, i.e. the anisotropic Gaussian filter and the destriping filter, and two stochastic filters, i.e. the DDK filter and the regularization filter, are analyzed and compared with GPS height time series from two study areas, i.e. the Europe area and the Amazon area.

The comparisons over the two study areas indicate that no single filtering scheme can produce consistently superior performance to other filters. However, several phenomena can be observed. In general, the stochastic filers provide better performance than the deterministic filters in both study areas. The DDK 1 filter outperforms other filters in the Europe area while the regularization filter of parameter $\lambda = 4$ is selected as the optimal filter in the Amazon area.

In terms of the stochastic filter group, it is shown that the performance of the DDK filters depend on the study area. The DDK 1 and DDK 2 which show good performances in the Europe area turn out to be inferior to other DDK filters in the Amazon area. In particular, in the Amazon area, the DDK filters do not display better performances than most of the deterministic filtering schemes, e.g. the isotropic Gaussian filters with a low smoothing radius combined with the destriping filter. While in the regularization filter group, the parameter $\lambda = 4$ turns out to produce consistently better and reliable results over both two study areas. This filter choice shows better or comparable statistics with respect to the deterministic filters in both study areas.

In the deterministic filter group, we arrive at the same conclusion as King et al. (2006) that a smoothing radius around 500 km reaches best performance if only the isotropic Gaussian filter is applied. However, this is not true when combined with the destriping filter. The advantage of combining the destriping filter with the isotropic Gaussian filter is demonstrated in both study areas. It is highly recommended to use the Gaussian filter with a low smoothing radius, e.g. around 300 km, combined with the destriping filter, which produces consistent good results in both the Europe area and the Amazon area with respect to other deterministic filtering scenarios. The performance of the anisotropic Gaussian filter decreases with increasing smoothing radii. Besides, the anisotropic Gaussian filter only shows its better performance as opposed to the Gaussian filter at low smoothing radii. However, this point is not held when they are combined with the destriping filter. In view of the performance of all deterministic filters, the study concludes that the optimal filtering scheme in this filter group is the combination of the Gaussian filter of a low smoothing radius with the destriping filter.

Elastic loading induced displacements modeling Predicting displacements due to environmental loading is based on the well-established loading theory. The classic Green function approach can be applied at various scales. Within a limited spatial extent, the half-space approaches are applied as well in practice. To investigate the differences between different approaches, a high spatial resolution local load dataset from the lower Mississippi river area is used.

Firstly, two half-space approaches, i.e. the point load approach and the surface load approach, are investigated and compared. It is shown that the two half-space approaches are practically

equivalent using the local data. However, the point load approach is recommended for practical use in view of the computational efficiency.

Using the local load dataset, the difference between the global Green function approach and the half-space approach is analyzed. It is demonstrated that deformations estimated from the half-space approach agrees better with the observed displacements at the considered 11 GPS sites than these from the Green function approach. However, neither of them show satisfactory agreements with the observed displacements if only the local load data is considered. The reason for that is explained by deploying two global hydrological models, i.e. GLDAS and MERRA, which demonstrates strong effects of the global load beyond the study region. A reduction of the global environmental loading effects beforehand might be advantageous to probe the local geological structure using the half-space approach.

Moreover, the impacts of site-dependent Green functions are studied using the high spatial resolution load data . We use two types of site-dependent Green functions which were generated by modifying the local crustal structure in the REF Earth models using the CRUST 1.0 and CRUST 2.0 models. With respect to the SNREI-based Green functions, no significant absolute differences (less than 0.27 mm according to RMS of difference) are observed due to the limited local load. Nevertheless, big differences in terms of relative RMS are obtained, more than 25 % in the horizontal components and bigger than 5 % in the vertical component. In contrast to less than 2 % uncertainties due to the Green functions reported by Petrov and Boy (2004), we show that the site-dependent Green functions could contribute more uncertainties to the estimated displacements. The results shown in our study agrees well with Dill et al. (2015) who applied the grid-dependent Green functions using the global environmental loading models.

6.2 Outlook

THIS thesis has investigated and advanced three different aspects regarding the Earth's surface loading and its induced elastic displacements. Several remaining issues still exist and they require further investigations.

Alternative approaches for time variable seasonal signals modeling SSA, introduced in this thesis, has its own limitations in separating time variable seasonal signals, e.g. optimal choice of embedding window size M. Recently, a new data adaptive approach named singular spectrum decomposition (SSD), which takes its origin from SSA, was introduced by Bonizzi et al. (2014). SSD overcomes the limitation of SSA by automatically selecting the window size, which makes singular spectral analysis fully data-driven. The automatic analysis characteristic of SSD might make it possible for global scale GPS time series analysis, which is time-consuming using SSA.

In addition to SSD, another data adaptive approach named EMD (Empirical Mode Decomposition) is widely used in signal decomposition. Based on a sifting process, EMD decomposes the time series into several intrinsic mode function (IMF) with different time scales. In the climate field, EMD has shown its potentialities in separating the modulated annual cycle (Wu et al., 2008). Certainly, EMD will be a potential tool in extracting time variable geodetic seasonal signals.

In short, further studies on time variable season signals modeling will be continued using SSA as well as the above-mention SSD and EMD. Comparisons between different approaches will be interesting and each approach could serve as a validation tool for another.

Perspectives on comparing GPS and GRACE In our study, we have applied five types of commonly used filters to evaluate their performance when comparing with GPS. Several other filters exist and it might be worth implementing one thorough evaluation of all up-to-date filters.

In addition, the comparison between GPS and GRACE is normally conducted point-wise. As GRACE has its spatial resolution around 400 km, it might be interesting to apply PCA to a regional GPS network to extract common spatial signals from both GPS observed displacements and GRACE derived deformations and compare afterwards.

Perspectives on elastic displacements modeling As presented in Chapter 5, other crustal models based Green functions exist in the literature, e.g. grid-dependent Green functions from Dill et al. (2015). Further comparison involving different types of Green functions is required using the local load to further evaluate uncertainties due to Green functions. Besides, the comparison between different Green functions could also be extended to a global study using the environmental loading models or GRACE.

What's more, as discussed in Chapter 5, we have not implemented the empirical Green function approach proposed by Seitz and Krügel (2009), which provides us an alternative approach to investigate site-dependent Green functions. This work will be done in future. Likewise, evaluating the difference between this empirical Green function approach and the site-dependent or grid-dependent Green function approach will be worthy of trying in future.

Bibliography

Allen, M and Smith, L (1996). Monte Carlo SSA: detecting irregular oscillations in the presence of colored noise. *Journal of Climate*, **9**(12):3373–3404. doi:10.1175/1520-0442(1996)009<3373:MCSDIO>2.0.CO;2.

Allen, MR and Robertson, AW (1996). Distinguishing modulated oscillations from coloured noise in multivariate datasets. *Climate Dynamics*, **12**(11):775–784. doi:10.1007/s003820050142.

Alsdorf, DE, Rodrguez, E and Lettenmaier, DP (2007). Measuring surface water from space. *Rev Geophys*, **45**(2):RG2002. doi:10.1029/2006RG000197.

Altamimi, Z, Collilieux, X and Métivier, L (2011). ITRF2008: an improved solution of the international terrestrial reference frame. *Journal of Geodesy*, **85**(8):457–473. doi:10.1007/s00190-011-0444-4.

Amosu, A, Smalley, R and Puchakayala, J (2012). Modeling Earth deformation from the 2011 inundation in the Mississippi river basin using hydrologic and geodetic data. *AGU Fall Meeting Abstracts*, p. A891.

Argus, DF, Fu, Y and Landerer, FW (2014). Seasonal variation in total water storage in California inferred from GPS observations of vertical land motion. *Geophys Res Lett*, **41**:1971–1980. doi:10.1002/2014GL059570.

Arnoso, J, Bos, MS, Benavent, M, Penna, NT et al. (2013). OTL calculations for studying the elastic response of the upper crust in Gran Canaria (Canary Archipelago). In: *17th International Symposium on Earth Tides, Warsaw*.

Bassin, C, Laske, G and Masters, G (2000). The current limits of resolution for surface wave tomography in North America. *EOS*, **81**:F897.

Baur, O (2012). On the computation of mass-change trends from GRACE gravity field time-series. *Journal of Geodynamics*, **61**(0):120–128. doi:10.1016/j.jog.2012.03.007.

Baur, O, Kuhn, M and Featherstone, WE (2009). GRACE-derived ice-mass variations over Greenland by accounting for leakage effects. *J Geophys Res*, **114**(B6):B06,407. doi:10.1029/2008JB006239.

Becker, JM and Bevis, M (2004). Love's problem. *Geophysical Journal International*, **156**(2):171–178. doi:10.1111/j.1365-246X.2003.02150.x.

Belda, S, García-García, D and Ferrándiz, JM (2015). On the decorrelation filtering of RL05 GRACE data for global applications. *Geophysical Journal International*, **200**(1):173–184. doi:10.1093/gji/ggu386.

Bennett, RA (2008). Instantaneous deformation from continuous GPS: contributions from quasi-periodic loads. *Geophysical Journal International*, **174**(3):1052–1064. doi:10.1111/j.1365-246X.2008.03846.x.

Bettadpur, S (2012). *UTCSR Level-2 Processing Standards Document for Level-2 Product Release 0005*. Tech. Rep. GRACE 327-742, Center for Space Research (CSR), the University of Texas at Austin.

Beutler, G, Brockmann, E, Gurtner, W, Hugentobler, U et al. (1994a). Extended orbit modeling techniques at the CODE processing center of the international GPS service for geodynamics (IGS): theory and initial results. *Manuscr Geod*, **19**:367–386.

Beutler, G, Mueller, I and Neilan, R (1994b). The international GPS Service for Geodynamics: development and start of official service on 1 january 1994. *Bulltein of Geodesique*, **68**:39–70.

Bevis, M, Alsdorf, D, Kendrick, E, Fortes, LP et al. (2005). Seasonal fluctuations in the mass of the Amazon River system and Earth's elastic response. *Geophys Res Lett*, **32**(16):L16,308. doi:10.1029/2005GL023491.

Bevis, M, Kendrick, E, Cser, A and Smalley Jr., R (2004). Geodetic measurement of the local elastic response to the changing mass of water in Lago Laja, Chile. *Physics of the Earth and Planetary Interiors*, **141**(2):71–78. doi:10.1016/j.pepi.2003.05.001.

Bevis, M, Wahr, J, Khan, SA, Madsen, FB et al. (2012). Bedrock displacements in Greenland manifest ice mass variations, climate cycles and climate change. *Proceedings of the National Academy of Sciences*, **109**(30):11,944–11,948. doi:10.1073/pnas.1204664109.

Blewitt, G (1989). Carrier phase ambiguity resolution for the Global Positioning System applied to geodetic baselines up to 2000 km. *J Geophys Res*, **94**(B8):10,187–10,203. doi:10.1029/JB094iB08p10187.

——— (2003). Self-consistency in reference frames, geocenter definition, and surface loading of the solid Earth. *J Geophys Res*, **108**(B2):2103. doi:10.1029/2002JB002082.

——— (2007). GPS and space-based geodetic methods. *Treatise on Geophysics*, **3**:351–390.

Blewitt, G, Lavallée, D, Clarke, P and Nurutdinov, K (2001). A new global mode of Earth deformation: seasonal cycle detected. *Science*, **294**(5550):2342–2345. doi:10.1126/science.1065328.

Bonizzi, P, KAREL, JMH, MESTE, O and PEETERS, RLM (2014). Singular spectrum decomposition: a new method for time series decomposition. *Adv Adapt Data Anal*, p. 1450011. doi:10.1142/S1793536914500113.

Borsa, AA, Agnew, DC and Cayan, DR (2014). Ongoing drought-induced uplift in the western United States. *Science*, pp. 1587–1590. doi:10.1126/science.1260279.

Boussinesq, J (1885). Applications des Potentials a l' Equilibre et Mouvement des Solides Elastiques. p. 231.

Börgens, E and Eicker, A (2014). Comparison of the Gaussian and the DDK filter method for GRACE. In: *EGU General Assembly 2014, Vienna*.

Broomhead, D and King, GP (1986). Extracting qualitative dynamics from experimental data. *Physica D: Nonlinear Phenomena*, **20**(2-3):217–236. doi:10.1016/0167-2789(86)90031-X.

Cazenave, A and Chen, J (2010). Time-variable gravity from space and present-day mass redistribution in the Earth system. *Earth and Planetary Science Letters*, **298**(3-4):263–274. doi:10.1016/j.epsl.2010.07.035.

Chambers, DP (2006). Evaluation of new GRACE time-variable gravity data over the ocean. *Geophys Res Lett*, **33**(17):L17,603. doi:10.1029/2006GL027296.

Chambers, DP, Wahr, J and Nerem, RS (2004). Preliminary observations of global ocean mass variations with GRACE. *Geophys Res Lett*, **31**(13):L13,310. doi:10.1029/2004GL020461.

Chambers, DP and Willis, JK (2008). Analysis of large-scale ocean bottom pressure variability in the North Pacific. *J Geophys Res*, **113**(C11):C11,003. doi:10.1029/2008JC004930.

——— (2009). Low-frequency exchange of mass between ocean basins. *J Geophys Res*, **114**(C11):C11,008. doi:10.1029/2009JC005518.

Chanard, K, Avouac, JP, Ramillien, G and Genrich, J (2014). Modeling deformation induced by seasonal variations of continental water in the himalaya region: Sensitivity to earth elastic structure. *J Geophys Res Solid Earth*, **119**:5097–5113. doi:10.1002/2013JB010451.

Chen, JL, Tapley, B and Wilson, C (2006). Alaskan mountain glacial melting observed by satellite gravimetry. *Earth and Planetary Science Letters*, **248**(1-2):368–378. doi:10.1016/j.epsl.2006.05.039.

Chen, JL, Wilson, C, Famiglietti, J and Rodell, M (2007a). Attenuation effect on seasonal basin-scale water storage changes from GRACE time-variable gravity. *Journal of Geodesy*, **81**(4):237–245. doi:10.1007/s00190-006-0104-2.

Chen, JL, Wilson, CR, Blankenship, D and Tapley, BD (2009). Accelerated Antarctic ice loss from satellite gravity measurements. *Nature Geosci*, **2**(12):859–862. doi:10.1038/ngeo694.

Chen, JL, Wilson, CR and Tapley, BD (2010). The 2009 exceptional Amazon flood and interannual terrestrial water storage change observed by GRACE. *Water Resour Res*, **46**(12):W12,526. doi:10.1029/2010WR009383.

Chen, JL, Wilson, CR, Tapley, BD and Grand, S (2007b). GRACE detects coseismic and postseismic deformation from the Sumatra-Andaman earthquake. *Geophys Res Lett*, **34**(13):L13,302. doi:10.1029/2007GL030356.

Chen, Q, van Dam, T, Sneeuw, N, Collilieux, X et al. (2013). Singular spectrum analysis for modeling seasonal signals from GPS time series. *Journal of Geodynamics*, **72**(0):25–35. doi:10.1016/j.jog.2013.05.005.

Chen, Q, Weigelt, M, Sneeuw, N and van Dam, T (2015). On time-variable seasonal signals: Comparison of SSA and Kalman filtering based approach. In: *International Association of Geodesy Symposia*, vol. 142, pp. 1–6–. Springer Berlin Heidelberg. doi:10.1007/1345_2015_4.

Cheng, M, Ries, J and Tapley, B (2013). Geocenter variations from analysis of SLR data. In: Altamimi, Z and Collilieux, X, eds., *International Association of Geodesy Symposia*, vol. 138, pp. 19–25. Springer Berlin Heidelberg. doi:10.1007/978-3-642-32998-2_4.

Cheng, M, Ries, JC and Tapley, BD (2011). Variations of the Earth's figure axis from satellite laser ranging and GRACE. *J Geophys Res*, **116**(B1):B01,409. doi:10.1029/2010JB000850.

Chew, CC and Small, EE (2014). Terrestrial water storage response to the 2012 drought estimated from GPS vertical position anomalies. *Geophys Res Lett*, **41**:61456151. doi:10.1002/2014GL061206.

Collilieux, X, Métivier, L, Altamimi, Z, van Dam, T et al. (2011). Quality assessment of GPS reprocessed terrestrial reference frame. *GPS Solut*, **15**:219–231. doi:10.1007/s10291-010-0184-6.

Creutzfeldt, B, Ferré, T, Troch, P, Merz, B et al. (2012). Total water storage dynamics in response to climate variability and extremes: Inference from long-term terrestrial gravity measurement. *J Geophys Res*, **117**(D8):D08,112. doi:10.1029/2011JD016472.

Crowley, JW, Mitrovica, JX, Bailey, RC, Tamisiea, ME et al. (2006). Land water storage within the Congo Basin inferred from GRACE satellite gravity data. *Geophys Res Lett*, **33**(19):L19,402. doi:10.1029/2006GL027070.

Dach, R, Böhm, J, Lutz, S, Steigenberger, P et al. (2011). Evaluation of the impact of atmospheric pressure loading modeling on gnss data analysis. *Journal of Geodesy*, **85**(2):75–91. doi:10.1007/s00190-010-0417-z.

Dahle, C, Flechtner, F, Gruber, C, König, D et al. (2012). *GFZ GRACE Level-2 Processing Standards Document for Level-2 Product Release 0005*. Tech. Rep. Scientific Technical Report STR12/02 Data, Revised Edition, January 2013, Deutsches GeoForschungsZentrum GFZ. doi:10.2312/GFZ.b103-1202-25. GRACE 327-743.

——— (2014). GFZ RL05: An improved time-series of monthly GRACE gravity field solutions. In: Flechtner, F, Sneeuw, N and Schuh, WD, eds., *Advanced Technologies in Earth Sciences*, pp. 29–39.

van Dam, T, Altamimi, Z, Collilieux, X and Ray, J (2010). Topographically induced height errors in predicted atmospheric loading effects. *J Geophys Res*, **115**(B7):B07,415. doi:10.1029/2009JB006810.

van Dam, T, Collilieux, X, Wuite, J, Altamimi, Z et al. (2012). Nontidal ocean loading: amplitudes and potential effects in GPS height time series. *Journal of Geodesy*, **86**(11):1043–1057. doi:10.1007/

s00190-012-0564-5.

van Dam, T, Plag, H, Francis, O and Gegout, P (2003). GGFC Special Bureau for Loading: Current status and plans. In: *IERS Technical Note*, vol. 30, pp. 180–198.

van Dam, T, Wahr, J and Lavallée, D (2007). A comparison of annual vertical crustal displacements from GPS and Gravity Recovery and Climate Experiment (GRACE) over Europe. *J Geophys Res*, **112**:B03,404. doi:10.1029/2006JB004335.

van Dam, T, Wahr, J, Milly, PCD, Shmakin, AB et al. (2001). Crustal displacements due to continental water loading. *Geophys Res Lett*, **28**(4):651–654. doi:10.1029/2000GL012120.

van Dam, TM, Blewitt, G and Heflin, MB (1994). Atmospheric pressure loading effects on global positioning system coordinate determinations. *J Geophys Res*, **99**(B12):23,939–23,950. doi:10.1029/94JB02122.

van Dam, TM and Wahr, JM (1987). Displacements of the Earth's surface due to atmospheric loading: Effects on gravity and baseline measurements. *J Geophys Res*, **92**(B2):1281–1286. doi:10.1029/JB092iB02p01281.

Davis, JL, Elgered, G, Niell, AE and Kuehn, CE (1993). Ground-based measurement of gradients in the wet radio refractivity of air. *Radio Sci*, **28**(6):1003–1018. doi:10.1029/93RS01917.

Davis, JL, Elósegui, P, Mitrovica, JX and Tamisiea, ME (2004). Climate-driven deformation of the solid earth from GRACE and GPS. *Geophys Res Lett*, **31**(24):L24,605. doi:10.1029/2004GL021435.

Davis, JL, Tamisiea, ME, Elósegui, P, Mitrovica, JX et al. (2008). A statistical filtering approach for Gravity Recovery and Climate Experiment (GRACE) gravity data. *J Geophys Res*, **113**(B4):B04,410. doi:10.1029/2007JB005043.

Davis, JL, Wernicke, BP, Bisnath, S, Niemi, NA et al. (2006). Subcontinental-scale crustal velocity changes along the Pacific-North America plate boundary. *Nature*, **441**(7097):1131–1134. doi:10.1038/nature04781.

Davis, JL, Wernicke, BP and Tamisiea, ME (2012). On seasonal signals in geodetic time series. *J Geophys Res*, **117**(B1):B01,403. doi:10.1029/2011JB008690.

De Viron, O, Panet, I, Mikhailov, V, Van Camp, M et al. (2008). Retrieving earthquake signature in grace gravity solutions. *Geophysical Journal International*, **174**(1):14–20. doi:10.1111/j.1365-246X.2008.03807.x.

Devaraju, B (2015). *Understanding filtering on the sphere: Experiences from filtering GRACE data*. Ph.D. thesis, Institute of Geodesy, University of Stuttgart.

Devaraju, B, Lorenz, C, Tourian, MJ and Sneeuw, N (2012). On the cyclo-stationarity of the time-variable Kaula rule. In: *EGU General Assembly 2012, Vienna*.

Dill, R and Dobslaw, H (2013). Numerical simulations of global-scale high-resolution hydrological crustal deformations. *J Geophys Res*, **118**:5008–5017. doi:10.1002/jgrb.50353.

Dill, R, Klemann, V, Martinec, Z and Tesauro, M (2015). Applying local Green's functions to study the influence of the crustal structure on hydrological loading displacements. *Journal of Geodynamics*, **88**:14–22. doi:10.1016/j.jog.2015.04.005.

Döll, P, Kaspar, F and Lehner, B (2003). A global hydrological model for deriving water availability indicators: model tuning and validation. *Journal of Hydrology*, **270**(1-2):105–134. doi:10.1016/S0022-1694(02)00283-4.

Dong, D, Dickey, JO, Chao, Y and Cheng, MK (1997). Geocenter variations caused by atmosphere, ocean and surface ground water. *Geophys Res Lett*, **24**(15):1867–1870. doi:10.1029/97GL01849.

Dong, D, Fang, P, Bock, Y, Cheng, MK et al. (2002). Anatomy of apparent seasonal variations from GPS-derived site position time series. *J Geophys Res*, **107**(B4):2075. doi:10.1029/2001JB000573.

Dong, D, Fang, P, Bock, Y, Webb, F et al. (2006). Spatiotemporal filtering using principal component analysis and Karhunen-Loeve expansion approaches for regional GPS network analysis. *J Geophys Res*, **111**(B3):B03,405. doi:10.1029/2005JB003806.

Dow, J, Neilan, R and Rizos, C (2009). The international GNSS Service in a changing landscape of Global Navigation Satellite Systems. *Journal of Geodesy*, **83**(3-4):191–198. doi:10.1007/s00190-008-0300-3.

Duan, X, Guo, J, Shum, C and Wal, W (2009). On the postprocessing removal of correlated errors in GRACE temporal gravity field solutions. *Journal of Geodesy*, **83**(11):1095–1106. doi:10.1007/s00190-009-0327-0.

D'Urso, MG and Marmo, F (2013). On a generalized Love's problem. *Computers & Geosciences*, **61**(0):144–151. doi:10.1016/j.cageo.2013.09.002.

Dziewonski, A, Hales, A and Lapwood, E (1975). Parametrically simple earth models consistent with geophysical data. *Physics of the Earth and Planetary Interiors*, **10**(1):12–48. doi:10.1016/0031-9201(75)90017-5.

Dziewonski, AM and Anderson, DL (1981). Preliminary Reference Earth Model (PREM). **25**:297–356.

Eicker, A, Schumacher, M, Kusche, J, Döll, P et al. (2014). Calibration/data assimilation approach for integrating GRACE data into the WaterGAP Global Hydrology Model (WGHM) using an ensemble kalman filter: First results. *Surveys in Geophysics*, **35**(6):1285–1309. doi:10.1007/s10712-014-9309-8.

Elósegui, P, Davis, JL, Mitrovica, JX, Bennett, RA et al. (2003). Crustal loading near Great Salt Lake, Utah. *Geophys Res Lett*, **30**(3):1111–1114. doi:10.1029/2002GL016579.

Evans, AG, Swift, ER, Cunningham, JP, Hill, RW et al. (2002). The global positioning system geodesy odyssey. *Navigation*, **49**(1):7–33. doi:10.1002/j.2161-4296.2002.tb00252.x.

Farrell, WE (1972). Deformation of the Earth by surface loads. *Rev Geophys*, **10**(3):761–797.

Featherstone, W and Vaníek, P (1996). The usage of Stokes in the Possessive. **5**:153–154.

Flechtner, F, Dobslaw, H and Fagiolini, E (2014a). *AOD1B Product Description Document for Product Release 05*. Tech. rep., GFZ German Research Centre for Geosciences.

Flechtner, F, Morton, P, Watkins, M and Webb, F (2014b). Status of the GRACE Follow-on mission. In: Marti, U, ed., *Proceedings of the International Association of Geodesy Symposia Gravity, Geoid and Height System (GGHS2012)*, vol. 141, pp. 117–121. doi:10.1007/978-3-319-10837-7_15.

Forootan, E and Kusche, J (2012). Separation of global time-variable gravity signals into maximally independent components. *Journal of Geodesy*, **86**(7):477–497. doi:10.1007/s00190-011-0532-5.

Francis, O and Dehant, V (1987). Recomputation of the Green's functions for tidal loading estimations. *Marées terrestres*, (100):6962–6986.

Frappart, F, Ramillien, G, Leblanc, M, Tweed, SO et al. (2011). An independent component analysis filtering approach for estimating continental hydrology in the GRACE gravity data. *Remote Sensing of Environment*, **115**(1):187–204. doi:10.1016/j.rse.2010.08.017.

Freymueller, J (2009). Seasonal position variations and regional reference frame realization. In: Drewes, H, ed., *Geodetic Reference Frames*, *International Association of Geodesy Symposia*, vol. 134, pp. 191–196. Springer Berlin Heidelberg. doi:10.1007/978-3-642-00860-3_30.

Fu, Y, Argus, DF, Freymueller, JT and Heflin, MB (2013). Horizontal motion in elastic response to seasonal loading of rain water in the Amazon Basin and monsoon water in southeast Asia observed by GPS and inferred from GRACE. *Geophys Res Lett*, **40**:6048–6053. doi:10.1002/2013GL058093.

Fu, Y, Argus, DF and Landerer, FW (2014). GPS as an independent measurement to estimate terrestrial water storage variations in Washington and Oregon. *J Geophys Res Solid Earth*, **120**:B011,415. doi: 10.1002/2014JB011415.

Fu, Y, Freymueller, JT and Jensen, T (2012). Seasonal hydrological loading in southern Alaska observed by GPS and GRACE. *Geophys Res Lett*, **39**(15):L15,310. doi:10.1029/2012GL052453.

Galván, R, Gende, M and Brunini, C (2015). Regional model to estimate vertical deformations due to loading seasonal changes. In: *International Association of Geodesy Symposia*, pp. 1–10. Springer Berlin Heidelberg. doi:10.1007/1345_2015_101.

Gazeaux, J, Williams, S, King, M, Bos, M et al. (2013). Detecting offsets in GPS time series: first results from the detection of offsets in GPS experiment. *J Geophys Res Solid Earth*, **118**(5):2397–2407. doi: 10.1002/jgrb.50152.

Gegout, P (2013). Earth's elastic deformation: Reference and site-dependent Love numbers. In: *EGU General Assembly Conference Abstracts*, vol. 15, p. 4853.

Gegout, P, Böhm, J and Wijaya, D (2010). Practical numerical computation of Love numers and applications. *in WG1 and WG2 Workshop of COST Action ES0701, Vienna*.

Ghil, M, Allen, MR, Dettinger, MD, Ide, K et al. (2002). Advanced spectral methods for climatic time series. *Rev Geophys*, **40**(1):1003. doi:10.1029/2000RG000092.

Ghil, M and Taricco, C (1997). Advanced spectral analysis methods. In: Castagnoli, G and Provenzale, A, eds., *Past and Present Variability of Solar-Terrestrial System: Measurement, Data Analysis and Theoretical Models*, pp. 137–159.

Güntner, A (2008). Improvement of global hydrological models using grace data. *Surveys in Geophysics*, **29**(4-5):375–397. doi:10.1007/s10712-008-9038-y.

Golyandina, N, Nekrutkin, V and Zhigljavsky, A (2001). *Analysis of Time Series Structure: SSA and Related techniques*. 1st edn. CRC Press.

Golyandina, N and Zhigljavsky, A (2013). *Singular Spectrum Analysis for Time Series*. SpringerBriefs in Statistics. Springer Berlin / Heidelberg.

Greff-Lefftz, M and Legros, H (1997). Some remarks about the degree-one deformation of the Earth. *Geophys J Int*, **131**(3):699–723. doi:10.1111/j.1365-246X.1997.tb06607.x.

Gross, R, Beutler, G and Plag, HP (2009). Integrated scientific and societal user requirements and functional specifications for the GGOS. In: Plag, HP and Pearlman, M, eds., *Global Geodetic Observing System*, pp. 209–224. Springer Berlin Heidelberg. doi:10.1007/978-3-642-02687-4_7.

Guo, JY, Li, YB, Huang, Y, Deng, HT et al. (2004). Green's function of the deformation of the Earth as a result of atmospheric loading. *Geophys J Int*, **159**(1):53–68. doi:10.1111/j.1365-246X.2004.02410.x.

Hammond, WC (2005). The ghost of an earthquake. *Science*, **310**(5753):1440–1442. doi:10.1126/science.1121349.

Han, SC, Jekeli, C and Shum, CK (2004). Time-variable aliasing effects of ocean tides, atmosphere, and continental water mass on monthly mean GRACE gravity field. *J Geophys Res*, **109**(B4):B04,403. doi:10.1029/2003JB002501.

Han, SC, Sauber, J and Luthcke, S (2010). Regional gravity decrease after the 2010 Maule (Chile) earthquake indicates large-scale mass redistribution. *Geophys Res Lett*, **37**(23):L23,307. doi: 10.1029/2010GL045449.

Han, SC, Sauber, J and Riva, R (2011). Contribution of satellite gravimetry to understanding seismic source processes of the 2011 Tohoku-Oki earthquake. *Geophys Res Lett*, **38**(24):L24,312–. doi: 10.1029/2011GL049975.

Han, SC, Shum, CK, Bevis, M, Ji, C et al. (2006). Crustal dilatation observed by GRACE after the 2004 Sumatra-Andaman Earthquake. *Science*, **313**(5787):658–662. doi:10.1126/science.1128661.

Han, SC, Shum, CK, Jekeli, C, Kuo, CY et al. (2005). Non-isotropic filtering of GRACE temporal gravity for geophysical signal enhancement. *Geophys J Int*, **163**(1):18–25.

Harig, C and Simons, FJ (2012). Mapping Greenlands mass loss in space and time. *Proceedings of the National Academy of Sciences*, **109**(49):19,934–19,937. doi:10.1073/pnas.1206785109.

Heiskanen, WA and Moritz, H (1967). *Physical Geodesy*. San Francisco : W. H. Freeman (reprinted by TU Graz).

Heki, K (2001). Seasonal modulation of interseismic strain buildup in northeastern Japan driven by snow loads. *Science*, **293**(5527):89–92. doi:10.1126/science.1061056.

Herring, T (1999). Geodetic applications of GPS. *Proceedings of the IEEE*, **87**(1):92–110. doi:10.1109/5.736344.

Horwath, M and Dietrich, R (2009). Signal and error in mass change inferences from GRACE: the case of Antarctica. *Geophysical Journal International*, **177**(3):849–864. doi:10.1111/j.1365-246X.2009.04139.x.

Jekeli, C (1981). *Alternative methods to smooth the Earth's gravity field*. Tech. Rep. 327, Department of Geodetic Science and Surveying, The Ohio State University.

Kalnay, E, Kanamitsu, M, Kistler, R, Collins, W et al. (1996). The NCEP/NCAR 40-year reanalysis project. *Bull Amer Meteor Soc*, **77**(3):437–471. doi:10.1175/1520-0477(1996)077<0437:TNYRP>2.0.CO;2.

Kennett, BLN and Engdahl, ER (1991). Traveltimes for global earthquake location and phase identification. *Geophysical Journal International*, **105**(2):429–465. doi:10.1111/j.1365-246X.1991.tb06724.x.

Kennett, BLN, Engdahl, ER and Buland, R (1995). Constraints on seismic velocities in the Earth from traveltimes. *Geophysical Journal International*, **122**(1):108–124. doi:10.1111/j.1365-246X.1995.tb03540.x.

Khan, MAR and Poskitt, DS (2012). Moment tests for window length selection in singular spectrum analysis of short- and long-memory processes. *Journal of Time Series Analysis*, **34**:141–155. doi:10.1111/j.1467-9892.2012.00820.x.

Khan, SA, Wahr, J, Bevis, M, Velicogna, I et al. (2010). Spread of ice mass loss into northwest Greenland observed by GRACE and GPS. *Geophys Res Lett*, **37**(6):L06,501. doi:10.1029/2010GL042460.

King, M, Moore, P, Clarke, P and Lavallée, D (2006). Choice of optimal averaging radii for temporal GRACE gravity solutions, a comparison with GPS and satellite altimetry. *Geophys J Int*, **166**(1):1–11.

Klees, R, Revtova, EA, Gunter, BC, Ditmar, P et al. (2008). The design of an optimal filter for monthly GRACE gravity models. *Geophysical Journal International*, **175**(2):417–432. doi:10.1111/j.1365-246X.2008.03922.x.

Klees, R, Zapreeva, EA, Winsemius, HC and Savenije, HHG (2007). The bias in GRACE estimates of continental water storage variations. *Hydrol Earth Syst Sci*, **11**(4):1227–1241. doi:10.5194/hess-11-1227-2007.

Kleusberg, A (2009). *Satellite Navigation*. Lecture notes, Institute of Navigation, University of Stuttgart.

Koch, KR and Kusche, J (2002). Regularization of geopotential determination from satellite data by variance components. *Journal of Geodesy*, **76**(5):259–268. doi:10.1007/s00190-002-0245-x.

Kondrashov, D and Ghil, M (2006). Spatio-temporal filling of missing points in geophysical data sets. *Nonlinear Processes in Geophysics*, **13**(2):151–159. doi:10.5194/npg-13-151-2006.

Kurtenbach, E, Mayer-Gürr, T and Eicker, A (2009). Deriving daily snapshots of the Earth's gravity field from GRACE L1B data using Kalman filtering. *Geophys Res Lett*, **36**(17):L17,102. doi:10.1029/2009GL039564.

Kusche, J (2007). Approximate decorrelation and non-isotropic smoothing of time-variable GRACE-type gravity field models. *J Geodesy*, **81**(11):733–749.

——— (2010). Time-variable gravity field and global deformation of the Earth. In: *Handbook of Geomathematics*, pp. 253–268. Springer.

Kusche, J, Schmidt, R, Petrovic, S and Rietbroek, R (2009). Decorrelated GRACE time-variable gravity solutions by GFZ, and their validation using a hydrological model. *Journal of Geodesy*, **83**(10):903–913. doi:10.1007/s00190-009-0308-3.

Kustowski, B, Ekström, G and Dziewonski, AM (2008). Anisotropic shear-wave velocity structure of the Earth's mantle: A global model. *J Geophys Res*, **113**(B6):B06,306. doi:10.1029/2007JB005169.

Lambeck, K (1988). *Geophysical geodesy: the slow deformations of the Earth*. Clarendon Press.

Landerer, FW and Swenson, SC (2012). Accuracy of scaled grace terrestrial water storage estimates. *Water Resour Res*, **48**(4):W04,531. doi:10.1029/2011WR011453.

Langbein, J (2004). Noise in two-color electronic distance meter measurements revisited. *J Geophys Res*, **109**(B4):B04,406. doi:10.1029/2003JB002819.

Larson, KM, Bodin, P and Gomberg, J (2003). Using 1-hz GPS data to measure deformations caused by the Denali fault earthquake. *Science*, **300**(5624):1421–1424. doi:10.1126/science.1084531.

Larson, KM, Cervelli, P, Lisowski, M, Miklius, A et al. (2001). Volcano monitoring using the Global Positioning System: Filtering strategies. *J Geophys Res*, **106**(B9):19,453–19,464. doi:10.1029/2001JB000305.

Larson, KM, Freymueller, JT and Philipsen, S (1997). Global plate velocities from the Global Positioning System. *J Geophys Res*, **102**(B5):9961–9981. doi:10.1029/97JB00514.

Larson, KM and Small, EE (2013). Using GPS to study the terrestrial water cycle. *Eos Trans AGU*, **94**(52):505–506. doi:10.1002/2013EO520001.

Larson, KM, Small, EE, Gutmann, ED, Bilich, AL et al. (2008). Use of GPS receivers as a soil moisture network for water cycle studies. *Geophys Res Lett*, **35**(24):L24,405. doi:10.1029/2008GL036013.

Laske, G, Masters, G, Ma, Z and Pasyanos, M (2013). Update on CRUST1.0-A 1-degree global model of Earths crust. In: *EGU General Assembly Conference Abstracts*, vol. 15, p. 2658.

Latychev, K, Mitrovica, JX, Tromp, J, Tamisiea, ME et al. (2005). Glacial isostatic adjustment on 3-d Earth models: a finite-volume formulation. *Geophysical Journal International*, **161**(2):421–444. doi:10.1111/j.1365-246X.2005.02536.x.

Lemoine, JM, Bruinsma, S, Loyer, S, Biancale, R et al. (2007). Temporal gravity field models inferred from GRACE data. *Advances in Space Research*, **39**(10):1620–1629. doi:10.1016/j.asr.2007.03.062.

de Linage, C, Kim, H, Famiglietti, JS and Yu, JY (2013). Impact of Pacific and Atlantic sea surface temperatures on interannual and decadal variations of GRACE land water storage in tropical South America. *J Geophys Res Atmos*, **118**:10,811–10,829. doi:10.1002/jgrd.50820.

Lombard, A, Garcia, D, Ramillien, G, Cazenave, A et al. (2007). Estimation of steric sea level variations from combined GRACE and Jason-1 data. *Earth and Planetary Science Letters*, **254**(1-2):194–202. doi:10.1016/j.epsl.2006.11.035.

Long, D, Scanlon, BR, Longuevergne, L, Sun, AY et al. (2013). GRACE satellite monitoring of large depletion in water storage in response to the 2011 drought in Texas. *Geophys Res Lett*, **40**(13):3395–3401. doi:10.1002/grl.50655.

Longman, IM (1962). A Green's function for determining the deformation of the Earth under surface mass loads: 1. theory. *J Geophys Res*, **67**(2):845–850. doi:10.1029/JZ067i002p00845.

——— (1963). A Green's function for determining the deformation of the Earth under surface mass loads: 2. computations and numerical results. *J Geophys Res*, **68**(2):485–496. doi:10.1029/JZ068i002p00485.

Longuevergne, L, Scanlon, BR and Wilson, CR (2010). GRACE hydrological estimates for small basins: Evaluating processing approaches on the High Plains Aquifer, USA. *Water Resour Res*, **46**(11):W11,517. doi:10.1029/2009WR008564.

Lorenz, C (2009). *Applying stochastic constrains on time-variable GRACE data*. Master's thesis, Institude of Geodesy, University of Stuttgart.

Lorenz, C, Kunstmann, H, Devaraju, B, Tourian, MJ et al. (2014). Large-scale runoff from landmasses: A global assessment of the closure of the hydrological and atmospheric water balances. *J Hydrometeor*, **15**(6):2111–2139. doi:10.1175/JHM-D-13-0157.1.

Love, AEH (1909). The yielding of the Earth to disturbing forces. *Proceedings of the Royal Society of London Series A, Containing Papers of a Mathematical and Physical Character*, **82**(551):73–88.

——— (1929). The stress produced in a semi-infinite solid by pressure on part of the boundary. *Philosophical Transactions of the Royal Society of London Series A, Containing Papers of a Mathematical or Physical Character*, **228**:377–420.

Lyard, F, Lefevre, F, Letellier, T and Francis, O (2006). Modelling the global ocean tides: modern insights from FES2004. *Ocean Dynamics*, **56**(5-6):394–415. doi:10.1007/s10236-006-0086-x.

Mao, A, Harrison, CGA and Dixon, TH (1999). Noise in GPS coordinate time series. *J Geophys Res*, **104**(B2):2797–2816. doi:10.1029/1998JB900033.

Marques, C, Ferreira, J, Rocha, A, Castanheira, J et al. (2006). Singular spectrum analysis and forecasting of hydrological time series. *Physics and Chemistry of the Earth, Parts A/B/C*, **31**(18):1172–1179. doi:10.1016/j.pce.2006.02.061.

Matsuo, K and Heki, K (2010). Time-variable ice loss in Asian high mountains from satellite gravimetry. *Earth and Planetary Science Letters*, **290**(1-2):30–36. doi:10.1016/j.epsl.2009.11.053.

McCarthy, DD (1996). IERS conventions (1996). *IERS Technical Note*, **21**:1–95.

Memin, A, Rogister, Y, Hinderer, J, Llubes, M et al. (2009). Ground deformation and gravity variations modelled from present-day ice thinning in the vicinity of glaciers. *Journal of Geodynamics*, **48**(3-5):195–203. doi:10.1016/j.jog.2009.09.006.

Miranda, A, Le Borgne, YA and Bontempi, G (2008). New routes from minimal approximation error to principal components. *Neural Processing Letters*, **27**(3):197–207. doi:10.1007/s11063-007-9069-2.

Montagner, JP and Kennett, BLN (1996). How to reconcile body-wave and normal-mode reference earth models. *Geophysical Journal International*, **125**(1):229–248. doi:10.1111/j.1365-246X.1996.tb06548.x.

Métivier, L, Greff-Lefftz, M and Diament, M (2005). A new approach to computing accurate gravity time variations for a realistic Earth model with lateral heterogeneities. *Geophysical Journal International*, **162**(2):570–574. doi:10.1111/j.1365-246X.2005.02692.x.

Munekane, H (2007). Ocean mass variations from GRACE and tsunami gauges. *J Geophys Res*, **112**(B7):B07,403. doi:10.1029/2006JB004618.

Munk, W and MacDonald, G (1960). *The Rotation of the Earth: A Geophysical Discussion*. Cambridge University Press.

Nahmani, S, Bock, O, Bouin, MN, Santamara-Gmez, A et al. (2012). Hydrological deformation induced by the west African monsoon: Comparison of GPS, GRACE and loading models. *J Geophys Res*,

117(B5):B05,409. doi:10.1029/2011JB009102.

Nash, J and Sutcliffe, J (1970). River flow forecasting through conceptual models part I – a discussion of principles. *Journal of Hydrology*, **10**(3):282–290. doi:10.1016/0022-1694(70)90255-6.

Nielsen, K, Khan, SA, Spada, G, Wahr, J et al. (2013). Vertical and horizontal surface displacements near Jakobshavn Isbrae driven by melt-induced and dynamic ice loss. *J Geophys Res Solid Earth*, **118**:1–8. doi:10.1002/jgrb.50145.

Nikolaidis, R (2002). *Observation of Geodetic and Seismic Deformation with the Global Positioning System*. Ph.D. thesis, University of California.

Nikolaidis, RM, Bock, Y, de Jonge, PJ, Shearer, P et al. (2001). Seismic wave observations with the Global Positioning System. *J Geophys Res*, **106**(B10):21,897–21,916. doi:10.1029/2001JB000329.

Nordman, M, Mäkinen, J, Virtanen, H, Johansson, JM et al. (2009). Crustal loading in vertical GPS time series in Fennoscandia. *Journal of Geodynamics*, **48**(3-5):144–150. doi:10.1016/j.jog.2009.09.003.

Paulson, A, Zhong, S and Wahr, J (2007). Limitations on the inversion for mantle viscosity from post-glacial rebound. *Geophysical Journal International*, **168**(3):1195–1209. doi:10.1111/j.1365-246X.2006.03222.x.

Penna, NT, King, MA and Stewart, MP (2007). GPS height time series: Short-period origins of spurious long-period signals. *J Geophys Res*, **112**(B2):B02,402. doi:10.1029/2005JB004047.

Petit, G and Luzum, B (2010). IERS Conventions. (IERS Technical Note 36):179.

Petrov, L and Boy, JP (2004). Study of the atmospheric pressure loading signal in very long baseline interferometry observations. *J Geophys Res*, **109**(B3):B03,405. doi:10.1029/2003JB002500.

Phillips, T, Nerem, RS, Fox-Kemper, B, Famiglietti, JS et al. (2012). The influence of ENSO on global terrestrial water storage using GRACE. *Geophys Res Lett*, **39**(16):L16,705. doi:10.1029/2012GL052495.

Pinel, V, Sigmundsson, F, Sturkell, E, Geirsson, H et al. (2007). Discriminating volcano deformation due to magma movements and variable surface loads: application to Katla subglacial volcano, Iceland. *Geophysical Journal International*, **169**(1):325–338. doi:10.1111/j.1365-246X.2006.03267.x.

Plag, HP, Jüttner, HU and Rautenberg, V (1996). On the possibilty of global and regional inversion of exogenic deformations for mechanical properties of the Earth's interior. *Journal of Geodynamics*, **21**(3):287–308. doi:10.1016/0264-3707(95)00034-8.

Plaut, G and Vautard, R (1994). Spells of low-frequency oscillations and weather regimes in the northern hemisphere. *J Atmos Sci*, **51**(2):210–236. doi:10.1175/1520-0469(1994)051<0210:SOLFOA>2.0.CO;2.

Rangelova, E, Sideris, M and Kim, J (2012). On the capabilities of the multi-channel singular spectrum method for extracting the main periodic and non-periodic variability from weekly GRACE data. *Journal of Geodynamics*, **54**(0):64–78. doi:10.1016/j.jog.2011.10.006.

Rangelova, E, van der Wal, W, Braun, A, Sideris, MG et al. (2007). Analysis of Gravity Recovery and Climate Experiment time-variable mass redistribution signals over North America by means of principal component analysis. *J Geophys Res*, **112**(F3):F03,002. doi:10.1029/2006JF000615.

Rast, M, Johannessen, J and Mauser, W (2014). Review of understanding of Earths hydrological cycle: Observations, theory and modelling. *Surveys in Geophysics*, **35**:491–513. doi:10.1007/s10712-014-9279-x.

Reichle, RH, Koster, RD, De Lannoy, GJM, Forman, BA et al. (2011). Assessment and enhancement of MERRA land surface hydrology estimates. **24**(24):6322–6338. doi:10.1175/JCLI-D-10-05033.1.

Riegger, J, Tourian, M, Devaraju, B and Sneeuw, N (2012). Analysis of grace uncertainties by hydrological and hydro-meteorological observations. *Journal of Geodynamics*, **59-60**(0):16–27. doi:

10.1016/j.jog.2012.02.001.

Rietbroek, R (2014). *Retrieval of Sea Level and Surface Loading Variations from Geodetic Observations and Model Simulations: an Integrated Approach*. Ph.D. thesis, Institute of Geodesy and Geoinformation, University of Bonn.

Rietbroek, R, Fritsche, M, Brunnabend, SE, Daras, I et al. (2012). Global surface mass from a new combination of GRACE, modelled OBP and reprocessed GPS data. *Journal of Geodynamics*, **59-60**(0):64–71. doi:10.1016/j.jog.2011.02.003.

Rietbroek, R, Fritsche, M, Dahle, C, Brunnabend, SE et al. (2014). Can GPS-derived surface loading bridge a GRACE mission gap? *Surveys in Geophysics*, **35**(6):1–17. doi:10.1007/s10712-013-9276-5.

Rodell, M, Chen, J, Kato, H, Famiglietti, J et al. (2007). Estimating groundwater storage changes in the Mississippi river basin (USA) using GRACE. *Hydrogeology Journal*, **15**(1):159–166–. doi:10.1007/s10040-006-0103-7.

Rodell, M, Houser, PR, Jambor, U, Gottschalck, J et al. (2004). The global land data assimilation system. *Bull Amer Meteor Soc*, **85**(3):381–394. doi:10.1175/BAMS-85-3-381.

Rodell, M, Velicogna, I and Famiglietti, JS (2009). Satellite-based estimates of groundwater depletion in India. *Nature*, **460**(7258):999–1002. doi:10.1038/nature08238.

Rowlands, DD, Luthcke, SB, Klosko, SM, Lemoine, FGR et al. (2005). Resolving mass flux at high spatial and temporal resolution using GRACE intersatellite measurements. *Geophys Res Lett*, **32**(4):L04,310–. doi:10.1029/2004GL021908.

Sasgen, I, Martinec, Z and Fleming, K (2006). Wiener optimal filtering of GRACE data. *Studia Geophysica et Geodaetica*, **50**(4):499–508. doi:10.1007/s11200-006-0031-y.

Scheller, M (2012). *Bestimmung hydrologischer Massenvariationen aus GRACE Daten am Beispiel sibirischer Flusssysteme*. Ph.D. thesis, Institute of Planetary Geodesy, Technical Unversity of Dresden.

Schmidt, R, Flechtner, F, Meyer, U, Neumayer, KH et al. (2008a). Hydrological signals observed by the GRACE satellites. *Surveys in Geophysics*, **29**(4-5):319–334. doi:10.1007/s10712-008-9033-3.

Schmidt, R, Petrovic, S, Güntner, A, Barthelmes, F et al. (2008b). Periodic components of water storage changes from GRACE and global hydrology models. *J Geophys Res*, **113**(B8):B08,419. doi:10.1029/2007JB005363.

Schoellhamer, DH (2001). Singular spectrum analysis for time series with missing data. *Geophys Res Lett*, **28**(16):3187–3190. doi:10.1029/2000GL012698.

Schrama, EJO, Wouters, B and Lavallée, DA (2007). Signal and noise in Gravity Recovery and Climate Experiment (GRACE) observed surface mass variations. *J Geophys Res*, **112**(B8):B08,407. doi:10.1029/2006JB004882.

Seitz, F and Krügel, M (2009). Inverse model approach for vertical load deformations in consideration of crustal inhomogeneities. In: Drewes, H, ed., *International Association of Geodesy Symposia*, vol. 134, pp. 23–29. doi:10.1007/978-3-642-00860-3_4.

Seitz, F, Schmidt, M and Shum, C (2008). Signals of extreme weather conditions in Central Europe in GRACE 4-D hydrological mass variations. *Earth and Planetary Science Letters*, **268**(1-2):165–170. doi:10.1016/j.epsl.2008.01.001.

Sheard, B, Heinzel, G, Danzmann, K, Shaddock, D et al. (2012). Intersatellite laser ranging instrument for the GRACE follow-on mission. *Journal of Geodesy*, **86**(12):1083–1095. doi:10.1007/s00190-012-0566-3.

Shida, T and Matsuyama, M (1912). Change of the plumb line referred to the axis of the Earth as found from the results of the internazional latitude observations. *Memoirs of the College of Science and*

Engineering, **4**:277–284.

Singh, S and Ben-Menahem, A (1968). On the summation of certain Legendre series. *Journal of Engineering Mathematics*, **2**(3):275–282. doi:10.1007/BF01535777.

Smalley, R, Ellis, MA, Paul, J and Van Arsdale, RB (2005). Space geodetic evidence for rapid strain rates in the New Madrid seismic zone of central USA. *Nature*, **435**(7045):1088–1090. doi:10.1038/nature03642.

Sánchez, L, Seemüller, W, Drewes, H, Mateo, L et al. (2013). Long-term stability of the SIRGAS reference frame and episodic station movements caused by the seismic activity in the SIRGAS region. In: Altamimi, Z and Collilieux, X, eds., *International Association of Geodesy Symposia*, vol. 138, pp. 153–161. Springer Berlin Heidelberg. doi:10.1007/978-3-642-32998-2_24.

Sánchez, L and Seitz, M (2011). *Recent activities of the IGS Regional Network Associate Analysis Centre for SIRGAS (IGS RNAAC SIR)*. Tech. Rep. 87, Deutsches Geodätisches Forschungsinstitut.

Sneeuw, N (1994). Global spherical harmonic analysis by least-squares and numerical quadrature methods in historical perspective. *Geophysical Journal International*, **118**(3):707–716. doi:10.1111/j.1365-246X.1994.tb03995.x.

——— (2006). *Physical Geodesy*. Lecture notes, Institute of Geodesy, University of Stuttgart.

Sneeuw, N, Flury, J and Rummel, R (2005). Science requirements on future missions and simulated mission scenarios. In: Flury, J and Rummel, R, eds., *Future Satellite Gravimetry and Earth Dynamics*, pp. 113–142–. Springer New York. doi:10.1007/0-387-33185-9_10.

Sneeuw, N, Lorenz, C, Devaraju, B, Tourian, M et al. (2014). Estimating runoff using hydro-geodetic approaches. *Surveys in Geophysics*, pp. 1–27. doi:10.1007/s10712-014-9300-4.

Spratt, RS (1982). Modelling the effect of atmospheric pressure variations on gravity. *Geophysical Journal International*, **71**(1):173–186. doi:10.1111/j.1365-246X.1982.tb04991.x.

Steckler, MS, Nooner, SL, Akhter, SH, Chowdhury, SK et al. (2010). Modeling Earth deformation from monsoonal flooding in Bangladesh using hydrographic, GPS, and Gravity Recovery and Climate Experiment (GRACE) data. *J Geophys Res*, **115**(B8):B08,407. doi:10.1029/2009JB007018.

Steffen, H, Wu, P and Wang, H (2010). Determination of the Earth's structure in Fennoscandia from GRACE and implications for the optimal post-processing of GRACE data. *Geophysical Journal International*, **182**(3):1295–1310. doi:10.1111/j.1365-246X.2010.04718.x.

Swenson, S, Chambers, D and Wahr, J (2008). Estimating geocenter variations from a combination of GRACE and ocean model output. *J Geophys Res*. doi:10.1029/2007JB005338.

Swenson, S and Wahr, J (2002). Methods for inferring regional surface-mass anomalies from Gravity Recovery and Climate Experiment (GRACE) measurements of time-variable gravity. *J Geophys Res*, **107**(B9):B9, 2193. doi:10.1029/2001JB000576.

——— (2006). Post-processing removal of correlated errors in GRACE data. *Geophys Res Lett*, **33**:L08,402. doi:10.1029/2005GL025285.

Swenson, SC and Wahr, JM (2011). Estimating signal loss in regularized GRACE gravity field solutions. *Geophysical Journal International*, **185**(2):693–702. doi:10.1111/j.1365-246X.2011.04977.x.

Syed, TH, Famiglietti, JS, Chen, J, Rodell, M et al. (2005). Total basin discharge for the Amazon and Mississippi river basins from GRACE and a land-atmosphere water balance. *Geophys Res Lett*, **32**(24):L24,404. doi:10.1029/2005GL024851.

Tamisiea, ME, Leuliette, EW, Davis, JL and Mitrovica, JX (2005). Constraining hydrological and cryospheric mass flux in southeastern Alaska using space-based gravity measurements. *Geophys Res Lett*, **32**(20):L20,501. doi:10.1029/2005GL023961.

Tamisiea, ME, Mitrovica, JX and Davis, JL (2007). GRACE gravity data constrain ancient ice geometries and continental dynamics over Laurentia. *Science*, **316**(5826):881–883. doi:10.1126/science.1137157.

Tapley, B, Ries, J, Bettadpur, S, Chambers, D et al. (2005). GGM02 - an improved earth gravity field model from GRACE. *Journal of Geodesy*, **79**(8):467–478. doi:10.1007/s00190-005-0480-z.

Tapley, BD, Bettadpur, S, Ries, JC, Thompson, PF et al. (2004). GRACE Measurements of Mass Variability in the Earth System. *Science*, **305**(5683):503–505.

Tesauro, M, Audet, P, Kaban, MK, Bürgmann, R et al. (2012). The effective elastic thickness of the continental lithosphere: Comparison between rheological and inverse approaches. *Geochem Geophys Geosyst*, **13**(9):Q09,001. doi:10.1029/2012GC004162.

Tesmer, V, Steigenberger, P, van Dam, T and Mayer-Gürr, T (2011). Vertical deformations from homogeneously processed GRACE and global GPS long-term series. *J Geodesy*, **85**(5):291–310.

Tesmer, V, Steigenberger, P, Rothacher, M, Boehm, J et al. (2009). Annual deformation signals from homogeneously reprocessed VLBI and GPS height time series. *Journal of Geodesy*, **83**:973–988. doi:10.1007/s00190-009-0316-3.

Thomas, AC, Reager, JT, Famiglietti, JS and Rodell, M (2014). A GRACE-based water storage deficit approach for hydrological drought characterization. *Geophys Res Lett*, **41**:1537–1545. doi:10.1002/2014GL059323.

Tourian, M, Elmi, O, Chen, Q, Devaraju, B et al. (2015). A spaceborne multisensor approach to monitor the desiccation of Lake Urmia in Iran. *Remote Sensing of Environment*, **156**(0):349–360. doi:10.1016/j.rse.2014.10.006.

Tralli, D and Lichten, S (1990). Stochastic estimation of tropospheric path delays in global positioning system geodetic measurements. **64**(2):127–159. doi:10.1007/BF02520642.

Tregoning, P, Watson, C, Ramillien, G, McQueen, H et al. (2009). Detecting hydrologic deformation using GRACE and GPS. *Geophys Res Lett*. doi:10.1029/2009GL038718.

Trupin, AS, Meier, MF and Wahr, JM (1992). Effect of melting glaciers on the Earth's rotation and gravitational field: 1965-1984. *Geophysical Journal International*, **108**(1):1–15. doi:10.1111/j.1365-246X.1992.tb00835.x.

Vautard, R and Ghil, M (1989). Singular spectrum analysis in nonlinear dynamics, with applications to paleoclimatic time series. *Physica D: Nonlinear Phenomena*, **35**(3):395–424. doi:10.1016/0167-2789(89)90077-8.

Vautard, R, Yiou, P and Ghil, M (1992). Singular-spectrum analysis: A toolkit for short, noisy chaotic signals. *Physica D: Nonlinear Phenomena*, **58**(1-4):95–126. doi:10.1016/0167-2789(92)90103-T.

Velicogna, I and Wahr, J (2006a). Acceleration of Greenland ice mass loss in spring 2004. *Nature*, **443**(7109):329–331. doi:10.1038/nature05168.

——— (2006b). Measurements of time-variable gravity show mass loss in Antarctica. *Science*, **311**(5768):1754–1756. doi:10.1126/science.1123785.

Wahr, J, van Dam, T, Larson, K and Francis, O (2001). GPS measurements of vertical crustal motion in Greenland. *J Geophys Res*, **106**(D24):33,755–33,759. doi:10.1029/2001JD900154.

Wahr, J, Khan, SA, van Dam, T, Liu, L et al. (2013). The use of GPS horizontals for loading studies, with applications to northern California and southeast Greenland. *J Geophys Res: Solid Earth*. doi:10.1002/jgrb.50104.

Wahr, J, Molenaar, M and Bryan, F (1998). Time variability of the Earth's gravity field: Hydrological and oceanic effects and their possible detection using GRACE. *J Geophys Res*, **103**(B12):30,205–30,229.

Wahr, J, Swenson, S and Velicogna, I (2006). Accuracy of GRACE mass estimates. *Geophys Res Lett*, **33**(6):L06,401. doi:10.1029/2005GL025305.

——— (2007). Some hydrological and cryospheric applications of GRACE. In: *GRACE Science Team Meeting and DFG SPP1257 Symposium*.

van der Wal, W (2009). *Contributions of Space Gravimetry to Postglacial Rebound Modeling with Different Rheologies*. Ph.D. thesis, Department of Geomatics Engineering, Unversity of Calgary.

Wang, H, Xiang, L, Jia, L, Jiang, L et al. (2012). Load Love numbers and Green's functions for elastic Earth models PREM, iasp91, ak135, and modified models with refined crustal structure from Crust 2.0. *Computers & Geosciences*, **49**(0):190–199. doi:10.1016/j.cageo.2012.06.022.

Wang, L, van Dam, T, Weigelt, M, Chen, Q et al. (2013). An inversion approach for determining water storage changes from 3-D GPS coordinates time series in Europe. In: *IAG Scientific Assembly, Potsdam*.

Wang, R and Wang, H (2007). A fast converging and anti-aliasing algorithm for Green's functions in terms of spherical or cylindrical harmonics. *Geophysical Journal International*, **170**(1):239–248. doi:10.1111/j.1365-246X.2007.03385.x.

Watkins, M and Yuan, DY (2012). *JPL Level-2 Processing Standards Document for Level-2 Product Release 05*. Tech. Rep. GRACE 327-744, Jet Propulsion Laboratory, Pasadena.

Werth, S, Güntner, A, Schmidt, R and Kusche, J (2009). Evaluation of GRACE filter tools from a hydrological perspective. *Geophysical Journal International*, **179**(3):1499–1515.

Williams, SDP (2003a). The effect of coloured noise on the uncertainties of rates estimated from geodetic time series. *Journal of Geodesy*, **76**(9):483–494. doi:10.1007/s00190-002-0283-4.

——— (2003b). Offsets in Global Positioning System time series. *J Geophys Res*, **108**(B6):2310. doi:10.1029/2002JB002156.

Williams, SDP and Penna, NT (2011). Non-tidal ocean loading effects on geodetic GPS heights. *Geophys Res Lett*, **38**(9):L09,314. doi:10.1029/2011GL046940.

Willis, JK, Chambers, DP and Nerem, RS (2008). Assessing the globally averaged sea level budget on seasonal to interannual timescales. *J Geophys Res*, **113**(C6):C06,015. doi:10.1029/2007JC004517.

Winch, D and Roberts, P (1995). Derivatives of addition theorems for Legendre functions. *The Journal of the Australian Mathematical Society Series B Applied Mathematics*, **37**:212–234. doi:10.1017/S0334270000007670.

Wouters, B, Bonin, JA, Chambers, DP, Riva, REM et al. (2014). GRACE, time-varying gravity, earth system dynamics and climate change. *Reports on Progress in Physics*, **77**(11):116,801. doi:10.1088/0034-4885/77/11/116801.

Wu, X, Ray, J and van Dam, T (2012). Geocenter motion and its geodetic and geophysical implications. *Journal of Geodynamics*, **58**(0):44–61. doi:10.1016/j.jog.2012.01.007.

Wu, Z, Schneider, E, Kirtman, B, Sarachik, E et al. (2008). The modulated annual cycle: an alternative reference frame for climate anomalies. *Climate Dynamics*, **31**(7-8):823–841. doi:10.1007/s00382-008-0437-z.

Zhang, J, Bock, Y, Johnson, H, Fang, P et al. (1997). Southern California permanent GPS geodetic array: Error analysis of daily position estimates and site velocities. *J Geophys Res*, **102**(B8):18,035–18,055. doi:10.1029/97JB01380.

Zhang, Z, Chao, B, Chen, J and Wilson, C (2015). Terrestrial water storage anomalies of Yangtze river basin droughts observed by GRACE and connections with ENSO. *Global and Planetary Change*, **126**(0):35–45. doi:10.1016/j.gloplacha.2015.01.002.

Zhang, ZZ, Chao, BF, Lu, Y and Hsu, HT (2009). An effective filtering for GRACE time-variable gravity: Fan filter. *Geophys Res Lett*, **36**(17):L17,311. doi:10.1029/2009GL039459.

Zhao, W, Amelung, F, Dixon, TH, Wdowinski, S et al. (2014). A method for estimating ice mass loss from relative InSAR observations: Application to the Vatnajökull ice cap, Iceland. *Geochem Geophys Geosyst*, **15**(1):108–120. doi:10.1002/2013GC004936.

Zou, R, Freymueller, JT, Ding, K, Yang, S et al. (2013). Evaluating seasonal loading models and their impact on global and regional reference frame alignment. *J Geophys Res Solid Earth*, **119**:1337–1358. doi:10.1002/2013JB010186.

Appendix A

Practical steps for computing total water storage changes from GRACE

THIS appendix presents the practical steps to compute total water storage (TWS) changes which are applied in this thesis.

- The GRACE level 2 products which are presented in the fully normalized gravity spherical harmonic coefficients can be downloaded from ICGEM (International Centre for Global Earth Models, GFZ) or PODAAC (Physical Oceanography Distributed Active Archive Center, NASA). In this thesis, the GRACE GSM RL05a solution from GFZ (Dahle et al., 2014) are mostly used.
- The degree-1 coefficients which are provided by Swenson et al. (2008) are added back to the GRACE GSM products. This step is especially important when EWH are further convolved in the spatial domain to compute the surface displacements in order to compare with the ground-fixed measurements. The data can be downloaded from GRACE Tellus.
- The zonal degree 2 coefficients C_{20} are replaced by the SLR-derived solutions (Cheng et al., 2011), which can be accessed via GRACE Tellus.
- The static gravity part should be removed so as to obtain the time variable gravity part, which can be done by removing a long-term mean of each coefficient or other static fields. In this thesis, a long-term mean is calculated from 2005 to 2010 based on the reasons that: 1) the GRACE data during this period is continuous; 2) the cyclostationary characteristic of the GRACE signal requires the mean field to be calculated within integer years (Sneeuw et al., 2014).
- Filtering GRACE data is required because higher degree coefficients are highly contaminated by correlated noise. The filters described in Chapter 4 are normally applied.
- The last step is to compute the TWS changes in terms of the surface mass density changes using Eq. (2.17), which can be further represented in equivalent water height (EWH) by dividing the water density.

Appendix B

Convolution in the spectral domain for horizontal components

THE detailed derivation for the vertical component has been shown in Section 2.2.3. Here we complement Section 2.2.3 by adding the complete derivations for the horizontal components.

In the light of Winch and Roberts (1995), the derivatives of the addition theorem with respect to P can be formulated as Eq. (B.1a) and Eq. (B.1b)

$$\frac{\partial \bar{P}_n(\cos\psi_{PQ})}{\partial \psi_{PQ}}\cos\alpha = \frac{1}{2n+1}\sum_{m=0}^{n}\frac{\partial \bar{P}_{nm}(\cos\theta_P)}{\partial\theta_P}\bar{P}_{nm}(\cos\theta_Q)\cos m(\lambda_P-\lambda_Q)\,, \tag{B.1a}$$

$$\frac{\partial \bar{P}_n(\cos\psi_{PQ})}{\partial \psi_{PQ}}\sin\alpha = \frac{1}{2n+1}\sum_{m=1}^{n}\frac{m}{\sin\theta_P}\bar{P}_{nm}(\cos\theta_P)\bar{P}_{nm}(\cos\theta_Q)\sin m(\lambda_P-\lambda_Q)\,. \tag{B.1b}$$

Similarly, applying Eq. (B.1b) together with Eq. (2.23b) to Eq. (2.29b), we derive step by step

$$\begin{aligned}
d_e(\theta_P,\lambda_P) &= -\frac{R^3}{M}\iint \sin\alpha\cdot\Delta\sigma(\theta_Q,\lambda_Q)\frac{1}{2n+1}\sum_{n=1}^{\infty}l'_n\frac{\partial\bar{P}_n(\cos\psi_{PQ})}{\partial\psi_{PQ}}d\Omega\\
&= -\frac{R^3}{M}\sum_{n=1}^{\infty}\frac{l'_n}{2n+1}\iint\Delta\sigma(\theta_Q,\lambda_Q)\sum_{m=1}^{n}\frac{m}{\sin\theta_P}\bar{P}_{nm}(\cos\theta_P)\bar{P}_{nm}(\cos\theta_Q)\\
&\cdot(\sin m\lambda_P\cos m\lambda_Q-\cos m\lambda_P\sin m\lambda_Q)d\Omega\\
&= -\frac{4\pi R^4\rho_w}{M}\sum_{n=1}^{\infty}\frac{l'_n}{2n+1}\sum_{m=1}^{n}\frac{m\bar{P}_{nm}(\cos\theta_P)}{\sin\theta_P}\Big(\frac{\sin m\lambda_P}{4\pi a\rho_w}\iint\Delta\sigma(\theta_Q,\lambda_Q)\\
&\cdot\bar{P}_{nm}(\cos\theta_Q)\cos m\lambda_Q-\frac{\cos m\lambda_P}{4\pi a\rho_w}\iint\Delta\sigma(\theta_Q,\lambda_Q)\bar{P}_{nm}(\cos\theta_Q)\sin m\lambda_Q\Big)d\Omega\\
&= -\frac{3a\rho_w}{\rho_e}\sum_{n=1}^{\infty}\frac{l'_n}{2n+1}\sum_{m=1}^{n}\frac{m\bar{P}_{nm}(\cos\theta_P)}{\sin\theta_P}(\sin m\lambda_P\Delta C^{\sigma}_{nm}-\cos m\lambda_P\Delta S^{\sigma}_{nm})\,,
\end{aligned} \tag{B.2}$$

and apply Eq. (2.16), we eventually obtain the spherical harmonics approach for the East component, see Eq. (B.3),

$$d_e(\theta_P,\lambda_P) = \frac{R}{\sin\theta}\sum_{n=1}^{\infty}\frac{l'_n}{1+k'_n}\sum_{m=0}^{n}\bar{P}_{nm}(\cos\theta_P)m(-\Delta\bar{C}_{nm}\sin m\lambda_P+\Delta\bar{S}_{nm}\cos m\lambda_P)\,. \tag{B.3}$$

For the North component, using Eq. (B.1a) together with Eq. (2.23b) to Eq. (2.29a), we receive

$$
\begin{aligned}
d_n(\theta_P,\lambda_P) &= -\frac{R^3}{M}\iint \cos\alpha\cdot\Delta\sigma(\theta_Q,\lambda_Q)\sum_{n=1}^{\infty} l'_n \frac{\partial \bar{P}_n(\cos\psi_{PQ})}{\partial\psi_{PQ}} d\Omega \\
&= -\frac{R^3}{M}\sum_{n=1}^{\infty}\frac{l'_n}{2n+1}\iint \Delta\sigma(\theta_Q,\lambda_Q)\sum_{m=0}^{n}\frac{\partial \bar{P}_{nm}(\cos\theta_P)}{\partial\theta_P}\bar{P}_{nm}(\cos\theta_Q)\cos m(\lambda_P-\lambda_Q)d\Omega \\
&= -\frac{4\pi R^4\rho_{\mathrm{w}}}{M}\sum_{n=1}^{\infty}\frac{l'_n}{2n+1}\sum_{m=0}^{n}\frac{\partial \bar{P}_{nm}(\cos\theta_P)}{\partial\theta_P}\Big(\frac{\cos m\lambda_P}{4\pi a\rho_{\mathrm{w}}}\iint \Delta\sigma(\theta_Q,\lambda_Q) \\
&\cdot \bar{P}_{nm}(\cos\theta_Q)\cos m\lambda_Q + \frac{\sin m\lambda_P}{4\pi a\rho_{\mathrm{w}}}\iint \Delta\sigma(\theta_Q,\lambda_Q)\bar{P}_{nm}(\cos\theta_Q)\sin m\lambda_Q\Big)d\Omega \\
&= -\frac{3R\rho_{\mathrm{w}}}{\rho_{\mathrm{e}}}\sum_{n=1}^{\infty}\frac{l'_n}{2n+1}\sum_{m=0}^{n}\frac{\partial \bar{P}_{nm}(\cos\theta_P)}{\partial\theta_P}\left(\cos m\lambda_P\Delta C^{\sigma}_{nm}+\sin m\lambda_P\Delta S^{\sigma}_{nm}\right), \qquad \text{(B.4)}
\end{aligned}
$$

and apply Eq. (2.16), we finally obtain the spherical harmonics approach for the North component, see Eq. (B.5),

$$
d_n(\theta_P,\lambda_P) = -R\sum_{n=1}^{\infty}\frac{l'_n}{1+k'_n}\sum_{m=0}^{n}\frac{\partial \bar{P}_{nm}(\cos\theta_P)}{\partial\theta_P}\left(\Delta\bar{C}_{nm}\cos m\lambda_P+\Delta\bar{S}_{nm}\sin m\lambda_P\right). \qquad \text{(B.5)}
$$

Acknowledgments

Time flies and now I have reached the end of my PhD study period. When I look back, it has been a valuable and unforgettable period full of struggling, happiness and success. I could have not finished my thesis without numerous help and assistances from many people. At this moment, I would like to express my gratitudes to all of you.

First of all, my sincere gratitude goes to my supervisor Prof. Dr.-Ing. Nico Sneeuw who has given me his tremendous supports and guidances throughout my PhD study. I have enjoyed every discussion with you as well as your valuable comments on my thesis. You seem to me not only an excellent supervisor but also a good friend. Thank you.

I am also grateful to my co-supervisor Prof. Tonie van Dam who brought me into the interesting loading field. Three visits to your research group helped me a lot in finalizing this thesis and also opened new doors for future research possibilities. Thank you.

I thank also all former and current colleagues from the Institute of Geodesy, University of Stuttgart, for your help and company. In particular, thank you, Dr. Balaji Devaraju, for your assistances in GRACE data filtering, GMT plotting and so on. Thank you, Dr. Matthias Weigelt, Dr. Mohammad J. Tourian, Dr. Markus Antoni, Matthias Roth and Christof Lorenz for your valuable help and discussions. Special thanks also go to Ms. Anita Vollmer for your kind help in dealing with whatever German documents.

I also greatly appreciate all the colleagues from the Geophysics Laboratory, University of Luxembourg. Good memories from three visits to there always stay in my mind. Especially, I thank Dr. Zhao Li and Lin Wang very much for your help and fruitful discussions over loading theory and Green's functions.

One week stay in DGFI (German Geodetic Research Institute, Munich) enriched a lot my understanding in my research. I appreciate all the colleagues there as well, especially Prof. Dr.-Ing. Florian Seitz for your generous host.

Many datasets are used in this thesis and data providers are sincerely acknowledged. I appreciate Dr. Xavier Collilieux (IGN, France) and Dr. Laura Sánchez (DGFI) for providing GPS datasets, GFZ GRACE team for making GRACE data available, Dr. Pascal Gegout (CNRS, France) for providing site-dependent loading Love numbers, Dr. Adewale Amosu (CERI, University of Memphis, America) for providing local loading dataset.

Life is not easy in a foreign country and I always recall those good time with all my Chinese friends in Stuttgart. It is hard to mention all your names here but I appreciate you very much for making my life here enjoyable and unforgettable. Thank you. Particularly, Dr. Wei Zhao is greatly acknowledged for helping me at the very beginning of my life here.

Financial supports from China Scholarship Council are high thanked during my PhD study. Developers of the GMT software which helps me to produce many figures in my thesis are also appreciated here.

Most importantly, my father Zufu Chen and my mother Yeju Qin are sincerely appreciated for your endless love and support. I am so indebted to you as I could not spend much time with you over the past years. My special thanks also go to my dear sister Ying Chen for taking care of our parents when I was away from home. Last but not least, I am so grateful to my wife Maojing Ye for your unconditional understanding, encouragement and support. You are the one I will cherish forever and I promise here I will never ever stay far away from you from now on. Be with you all the time in our future.